UNIVERSIDADE ESTADUAL DE CAMPINAS
Faculdade de Engenharia Química

BRUNA ALICE GOMES DE MELO

PADRONIZAÇÃO DO L-PRP E FORMAÇÃO DE REDES POLIMÉRICAS SEMI-INTERPENETRADAS DE ÁCIDO HIALURÔNICO E FIBRINA DO L-PRP NA DIFERENCIAÇÃO CONDROGÊNICA E OSTEOGÊNICA DE CÉLULAS MESENQUIMAIS DE TECIDO ADIPOSO HUMANO

CAMPINAS
2019

UNIVERSIDADE ESTADUAL DE CAMPINAS
Faculdade de Engenharia Química

PADRONIZAÇÃO DO L-PRP E FORMAÇÃO DE REDES POLIMÉRICAS SEMI-INTERPENETRADAS DE ÁCIDO HIALURÔNICO E FIBRINA DO L-PRP NA DIFERENCIAÇÃO CONDROGÊNICA E OSTEOGÊNICA DE CÉLULAS MESENQUIMAIS DE TECIDO ADIPOSO HUMANO

Bruna Alice Gomes de Melo
Doutoranda

Profa. Dra. Maria Helena Andrade Santana
Orientadora

Apresentação da Tese de Doutorado para obtenção do título de Doutora em Engenharia Química pela Faculdade de Engenharia Química da Universidade Estadual de Campinas.

ESTE EXEMLAR CORRESPONDE À VERSÃO FINAL DA TESE DEFENDIDA PELA ALUNA BRUNA ALICE GOMES DE MELO E ORIENTADA PELA PROF.ª DR.ª MARIA HELENA ANDRADE SANTANA

CAMPINAS
2019

Ficha catalográfica
Universidade Estadual de Campinas
Biblioteca da Área de Engenharia e Arquitetura
Elizangela Aparecida dos Santos Souza - CRB 8/8098

M491p

Melo, Bruna Alice Gomes de, 1985-
Padronização do L-PRP e formação de redes poliméricas semi-interpenetradas de ácido hialurônico e fibrina do L-PRP na diferenciação condrogênica e osteogênica de células mesenquimais de tecido adiposo humano / Bruna Alice Gomes de Melo. – Campinas, SP : [s.n.], 2019.

Orientador: Maria Helena Andrade Santana.
Tese (doutorado) – Universidade Estadual de Campinas, Faculdade de Engenharia Química.

1. Plaqueta (Sangue). 2. Leucócitos. 3. Fibrina. 4. Ácido hialurônico. 5. Células mesenquimais estromais. I. Santana, Maria Helena Andrade, 1951-. II. Universidade Estadual de Campinas. Faculdade de Engenharia Química. III. Título.

Informações para Biblioteca Digital

Título em outro idioma: L-PRP standardization and formation of semi-interpenetrating polymer networks of hyaluronic acid and fibrin form L-PRP for chondrogenic and osteogenic differentiation of human adipose-derived mesenchymal stem cells
Palavras-chave em inglês:
Platelet (Blood)
Leukocytes
Fibrin
Hyaluronic acid
Stromal mesenchymal cells
Área de concentração: Engenharia Química
Titulação: Doutora em Engenharia Química
Banca examinadora:
Maria Helena Andrade Santana [Orientador]
Ângela Cristina Malheiros Luzo
Willian Dias Belangero
Bradley David Olsen
Maria Helena Ambrósio Zanin
Ana Luiza Garcia Millas Massaguer
Data de defesa: 24-04-2019
Programa de Pós-Graduação: Engenharia Química

- ORCID do autor: https://orcid.org/0000-0001-6401-1102
- Currículo Lattes do autor: http://buscatextual.cnpq.br/buscatextual/visu

Identificação e informações acadêmicas do(a) aluno(a)

FOLHA DE APROVAÇÃO

Folha de Aprovação da Defesa de Tese defendida por Bruna Alice Gomes de Melo aprovada em 24 de abril de 2019 pela banca examinadora constituída pelos seguintes doutores:

Profa. Dra. Maria Helena Andrade Santana
FEQ / UNICAMP

Dra. Ângela Cristina Malheiros Luzo
Hemocentro-UNICAMP

Prof. Dr. William Dias Belangero
FCM / UNICAMP

Dr. Bradley David Olsen
Massachusetts Institute of Technology (MIT)

Dra. Maria Helena Ambrósio Zanin
IPT – Instituto de Pesquisas Tecnológicas

Dra. Ana Luiza Garcia Millas Massaguer
Soluções em Biotecnologia 3D

ATA da Defesa com as respectivas assinaturas dos membros encontra-se no SIGA/Sistema de Fluxo de Dissertação/Tese e na Secretaria do Programa da Unidade.

AGRADECIMENTOS

Finalizar o doutorado no momento da ascensão de um presidente que é contrário à capacitação do povo brasileiro pelo acesso à educação gratuita e de qualidade, e contrário ao crescimento e à prosperidade do país, o que só é possível pelo investimento em ciência e tecnologia, não foi uma tarefa fácil. Termino de escrever essa tese com a esperança de que esse terrível momento é passageiro, e que o povo do meu país amado terá recoberto a lucidez, para assim, podermos retomar o caminho da prosperidade educacional, intelectual, científica e tecnológica.

Agradeço inicialmente à Prof.ª Maria Helena A. Santana por ter me guiado pelo caminho científico, e me dado a oportunidade de realizar esse trabalho o qual tenho imenso carinho.

Agradeço à Dr.ª Ângela C. M. Luzo, pela colaboração e fornecimento das células mesenquimais de tecido adiposo humano e à Dr.ª Adriana da Silva S. Duarte pela ajuda com o cultivo das células e os ensaios de RT-PCR.

Ao Prof. Dr. Marcos Akira D'Ávila, pelo uso do rêometro, e aos seus alunos, pela ajuda com a realização dos experimentos.

Ao Prof. Dr. William Dias Belangero, pelo uso do laboratório, e à Nilza Batista, pela grande ajuda com o uso do ponto crítico e com os experimentos de histologia.

À equipe do LRAC, principalmente Lucélia Silva, Hugo Teixeira, Celso Camargo e Adilson Brandão, pelos ensaios realizados e esclarecimentos prestados.

Aos doadores que literalmente deram o sangue pela ciência, e tornaram o meu trabalho possível.

Aos membros da banca avaliadora do doutorado, Dr.ª Ângela C. M. Luzo, Prof. Dr. Bradley David Olsen, Prof. Dr. William Dias Belangero, Dr.ª Maria Helena Ambrósio Zanin e Dr.ª Ana Luiza Garcia Millas Massaguer, que dedicaram seu tempo para a leitura do texto, e pelos comentários valiosos, que ajudaram a melhorar o trabalho.

Ao técnico do LDPB, Gilson Maia, pelo companheirismo e ajuda em muitos momentos durantes todos esses anos em que estive no laboratório. Agradeço também aos muitos amigos que fiz no LDPB, Fernanda Motta, Sofia Galdames, Andréa Shimojo, Valéria Santos, Amanda Marcelino, André Cavalcanti, Fabiane Moreira, Denise Vilalba, Carla França e Daniel Pereira,

pela companhia, auxílio com experimentos e ideias, e por ajudarem a tornar o trabalho mais leve e prazeroso.

Aos inúmeros amigos que fiz na FEQ, principalmente Amanda Noronha e Laise Maia, que foram minhas grandes amigas e companheiras de pós graduação.

À Unicamp, minha universidade querida. Que privilégio ter vivido e aprendido tanto nesse lugar ao longo de 12 anos.

Agradeço imensamente à Dr.ª Su Ryon Shin, do Shin Lab na Harvard Medical School/Brigham and Women's Hospital, por ter me acolhido em um momento de extrema dificuldade durante meu doutorado sanduíche, e me possibilitado realizar um trabalho de extrema qualidade, e também por todo aprendizado adquirido sob sua supervisão. Agradeço ainda às grandes amigas que ganhei nesse período, Yasamin Aliashrafi, Shreya Mehrotra e Raquel Rodrigues, pelo companheirismo, auxílio nos experimentos e amizade, que tornaram meus dias nesse lugar frio muito mais caloroso.

Agradeço à minha família, especialmente minha mãe querida Rosa, meus irmãos Karla, Jéssica e Diego, minha sobrinha linda Lavínia e meu pai Expedito, por todo apoio ao longo desses anos. Agradeço também meu namorado Alex Dante, pelo companheirismo mesmo estando longe, pelo apoio, amor e amizade.

Agradeço por fim, à Fundação de Amparo à Pesquisa do Estado de São Paulo (FAPESP), Processo 2015/23134-8, por financiar o projeto, tornando a realização desse trabalho possível.

I didn't come to play, I came to slay!

Shea Couleé

RESUMO

O plasma rico em leucócitos e plaquetas (L-PRP) é um produto autólogo, no qual plaquetas, leucócitos e outros componentes do sangue total são concentrados em uma pequena fração de plasma. Atualmente, os concentrados de leucócitos e plaquetas são reconhecidos como produtos biológicos versáteis e eficientes para a regeneração tecidual, com uma ampla gama de aplicações clínicas, sendo muito utilizado em tratamentos da osteoartrite. O ácido hialurônico (AH) é um polissacarídeo endógeno presente na matriz extracelular da cartilagem articular e no fluido sinovial. A associação entre L-PRP e AH exógeno de diferentes massas molares (MM), tem mostrado benefícios sinérgicos no tratamento de lesões de cartilagem e osso, promovendo redução da inflamação, alívio da dor e prolongamento dos efeitos individuais dos seus componentes. Apesar da crescente inclusão do AH com o L-PRP nos protocolos clínicos, a literatura ainda é escassa na descrição dos protocolos de preparação tanto do L-PRP quanto da mistura L-PRP-AH. Além disso, os mecanismos envolvidos, a formação das novas estruturas e o comportamento biológico proveniente dessa associação carece de caracterização. Sendo assim, esse trabalho teve como objetivo padronizar as condições de obtenção do L-PRP e estudar *in vitro* as estruturas formadas pela associação L-PRP e AH de baixa e alta MM, assim como sua influência na liberação de fatores solúveis que direcionam a diferenciação condrogênica e osteogênica de células mesenquimais do tecido adiposo humano (h-AdMSCs). Pelo delineamento de condições de centrifugação do sangue total, foi possível obter L-PRP com razões plaqueta/leucócito e linfócito/granulócito bem definidas, que resultaram em diferentes comportamentos biológicos. A mistura homogênea e controlada do L-PRP e AH formou redes poliméricas semi-interpenetradas (semi-RPIs) de fibrina-AH, após ativação do L-PRP com trombina/cálcio, com propriedades estruturais e reológicas ajustáveis dependendo da MM do AH. A presença dos AHs também influenciou diretamente na liberação de fatores de crescimento e citocinas pelas plaquetas e leucócitos presentes nas semi-RPIs, assim como na adesão, crescimento e diferenciação condrogênica e osteogênica das h-AdMSCs. Esses resultados são relevantes para a padronização da produção do L-PRP, da mistura L-PRP-AH e dos hidrogéis fibrina-AH, visando aprimorar os protocolos clínicos. Além disso, o trabalho contribui para o entendimento dos fenômenos envolvidos na associação L-PRP-AH que levam à regeneração tecidual.

Palavras-chave: Plaqueta; leucócito; fibrina; ácido hialurônico; células mesenquimais.

ABSTRACT

Leukocyte- and platelet rich plasma (L-PRP) is an autologous product, in which platelets, leukocytes, and other blood components are concentrated in a small fraction of plasma. Nowadays, concentrated of leukocytes and platelets are recognized as versatile biological products that are effective for tissues regeneration, presenting a wide range of clinical applications, and being largely used in the treatment of osteoarthritis. Hyaluronic acid (HA) is an endogenous polysaccharide present in the extracellular matrix (ECM) of articular cartilage and synovial fluid. The association between L-PRP and exogenous HA of different molar masses (MM) has shown synergistic benefits in the treatment of cartilage and bone injuries, promoting reduction of inflammation, pain relief and prolongation of the effects of the individual components. Despite the growing inclusion of HA associated with L-PRP in clinical protocols, there is a lack of information in the literature concerning the standardization of L-PRP and L-PRP-HA preparation. In addition, the involved mechanisms, formation of new structures and biological behavior resulted from this interaction lacks characterization. Therefore, this work aimed to standardize L-PRP preparation and study the structures formed from L-PRP-HA association, using HA of low and high MM (LMM and HMM, respectively). Their influence on soluble factors release was investigated, and on chondrogenic and osteogenic differentiation of human adipose-derived mesnchymal stem cells (h-AdMSCs) *in vitro*. By designing the whole blood centrifugation conditions, it was possible to obtain L-PRP with well-defined platelet/leukocyte and lymphocyte/granulocyte ratios that resulted in different biological behavior. The homogeneous and controlled mixture of L-PRP and HA formed fibrin-HA semi-interpenetrating polymer networks (semi-IPNs), after L-PRP activation by thrombin/calcium, with structure and rheological properties tunable with HA MM. The presence of HAs directly influenced the release of growth factors and cytokines by platelets and leukocytes present in the semi-IPNs, as well as the adhesion, growth and chondrogenic and osteogenic differentiation of h-AdMSCs. These results are relevant to standardize the preparation of L-PRP, L-PRP-HA mixture and fibrin-HA hydrogels, aiming to improve clinical protocols. In addition, this work contributes to the understanding of the phenomena involved in the L-PRP-HA association that lead to tissues regeneration.

Keywords: Platelet; leukocyte; fibrin; hyaluronic acid; mesenchymal stem cells.

LISTA DE ABREVIATURAS E SIGLAS

3D	Tridimensional
ACD-A	Anticoagulante citrato ácido dextrose
AH	Ácido hialurônico
BC	*Buffy coat*
BL	Camada inferior
Ca^{2+}	Íon cálcio
Ca	Cálcio
$CaCl_2$	Cloreto de cálcio
CD44	Glicoproteína transmembrana
DAPI	*2-(4-amidinophenyl)-1-indole-6-carboxamidine*
DI	Água deionizada
DMEM	*Dulbecco's Modified Eagle Medium* (meio de cultura)
DMSO	Dimetilsulfóxido
EDS	Espectroscopia de raios X por dispersão em energia
ECM	*Extracellular matrix*
FBS	Soro fetal bovino
FC	Fator de crescimetno
FGF	Fator de crescimento fibroblástico
Fp	Fibrinopeptídeo
FTIR	Espectroscopia no infravermelho com transformada de Fourier
G’	Módulo de armazenamento
G”	Módulo de perda
GAG	Glicosaminoglicano
GF	*Growth factor*
GlcUA	Ácido D-glicurônico
GlcNAc	N-acetilglicosamina
HA	*Hyaluronic acid*
h-AdMSC	Células mesenquimais de tecido adiposo humano
hMSC	Células mesenquimais de medula óssea humana
HMM	Ácido hialurônico de alta massa molar *(high molar mass HA)*
HPRT	Hipoxantina-guanina fosforibosiltransferase

IL	Interleucina
IPN	*Interpenetrating polymer network*
K	*Consistency index*
L_0	Diâmetro da amostra cortada para reologia
LMM	Ácido hialurônico de baixa massa molar *(low molar mass HA)*
L-PRP	Plasma rico em leucócitos e em plaquetas
L-PRF	Plasma rico em fibrina
m	Índice de consistência
MEC	Matriz extracelular
MEV	Microscopia eletrônica de varredura
MEM	M*inimum Essential Media*
MM	Massa molar
MSC	Células mesenquimais
MTT	Bbrometo de [3-(4,5-dimetiltiazol-2yl)-2,5-difenil tetrazolium]
n	Índice da Lei das Potências
NaOH	Hidróxido de sódio
Na_2CO_3	Carbonato de sódio
P	Potássio
P-PRP	Plasma predominantemente rico em plaquetas (pobre em leucócitos
PBS	Tampão fosfato salino
PRP	Plasma rico em plaquetas
PDGF	Fator de crescimento derivado de plaqueta
PDMS	Polidimetil siloxano
PEG	Polietileno glicol
ROS	*Reactive oxygen species*
RPI	Rede polimérica interpenetrada
RT-PCR	Reação em cadeia polimerase em tempo real
SD	*Standard deviation*
SEM	*Scanning electron microscopy*
Semi-RPI	Rede polimérica semi-interpenetrada
Semi-IPN	*Semi-interpenetrating polymer network*
Sox 9	Fator de transcrição Sox 9
TGF	Fator de crescimento transformador

TLR	Receptor do tipo Toll
TNF	Tumor de necrose tumoral
UL	Camada superior
UV	Luz ultravioleta
VEGF	Fator de crescimento vascular endotelial
W_d	Massa dos hidrogéis secos antes do intumescimento
W_s	Massa dos hidrogéis depois do intumescimento
W_i	Massa dos hidrogéis secos antes da degradação
W_f	Massa dos hidrogéis depois da degradação

SUMÁRIO

CAPÍTULO 1:
INTRODUÇÃO GERAL

1. INTRODUÇÃO GERAL

1.1. Colocação do problema

O plasma rico em plaquetas (P-PRP) é um produto autólogo, produzido por meio da centrifugação do sangue total, processo que permite separar eritrócitos e concentrar os demais componentes do sangue em uma pequena fração de plasma (Marx et al., 1998). Devido à alta concentração de plaquetas, o PRP é frequentemente utilizado em tratamentos onde a cicatrização de feridas e regeneração tecidual é dificultada. Isso porque as plaquetas quando ativadas, liberam fatores de crescimento (FCs), os quais juntamente com os linfócitos, monócitos, macrófagos e granulócitos, possuem papel fundamental na cascata de cicatrização e no processo de formação de novos tecidos (Everts et al., 2006a; Zhu et al., 2013). Além disso, a sua ativação desencadeia a decomposição do fibrinogênio em fibras de fibrina, que se estruturam numa rede cuja arquitetura funciona como um suporte natural para a adesão, proliferação e diferenciação das células tronco até a formação do novo tecido (Miron et al., 2016; Wolberg, 2007). Dessa forma, o PRP vem sendo amplamente utilizado em tratamentos de osteoartitre, promovendo redução da inflamação, alívio da dor e regeneração dos tecidos cartilaginoso e ósseo (Filardo, Kon, Teresa, et al. 2012; McCarrel et al. 2012; Riboh et al. 2015).

Dentre as formulações mais difundidas, estão o PRP pobre em leucócitos (P-PRP) e o plasma rico em leucócitos e em plaquetas (L-PRP). Apesar do papel fundamental dos leucócitos, a literatura reporta em sua grande maioria o preparo e estudos de aplicações do P-PRP, visando minimizar seu efeito catabólico, representado principalmente pela alta secreção de citocinas inflamatórias (Sundman et al., 2011). Por esse motivo, ainda há controvérsias quanto ao uso clínico do L-PRP na medicina regenerativa. Diante da complexidade do sistema, o efeito conjunto de plaquetas e leucócitos promove um balanço anabólico/catabólico cujos mecanismos moleculares e celulares ainda não são completamente entendidos.

Durante o processo de cicatrização da cartilagem, células mesenquimais (MSCs) autólogas são recrutadas para o local da lesão pelos FCs e citocinas, e estimuladas à se proliferar, diferenciar e produzir matriz extracelular (MEC), formando o novo tecido (Qian et al., 2017). Devido à baixa disponibilidade local dos condrócitos, MSCs exógenas vêm sendo muito empregadas em terapias celulares e na medicina regenerativa, pois são altamente disponíveis em diferentes tecidos, e possuem grande capacidade de se diferenciar em diversos tipos de células (Caplan, 1991). Uma das maiores fontes de MSCs é o tecido adiposo humano,

e as MSCs derivadas desse tecido (h-AdMSCs) possuem a vantagem se serem obtidas e isoladas ainda mais facilmente, por exemplo, durante o processo de lipoaspiração (Doran, 2015). Além disso, seu uso em estudos envolvendo a regeneração da cartilagem tem mostrado resultados positivos e com potencial elevado quando associadas ao PRP (Tobita et al., 2015; Van Pham et al., 2013).

O ácido hialurônico (AH) é um polissacarídeo natural encontrado em tecidos conjuntivos de mamíferos, muito empregado em aplicações cosmética e farmacêutica. Isso devido principalmente ao seu alto grau de hidratação e viscoelasticidade, características das quais resultam o seu uso clínico mais difundido, em aplicações estéticas e reparo de articulações (Balazs and Denlinger, 1993; Papakonstantinou et al., 2012). A forma nativa do AH, ou seja, a mais amplamente distribuída em tecidos conjuntivos, é a de alta massa molar (MM) (10^6 - 10^7 Da). Naturalmente, esse AH é degradado em frações de baixa MM e oligossacarídeos por hialuronidases e espécies reativas de oxigênio, que possuem outras funções fisiológicas específicas, como as de sinalização e de estímulo à angiogênese (Slevin et al., 2002). A aplicação do AH exógeno de diferentes MM em pacientes com lesões articulares tem mostrado alta capacidade de estímulo para a formação de AH endógeno, contribuindo para a restauração da MEC e viscoelasticidade do microambiente (Bhandari et al., 2017; Shewale et al., 2017).

Os efeitos sinérgicos da associação entre o L-PRP e o AH exógeno em aplicações clínicas tem mostrado resultados promissores nos tratamentos da osteoartrite em relação à ambos os materiais individualmente (Lana et al., 2016; Marmotti et al., 2012). A associação do L-PRP com o AH não reticulado forma redes poliméricas semi-interpenetradas (semi-RPIs), caraterizadas como redes formadas por dois ou mais polímeros, onde ao menos um deles está sob forma linear, ou seja, não reticulada (Dong et al., 2012). Após a ativação do L-PRP com a mistura trombina/cálcio, a fibrina polimeriza na presença de glóbulos emaranhados de AH, cuja conformação e tamanho globular varia de acordo com a concentração e MM do AH, resultando em uma rede estável com AH e fibrina interagidos por ligações eletrostáticas e hidrofóbicas (LeBoeuf et al., 1986; Vadalá et al., 2017; Weigelt et al., 1986). A presença do AH altera as propriedades das redes, o estado de ativação dos leucócitos, e a resposta celular, modulados pela MM do AH, o que consequentemente, influencia no processo regenerativo (de la Motte, 2011; Komorowicz et al., 2016; Leboeuf et al., 1987).

Dentro desse contexto, esse trabalho de doutorado foi desenvolvido para contornar a ausência da padronização do preparo do L-PRP e da mistura L-PRP-AH, cuja abordagem é fundamental para compreender os fenômenos envolvidos no processo de regeneração da

cartilagem e do osso. Dessa forma, o trabalho envolveu aspectos que incluiu interações interdisciplinares com pesquisadores das áreas de ortopedia, hematologia e engenharia. O estudo foi composto pelo delineamento das condições de centrifugação do sangue total, visando obter diferentes formulações de L-PRP, onde faixas de aceleração centrífuga foram bem definidas, estabelecendo-se diferentes razões plaquetas/leucócitos e linfócitos/granulócitos; pela padronização das condições de mistura do L-PRP e AH, visando a formação de misturas homogêneas e semi-RPIs estáveis; pela caracterização das propriedades estruturais e reológicas das semi-RPIs; e pelo estudo da resposta biológica às semi-RPIs, quanto à liberação de fatores solúveis e à diferenciação condrogênica e osteogênica das h-AdMSCs.

1.2. Objetivo e metas

O objetivo geral do trabalho foi a padronização do preparo do L-PRP e da mistura L-PRP-AH para a formação redes semi-interpenetradas de fibrina e AH de diferentes MM, visando estudar os efeitos do balanço anabólico/catabólico do L-PRP e a presença do AH na diferenciação condrogênica e osteogênica de h-AdMSCs.

Para atingir o objetivo proposto, o projeto seguiu as seguintes metas:

- Preparo e caracterização das formulações de L-PRP em condições operacionais de centrifugação, padronizadas para obtenção de razões definidas de plaquetas e leucócitos;
- Estudo dos efeitos das razões plaquetas/leucócitos e linfócitos/granulócitos de L-PRPs no balanço anabólico/catabólico do microambiente e na resposta de h-AdMSCs;
- Preparo de semi-RPIs formadas pela mistura entre L-PRP e AH de baixa e alta MM, sob condições controladas de preparo;
- Caracterização dos efeitos da associação L-PRP-AH nas propriedades reológicas da mistura e das semi-RPIs, assim como na estrutura e arquitetura das redes;
- Estudo dos efeitos das semi-RPIs na liberação de FCs (PDGF-BB, TGF-β1, VEGF) e citocinas (IL-1β; IL-6, IL-8 e IL10);
- Caracterização do comportamento celular como adesão, viabilidade, crescimento e diferenciação condrogênica e osteogênica das h-AdMSCs cultivadas nas semi-RPIs.

CAPÍTULO 2:
REVISÃO DA LITERATURA

2. REVISÃO DA LITERATURA

2.1. Plasma-rico em plaquetas (PRP)

O PRP é um produto autólogo preparado a partir do sangue total do doador ou paciente, onde estão concentrados plaquetas, leucócitos (linfócitos e granulócitos), proteínas e outros componentes dispersos numa pequena fração de plasma. PRP é uma definição geral, a qual começou a ser empregada nos anos 90, quando o mesmo passou a ser utilizado em diferentes áreas da medicina regenerativa (Marx et al., 1998; Tayapongsak et al., 1994). Dentre as formulações mais difundidas estão o plasma predominantemente rico em plaquetas (P-PRP), sendo a formulação mais reportada na literatura, e o plasma rico em leucócitos e em plaquetas (L-PRP), que devido à presença de plaquetas e leucócitos na composição secreta fatores anabólicos (FCs e citocinas anti-inflamatórias) e catabólicos (citocinas inflamatórias, metaloproteínas e espécies reativas de oxigênio) (Dohan Ehrenfest et al., 2009). Apesar de deletérias para as células e MEC quando em excesso, os fatores catabólicos possuem papel fundamental na cascata da cicatrização (Anitua et al., 2015; Yin et al., 2016). Dessa forma, a aplicação clínica de formulações ricas em leucócitos vem crescendo e tem mostrado resultados efetivos no tratamento de lesões, principalmente nas quais a regeneração tecidual é dificultada (Cieslik-Bielecka et al. 2009; Jia et al. 2018; Liu et al. 2018; Riboh et al. 2015a; Yerlikaya et al. 2018). A composição e concentração de plaquetas e leucócitos pode variar de acordo com a necessidade do paciente, como local, gravidade e estágio da lesão, podendo ser controlada no processo de preparação do L-PRP.

2.1.1. Preparo do L-PRP

O método de preparo do L-PRP mais empregado é a centrifugação, processo em que é possível separar as células vermelhas, ou eritrócitos, e concentrar as plaquetas e leucócitos no plasma. Inicialmente, o sangue total é coletado na presença de anticoagulante para evitar a coagulação e ativação plaquetária. Após a centrifugação, três camadas de sangue são formadas, a camada superior ou sobrenadante, que é predominantemente rico em plaquetas; a camada intermediária ou *buffy coat*, onde os leucócitos são concentrados; e a camada inferior, onde os eritrócitos ficam sedimentados. A coleta do sobrenadante resulta na obtenção do P-PRP e a coleta do sobrenadante e *buffy coat* resulta na obtenção do L-PRP (Figura 1).

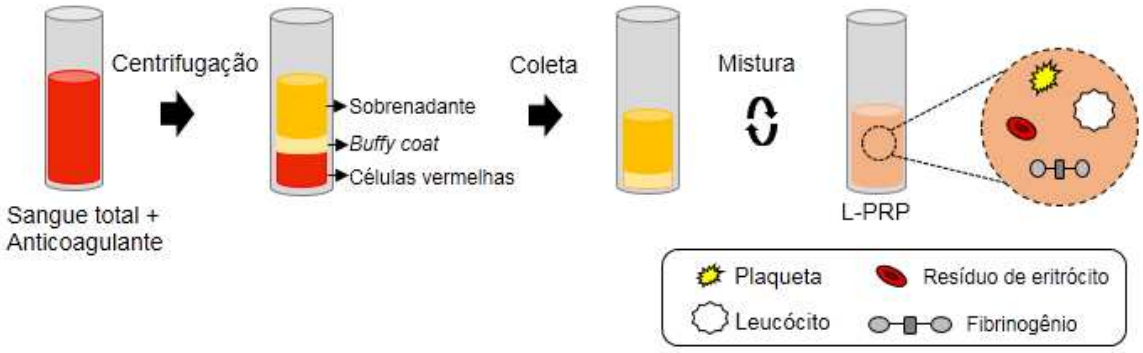

Figura 1. Esquema ilustrando a obtenção do L-PRP por centrifugação.

A centrifugação, apesar da simplicidade da operação, é um processo complexo, onde fatores como aceleração, tempo, número de ciclos, além das propriedades estruturais dos componentes do sangue influenciam diretamente na sua separação e na composição do L-PRP (de Melo et al. 2018; Perez et al. 2014; Perez et al. 2013). Por isso a importância da padronização do preparo, para que esse seja de forma reprodutível, e que haja um consenso sobre a composição dos diferentes tipos de formulações a serem aplicadas clinicamente, embora a concentração dos componentes do sangue também dependa fortemente de cada doador (Ehrenfest et al., 2014; Weibrich et al., 2001).

Uma vez preparado, o L-PRP está pronto para ser ativado, formar as redes de fibrina e desencadear a liberação dos FCs, que juntamente com outros componentes, estimularão o processo de regeneração do tecido lesado.

2.1.2. Ativação e formação das fibras de fibrina

A ativação do L-PRP é feita a partir de um conjunto de reações que compõem a parte final da cascata de coagulação do sangue, na qual a trombina, tendo o cálcio como cofator, decompõe o fibrinogênio em fibras de fibrina. O fibrinogênio é clivado pela trombina nos terminais N das cadeias Aα e Bβ, processo que libera os fibrinopeptídeos FpA e FpB, deixando as cadeias α e β disponíveis para reagir com os terminais C das cadeias γ, e assim, iniciar a reação de polimerização (Figura 2A) (Scheraga, 2004). Essa reação forma uma rede 3D, com fibras de fibrina interconectadas de forma aleatória, sendo um microambiente favorável para garantir o suporte celular (Figura 2B).

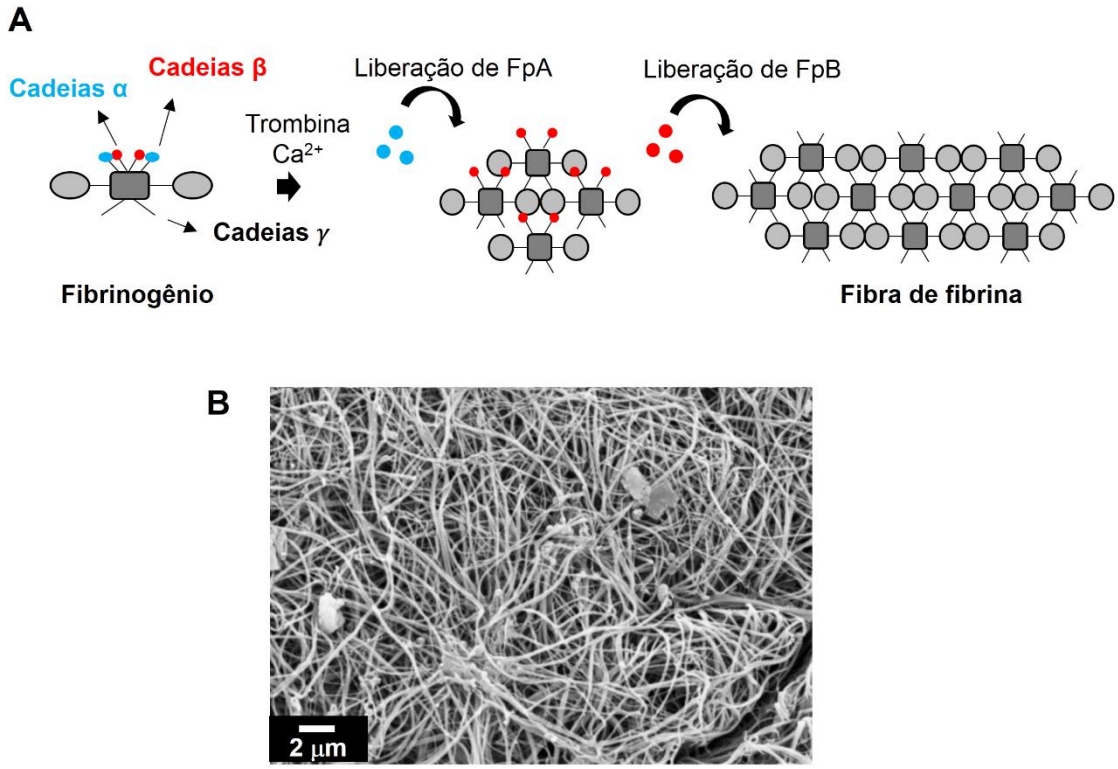

Figura 2. Formação das redes de fibras. (A) Esquema representando a formação de fibra de fibrina através da ativação do fibrinogênio por trombina e cálcio, que liberam fibrinopeptídeos, permitindo a reação de polimerização. (B) Imagem de uma rede de fibrina do L-PRP preparado em nosso laboratório, obtida por microscopia eletrônica de varredura (MEV).

In vitro, o L-PRP é usualmente ativado com uma combinação de soro autólogo contendo trombina (proveniente do mesmo doador) e cloreto de cálcio. Normalmente as fibras crescem com maior velocidade na direção longitudinal e mais lentamente na direção lateral, características que, assim como as propriedades físicas e reológicas, podem ser alteradas de acordo com variação da concentração de fibrinogênio, trombina, força iônica, proporção trombina e cálcio, ou pela presença de outros fatores externos, como o AH (Leboeuf et al. 1987; Komorowicz et al. 2016; Perez et al. 2014).

Muitos trabalhos da literatura dentro da engenharia de tecidos utilizam as redes de fibrina como suporte sozinha, ou combinada com outros polímeros na forma de RPIs ou semi-RPIs, visando o estudo da regeneração de diversos tipos de tecidos (Arulmoli et al., 2016; Bensaïd et al., 2003; Vadalá et al., 2017; Zhang et al., 2016). Para essa finalidade, a fibrina mais utilizada é a comercial, proveniente do plasma humano ou bovino, sendo explorada geralmente apenas como suporte 3D para células. No entanto, a fibrina formada a partir do L-PRP garante não só suporte, mas também um microambiente biologicamente rico, podendo garantir maior

eficiência na migração, proliferação e diferenciação celular (Bielecki et al., 2008; Kazemi and Fakhrjou, 2015).

2.1.3. Fatores de crescimento (FCs) e citocinas

As plaquetas são os menores componentes do sangue, e possuem dentro de sua estrutura inúmeras biomoléculas, como serotonina, lisossomo, glicogênio, cálcio e α-grânulos, que por sua vez contêm FCs e outras proteínas. Quando ativadas, no momento da lesão, as plaquetas mudam da forma arredondada para alongada, e nesse processo, os FCs são liberados e começam a atuar no instante da injúria, sinalizando e regulando o comportamento celular (Everts et al. 2006). Os FCs mais abundantes nas plaquetas são o FC derivado de plaquetas (PDGF), o FC transformador (TGF-β) e o FC vascular endotelial (VEGF). O PDGF, que existe na forma de diferentes isômeros, como o PDGF-BB, possui papel fundamental na cascata de cicatrização, regulando o comportamento de diferentes tipos celulares e estimulando a mitose, quimiotaxia de células (MSCs, fibroblastos, condrócitos e osteócitos, por exemplo), produção de outros FCs, e produção de MEC como colágeno e glicosaminoglicanos (GAGs), sendo portanto, de extrema importância para a regeneração da cartilagem (Hung et al., 2015; Schmidt et al., 2006). Juntamente com o PDGF, o TGF-β é um dos primeiros FCs liberados após uma lesão. Ele existe em três isoformas, TGF-β1, TGF-β2 e TGF-β3, sendo o TGF-β1 um dos mais importantes para funções de regeneração do tecido conjuntivo (Chen et al., 2018; Wang et al., 2014). Esse FC regula diversos processos biológicos durante a cascata de cicatrização, como o estímulo à migração, proliferação e diferenciação celular, síntese e preservação de MEC, além de possuir efeitos imunossupressores, anti-inflamatórios e angiogênicos. O TGF-β1 possui ainda grande atividade na regeneração da cartilagem e osso, regulando funções condrogênicas, como a diferenciação das MSCs em condrócitos, estimulando a produção de agregam e colágeno, prevenindo a perda de GAGs, além de recrutar precursores de osteoclastos para formação do tecido ósseo (Janssens et al., 2005; Roman-Blas et al., 2007). O VEGF é o FC responsável principalmente pelo processo de angiogênese, mitogênese, recrutamento e proliferação de células endoteliais (Shiojima and Walsh, 2004). Além disso, são mediadores da ossificação endocondral, processo em que a cartilagem serve como uma espécie de molde para a formação de novo tecido ósseo. No período pós-natal, o VEGF também regula a homeostase e o desenvolvimento da cartilagem, contribuindo com a sobrevivência dos condrócitos em regiões de baixa concentração de oxigênio (Nagao et al., 2017).

Não existem dúvidas a respeito da importância da presença das plaquetas e consequentemente, dos FCs na composição do L-PRP, e como esses componentes favorecem uma eficiente regeneração da cartilagem articular. Diferentemente, a presença dos leucócitos no L-PRP gera muita discussão na literatura, uma vez que a expressão de citocinas inflamatórias, espécies reativas de oxigênio e proteases pode intensificar o efeito catabólico em relação ao anabólico durante o processo regenerativo, como por exemplo, estimular a degradação da MEC (Boswell et al., 2013; Zhou et al., 2015a). No entanto, os leucócitos também possuem funções específicas e fundamentais na cascata de cicatrização, principalmente na fase inflamatória, com propriedades imunológicas, antibacterianas e de controle sobre a migração, proliferação e diferenciação de diferentes tipos de células (Cieslik-Bielecka et al., 2009; Cieslik-Bielecki et al., 2012).

Os monócitos são os menos abundantes no sangue total e consequentemente, no L-PRP. Eles são os precursores dos macrófagos, os quais após a fase inflamatória, migram para o local da lesão e iniciam a remoção de detritos por fagocitose, além de secretar FCs responsáveis por recrutar fibroblastos, promover angiogênese e organizar a nova MEC a ser formada (Das et al., 2015). Os linfócitos, que assim como os monócitos são os componentes não granulares dos leucócitos, também modulam a atividade dos fibroblastos, porém, sua atuação é principalmente na prevenção da imunossupressão durante a lesão (Schäffer and Barbul, 1998). Os neutrófilos, que são a porção mais abundante dos granulócitos, possuem papel crucial na defesa do organismo contra infecções. Eles são os primeiros leucócitos recrutados no momento da lesão, e logo nos primeiros estágios, são ativados e estimulados à liberar proteases e espécies reativas de oxigênio, que contribuem com a limpeza do local removendo bactérias e detritos celulares por fagocitose (Faurschou and Borregaard, 2003; Wilgus et al., 2013). Além disso, as espécies reativas de oxigênio liberadas pelos neutrófilos também são relacionados ao estímulo da atividade celular e proliferação, processo chamado de *cellular waking up* (Lyublinskaya et al., 2015).

A maior preocupação a respeito da presença dos leucócitos é um desbalanço da razão plaquetas/leucócitos, e também da razão linfócitos/granulócitos, que pode acarretar em maior secreção de citocinas inflamatórias do que a encontrada fisiologicamente (Sundman et al., 2011). As citocinas são importantes mediadores da inflamação, e são secretadas principalmente pelos leucócitos, mas também por fibroblastos e células mesenquimais autólogas durante o processo de cicatrização (Apte, 1995; Waterman et al., 2010). A interleucina IL-1 é um potente pró-inflamatório, e juntamente com o TNF-α, outro mediador da inflamação, regula a atividade

do TGF-β durante a regeneração da cartilagem, promovendo um balanço anabólico/catabólico necessário para bom funcionamento do processo regenerativo (Roman-Blas et al., 2007). As citocinas IL-6 e IL-8 também são pró-inflamatórias, e possuem a capacidade de regular a homeostase óssea e capacidade angiogênica (Scheller et al., 2011). Em contrapartida, a IL-10 é uma citocina anti-inflamatória com a função de controlar a produção de mediadores inflamatórios e atuar como imunorregulador contra infecções (Couper et al., 2008).

Diante das questões sobre a composição do L-PRP e sua aplicação clínica, torna-se necessário estudar os efeitos da razão plaqueta/leucócito na liberação de fatores anabólicos e catabólicos, e nas vias que levam à regeneração da cartilagem e osso, visto que uma das maiores aplicações do L-PRP é no tratamento da osteoartrite. Além disso, existe a necessidade de se estabelecer condições padronizadas para o preparo do L-PRP, tais como os parâmetros de centrifugação, que é muito divergente na literatura e nem sempre é especificado, principalmente quando se utilizam kits comerciais, tornando difícil a comparação de resultados. Através da padronização do preparo do L-PRP, pode-se elucidar e modular os efeitos da concentração de plaquetas e leucócitos, assim como as razões plaquetas/leucócitos e também linfócitos/granulócitos na atividade de MSCs e na sua capacidade de diferenciação.

2.2. Células mesenquimais do tecido adiposos humano (h-AdMSCs)

Terapias celulares utilizando MSCs para tratamento da osteoartrite e outras doenças vêm crescendo, pois sua aplicação no local da lesão sozinhas ou somadas à biomateriais de suporte e enriquecidos biologicamente podem induzir uma reposta à regeneração mais acelerada e eficiente (Gao et al., 2017; Iijima et al., 2018; Li et al., 2018). Devido à baixa disponibilidade de condrócitos e o estado de quiescência dessas células adultas, as MSCs se tornaram uma opção mais viável para a medicina regenerativa da cartilagem. Isso porque essas células possuem alta disponibilidade e capacidade de se diferenciar em condrócitos, além de outros tipos celulares, como osteócitos (Caplan, 1991). A alta disponibilidade das MSCs se dá pelo fato de estarem presentes em diversos tecidos, como a medula óssea, o cordão umbilical e o tecido adiposo, sendo o processo de isolamento, expansão e diferenciação muito simples (Hass et al., 2011; Rosenbaum et al., 2008). O potencial regenerativo dessas células, além da sua capacidade de diferenciação, também se deve à vasta gama de biomoléculas secretadas por elas, como diferentes FCs, além de possuir caráter imunorregulatório, contribuindo para o tratamento de diversos tipos de doenças (Caplan, 2007; Tamama and Kerpedjieva, 2012; Zhao et al., 2016).

As células provenientes do tecido adiposo, as h-AdMSCs, possuem a vantagem de seu isolamento ser muito mais simples comparando-se com a extração das MSCs da medula óssea, por exemplo. As h-AdMSCs estão presentes no tecido adiposo subcutâneo, frequentemente removido por processos cirúrgicos como a lipoaspiração, com seu isolamento da gordura feito a partir de tratamento enzimático e mecânico, de maneira simples e sem a necessidade de equipamentos sofisticados (Araña et al., 2013; Manzini et al., 2015).

2.2.1. Efeito do L-PRP na atividade das h-AdMSCs

A capacidade de regeneração da cartilagem pode ser potencialmente aumentada pela associação entre h-AdMSCs e o PRP. Diversos trabalhos na literatura têm mostrado a capacidade do L-PRP de estimular o crescimento e diferenciação das h-AdMSCs por diferentes vias de sinalização, graças ao rico microambiente proporcionado pelo L-PRP usado como suplemento ou suporte (Lai et al., 2018; Liou et al., 2018; Xie et al., 2012). Terapias as quais as h-AdMSCs juntamente com L-PRP foram transplantadas em modelos animais induzidos à doenças da cartilagem e osso, mostraram efeito regenerativo superior ao tratamento apenas com h-AdMSCs (Barba-Recreo et al., 2015; Tajima et al., 2015). Nos estudos clínicos, a aplicação de L-PRP contendo h-AdMSCs em pacientes com doenças articulares tem mostrado resultados positivos, com efetiva redução da dor e aumento do funcionamento dos joelhos, indicando a regeneração do tecido lesionado (Koh et al., 2013; Pak et al., 2013).

2.3. Cartilagem articular

A cartilagem articular é um tecido único, e se diferencia dos outros tecidos pela baixa concentração celular, baixa vascularização, limitada presença de vasos linfáticos e nervos. Por isso, uma vez iniciado o processo de degeneração do tecido devido à ação do tempo, esforços excessivos ou fatores genéticos, a cartilagem dificilmente irá se regenerar de forma natural e espontânea (Huber et al., 2000). Dessa forma, a área da medicina regenerativa tem buscado alternativas para contornar o avanço de doenças articulares e a regeneração do tecido que sejam menos invasivas, de baixo custo, e que promovam resultado a longo prazo (Hunziker, 2001). Sendo assim, o PRP e suas variações têm se mostrado eficientes no tratamento de doenças musculoesqueléticas, dentre elas, a oateoartrite, que resulta na degeneração da cartilagem e do osso, causando rigidez e dor intensa (Sampson et al., 2010). A aplicação intra-articular do L-PRP e a alta concentração de FCs e citocinas aceleram a regeneração graças às funções

específicas dessas biomoléculas, que regulam a proliferação celular e a produção de MEC até a formação do novo tecido, cuja composição é bastante heterogênea e varia de acordo com cada camada.

2.3.1. Estrutura e composição

Apesar de avascular, alifático e com poucos nervos, a cartilagem articular é um tecido heterogêneo, cuja composição e concentração varia com sua profundidade. Ele possui quatro diferentes camadas, a superficial ou de repouso, a intermediária ou de proliferação, a profunda ou hipertrófica, e a camada da cartilagem calcificada (Figura 3). Cada camada é composta por diferentes concentrações de condrócitos, que juntos correspondem a apenas de 1 a 5% do volume total do tecido, com o restante correspondendo à MEC e água, cuja interação e organização é responsável pela capacidade da cartilagem articular de suportar altas cargas mecânicas (Buckwalter et al., 2001; Espinosa and Foster, 2016).

A camada superficial é a que fica em contato com o fluido sinovial e é a menor das quatro, correspondendo em torno de 15% do tecido. Nela é encontrada a maior concentração de condrócitos, que possuem formato achatado e orientação paralela à superfície; alta concentração de água e baixa concentração de GAGs. Ela possui duas camadas distintas de colágeno, uma paralela e outra perpendicular à superfície, o que garante resistência mecânica e atua como barreira para a passagem de biomoléculas indesejáveis do fluido sinovial para o tecido (Huber et al., 2000). A partir da camada intermediária, a concentração de condrócitos começa a diminuir e as células possuem formato menos achatado e mais arredondado. A sua orientação se faz de forma aleatória, assim como a das fibrilas de colágeno. A concentração de GAG's aumenta ao mesmo tempo que a de água diminui. Essa é a camada que corresponde à maior porcentagem de todo o tecido, em torno de 55%, e é onde os condrócitos estão mais ativos à proliferação (Espinosa and Foster, 2016). A camada mais profunda é a que está em contato com a zona calcificada, correspondendo à 35% do tecido. Nela a concentração de condrócitos é ainda menor e eles estão alinhados perpendicularmente à superfície. A concentração de GAG's e colágeno aumenta e a de água diminui consideravelmente. A alta concentração de GAG's e o alinhamento perpendicular das fibrilas de colágeno conferem a essa camada o maior módulo de compressão, necessário para suportar a alta carga mecânica exercida sobre a cartilagem (Schinagl et al., 1997). Na última camada, a calcificada, os condrócitos são arredondados, em baixa concentração, e não há a presença de GAG's. As fibrilas de colágeno são mais grossas e

ancoradas pela matriz calcificada (Di Bella et al., 2015; Huber et al., 2000; Hunziker, 2001).

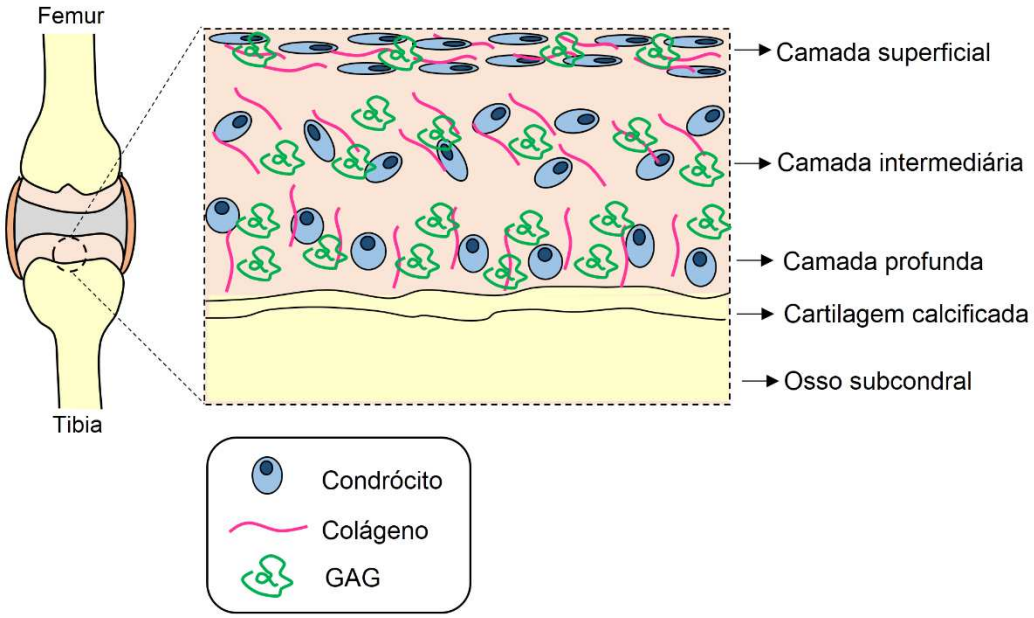

Figura 3. Esquema ilustrando o microambiente da cartilagem articular, destacando a concentração e orientação de condrócitos, colágeno e GAG's nas diferentes camadas do tecido.

2.3.2. Regeneração pelo uso do L-PRP

A engenharia de tecidos tem a finalidade de construir ou regenerar um tecido danificado pela combinação de células, de um suporte celular 3D formado por um material ou uma combinação de materiais biocompatíveis e biodegradáveis, além de biomoléculas sinalizadoras, que irão orquestrar o comportamento celular. Esse conjunto representa o chamado triângulo da proliferação (Figura 4), o qual o L-PRP se encaixa pela formação de um suporte celular através da polimerização e formação das redes de fibrina, e pela rica concentração de FCs e citocinas na composição (Barnett Jr and Pomeroy, 2007).

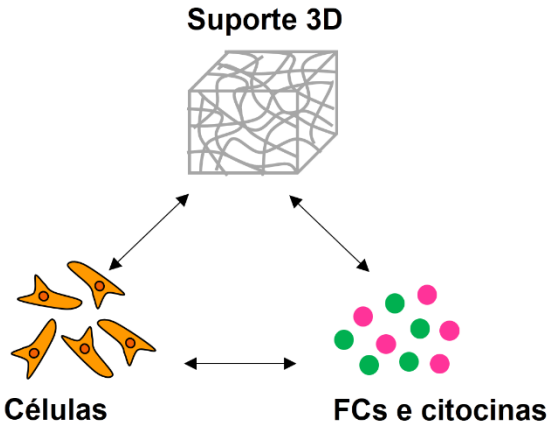

Figura 4. Esquema representando o triângulo da proliferação, o qual as células, o suporte 3D e as biomoléculas são os componentes fundamentais na engenharia de tecidos.

Diferentes técnicas vem sendo empregadas para que a cartilagem articular desenvolvida *in vitro* seja o mais próxima possível do tecido nativo, em termos de composição, concentração, arquitetura, organização e propriedades mecânicas (Klein et al., 2009; Leijten et al., 2016; Li et al., 2017; O'Connell et al., 2017; Zhu et al., 2018). Para isso, diferentes biomateriais tem sido utilizados, e combinações desenvolvidas para garantir um suporte apropriado para as células, e que quando inserido no organismo, se degrade no tempo suficiente da formação do novo tecido.

Além da formação do tecido mimético *in vitro*, processo mais comum na engenharia de tecidos e que precede o implante no paciente, existem os biomateriais injetáveis, com a presença ou não de células que formarão o suporte 3D *in situ,* logo após a aplicação (Gaffey et al., 2015; Liu et al., 2017; Shimojo et al., 2016) Para isso, o biomaterial precisa apresentar propriedades reológicas que permitam uma fácil fluidez pela seringa, e que permaneçam no local desejado após a aplicação, ou seja, que tenha comportamento pseudoplástico, possuindo caráter de um fluido sob alta tensão de cisalhamento e caráter de gel sob baixa tensão (Gaffey et al., 2015; Lee, 2013).

O processo de regeneração do tecido compreende em três fases, a da inflamação, da proliferação celular e da remodelação (Zhu et al., 2013). A injeção do L-PRP em pacientes com osteoartrite contribui com a aceleração do processo de todas as fases, graças às plaquetas e leucócitos que expressam os FCs e citocinas responsáveis por orquestrar o processo inflamatório, a proliferação celular e a produção da MEC. A injeção de PRP para tratamento da cartilagem articular foi proposto pela primeira vez como uma alternativa de regeneração rápida de joelhos de atletas, sem a necessidade de cirurgia (Sánchez et al., 2003). Embora possua baixa resistência mecânica, e portanto, não seja adequado para substituir o tecido, a matriz 3D

formada pela ativação do L-PRP garante suporte e estímulo rápido para as células até formação do novo tecido e recuperação do microambiente. Resultados clínicos têm mostrado significativa redução da inflamação e da dor, aumento da mobilidade e função dos joelhos dos pacientes, sugerindo a regeneração tecidual pelo uso do L-PRP (Filardo et al. 2011; Kon et al. 2009; Riboh et al. 2015).

Logo após sua aplicação no local da lesão (Figura 5A), o L-PRP (pré-ativado ou ativado *in situ*) forma redes de fibrina, onde as plaquetas e leucócitos iniciam o processo de liberação gradual dos FCs de citocinas no local, que por diversas vias de sinalização orquestram a cicatrização (Figura 5B). As células autólogas são estimuladas a migrar para o local da lesão, proliferar, se diferenciar e produzir MEC (Figuras 5C) até a completa regeneração do tecido (Figura 5D).

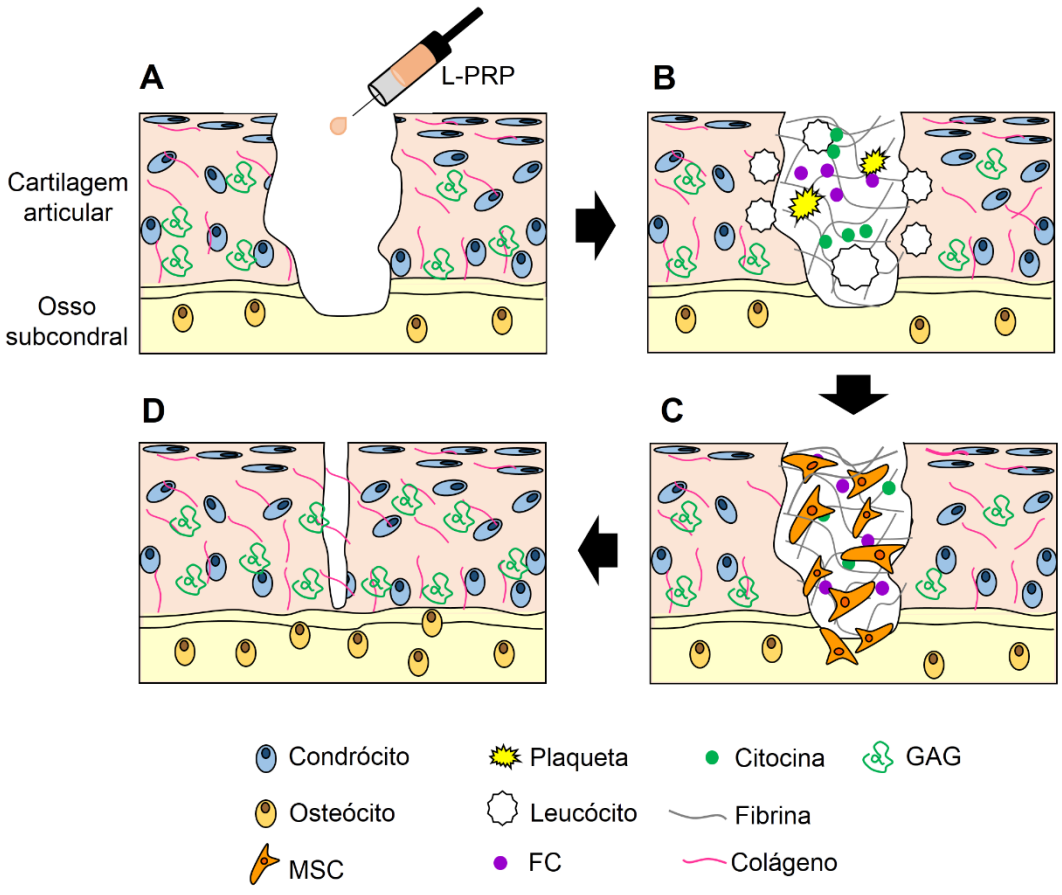

Figura 5. Esquema ilustrando as fases da regeneração da cartilagem articular. (A) Aplicação do L-PRP no local degenerado. (B) Formação das redes de fibrina, onde os FCs e citocinas são gradualmente liberados. (C) Migração das células autólogas para o local da lesão. (D) Regeneração do tecido.

2.4. Ácido Hialurônico (AH)

Além do PRP, o AH é um biomaterial muito utilizado como suporte 3D para cultivo das h-AdMSCs, como biotinta para impressão 3D de osso e cartilagem, como biomaterial injetável para terapias celulares e como viscossuplemento para reparo de articulações. Suas propriedades são facilmente manipuláveis variando-se a MM, concentração e reticulação, formando IPNs e semi-IPNs pela interação com outros polímeros. O AH também é um dos principais componentes da MEC da cartilagem, o que contribui para a organização e reestruturação do microambiente.

2.4.1. Estrutura e propriedades

O AH é um GAG, e portanto, um polissacarídeo linear composto de repetidas unidades dissacarídicas de ácido D-glicurônico (GlcUA) e N-acetilglicosamina (GlcNAc), unidas alternadamente por ligações glicosídicas β-1,3 e β-1,4 (Figura 6).

A ampla faixa de MM do AH, somada às suas estruturas secundárias e terciárias, que possuem inúmeros sítios para interações hidrofóbicas e hidrofílicas, conferem ao AH propriedades conformacionais, mecânicas e reológicas que podem ser manipuladas de acordo com seu tamanho, com o meio em que está inserido (pH, carga iônica) e pela reticulação entre si ou com outros polímeros (Garg and Hales, 2004; Lapčík et al., 1998). Em soluções aquosas, o AH se auto associa espontaneamente formando emaranhados globulares rígidos e aleatórios, devido às interações de hidrogênio, repulsão eletrostática e interações hidrofóbicas entre as cadeias, que são altamente hidratadas, conferindo ao AH o caráter de hidrogel (Blundell et al., 2006; Garg and Hales, 2004). Em altas concentrações ou para AH de altas MM (> 10^5 Da), os domínios moleculares diminuem, restringindo o movimento das macromoléculas, conferindo ao AH caráter viscoelástico (Balazs, 1968).

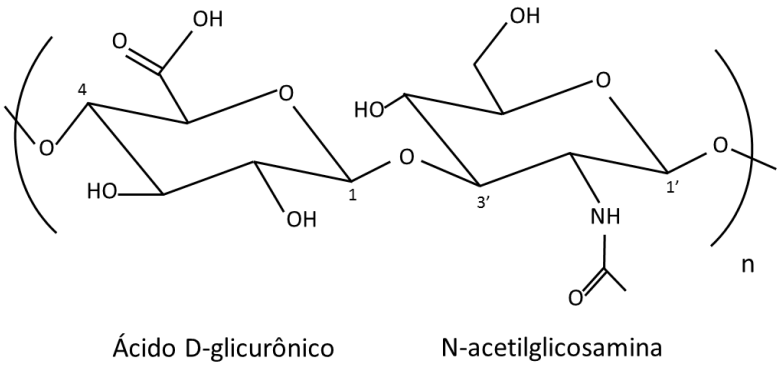

Figura 6. Dissacarídeo de AH formado pelos monossacarídeos GlcUA e GlcNAc, que em repetidas unidades formam as macromoléculas de AH.

O AH é encontrado naturalmente nos tecidos conjuntivos de mamíferos, como o fluido sinovial. Sua forma nativa é a de maior MM, que somada às altas concentrações no tecido conjuntivo, confere propriedades viscoelásticas ao fluido. Assim, à baixas frequências, ou longo tempo de deformação, as macromoléculas de AH possuem tempo suficiente para se ajustar e voltar à forma original pela quebra das ligações de hidrogênio, ocorrendo o desenovelamento das cadeias, o que confere ao fluido um caráter viscoso. A altas frequências, quando a resposta à deformação é rápida, as macromoléculas se enovelam rapidamente, resultando em um caráter elástico (Balazs, 1968; Gibbs et al., 1968). Dessa forma, o AH é um dos principais responsáveis por conferir às articulações a facilidade de locomoção, pois minimiza os efeitos da fricção e do desgaste das juntas.

Em casos de traumas ou doenças das articulações, o AH presente no fluido sinovial é degradado por proteases e espécies reativas de oxigênio, e a síntese da macromolécula é dificultada pelo caso grave de inflamação. Isso acarreta em alterações nas propriedades reológicas do fluido, e assim, sua função de minimizar a fricção e o desgaste da cartilagem e osso é prejudicada (Balazs et al., 1967; Ghosh and Guidolin, 2002). Dessa forma, o AH é utilizado em tratamentos de doenças articulares através da aplicação por injeção local, atuando como viscossuplemento para reposição do fluido sinovial visando o alívio das dores nos pacientes (Altman, 2000; Balazs and Denlinger, 1993; Bhandari et al., 2017).

2.4.2. Efeitos da massa molar (MM) do AH

A forma nativa do AH é a de alta MM ($10^6 – 10^7$ Da), sendo que o AH de baixa MM (< 10^4 Da) e oligossacarídeos são encontrados *in vivo* como um produto da degradação do

polissacarídeo, mediado pelas hialuronidases e espécies reativas de oxigênio (Slevin et al., 2002). À exceção de condições patológicas ou sob a ação do tempo, onde a degradação do AH nativo é acelerada resultando em perdas expressivas de fluido sinovial e MEC, a degradação do AH em menores moléculas leva à uma série de mecanismos benéficos para o organismo. Apesar de ser um mediador inflamatório, o AH de baixa MM é relacionado como um estimulador da angiogênese, da proliferação de células endoteliais e da produção de colágeno, conferindo à ele um importante papel no processo regenerativo (Noble, 2002a; Rooney et al., 1993; West et al., 1985). Devido aos benefícios apontados pela atividade do AH de baixa MM, ele vem sendo utilizado juntamente com o AH de alta MM em aplicações intra-articulares para regeneração da cartilagem (Petrella et al., 2011).

Além das aplicações intra-articulares, nos estudos da engenharia de tecidos e medicina regenerativa, o AH é utilizado como biomaterial para suporte 3D de células das mais variadas maneiras, em diferentes MM e proporções, com diferentes agentes reticulantes e formando IPNs e semi-IPNs com diversos tipos de polímero, dependendo do tipo de tecido a ser regenerado e aplicação desejada (Burdick et al., 2005; Collins and Birkinshaw, 2013; Cui et al., 2015; Kolesky et al., 2016). As vantagens da utilização do AH na medicina regenerativa, principalmente para cartilagem, se dá pelo fato de ele ser um componente natural da MEC e também por se ligar a receptores de membranas celulares específicos, contribuindo com as interações célula-célula e célula-matriz, sendo favorável para a adesão e proliferação celular nos suportes 3D (Goodison et al., 1999; Lam et al., 2014).

2.4.3. Associação L-PRP e AH

Devido à todas as vantagens apresentadas sobre o L-PRP e o AH no processo da regeneração da cartilagem e no tratamentos da osteoartrite, muitos estudos passaram a comparar a aplicação de ambos em pacientes lesionados, e os resultados mostraram uma superior eficiência do L-PRP em relação ao AH (Huang et al., 2019; Kon et al., 2011; Spakova et al., 2012). Naturalmente, ambos passaram a ser utilizados em associação nas aplicações clínicas, tendo mostrado resultados positivos com relação ao alívio da dor e à regeneração do tecido (Dallari et al., 2016; Lana et al., 2016).

Apesar dos efeitos positivos da aplicação conjunta do L-PRP e AH, poucos estudos se dedicaram a compreender os efeitos moleculares e celulares provenientes dessa associação. Uma vez que as matrizes possuem um papel fundamental na regeneração, pois dão suporte para

as células migrarem, proliferarem e se diferenciarem, o estudo dos efeitos da associação entre L-PRP e AH nas propriedades estruturais e mecânicas das fibras são extremamente importantes, porém, na literatura a maior abordagem se dá em relação aos hidrogéis e IPNs formados entre a fibrina comercial e o AH reticulado (Arulmoli et al., 2016; Lee and Kurisawa, 2013; Zhang et al., 2016), ou entre a fibrina do P-PRP e AH (Russo et al., 2016; Vadalá et al., 2017). Apesar do AH não reticulado resultar em menos resistência mecânica, sua utilização evita a introdução de substâncias químicas resultantes dos agentes reticulantes no organismo.

O AH livre (não reticulado) misturado ao L-PRP, se emaranha por entre as fibras após ativação e se liga à fibrina por interações não covalentes, o que resulta na alteração de suas propriedades estruturais e reológicas (Komorowicz et al., 2016; LeBoeuf et al., 1986; Rinaudo, 2008). Apesar dos diversos trabalhos disponíveis que se dedicaram a reportar os efeitos das interações do AH com a fibrina comercial, sua associação com o L-PRP carece ser estudada, uma vez que as semi-IPNs formadas dessa associação possuem uma grande diversidade de biomoléculas que podem interferir nas propriedades das fibras, assim como no comportamento biológico, como a liberação de FCs e citocinas, e resposta celular (Ehrenfest et al., 2012; Lam et al., 2011).

CAPÍTULO 3:
RESULTADOS E DISCUSSÃO

3. RESULTADOS E DISCUSSÃO

Este capítulo é apresentado na forma de artigos, contendo a metodologia empregada, resultados obtidos e discussão.

O primeiro artigo, *Distribution, Recovery and Concentration of Platelets and Leukocytes in L-PRP Prepared by Centrifugation,* publicado no periódico *Colloids and Surfaces B: Biointerfaces* (doi.org/10.1016/j.colsurfb.2017.10.046), trata do estudo dos efeitos da centrifugação na composição do L-PRP, visando modular a distribuição, recuperação e concentração de plaquetas e leucócitos, assim como as razões plaqueta/leucócito e linfócito/granulócito, além de padronizar protocolos de preparação do L-PRP.

O segundo artigo, *Centrifugation Conditions in L-PRP Preparation affect Soluble Factors Release and Mesenchymal Stem Cells Behavior*, que será submetido à periódico internacional indexado, trata do estudo da liberação de fatores de crescimento e citocinas pelas diferentes formulações de L-PRP padronizadas no artigo anterior, além de estudar seus efeitos na viabilidade e crescimento das h-AdMSCs.

O terceiro artigo, *Hyaluronic Acid and Fibrin from L-PRP form Semi-IPN with Tunable Properties Suitable for Regenerative Medicine*, que será submetido à periódico internacional indexado, trata do estudo das interações entre a fibrina do L-PRP, escolhido a partir dos resultados obtidos nos artigos anteriores, com AH de diferentes MM (baixa e alta). O artigo teve como finalidade produzir semi-IPNs sob condições controladas, e caracterizar as suas propriedades estruturais e reológicas, além das respostas celulares às redes de fibrina-AH.

O quarto e último artigo, *Investigating the role of fibrin from L-PRP-hyaluronic acid semi-IPNs in the release of soluble factors and in the chondrogenesis/osteogenesis of mesenchymal stem cells*, que será submetido à periódico internacional indexado, teve como objetivo estudar a influência das semi-IPNs na liberação de fatores solúveis e na diferenciação condrogênica e osteogênica *in vitro* das h-AdMSCs.

3.1. Distribution, Recovery and Concentration of Platelets and Leukocytes in L-PRP Prepared by Centrifugation

Artigo publicado no periódico *Colloids and Surfaces B: Biointerfaces* (doi.org/10.1016/j.colsurfb.2017.10.046).

Distribution, Recovery and Concentration of Platelets and Leukocytes in L-PRP Prepared by Centrifugation

Bruna Alice Gomes de Melo[1], Andréa Arruda Martins Shimojo[1], Amanda Gomes Marcelino Perez[1], José Fabio Santos Duarte Lana[2], Maria Helena Andrade Santana[1]*

[1]Department of Engineering of Materials and Bioprocesses, School of Chemical Engineering, University of Campinas, Campinas-SP, Brazil.

[2]Bone and Cartilage Institute, IOC, Indaiatuba-SP, Brazil

*Correspondence should be addressed to Maria Helena A. Santana; mariahelena.santana@gmail.com

ABSTRACT

Platelet-rich plasma (PRP) is an autologous product prepared from whole blood that is widely used in regenerative medicine. In clinical practice, discontinuous centrifugation is used for both hand- and machine-prepared PRP. However, separation of whole blood fractions via centrifugation is a complex process, and the lack of clear mechanisms limits the understanding and evaluation of PRP preparation methods. This paper focuses on the distribution, recovery and concentration factor of platelets and leukocytes in L-PRP (leukocyte and platelet-rich plasma) to define a concentration pattern for these blood components due to centrifugation conditions. Whole blood collected from three healthy donors was centrifuged for 10 min at 50 to 800 xg in a first step and then at 400 xg in a second step. The results from the first centrifugation step showed most platelets to be distributed in the upper layer (UL) and the buffy coat (BC), with approximately 14.5 ± 5.2% retained in the bottom layer (BL). Most leukocytes were present in the BL. The greatest platelet recoveries from L-PRP were obtained at up to 150 xg (88.5 ± 16.9%). The cumulative concentration factors with respect to the whole blood from the second centrifugation step were 6 and 1.2 for platelets and leukocytes, respectively. Thus, the concentration patterns delineated three centrifugation ranges with platelet/leukocyte ratios of 205 ± 18, 325 ± 15 and 107 ± 4 and lymphocyte/granulocyte ratios of 1.54 ± 0.74, 0.90 ± 0.08 and 0.42 ± 0.07. These findings contribute to a scientifically based standardization of L-PRP preparations.

Keywords: Platelet-rich plasma; leukocytes; erythrocytes; centrifugation; tissue regeneration.

3.1.1. Introduction

Platelet-rich plasma (PRP) is an autologous and non-immunogenic product from whole blood that has been widely used as a non-surgical treatment for articular cartilage injuries and osteoarthritis as well as in various other regenerative medical procedures (Marx, 2004; Tayapongsak et al., 1994).

Although the common terminology refers to PRP as a platelet concentrate in a small volume of plasma, it is known that PRP contains other healing components, such as leukocytes (neutrophils, eosinophils, basophils, monocytes and lymphocytes), progenitor endothelial cells, fibroblasts, and keratinocytes as well as a small number of premature stem cells. In addition to cellular components, PRP also contains molecular components such as growth factors (GFs) and a diverse family of immunomodulatory proteins (Anitua et al., 2012). However, as with most preparations described in the literature, many of these components have not yet been analyzed, thus limiting our understanding of PRP's biological effectiveness.

In clinical practice, hand-made or machine-made PRP is prepared by discontinuous centrifugation, whereby PRP is the supernatant from the sedimentation of erythrocytes in a first centrifugation step, which is then further concentrated by a second or more centrifugation steps. The supernatant comprises an upper layer (UL) that is rich in platelets only, P-PRP (pure platelet-rich plasma); the UL in combination with the intermediate layer or buffy coat (BC) constitutes the L-PRP (leukocyte and platelet-rich plasma) (Ehrenfest et al., 2014). Both P-PRP and L-PRP are prepared from whole blood collected in the presence of an anticoagulant to avoid platelet activation and degranulation.

Platelet and leukocyte-rich fibrin (L-PRF), developed by Dohan et al. (2006), is a dense fibrin matrix containing trapped platelets and leukocytes that is also prepared by centrifugation but does not require anticoagulant or agonists. Conceptually, platelet activation occurs via contact with the walls of the blood collection tube, and the slow polymerization generates a fibrin network similar to the natural one.

Ghanaati et al. (2014) performed extensive work on the effects of centrifugation conditions on the concentration of platelets and leukocytes in L-PRF. For example, decreasing the velocity and increasing the time (1500 rpm, 14 min) resulted in a greater amount of neutrophilic granulocytes in the fibrin matrix compared to 2700 rpm and 12 min, conditions under which neutrophils were largely found at the red blood cell interface. At a constant time

(8 min), decreasing the centrifugal acceleration (710 xg, 177 xg and 44 xg) dramatically increased the number of leukocytes and platelets (Choukroun and Ghanaati, 2017).

Presently, L-PRP preparations are primarily used in bone and cartilage repair (Lana et al. 2014). According to Ehrenfest et al. (2014), leukocytes have a strong influence on the release of GFs, particularly TGF-β1. Neutrophils, which are granulocytic leukocytes, have a crucial role in an organism's defense against infection (Carlyon et al., 2004). However, expression of numerous inflammatory cytokines and metalloproteins, in addition to the production of reactive oxygen species (ROS), can be deleterious to stem cell proliferation and differentiation (Faurschou and Borregaard, 2003; Spooner and Yilmaz, 2011). In turn, some studies have reported a positive correlation between ROS and cell proliferation, more specifically in the cell "waking up" process (Lyublinskaya et al., 2015). Lymphocytes, the second major type of leukocyte, produce GFs (Freeman et al., 1995) and are involved in modulating the fibroblast activity that stimulates wound healing (Peterson et al., 1987). Nonetheless, studies have shown that leukocytes can block stem cell differentiation and induce apoptosis (Wang et al., 2012).

Although this controversial role of leukocytes has been discussed in the literature, questions remain concerning whether a leukocyte-rich (L-PRP) or -poor (P-PRP) preparation is the most appropriate, depending on the specific needs (Bielecki et al. 2015; Marenzi et al. 2015; Yin et al. 2016; Zhou et al. 2015).

Sundman et al. (2011) emphasized that the effectiveness of PRP should be attributed to an optimal balance between the anabolic effect of GFs and the catabolic effect of cytokines and that a suitable range of platelet/leukocyte ratios would be beneficial for tissue regeneration. In addition, Parrish et al. (2016) verified that leukocyte-rich preparations stimulated tendon cell proliferation better than leukocyte-poor PRP preparations, attributing the effects to the importance of components other than platelets in the proper functioning of PRP.

Recently, Dohle et al. (2017) evaluated the effects of L-PRF on wound healing *in vitro*, observing a positive influence on angiogenesis via inflammatory processes, as mediated by the leukocytes present in the preparation

PRP activation causes the release of GFs primarily from platelets, whereas a fibrin network is generated from fibrinogen decomposition. The balance of PRP components and their association with the fibrin network are key for the development of PRP products (Anitua et al., 2012).

Different compositions can be obtained by varying centrifugation conditions, and standardization of PRP preparations is claimed in the literature. Despite the operational

simplicity, centrifugation of whole blood is a complex process (Graham, 2001; Hunter, 2009). In addition to size and density, other factors such as structural changes in erythrocytes, interactions among blood components, and the effects of the anticoagulant have important roles in separation and PRP composition. Moreover, the mechanisms governing whole blood centrifugation are not well known, and there is a paucity of research regarding this issue in the literature. Therefore, studies that enable PRP composition modulation via centrifugation conditions are important for the prediction, optimization and standardization of PRP preparations. Furthermore, such modulation would provide the appropriate conditions for preparing L-PRP with different platelet/leukocyte and lymphocyte/granulocyte ratios, which are useful for studying the effects of anabolic and catabolic compounds released from platelets and leukocytes, such as GFs and cytokines, on tissue regeneration.

In a previous work, we evaluated the relevant aspects of centrifugation on P-PRP composition by centrifuging whole blood in the range of 50 to 820 xg in the first centrifugation step, followed by further P-PRP concentration in the range of 400 to 1600 xg in a second centrifugation step (Perez et al. 2014). Here, we extend our previous findings by determining the distribution, recovery and concentration of platelets and leukocytes from L-PRP. We aimed to determine a concentration pattern for blood components, as modulated by centrifugation conditions. This approach has various purposes, such as to understand the molecular mechanisms involved, to provide centrifugation conditions for reliably preparing L-PRP for further studies and applications in clinical practice, and to enable mathematical modeling and simulation for predicting L-PRP compositions over a larger range of centrifugal accelerations and times.

3.1.2. Material and Methods

Assays using human blood were approved by the Ethics Committee of the School of Medical Sciences of Unicamp (Campinas; CAAE: 0972.0.146.000-11). Three healthy donors ranging in age from 30 to 40 years were selected based on the results of clinical laboratory tests.

3.1.2.1. Blood collection

Whole blood was collected by venous puncture from the three donors and placed in 8.5-mL tubes (BD Vacutainer®, USA) containing 1.5 mL of ACD-A (Acid Citrate Dextrose

Solution, Solution A) anticoagulant. After collection, 3.5 mL of the anticoagulated blood was transferred to empty 5-mL tubes; the reduced volume allowed samples from the same donor to be used for various centrifugation conditions.

3.1.2.2. Experimental design

L-PRP was prepared according to Perez et al. (2013, 2014). Briefly, whole blood in 3.5-mL tubes was centrifuged using a ROTINA 380R centrifuge (Hettich Zentrifugen, Tuttlingen, Germany), with the tubes positioned at 45° relative to the rotor. The first centrifugation step was performed in the range of 50 to 800 xg (50, 100, 150, 300, 500 and 800 xg) for 10 min at 25°C. This range was chosen to protect the platelets from the intense shear stress and to adequately separate the erythrocytes. This first centrifugation step generated three layers: the supernatant (UL), the intermediate layer (BC) and the bottom layer (BL), which consisted mostly of erythrocytes, as shown in Figure 3.1.1A. Each layer was collected using an automatic pipette, and the volume was measured to quantify platelet and leukocyte (lymphocyte and granulocyte) concentrations. Based on these data, the distribution, recovery and concentration factor were calculated as parameters for characterizing the performance of each centrifugation condition. The concentrations of the whole blood, three layers obtained by centrifugation, and L-PRP (UL + BC) were determined using an ABX Micros ES 60 hematologic analyzer (Horiba ABX Diagnostics, Montpellier, France). Sample measurements for each donor were performed in triplicate.

The L-PRP obtained from the first centrifugation (L-PRP$_{(1)}$) at 100 xg for 10 min was centrifuged a second time at 400 xg for 10 min to determine the cumulative concentration factor of the platelets and leukocytes with respect to the whole blood sample. Next, 70% of the supernatant, composed of platelet-poor plasma (PPP) (Anitua et al., 2005), was discarded to obtain L-PRP$_{(2)}$, as shown in Figure 3.1.1B. The conditions for the second centrifugation step were chosen to guarantee the integrity of the platelets, as demonstrated by Perez et al. (2013).

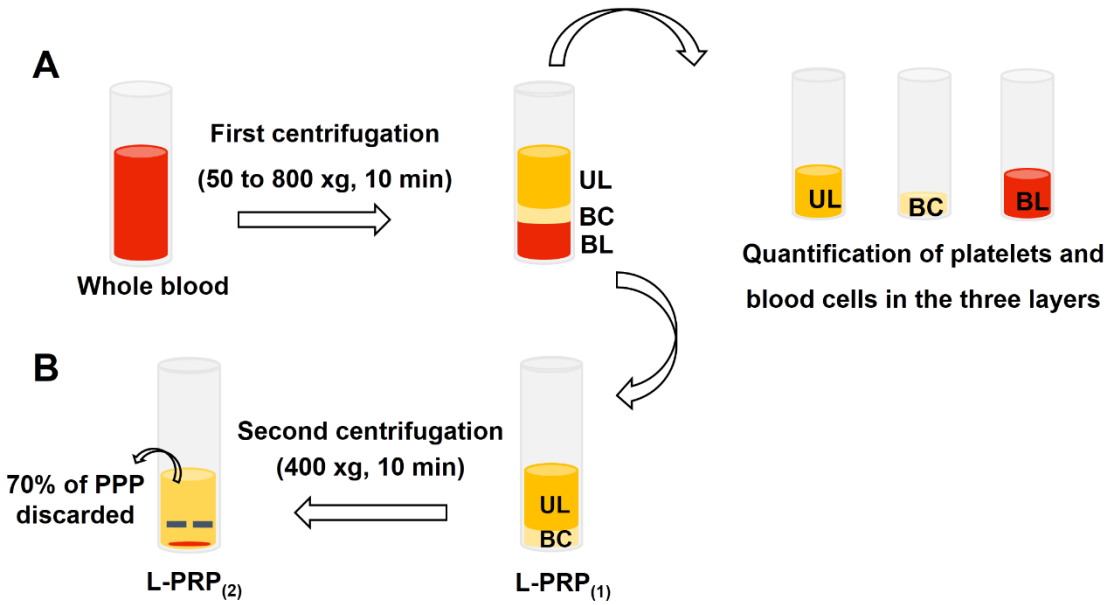

Figure 3.1.1. Schematic illustration of (A) whole blood centrifugation and the three layers (UL, BC and BL) obtained. (B) The second centrifugation of UL + BC (L-PRP$_{(1)}$) was performed to obtain L-PRP$_{(2)}$ after PPP removal.

3.1.2.3. Distribution, recovery and concentration factor parameters

The proportions of platelets and leukocytes in the UL, BC and BL fractions as well as their recovery and concentration factor in L-PRP were calculated using equations 3.1.1 to 3.1.3. We defined the distribution of a component as the ratio of its count in the collected fraction (UL, BC or BL) to its count in whole blood.

$$\%\ Distribution_{Pt,Leuk,Lymp,Gran} = \frac{([C]\ Pt, Leuk, Lymp, Gran_{fraction} \times V_{fraction})}{([C]\ Pt, Leuk, Lymp, Gran_{WB} \times V_{WB})} \times 100 \qquad \textbf{Equation 3.3.1}$$

$$\%\ Recovery_{Pt,Leuk,Lymp,Gran} = \frac{([C]\ Pt, Leuk, Lymp, Gran_{L-PRP} \times V_{L-PRP})}{([C]\ Pt, Leuk, Lymp, Gran_{WB} \times V_{WB})} \times 100 \qquad \textbf{Equation 3.1.2}$$

$$Concentration\ factor_{Pt,Leuk,Lymp,Gran} = \frac{[C]\ Pt, Leuk, Lymp, Gran_{\ L-PRP}}{[C]\ Pt, Leuk, Lymp, Gran_{WB}} \qquad \textbf{Equation 3.1.3}$$

where [C] is the concentration of each blood component, $V_{fraction}$ is the volume of the collected fraction after centrifugation, $V_{L\text{-}PRP}$ is the volume of L-PRP (UL+ BC), and V_{WB} is

the volume of whole blood. Pt, Leuk, Lymp, Gran and WB refer to platelets, leukocytes, lymphocytes, granulocytes and whole blood, respectively.

3.1.2.4. Statistical analysis

Unless otherwise specified, each experiment was carried out in triplicate. The results are presented as the mean ± standard deviation (SD). When relevant, one-way analysis of variance (ANOVA) with *Tukey's test* was used for statistical analysis. A 95% confidence level was considered significant ($p \leq 0.05$).

3.1.3. Results

3.1.3.1. Distribution of platelets, leukocytes, lymphocytes and granulocytes in whole blood layers

Centrifugation of whole blood results in three layers (UL, BC and BL), as shown in Figure 3.1.1. The component distributions in percentages with respect to whole blood in each of the three layers are shown in Figure 3.1.2. After gentle acceleration, platelets were found to be mainly located in the UL, with a maximum of 71.3 ± 2.0% at 50 xg. Upon increasing the acceleration, we observed a progressive decrease in the number of platelets in the UL due to their packaging in the BC, with a maximum of 40.3 ± 7.1% at 800 xg. Approximately 15% of platelets were lost in the BL over the entire range of accelerations (Figure 3.1.2A).

As expected, leukocytes were predominantly distributed in the BC (maximum of 32.2 ± 8.4%) and BL, varying at approximately 70% (Figure 3.1.2B). As shown in Figures 3.1.2C and 3.1.2D, lymphocytes and granulocytes were not equally distributed throughout the blood layers. At the lowest acceleration, 14.7 ± 1.2% of the lymphocytes and only 2.4 ± 0.6% of the total granulocytes were found in the UL. With increasing acceleration, both components appeared to migrate from the BL to the BC, from 19.7 ± 3.6% and 10.7 ± 6.8 at 50 xg to 49.1 ± 9.6% and 33.4 ± 6.9% at 800 xg for lymphocytes and granulocytes, respectively. The remaining cells were present in the BL.

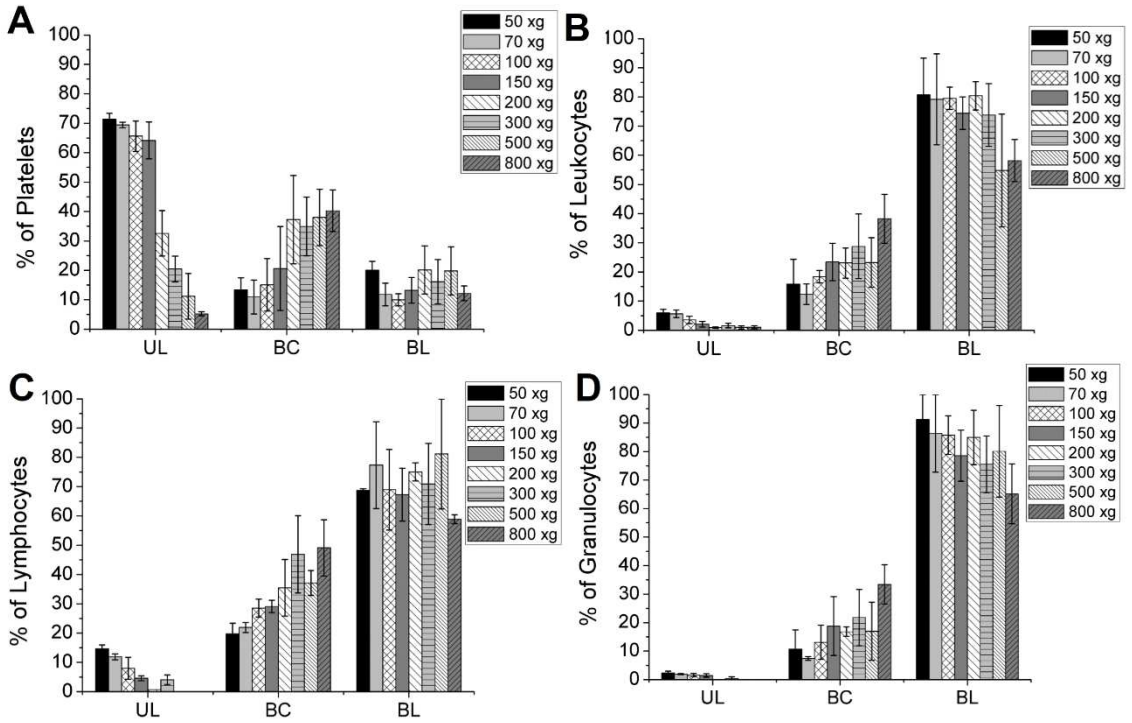

Figure 3.1.2. Distribution of (A) platelets, (B) leukocytes, (C) lymphocytes and (D) granulocytes in the blood layers (UL, BC and BL) formed after centrifugation of whole blood at 50 to 800 xg for 10 min.

3.1.3.2. Recovery of platelets, leukocytes, lymphocytes and granulocytes in L-PRP

The above distribution patterns defined the recovery of platelets and leukocytes in L-PRP$_{(1)}$, as shown in Figure 3.1.3. The maximum value for platelet recovery was 88.5 ± 16.9%, and that for leukocytes was between 11 and 18%. Most of the leukocytes recovered in L-PRP$_{(1)}$ were lymphocytes, with a maximum of 55.4 ± 10.5%. A significant increase in granulocytes occurred at the highest accelerations, which varied from 7.5 ± 1.9% at 50 xg to 34.6 ± 0.2 at 800 xg.

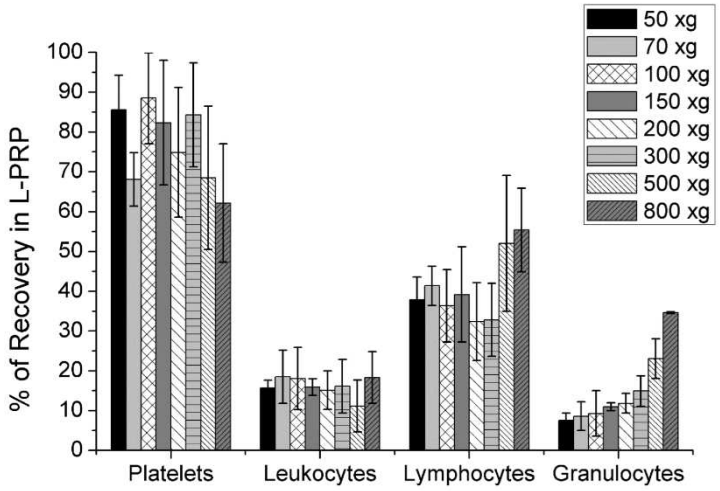

Figure 3.1.3. Recovery percentage of platelets, leukocytes, lymphocytes and granulocytes in L-PRP$_{(1)}$ at different centrifugal accelerations.

3.1.3.3. Concentration patterns

Figure 3.1.4A illustrates the concentration patterns of L-PRP$_{(1)}$ for the considered blood components as a function of centrifugation for the three donors. The curves allowed us to delineate three different ranges: the first ranged from 50 to 120 xg, the second from >120 to 300 xg, and the third from >300 to 800 xg. Platelet concentrations progressively decreased with increasing centrifugal acceleration. In contrast, leukocyte concentrations decreased in the first range, remained constant in the second, and increased in the third, particularly for granulocytes. These results led to platelet/leukocyte and lymphocyte/granulocyte ratios of 205 ± 18 and 1.54 ± 0.74; 325 ± 15 and 0.90 ± 0.08; and 107 ± 4 and 0.42 ± 0.07, for the first, second and third ranges, respectively, as summarized in Table 3.1.1.

The L-PRP$_{(1)}$ volume increased with acceleration from 1.4 to 2.2 mL and decreased with the hematocrit (range 0.31 to 0.37), as expected.

Figure 3.1.4B displays the distribution of blood components in the layers formed from centrifugation for the three delineated acceleration ranges.

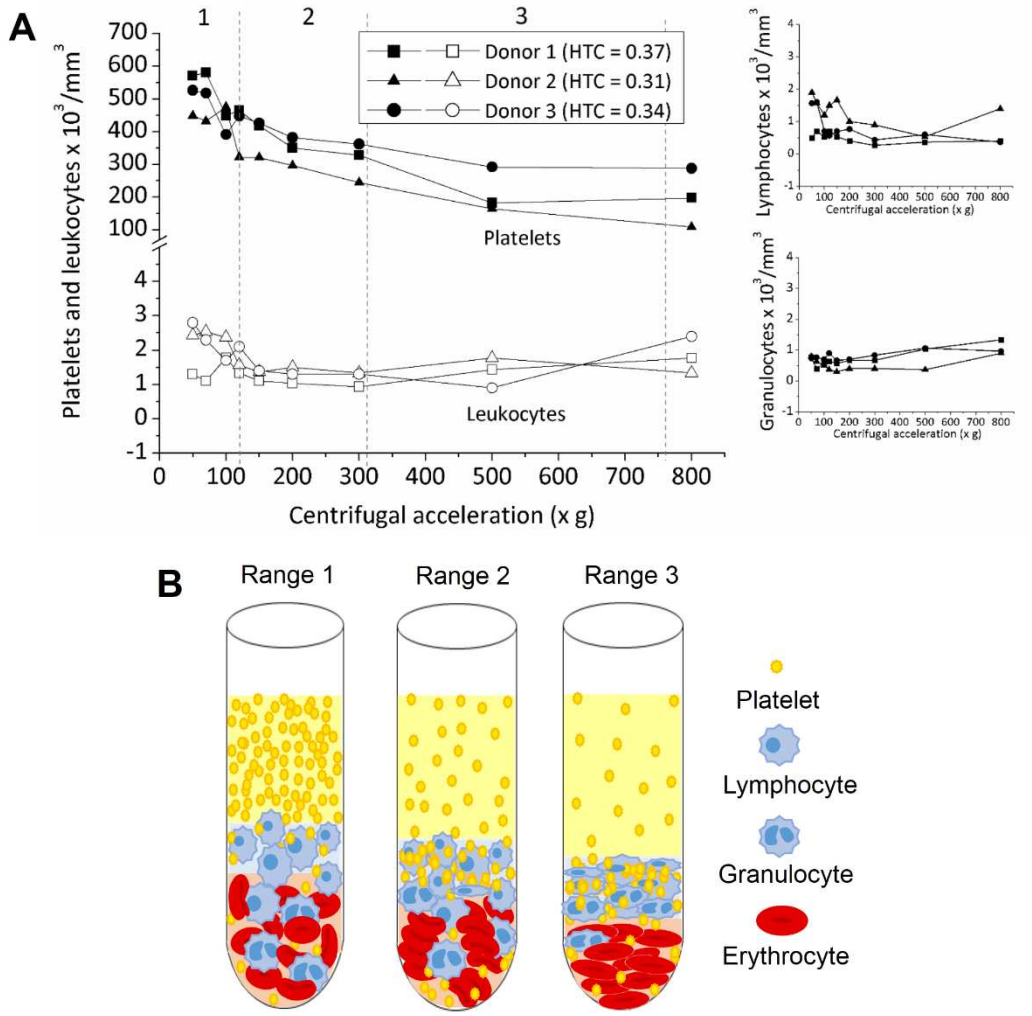

Figure 3.1.4. (A) Platelet, leukocyte, lymphocyte and granulocyte concentrations after the first centrifugation step (L-PRP$_{(1)}$) of whole blood from three donors at different accelerations. Three ranges were established, defining platelet/leukocyte and lymphocyte/granulocyte ratios: range 1 of 205 ± 18 and 1.54 ± 0.74, range 2 of 325 ± 15 and 0.90 ± 0.08, and range 3 of 107 ± 4 and 0.42 ± 0.07, respectively. (B) Representation of blood cell behavior upon gentle and intense centrifugal accelerations. At gentle accelerations (range 1), platelets were preferentially found in the UL, whereas leukocytes were the main component of the BC. In range 2, platelets and leukocytes were mainly in the BC due to plasma backflow through erythrocyte channels. In range 3, granulocytes migrated from the bottom layer to the BC due to erythrocyte compression.

3.1.3.4. Concentration factors

With regard to L-PRP$_{(1)}$, variations in the concentration factor with respect to whole blood were significant for platelets only in the range of 50 to 150 xg (1.9 ± 0.2), decreasing to 1.4 ± 0.2 at 200 xg and below 1 at the highest accelerations (500 and 800 xg). The leukocyte, lymphocyte, and granulocyte concentration factors were approximately 0.5 over the entire range of accelerations, i.e., they did not reach the baseline (Figure 3.1.5A).

Therefore, to concentrate leukocytes, the L-PRP$_{(1)}$ obtained at 100 xg (the range of the highest platelet concentration) was centrifuged a second time at 400 xg for 10 min; L-PRP$_{(2)}$ was obtained after discarding 70% of the upper volume. Figure 3.1.5B shows the experimental (4.3 ± 0.1) and theoretical (6.8 ± 0.7) values of the platelet concentration factor, as well as that of the leukocytes, which were 1.4 ± 0.6 for the experimental value and 1.2 ± 0.4 for the theoretical value.

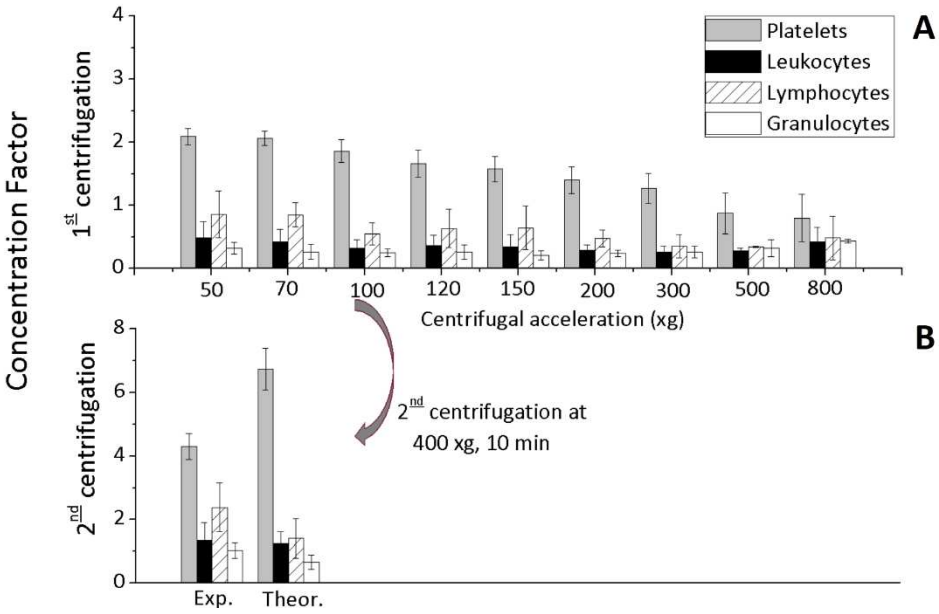

Figure 3.1.5. Concentration factors of platelets, leukocytes, lymphocytes and granulocytes in (A) L-PRP$_{(1)}$ at different centrifugal accelerations and in (B) L-PRP$_{(2)}$ at 400 xg.

Table 3.1.1. The different blood constituent ratios in whole blood and L-PRP after the first and second centrifugations. The ratios are presented in the three previously established spin ranges. Values represent the average of the three donors.

		Platelet/ Leukocyte Ratio	**Lymphocyte/ Granulocyte Ratio**
	Whole Blood	42 ± 10	0.62 ± 0.12
1st centrifugation	Range 1 (50 – 120 xg)	205 ± 18	1.54 ± 0.74
	Range 2 (>120 – 300 xg)	325 ± 15	0.90 ± 0.08
	Range 3 (>300 – 800 xg)	107 ± 4	0.42 ± 0.07
2nd centrifugation*	400 xg	149 ± 66	1.44 ± 0.41

*Experimental values.

3.1.4. Discussion

Distribution, recovery and concentration factor parameters characterized the separation and concentration behavior of platelets and leukocytes upon centrifugation of whole blood, and we were also able to delineate the concentration patterns that modulate the L-PRP composition based on centrifugation conditions. The results showed that separation is not only driven by the size, shape and density of blood components but is also dependent on erythrocyte association and packing during centrifugation. Consequently, with an increase in acceleration platelet levels in L-PRP decreased, whereas leukocyte levels increased in the BC.

Our previous studies on P-PRP revealed the velocity of platelet sedimentation as well as the recovery efficiency, both of which were correlated with the porosity of the erythrocytes present in the BL after sedimentation (Perez et al., 2013). Indeed, erythrocyte packing in the BL increased with centrifugal acceleration, and their sedimentation curves exhibited a sigmoidal shape with time. Micrographs of these erythrocytes showed a Rouleax-like

association at the initial times of the lowest accelerations, though dense packs were formed at the end of the centrifugation time.

Compared to the general sedimentation model described in the literature, Pribush et al. presented a more realistic description of erythrocyte sedimentation (Pribush et al., 2010a; Pribush et al., 2010b). The mechanism consisted of a primary linear aggregation of erythrocytes in quiescent blood that undergoes structural transformations, resulting in branched aggregates; a network structure is then formed, followed by their gradual collapse. The first phase of the erythrocyte network collapse is characterized by the formation of channels through which plasma backflow occurs. Experimental data support the assumptions that these channels propagate from bottom to top and that their diameter increases in the same direction. The shear generated by the flow is sufficient to break interparticle bonds and erode the walls of the channels, resulting in their disintegration into aggregate fragments that form a dense pack. Thus, the intensity of interparticle interactions determines the rate of network formation, the time at which its structural integrity is maintained, and the size of the fragments after collapse.

Because centrifugation shows characteristics similar to those of gravitational sedimentation, with the exceptions of time and intensity of force, it can be assumed that a common mechanism governs the phase separation in both sedimentation modes. Therefore, the proposed mechanism of gravitational erythrocyte sedimentation may shed light on knowledge of the distribution and recovery of platelets and leukocytes in L-PRP after centrifugation.

Considering that channels form within the erythrocyte network, platelets and leukocytes should rise from the lower layers of blood, reaching the upper volume at the interface. The total collapse of the network, structural reorganization, and deformation of erythrocytes must be responsible for trapping platelets and leukocytes in the bottom layer. When gentle accelerations (50 to 150 xg) were applied, the leukocytes trapped mainly consisted of granulocytes, which have a similar radius to but are denser than lymphocytes (Brown, 1989). Because platelets are smaller and less dense, they rose more easily to the UL, with approximately 15% not being carried along with the plasma backflow and remaining trapped in the BL (Figure 3.1.1A).

At higher accelerations (>300 and 800 xg), a significant number of granulocytes left the BL and accumulated in the BC because of the velocity of the plasma backflow. However, due to the rapid loss of integrity of the network, most of the total leukocytes remained in the BL (primarily large cells) (Figure 3.1.2B). Leukocytes in the BC were found to be predominantly lymphocytes (approximately 2-fold) as opposed to granulocytes (Figures 3.1.2C and D). Most of the platelets remained in the BC, trapped with leukocytes.

These results agree with those reported by Amable et al. (2013), who applied a range of 200 to 400 xg and observed that the lowest accelerations resulted in the highest platelet recoveries. Such differences in recovery values can be attributed to the anticoagulant, sodium citrate, was used in their work. Comparing the platelet behavior in L-PRP and P-PRP described by Perez et al. (2013), we observed that the decrease in platelet concentration with centrifugation was smoother for L-PRP due to the presence of the BC.

Despite the different nature of the preparations, our results are consistent with those of Choukroun et al., whereby the leukocyte concentration in L-PRF increased with decreasing centrifugal acceleration (Choukroun and Ghanaati, 2017).

The described distribution defined the recovery of blood components in L-PRP (Figure 3.1.3). The maximum concentration of platelets in L-PRP$_{(1)}$ was 2-fold that of whole blood at lower accelerations, which is considered a moderate concentration factor (Anitua et al., 2008). Similar results were obtained by Anitua et al. (2009) for the first centrifugation step at 460 xg for 8 min.

In our study, the first centrifugation step was not able to concentrate leukocytes due to losses in the BL, and a very similar result was obtained by Parrish et al. (2016), who used a commercial kit to prepare L-PRP. Although the second centrifugation step provided a preparation rich in platelets and leukocytes, there was a discrepancy between the experimental and theoretical values considering volume reduction (Figure 3.1.5B). These differences can be explained by incipient platelet aggregation at 400 xg, as observed by Perez et al. (2014) in the p-selectin assay. Therefore, higher accelerations increased platelet aggregation until the integrity was lost. This effect was observed for whole blood from each donor in our study.

The three ranges defined in the curves shown in Figure 3.1.4A describe platelet/leukocyte and lymphocyte/granulocyte ratios, as summarized in Table 3.1.1. Platelet/leukocyte ratios increased from the first to the second range of acceleration due to the decrease in platelets and stability of the leukocyte concentration. In the third range, the ratios decreased significantly due to the increase in lymphocytes and granulocytes from the BL to the BC. Additionally, the content of granulocytes tended to be superior to that of lymphocytes, as the lymphocyte/granulocyte ratio was < 1 (Table 3.1.1).

Various reports in the literature discuss the role of leukocytes in L-PRP preparations. However, few studies highlight the effects of the platelet/leukocyte ratio on PRPs (Boswell et al., 2013; McCarrel et al., 2012; Parrish et al., 2016), which may provide a balance with regard to cell proliferation and differentiation. Parrish & Roides (2017) claimed that ratios closer to

those found under physiological conditions may produce more effective L-PRP. They also observed that L-PRP stimulated tendon cell proliferation, attributing this impact to the balance between platelets and leukocytes (Parrish et al., 2016).

Despite such evidence, it should be considered that different platelet/leukocyte ratios might be necessary for treating different injuries, with dependence on the degree of injury and the tissue to be regenerated. Therefore, studies involving the preparation, characterization and understanding of blood component distribution in L-PRP are great relevance to the clinical and research areas.

Finally, the results of this study were obtained by centrifuging a whole blood volume of 3.5 mL including ACD-A anticoagulant. Thus, extension of these results to higher volumes and other anticoagulants should be performed with caution due to the differences in centrifugal force and electrostatic interactions with various anticoagulants. Higher volumes and ionic forces in the medium will require higher accelerations to obtain the same distribution and packing, and these aspects need to be determined.

3.1.5. Conclusions

The general conclusion drawn from the results reported herein is that the L-PRP composition can be modulated by centrifugation conditions (acceleration and time). We observed that concentration patterns delineated platelet/leukocyte and lymphocyte/granulocyte ratios with different anabolic/catabolic balances, allowing for reliable L-PRP preparations that will be useful for further studies and therapeutic purposes.

Author Contributions

All authors contributed to the conception and design of the study and to the acquisition and analysis of the data. All authors contributed to the drafting and revision of the article and approved the final version to be submitted.

Declaration of Interest

This work was supported by FAPESP (São Paulo Research Foundation). Grant numbers 2014/27200-2, 2015/23134-8 and 2016/10132-0.

3.2. Centrifugation Conditions in L-PRP Preparation affect Soluble Factors Release and Mesenchymal Stem Cells Behavior

Artigo a ser submetido à periódico internacional indexado.

Centrifugation Conditions in L-PRP Preparation affect Soluble Factors Release and Mesenchymal Stem Cells Behavior

Bruna Alice Gomes de Melo[1], Ângela Cristina Malheiros Luzo[2], José Fabio Santos Duarte Lana[3] & Maria Helena Andrade Santana[1]*

[1]Department of Engineering of Materials and Bioprocesses, School of Chemical Engineering, University of Campinas, 13083-852, Campinas, SP, Brazil.

[2]Haematology & Hemotherapy Center, Umbilical Cord Blood Bank, University of Campinas, 13083-878, Campinas, SP, Brazil

[3]Bone and Cartilage Institute, 13334-170, Indaiatuba, SP, Brazil

*Correspondence should be addressed to lena@feq.unicamp.br, +55 (19) 35213921

ABSTRACT

Leukocyte and platelet-rich plasma (L-PRP) is an autologous product widely used in clinical applications to treat musculoskeletal diseases. Although the knowledge that centrifugation parameters directly influence the composition of L-PRP, the literature still claims for optimization and standardization of L-PRP preparations. In previous work, we delineated concentration patterns of platelet, leukocyte, lymphocyte, and granulocyte in L-PRPs prepared by centrifugation in the range of 100 to 800 xg. Here, we extended our findings by analyzing the growth factors and cytokines release, as well as the *in vitro* proliferation of human adipose-derived mesenchymal stem cells (h-AdMSCs) seeded in fibrin from L-PRP hydrogels. Different L-PRPs were prepared from a first spin at 100 xg ($L\text{-}PRP_{100}$) and 800 xg ($L\text{-}PRP_{800}$) for 10 min, followed by a second spin at 400 xg for 10 min and removal of 70% of the total volume ($L\text{-}PRP_{100\text{-}400}$ and $L\text{-}PRP_{800\text{-}400}$). After thrombin/calcium activation, fibrin hydrogels were formed ($fibrin_{100}$, $fibrin_{100\text{-}400}$, $fibrin_{800}$ and $fibrin_{800\text{-}400}$). Results showed that higher platelet and leukocyte concentrations were obtained for $L\text{-}PRP_{100}$ and $L\text{-}PRP_{100\text{-}400}$, as compared to $L\text{-}PRP_{800}$ and $L\text{-}PRP_{800\text{-}400}$. Although higher levels of the inflammatory factors IL-8 and TNF-α were secreted from $fibrin_{100\text{-}400}$ than from $fibrin_{800\text{-}400}$, the first favored h-AdMSCs proliferation, whereas cells in $fibrin_{800\text{-}400}$ presented the lowest proliferation rate. Therefore, instead of the absolute concentrations, platelet/leukocyte and lymphocyte/granulocyte ratios showed to play the major role in the anabolic/catabolic balance that modulated cell proliferation and minimized the catabolic effects of inflammatory factors.

Keywords: Platelet; leukocyte; fibrin; mesenchymal stem cell; growth factor; cytokine.

3.2.1. Introduction

In the past years, the benefits of the autologous leukocyte- and platelet-rich plasma (L-PRP) has been evidenced in the treatment of cartilage and bone diseases (Filardo et al. 2012; Lana et al. 2016; McCarrel et al. 2012; Riboh et al. 2015). Besides to growth factors (GFs), released from platelets alpha granules, L-PRP contains inflammatory cytokines secreted from leukocytes, which act in synergy modulating migration, proliferation, and differentiation of autologous cells through different pathways that lead to tissues regeneration (Andia and Maffulli, 2013; Anitua et al., 2012; Karin and Clevers, 2016). Depending on the site, the degree of the injury (acute or chronic) and treatment phase (early or late stage of healing), the leukocyte fraction must be adjusted from poor-leukocyte PRP (P-PRP) to L-PRP (Jubert et al. 2017; Middleton et al. 2012; Zhou et al. 2015). Modern classifications systems take account platelets and leucocyte levels besides other conditions such as the number of centrifugation spin, activation, the presence of erythrocytes and guided applications (Delong et al., 2012; Ehrenfest et al., 2014; Lana et al., 2017; Magalon et al., 2016).

Whether manual or by machine, L-PRP is prepared by centrifuging the patient's whole blood, in which platelets, leukocytes, proteins, and other components are concentrated in a small fraction of plasma. Platelet and leukocyte levels in L-PRP can be adjusted by varying the centrifugation conditions (de Melo et al. 2018; Perez et al. 2014). In a previous study, we determined the distribution and recovery of platelets and leukocytes (lymphocytes and granulocytes) in the supernatant, buffy coat, and erythrocyte layers, by centrifuging the whole blood from 100 to 800 xg (10 min and 25 ºC). The concentration patterns allowed identifying specific centrifugation ranges for the obtainment of distinct platelet/leukocyte and the associate lymphocyte/granulocyte ratios. As blood centrifugation is a separation process based on size and density of the components, as well as on the erythrocytes packing behavior, different recoveries of platelets and leukocytes could be obtained in L-PRP from a first spin (de Melo et al., 2018). In turn, a second centrifugation step under accelerations higher than 400 xg could lead to platelet aggregation and deactivation (Perez et al. 2014; Söderström et al. 2016). Therefore, choosing the centrifugation conditions for L-PRP preparation is crucial to achieving an appropriated performance.

When activated, L-PRP forms a 3D network, the fibrin clot, which acts as a scaffold for autologous cells to migrate, proliferate and differentiate at the injury site, behavior stimulated by the many GFs and cytokines (Ehrenfest et al., 2014; Wasterlain et al., 2012). Platelet-derived

GF (PDGF) and transforming GF (TGF-β) are the most abundant GFs present in the platelets alpha granules and are primarily responsible for modulating the wound healing process (Crane and Everts, 2008). They act in the early stages of healing by creating a concentration gradient to attract inflammatory agents, macrophages, mesenchymal stem cells (MSCs), fibroblasts and other cells to the injury site, in addition, to stimulate the secretion of more GFs, cells proliferation, differentiation, and production of extracellular matrix (ECM) (Caplan and Correa, 2011; Xu et al., 2018). On the other hand, activated leukocytes secrete inflammatory cytokines such as IL-1, IL-6, IL-8, and TNF-α, and play essential roles in healing during the inflammatory phase, acting as an immunoregulatory and antibacterial agent (Brat et al., 2005; Karin and Clevers, 2016; Roman-Blas et al., 2007). However, the catabolic effects of leukocytes, mainly due to neutrophils, could be harmful to cells and stimulate ECM degradation, among other effects (Wilgus et al., 2013). Therefore an appropriated anabolic/catabolic balance, is crucial for the regenerative process (Parrish et al., 2016; Sundman et al., 2011). Associated with endogenous MSCs, L-PRP composes the proliferation triangle, a term previously created in order to identify all necessary components to achieve an effective tissue regeneration (3D matrix, signaling molecules, and progenitor cells) (Barnett Jr and Pomeroy, 2007; Crane and Everts, 2008). Due to its high availability and great chondrogenic and osteogenic capability, exogenous MSCs have been used in cell-therapies and cartilage and bone engineering studies, presenting synergistic effects with L-PRP, such as increased GFs and cytokines secretion, cells migration, proliferation, and differentiation (Holmes et al., 2018; Jia et al., 2018; Xu et al., 2017).

In this work, we aimed to study the kinetics of GFs and cytokines release from activated L-PRP obtained by different centrifugation conditions, in addition to evaluate the viability and proliferation of MSCs from human adipose tissue (h-AdMSCs) seeded in the fibrin hydrogels. Results obtained here represents an advanced step towards understanding the effects of platelet/leukocyte ratio and catabolic/anabolic balance provided by different centrifugation conditions on cell behavior. The standardized preparations reduce variability and advice physicians and researchers to select appropriated parameters and operational conditions to obtain L-PRP with optimal yield and performance.

3.2.2. Material and Methods

3.2.2.1. Whole blood collection

The Ethics Committee of the Medical Sciences School of the University of Campinas (UNICAMP), CAAE: 0972.0.146.000-11, approved the use of human blood in this study, which was collected from a healthy donor in a tube containing the anticoagulant acid citrate dextrose solution A (ACD-A) (BD Vacutainer®, USA) prior to centrifugation.

3.2.2.2. L-PRP preparation

Centrifugation of the whole blood (3.5 mL) was carried out in a ROTINA 380R centrifuge (Hettich Zentrifugen, Tuttlingen, Germany), with the tubes positioned at 45º relative to the rotor. Four L-PRP formulations were prepared in one or two steps of centrifugation, as shown in the scheme of Figure 3.2.1A. In the first step, the whole blood was centrifuged at 100 xg and 800 xg for 10 min at 25 ºC, followed by the collection of the upper and middle layers using an automatic pipette, in order to obtain the L-PRP$_{100}$ and L-PRP$_{800}$. In the second step, L-PRP$_{100}$ and L-PRP$_{800}$ were centrifuged at 400 xg for 10 min at 25 ºC, and 70% of the supernatant (platelet-poor plasma, PPP) was discarded, obtaining the L-PRP$_{100\text{-}400}$ and L-PRP$_{800\text{-}400}$. L-PRPs and the whole blood were taken to an ABX Micros ES 60 hematologic analyzer (Horiba ABX Diagnostics, Montpellier, France) for blood components measurement. Three measurements of each sample were made by the equipment.

3.2.2.3. Concentration factor calculation

The concentration factor of platelets and leukocytes (including lymphocytes and granulocytes) were calculated relative to their concentration in the whole blood, according to Equation 3.2.1:

$$Concentration\ factor = \frac{[Platelet, Leukocyte, Lymphocyte, Granulocyte]_{L-PRP}}{[Platelet, Leukocyte, Lymphocyte, Granulocyte]_{Whole\ blood}} \qquad \textbf{Equation 3.2.1}$$

3.2.2.4. Fibrin hydrogels formation from L-PRP activation

The whole blood was collected in a tube containing serum clot activator (Greiner Bio-One Kremsmünster, Austria) and centrifuged at 2,000 xg for 15 min at 25 ºC. After centrifugation, serum containing thrombin was collected and mixed to 10% (w/v) $CaCl_2$ (Sigma-Aldrich, St. Louis, MO, USA) in a 9:1 ratio (serum: Ca^{2+} v/v). This mixture was added to the L-PRP formulations in the concentration of 20% (v/v), which was left to polymerize for at least 30 min, forming the $fibrin_{100}$, $fibrin_{800}$, $fibrin_{100\text{-}400}$ and $fibrin_{800\text{-}400}$ hydrogels.

3.2.2.5. Scanning electron microscopy (SEM) analysis

After polymerization and fibrin network formation, the hydrogels were fixed in a 4% paraformaldehyde and 2.5 % glutaraldehyde solution, prepared in phosphate buffer (PBS), pH 7.4, for 2 h at 4 ºC. Dehydration of fixed hydrogels was made by dipping them in ethanol of different concentrations (50, 70, 95 and 100%) at 15 min intervals. Then, samples were dried at the critical point in a dryer BAL-TEC CPD 030 (Schalksmühle, Germany). Dried samples were coated with gold in a Sputter Coater POLARON, SC7620 (VG Microtech, Uckfield, England), and SEM images taken in a LEO Electron Microscopy/Oxford (Cambridge, England). Fibers size were obtained by measuring at least 100 fibers from 3 distinct images, using the ImageJ software.

3.2.2.6. Kinetics of GFs and cytokines release

Fibrin hydrogels were prepared in a 48-well plate and incubated with Dulbecco's modified Eagle's medium (DMEM) low-glucose medium for 72 h in a humidified incubator at 37 ºC and 5% CO_2. At pre-determined times, the medium was collected and stored at -80 ºC. Then, the cumulative concentration of GFs (PDGF-BB, TGF-β1, and VEGF) and cytokines (IL-1β, IL-6, IL-8, and TNF-α,) was quantified using a Bio-plex Pro Kit in an equipment Bio-plex 200 (Bio-Rad, Hercules, USA). The experiment was performed in triplicate (n = 3) for each group.

3.2.2.7. h-AdMSCs isolation and culture in fibrin hydrogels

h-AdMSCs was isolated from human subcutaneous adipose tissue, and cultured according to a previous protocol (Manzini et al., 2015). Cells from passage 5 to 8 were trypsinized and resuspended in the L-PRP formulations at a concentration of 1 x 10^4 cells/ hydrogel. Fibrin was polymerized and hydrogels containing h-AdMSCs (Figure 3.2.1B) cultured with 750 µL of DMEM for 2 weeks in a humidified incubator at 37 ºC and 5% CO_2, with the medium being changed every three days. DMEM was not supplemented with FBS due to the high capacity of L-PRP to provide nutrients for cells survival and growth.(Murphy et al., 2012) The experiment was performed in triplicate (n = 3) for each group.

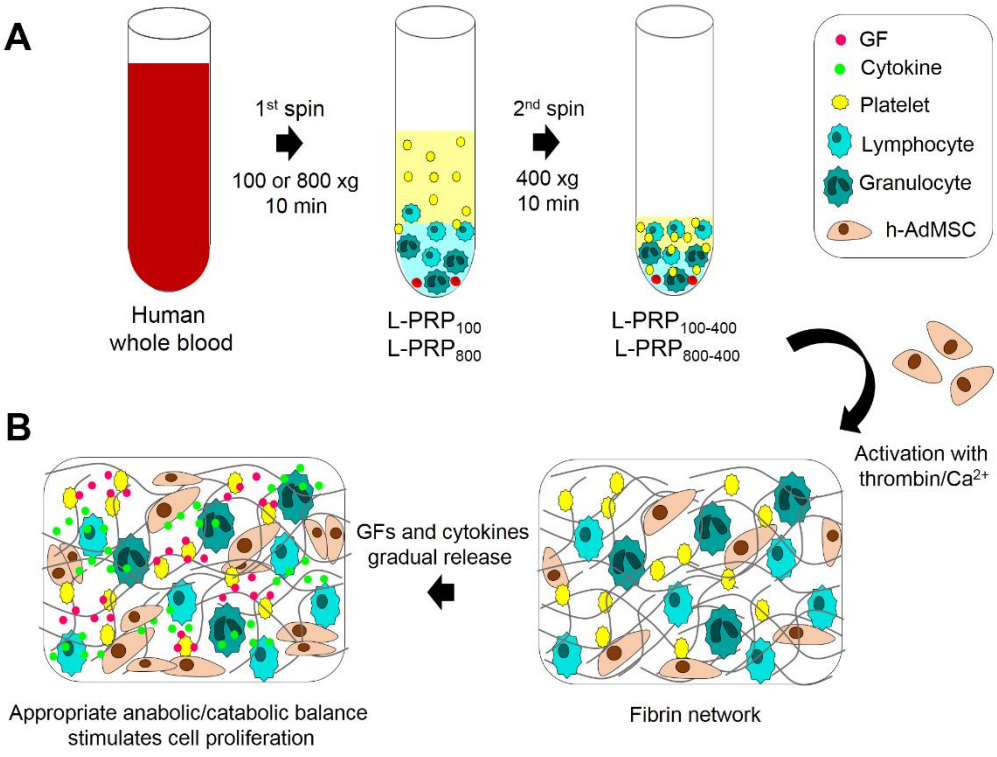

Figure 3.2.1. Schematic illustration of the experimental design. (A) Human whole blood was collected and centrifuged at 100 and 800 xg for 10 min to form L-PRP_{100} and L-PRP_{800}. These L-PRPs were submitted to a second spin at 400 xg for 10 min to form L-$PRP_{100\text{-}400}$ and L-$PRP_{800\text{-}400}$ after removal of 70% of the supernatant. (B) h-AdMSCs were resuspended in each L-PRP, followed by fibrin network formation after activation with thrombin/Ca^{2+}. Activated

platelets and leukocytes secrete GFs and cytokines that in an appropriate balance, stimulates cell proliferation.

3.2.2.8. Assessment of h-AdMSCs survival and growth

The number of viable cells in the fibrin hydrogels was assessed in the 7th day of culture using a Live/Dead Cell Imaging Kit (Thermo Fisher Scientific, Waltham, MA, USA). Samples were washed with PBS (pH 7.4) incubated with the live/dead reagent for 30 min, and taken to a confocal microscope (Leica Microscope TCS SP5 II, Wetzlar, Germany) for imaging. The numbers of living and dead cells were counted from 3 different images using the ImageJ software. To assess h-AdMSCs proliferation rate, at 3, 7, 10 and 14 days, fibrin hydrogels containing the cells were incubated with 1 mg/mL dimethyl-thia-zol-2-yl]-2,5-diphenyltetrazolium bromide (MTT) (Sigma-Aldrich, St Louis, USA) for 4 hours at 37 ºC, according to previous protocol (Mosmann, 1983). Then, MTT was replaced by dimethyl sulfoxide (DMSO) and left in a shaker for 30 min. Absorbance was measured at 595 nm, and the results expressed as the number of cells, calculated using a calibration curve previously prepared (R^2 = 0.9816). The experiment was performed in triplicate (n = 3) for each group.

3.2.2.9. Statistical analysis

Results are presented here as the mean ± standard deviation. One-way analysis of variance (ANOVA) with Tukey's test was used, with a 95% confidence level considered ($p < 0.05$).

3.2.3. Results

3.2.3.1. Concentration and ratio of blood components in the different L-PRP

The concentration of platelets, total leukocytes, lymphocytes and granulocytes in the whole blood was 149 ± 33, 3.8 ± 0.9, 1.4 ± 0.9 and 2.3 ± 0.4, respectively. L-PRP was prepared by collecting the upper and middle layers of centrifuged whole blood, presenting different

concentration of the components according to the applied speed (Figure 3.2.2A). The slower acceleration (100 xg) allowed the obtainment of an increased concentration of platelets, especially after two centrifugation steps (Figure 3.2.2B), as also observed for total leukocytes (Figure 3.2.2C). Lymphocytes represented the highest leukocytes portion, being highly concentrated in L-PRP$_{100\text{-}400}$ (Figure 3.2.2D). On the other hand, granulocytes concentration was higher in L-PRP$_{800}$ and L-PRP$_{800\text{-}400}$, as compared to L-PRPs from 100 xg (Figure 3.2.2E). As a consequence, the platelet/leukocyte and lymphocyte/granulocyte ratios were greater in both L-PRP$_{100}$ and L-PRP$_{100\text{-}400}$ in comparison to L-PRP$_{800}$ and L-PRP$_{800\text{-}400}$ (Figure 3.2.2F-G).

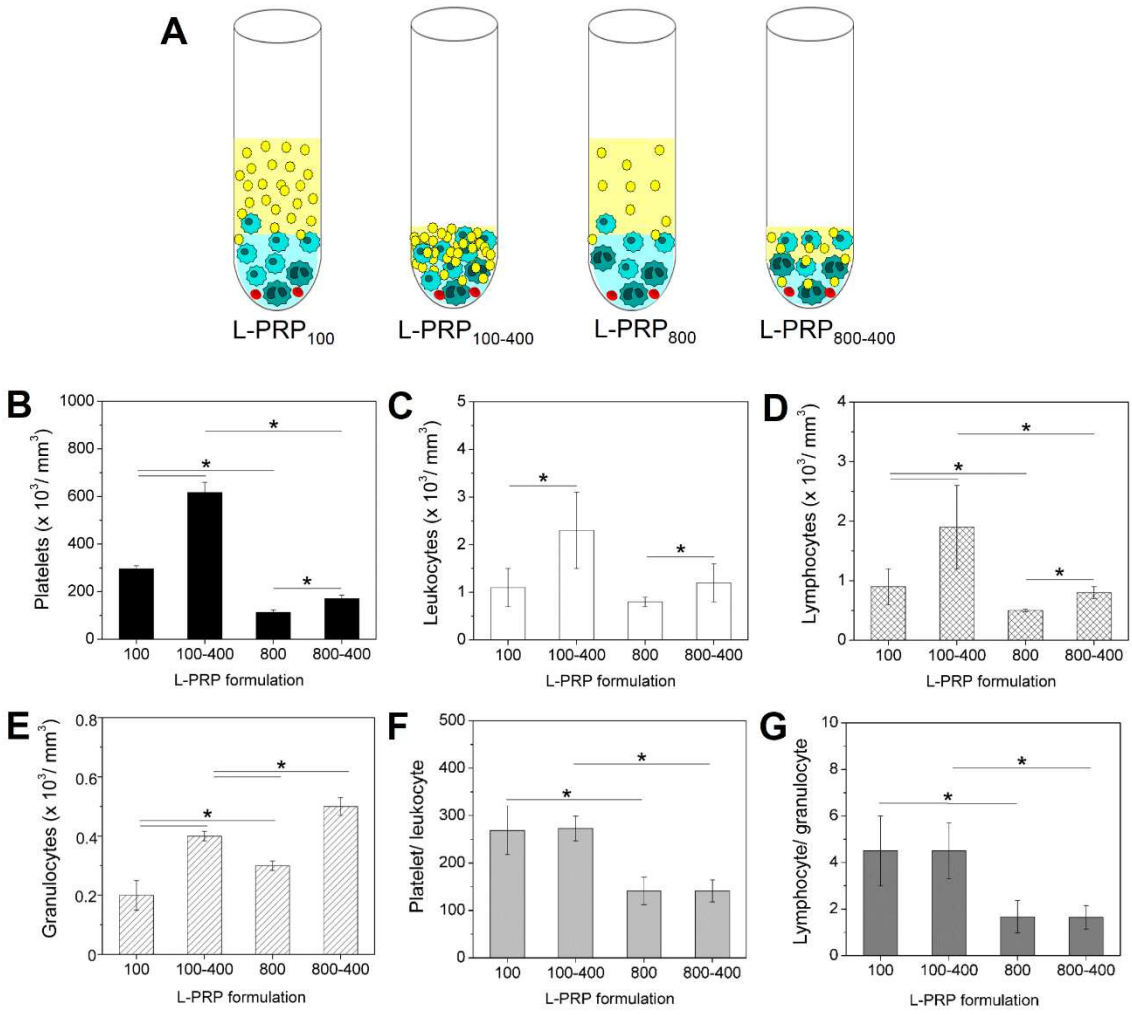

Figure 3.2.2. (A) Illustration representing the different L-PRPs after one or two centrifugation steps, demonstrating the composition changes by varying the preparation conditions.

Concentration of (A) platelets, (B) leukocytes, (C) lymphocytes and (D) granulocytes, obtained by measuring each L-PRP in a hematologic analyzer. The calculated ratio of (E) platelet/leukocyte and (F) lymphocyte/granulocyte in each L-PRP. *$p < 0.05$.

3.2.3.2. Concentration factors

The increase of blood components concentration in L-PRP relative to the whole blood was evaluated as concentration factors (Figure 3.2.3). The highest value was obtained for platelets in L-PRP$_{100}$ and L-PRP$_{100\text{-}400}$, being 1.98 ± 0.2 and 2.8 ± 0.3, respectively. The high speed significantly decreased the concentration factor of platelets, not reaching the baseline, being ~0.15 for L-PRP$_{800}$ and L-PRP$_{800\text{-}400}$. At this speed, it was also observed for total leukocytes, in which concentration factor was below 1 for the two formulations, due to the low concentration of granulocytes. However, a significant increase in this component was observed after the second centrifugation, being 0.17 ± 0.02 and 0.22 ± 0.03 for L-PRP$_{100\text{-}400}$ and L-PRP$_{800\text{-}400}$, respectively. Among all formulations, the highest concentration factor of lymphocytes was observed in L-PRP$_{100\text{-}400}$ (1.35 ± 0.2).

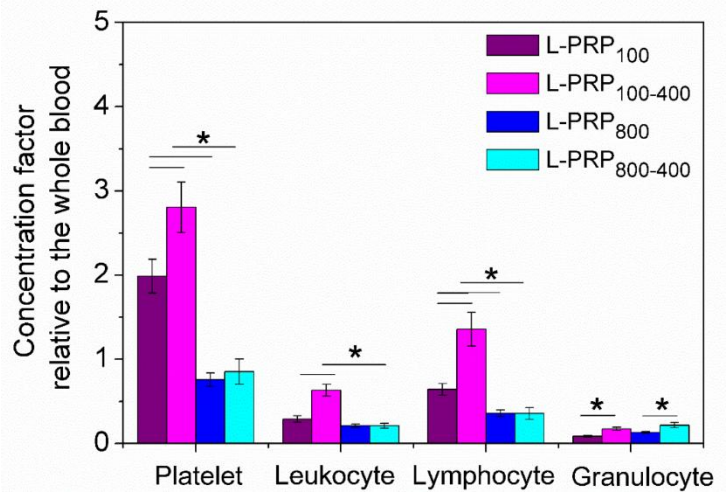

Figure 3.2.3. Concentration factors of platelets, total leukocytes, lymphocytes and granulocytes in the different L-PRPs relative to the whole blood.*$p < 0.05$.

3.2.3.3. Fibrin networks morphology

After activation of L-PRPs, fibrin networks were formed. The SEM images showed no substantial changes in morphology, with the structures presenting high porosity and interconnected fibers organization (Figure 3.2.4A). For all networks, fibers diameter varied from 100 to 200 nm, with the mean diameter being 161 ± 45, 176 ± 47, 189 ± 47 and 160 ± 34 nm for $fibrin_{100}$, $fibrin_{100\text{-}400}$, $fibrin_{800}$ and $fibrin_{800\text{-}400}$, respectively. We also observed less polydispersity in fibers diameter for samples prepared from 2 centrifugation steps (Figure 3.2.4B).

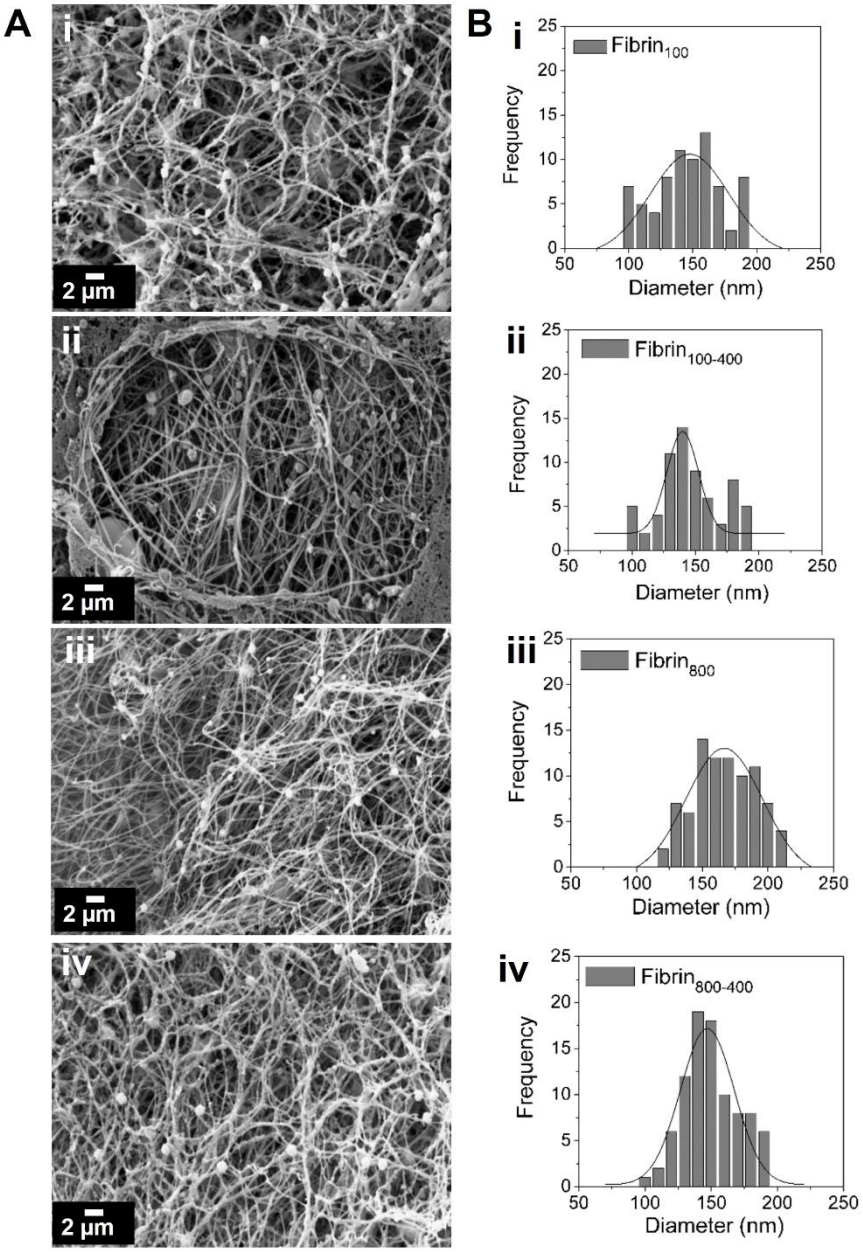

Figure 3.2.4. Characterization of the fibrin networks. (A) SEM images showing the networks morphology. (B) Frequency of fibers diameter measured using the ImageJ software. (i) $fibrin_{100}$, (ii) $fibrin_{100\text{-}400}$, (iii) $fibrin_{800}$ and (iv) $fibrin_{800\text{-}400}$.

3.2.3.4. Kinetics of GFs and cytokines release

The cumulative concentration of GFs and cytokines was measured during 72 h (Figure 3.2.5). It was observed that GFs release from fibrin increased proportionally with the increase of platelets in L-PRP. PDGF-BB presented a fast release in the first 3 h for $fibrin_{100}$ and $fibrin_{100\text{-}400}$, reaching 4230 ± 234 and 6290 ± 150 pg/mL at 72 h, respectively. For $fibrin_{800\text{-}400}$, the release was slower, but concentration reached a high level at 72 h, being 3335 ± 65 pg/mL. PDGF-BB concentration released from $fibrin_{800}$ was the smallest and reached the equilibrium rapidly, with values remaining below 1000 pg/mL (Figure 3.2.5A). TGF-β1 presented the highest level among all GFs, being released gradually with time. Its maximum concentration was 8576 ± 305, 11315 ± 840, 1092 ± 47 and 4490 ± 545 pg/mL for $fibrin_{100}$, $fibrin_{100\text{-}400}$, $fibrin_{800}$ and $fibrin_{800\text{-}400}$, respectively (Figure 3.2.5B). For VEGF, platelets seemed to rapidly release all its content in the first 3 hours, with values being below 150 pg/mL (Figure 3.2.5C).

The concentration of the cytokines IL-1β and IL-6 was < 10 pg/mL; therefore, its kinetics is not represented here. On the other hand, IL-8 was highly secreted, with concentration increasing with the increase of leukocytes in L-PRP. In the first 24 h, $fibrin_{100\text{-}400}$ and $fibrin_{800\text{-}400}$ presented a similar trend of release kinetics. Then, IL-8 secretion was sharply increased for $fibrin_{100\text{-}400}$, reaching 3490 ± 70 pg/mL at 72h, while for $fibrin_{800\text{-}400}$ the value was 2382 ± 136 pg/mL. For $fibrin_{100}$, IL-8 kinetics was slow up to 24 h, increasing sharply after this time, reaching 1013 ± 420 pg/mL. The concentration of this cytokine in $fibrin_{800}$ was below 200 pg/mL (Figure 3.2.5D). TNF-α was significantly higher released from $fibrin_{100\text{-}400}$ in comparison to the other formulations during all the times studied, being ~2.5-fold and ~4-fold greater than $fibrin_{800\text{-}400}$ and $fibrin_{100}$, respectively. Similarly to IL-8, the concentration of TNF-α released from $fibrin_{800}$ presented the smallest values (< 100 pg/mL) (Figure 3.2.5E).

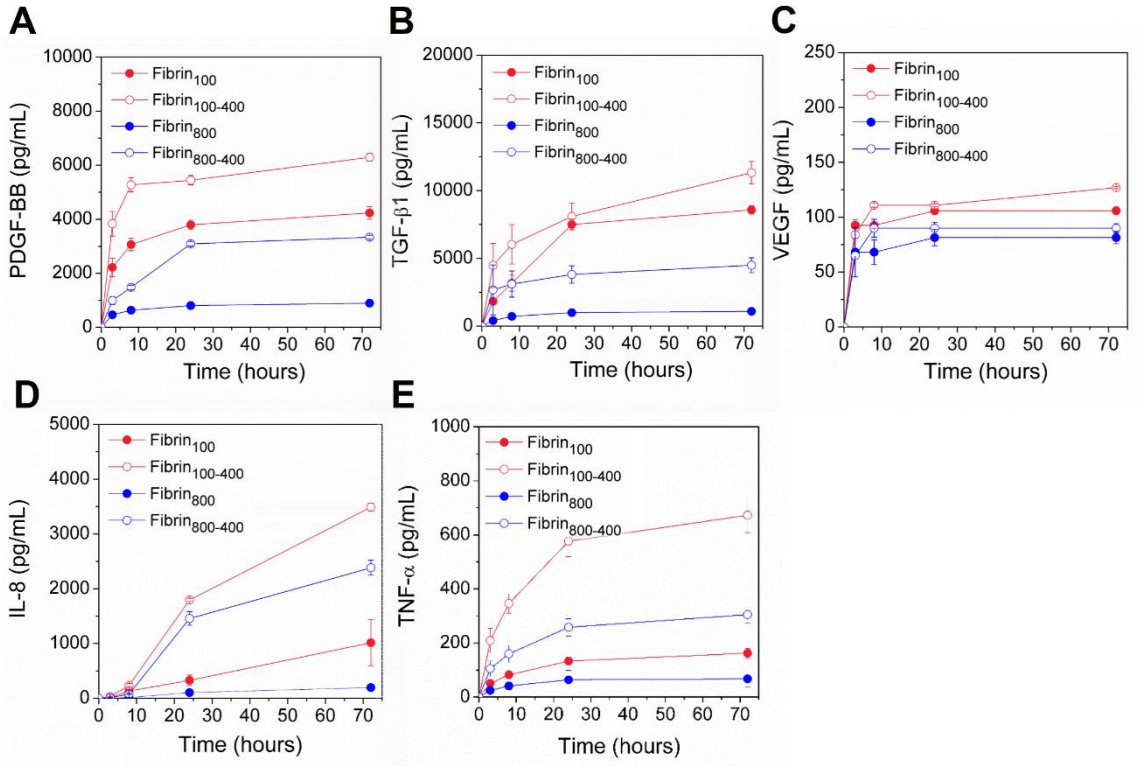

Figure 3.2.5. Kinetics of the GFs (A) PDGF-BB, (B) TGF-β1, (C) VEGF and the inflammatory cytokines (D) IL-8 and (E) TNF-α released from the hydrogels for 72 hours.

3.2.3.5. Viability and proliferation rate of h-AdMSCs in fibrin hydrogels

The h-AdMSCs were cultured in the fibrin hydrogels, and their behavior in the different microenvironments assessed as viability and proliferation rate. Images of living and dead cells were captured in a fluorescence confocal microscope using live/dead reagents after 7 days of culture. Results showed that the fibrin hydrogels were suitable to maintain cells viability, with h-AdMSCs presenting slightly elongated to rounded shape within the networks (Figure 3.2.6A). The number of viable cells in samples prepared at gentle centrifugal acceleration was significantly higher than in samples prepared at the higher speed, with viability being 87.2 ± 2.9, 86.1 ± 2.8, 75.6 ± 0.6 and 74.3 ± 3% for fibrin$_{100}$, fibrin$_{100\text{-}400}$, fibrin$_{800}$ and fibrin$_{800\text{-}400}$, respectively (Figure 3.2.6B). The h-AdMSCs were kept in culture for 2 weeks, and results showed increased growth in fibrin$_{100\text{-}400}$ for up to 7 days. Then, on the 10th day, the number of cells in fibrin$_{100}$, fibrin$_{800}$, and fibrin$_{800\text{-}400}$ increased significantly, reaching their maximum growth point. A lower proliferation rate was observed for h-AdMSCs in fibrin$_{800\text{-}400}$, with the number of cells being significantly smaller than the other conditions on day 10, and presenting a fastest dead phase on day 14 (Figure 3.2.6C).

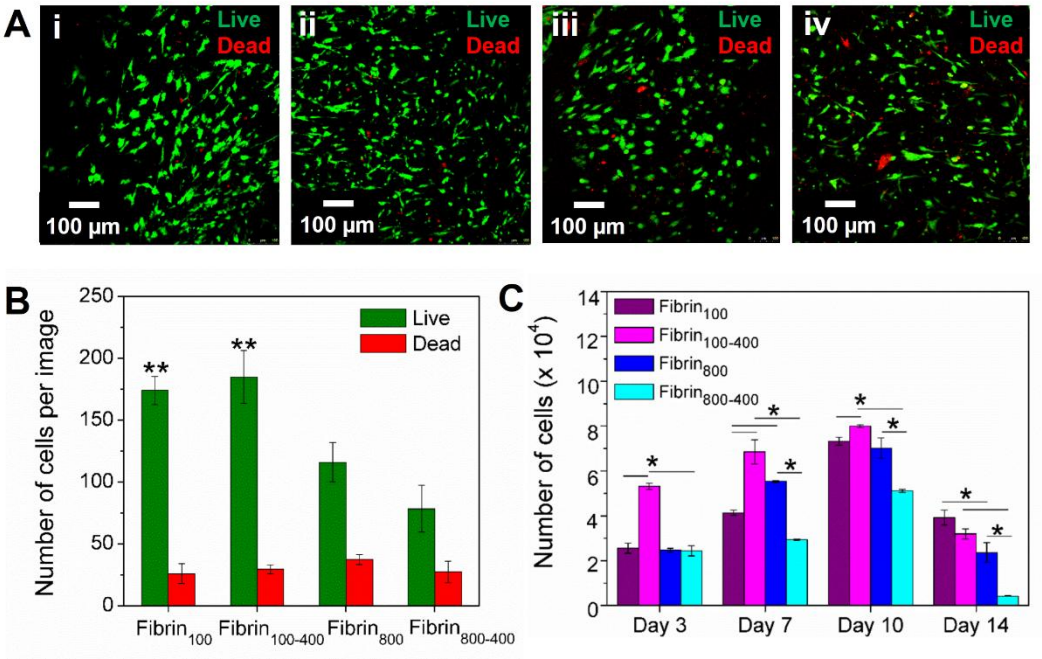

Figure 3.2.6. Assessment of h-AdMSCs behavior seeded in the four types of fibrin. (A) Cell viability in the 7th day of incubation in (i) fibrin$_{100}$, (ii) fibrin$_{100\text{-}400}$, (iii) fibrin$_{800}$ and (iv) fibrin$_{800\text{-}400}$. (B) Number living and dead h-AdMSCs in the fibrins incubated for 7 days, calculated from three different images using the ImageJ software. (C) The proliferation rate of h-AdMSCs seeded in the hydrogels for 2 weeks. *$p < 0.05$. **Significantly different from fibrin$_{800}$ and fibrin$_{800\text{-}400}$ ($p < 0.05$).

3.2.4. Discussion

In previous work, we reported the mechanisms of platelets and leukocytes recovery in L-PRP by centrifugation, which is driven by their size, density, and erythrocytes aggregation and sedimentation (de Melo et al., 2018). As predicted by theoretical calculations and experimentally confirmed, low centrifugal accelerations in the first spin (50 - 100 xg) contributes to high yields of platelets in P-PRP (upper layer) (Perez et al., 2013). If up to the 2010s, high spin ranges were used (Anitua et al., 2005; Anitua et al., 2007), nowadays, we observe that low speeds for a first spin became a consensus (Choukroun and Ghanaati, 2018; Ehrenfest et al., 2018; Söderström et al., 2016). At lower range of centrifugal accelerations, we have also observed the highest leukocytes recovery, with increased platelet/leukocyte and lymphocyte/granulocyte ratios in L-PRP, in comparison to accelerations ranging from 300 to 800 xg (de Melo et al., 2018). As microenvironments with distinct blood components ratios

lead to different biological responses, the standardization of the centrifugation conditions and the study of cell responses to different types of L-PRPs is essential to predict its behavior *in vivo*. In this work, we investigated the release of GFs and cytokines, and the response of h-AdMSCs to different fibrin microenvironments. For this, L-PRPs were prepared from two centrifugation extremes, 100 xg and 800 xg for the first spin, followed by a second spin at 400 xg and removal of 70% of the total volume.

A gentle centrifugal acceleration is essential to maintain platelets integrity and retain their morphological properties and activation capacity, which is crucial for their gradual content release mechanism. Under high centrifugal forces, platelets are submitted to high shear stress that can induce aggregation, activation and early GFs release, impairing the proper functioning of L-PRP (Perez et al. 2014; Ehrenfest et al. 2018; Söderström et al. 2016). As previously reported, platelets activation increases with the increase of centrifugation speed, resulting in changes in their biological signature (Söderström et al., 2016). Here, we observed that GFs release was proportional to platelets concentration, being higher for $fibrin_{100}$ and $fibrin_{100\text{-}400}$. For $fibrin_{800}$, the concentration of released GFs was minimum. However, the first spin at 800 xg did not damage platelets, once after the second centrifugation at 400 xg, an increased and gradual release of GFs was observed, indicating, therefore, the maintenance of platelets integrity.

Leukocytes secrete cytokines upon activation and strongly depend on the stimulus from the microenvironment (Chaly et al., 2000; Smyth et al., 1991). Here, we observed that IL-1β and IL-6 were not secreted even from fibrin prepared from L-PRP with the highest concentration of leukocytes ($L\text{-}PRP_{100\text{-}400}$). On the other hand, IL-8 and TNF-α were highly released from $fibrin_{100\text{-}400}$ and $fibrin_{800\text{-}400}$, with the concentration being proportional to the leukocytes amount. As previously reported, independent of stimulus, granulocytes are capable of synthesizing and secreting TNF-α (Dubravec et al., 1990), corroborating our results. TNF-α is immunostimulatory to lymphocytes, modulating the secretion of other cytokines, such as IL-8 (Chaly et al., 2000). It is also a potent neutrophil chemoattractant, recruiting these granulocytes to inflammatory sites for debridement and fight infections (Taub et al., 1996). Therefore, the L-PRP prepared from two centrifugation steps could be beneficial for applications in initial stages of wound healing (Spakova et al., 2012).

As different centrifugal accelerations and leukocytes concentration were related to morphological changes in fibrin network, which could interfere with platelet adhesion and soluble factors release (Anitua et al., 2015; Ehrenfest et al., 2018), we analyzed networks

morphology and fibers size by SEM. Here, we observed that for all conditions, it was formed interconnected fibers, with a random organization and networks with high porosity. The different concentrations of blood components did not seem to affect the networks morphology, but reduced polydispersity of fibers diameter.

Although the presence of leukocytes, especially granulocytic neutrophils, could be harmful to cells due to their catabolic effects (Wilgus et al., 2013), by assessing h-AdMSCs responses to the different microenvironments, we attested an opposite behavior. The highest concentration of inflammatory cytokines released from $fibrin_{100-400}$ did not impair h-AdMSCs viability and growth, which showed a superior proliferation rate, probably due to the balance provided by the high concentration of anabolic GFs. Although PDGF-BB and TGF-β1 concentration from $fibrin_{100}$ and $fibrin_{800}$ were significantly lower than in $fibrin_{100-400}$, an increase in cell growth as a response to these formulations was observed on day 10. On the other hand, h-AdMSCs proliferation was inhibited in $fibrin_{800-400}$, which released the second highest concentration of inflammatory cytokines and lower concentration of GFs, as compared to $fibrin_{100}$ and $fibrin_{100-400}$. Therefore, we concluded that rather than platelets and leukocytes absolute values, the ratio platelet/leukocyte drove cell behavior through the balance between the anabolic/catabolic effects. This balance is altered during an injury, being reconstituted by L-PRP, in which the microenvironment returns to a beneficial balance and homeostasis.

These results are coherent with the consensus that considerate 1 million platelets/ mm^3 in PRPs as a reference score in the literature because its anabolic effects are preserved (Delong et al., 2012). However, we recommend balanced platelet/leukocyte (> 200) and the correspondent lymphocyte/granulocyte ratios (> 1), which could present higher efficiency in the applications of L-PRP.

3.2.5. Conclusions

This study reports the influence of the operational process of L-PRP obtainment on its biological signature, in which cells behavior was mediated by the anabolic/catabolic balance provided by platelets and leukocytes. L-PRPs standardized as platelet/leukocyte ratios > 200 associated with lymphocyte/granulocyte ratios > 1 represent formulations that lead to optimal performance. Further studies must be carried out using a larger number of healthy donors, as well as with donors with musculoskeletal diseases, in order to a better delineation of the effects of the established platelet/leukocyte and lymphocyte/granulocyte ratios on cell behavior. We

believe these *in vitro* evaluations are relevant for physicians and researchers to standardize L-PRP preparations, as well as to understand and compare *in vitro* results.

Acknowledgment

The authors gratefully acknowledge funding by The São Paulo Research Foundation (FAPESP) Grant Nos. 2015/23134-8 and 2016/10

3.3. Hyaluronic acid and fibrin from L-PRP form semi-IPN with tunable properties for regenerative medicine

Artigo a ser submetido à periódico internacional indexado.

Hyaluronic acid and fibrin from L-PRP form semi-IPN with tunable properties for regenerative medicine

Bruna Alice Gomes de Melo[1], Carla Giometti França[1], José Luis Dávila[2], Marcos Akira d'Ávila[2], Ângela Cristina Malheiros Luzo[3], José Fabio Santos Duarte Lana[4] & Maria Helena Andrade Santana[1]*

[1]Department of Engineering of Materials and Bioprocesses, School of Chemical Engineering, University of Campinas, 13083-852, Campinas, SP, Brazil.

[2]Department of Manufacturing and Materials Engineering, School of Mechanical Engineering, University of Campinas, 13083-860, Campinas, SP, Brazil

[3]Haematology & Hemotherapy Center, Umbilical Cord Blood Bank, University of Campinas, 13083-878, Campinas, SP, Brazil

[4]Bone and Cartilage Institute, 13334-170, Indaiatuba, SP, Brazil

*Correspondence should be addressed to mariahelena.santana@gmail.com, +55 (19) 35213921

ABSTRACT

Local application of autologous platelet-rich plasma (PRP) associated with hyaluronic acid (HA) has been widely used in sequential injections for cartilage and bone regeneration. However, this association confers structural and rheological changes in comparison to the individual biomaterials, which have not been investigated. In this work, L-PRP (leukocyte- and platelet-rich PRP) was mixed under controlled conditions to non-crosslinked HA of low (~15 kDa) and high (> 2,000 kDa) MM (HMM and LMM, respectively), forming semi-interpenetrating polymer networks (semi-IPNs) after activation with thrombin/calcium. The polymerization time, networks morphology, swelling ratio, stability and rheological behavior of fibrin and semi-IPNs (fibrin-LMM HA and fibrin-HMM HA) were characterized, showing that hydrogels properties varied with the HA MM. In addition, we evaluated the response of human adipose-derived mesenchymal stem cells (h-AdMSCs) seeded in the different hydrogels, with results showing their superior viability in the semi-IPNs, as compared to fibrin. In conclusion, the preparation of fibrin-HA semi-IPNs under controlled mixture assured the formation of autologous and cell-friendly hydrogel matrices, with tunable properties according to the HA MM. These results are relevant for the standardization of clinical protocols aiming the use L-PRP and HA in regenerative medicine.

Keywords: Platelet; leukocyte; fibrin; hyaluronic acid; mesenchymal stem cell.

3.3.1. Introduction

Local injections of PRP (platelet-rich plasma) has been widely used for the treatment of cartilage and bone diseases, showing effective tissue regeneration (Gawai and Sobhana, 2015; Guadilla et al., 2012; Jubert et al., 2017; Spakova et al., 2012). The leukocyte- and platelet-rich plasma (L-PRP) consists of a richest PRP formulation, concentrated in platelets, leukocytes, proteins, and other components that after activation forms fibrin hydrogel, a biologically rich matrix suitable for cell growth (Ehrenfest et al., 2014). Fibrin from L-PRP acts as a reservoir of growth factors and cytokines, which are gradually released and contribute to the effectiveness of healing (Everts et al., 2007).

The efficacy of PRP, including L-PRP, in osteoarthritic patients has shown to be potentially increased when combined with exogenous hyaluronic acid (HA), by stimulating endogenous HA formation and contributing to signaling, restoration of joint viscoelasticity, and reduction of pain (Kurapati et al. 2018; Lana et al. 2016; Renevier et al. 2018; Yu et al. 2018). HA is a glycosaminoglycan present in the extracellular matrix (ECM) of joints in its high molar mass (HMM) form, maintaining tissue integrity, by promoting organization, elasticity, lubrication and shock absorption (Balazs et al., 1967). HMM HA is naturally degraded into smaller fragments forming a low molar mass (LMM) HA (Aya and Stern, 2014), which presents different biological properties, such as angiogenesis promotion and stimulation of inflammatory cytokines expression (Noble, 2002b; West et al., 1985). Due to these characteristics, LMM HA also plays an essential role in the healing process.

Clinical protocols report the sequential injection of L-PRP and HA, assuming that the movement of the patient's joint ensures an effective mixing (Andia and Abate, 2014; Kurapati et al., 2018; Lana et al., 2016), Due to the high viscosity of HA solutions, a poor L-PRP-HA mixture could result in nonhomogeneous hydrogels with weak interactions that may lead to phase separation, which might be prejudicial for cell support (Abbadessa et al., 2017; Rinaudo, 2008). Considering the importance of a previously formed matrix, recently a mixture of P-PRP (poor-leukocyte PRP) and non-crosslinked HA prepared by machine was developed (Vischer et al., 2018).

In vivo evaluations have shown benefits in mild and moderate knee osteoarthritis using an L-PRP-HMM HA prepared manually and applied in sequential injections (Lana et al., 2016). Positive results were also observed from the P-PRP and HA mixture, prepared by machine in grade II and III knee osteoarthritis (Renevier et al., 2018). However, the different preparation

and application methods may result in the formation of different structures, which can affect biological responses, making it difficult to compare results. Therefore, *in vitro* studies are essential to standardize the production and evaluate the properties and performance of PRP-HA hydrogel matrices.

Previous works have reported the fabrication of interpenetrating polymer networks (IPNs) from commercial fibrin and crosslinked HA, which presented positive response of cells to proliferation and differentiation (Arulmoli et al., 2016; Lee and Kurisawa, 2013; Zhang et al., 2016). However, HA crosslinked agents may lead to side products that could be harmful to the organism. An alternative to IPNs is the semi-IPN type, characterized as a network composed of polymers in both crosslinked and non-crosslinked forms. A fibrin-HA semi-IPN structure is formed by polymerized fibrin and non-crosslinked HA coils entangled between the fibers, binding specific sites of fibrin through physical crosslinking without covalent bonds, with variable packing arrangement and viscoelasticity, depending on the HA MM (Dong et al., 2012; LeBoeuf et al., 1986; Russo et al., 2016).

The capacity of fibrin from P-PRP mixed to non-crosslinked HA to form hydrogel matrices capable of supporting cells proliferation and differentiation was previously demonstrated (Russo et al., 2016; Vadalá et al., 2017). However, a leukocyte-rich formulation result in a different microenvironment that affect cell stimuli and responses (Zhou et al. 2015; Parrish et al. 2016). Therefore, a cell-friendly alternative biomaterial could be the semi-IPNs composed of autologous L-PRP and non-crosslinked HA. Because of the greater complexity in composition and preparation, as well as the smaller amount of works in the literature, the L-PRP-HA matrices lacks in standardization and characterization.

In this work, we prepared fibrin-HA semi-IPNs by mixing L-PRP and HA of low (~15 kDa) and high (> 2,000 kDa) MM (HMM and LMM, respectively), under controlled conditions. For L-PRP preparation, we used a protocol previously established by our group in order to obtain a known concentration range of platelets and leukocytes (de Melo et al., 2018). The fibrin-LMM HA and fibrin-HMM HA hydrogels were characterized according to their polymerization kinetics, morphology, swelling behavior, and stability. The formation of the semi-IPNs was attested by FTIR analysis and rheology characterization. The suitability of the semi-IPNs to support cells was attested by evaluating using human adipose-derived mesenchymal stem cells (h-AdMSCs) viability in the semi-IPNs. The results obtained here are valuable for standardizing protocols to produce semi-IPNs from autologous L-PRP and HA,

with tunable properties according to the HA MM, being useful clinically for regenerative medicine.

3.3.2. Material and Methods

3.3.2.1. Blood collection and L-PRP preparation

The use of human blood was approved by the Ethics Committee of the School of Medical Sciences of Unicamp (Campinas; CAAE: 0972.0.146.000-11). L-PRP was prepared as previously described (de Melo et al., 2018). Briefly, whole blood from a healthy donor was collected after the venous puncture in an 8.5-mL tube containing 1.5 mL of anticoagulant acid citrate dextrose solution A (ACD-A) (Vacutainer, BD Biosciences, Allschwil, Switzerland). After collection, 3.5 mL of the anticoagulated blood was transferred to empty 5-mL tubes and centrifuged at 100 xg for 10 min at 25 ºC in a ROTINA 380R centrifuge (Hettich Zentrifugen, Tuttlingen, Germany), with the tubes positioned at 45° relative to the rotor. L-PRP, composed of the top and middle layers of centrifuged blood, was collected and transferred to an empty tube for homogenization and quantification of components using an ABX Micros ES 60 hematologic analyzer (Horiba ABX Diagnostics, Montpellier, France). Three measurements of each sample were made by the equipment.

3.3.2.2. L-PRP-HA mixture and semi-IPNs preparation

L-PRP was mixed with LMM HA (~15 kDa, according to the manufacturer, Lifecore Biomedical, Chaska, MN, USA) and HMM HA (> 2000 kDa, according to the manufacturer, Euflexxa® Ferring Pharmaceuticals, Saint-Prex, Switzerland) at a 1:1 volumetric ratio, obtaining a final HA concentration of 1 mg/mL. L-PRP-HA combinations were homogenized for 30 min at 8 rpm and 25 ºC in a Phoenix Luferco homogenizer AP22 (Phoenix Luferco, Araraquara, SP, Brazil). Before semi-IPN preparation, autologous serum containing thrombin was prepared by collecting 5 mL of whole blood from the same donor in a Vacuette tube with a serum clot activator (Greiner Bio-One, Kremsmünster, Austria) and centrifuged for 15 min at 2,000 xg and 25 ºC. Serum was separated and mixed with 10% (w/v) calcium chloride at a volumetric ratio of 9:1 of serum to $CaCl_2$ (Sigma-Aldrich, St Louis, USA). Fibrinogen activation and semi-IPN formation were achieved by adding serum-Ca^{2+} to the homogeneous

mixture of L-PRP-HA at a concentration of 20% (v/v). After fibrin and semi-IPNs formation, the concentration of platelets and leukocytes present in the remaining plasma was quantified using the hematologic analyzer.

3.3.2.3. Polymerization time and fibers characterization

Fibrin polymerization kinetics was determined by measuring the optical densities of gelled fibrin and fibrin-HA at a 450-nm wavelength for 60 min, with time zero corresponding to the time of serum-Ca^{2+} addition, measured in a FilterMax F5 Multi-Mode Microplate reader (Molecular Devices, Sunnyvale, CA, USA). From the kinetics profiles obtained, the beginning of polymerization was established as the point where the optical density curve changed its initial slope. Radii and the mass/length ratios of fibrin fibers were characterized using the modified Carr's Equation (Equation 3.3.1) (Yeromonahos et al., 2010).

$$t\lambda^5 = \frac{2\pi^3 Cn\mu\left(\frac{dn^2}{dC}\right)\frac{44}{15}\left(\lambda^2 - \frac{184}{154}\pi^2 r^2 i^2\right)}{N} \qquad \textbf{Equation 3.3.1}$$

where t is solution turbidity, C is the initial fibrinogen concentration (g/cm^3); N is Avogadro's number; λ is the incident wavelength (cm) (340, 450, 500, 540, 600 and 640 nm); μ = mg/L, with mg being the protein mass (Da) in a fiber of length L (cm) and radius r (cm); and i is the refractive index (1.33). Next, $t\lambda^5$ was plotted against λ^2, resulting in a straight line whose slope yielded the mass/length ratio, and the ordinate at the origin gave the square of the average radius. The turbidity was calculated from its relationship with the optical density (OD) of the gelled fibrin measured as its absorbance (Equation 3.3.2):

$$t = 1 - exp(-OD.\ln(10)) \qquad \textbf{Equation 3.3.2}$$

The experiment was performed in triplicate (n = 3) for each group.

3.3.2.4. Scanning electron microscopy (SEM) analysis

Morphological and structural characterization of hydrogels was performed by fixing fibrin and semi-IPNs in a 4% paraformaldehyde and 2.5% glutaraldehyde solution prepared in PBS for 2 h. Then, samples were dehydrated in graded ethanol dilutions (50, 70, 95 and 100%) at 15 min intervals and dried at the critical point. After gold-coating in a Sputter Coater POLARON, SC7620 (VG Microtech, Uckfield, England), scanning electron microscopy images of the samples were taken using a LEO Electron Microscopy/Oxford (Cambridge, England). The average fibrin fibers diameter was determined by measuring 100 individual fibers from three different images using the ImageJ software.

3.3.2.5. Determination of fibrinogen concentration

The concentration of fibrinogen in L-PRP and fibrin network was determined as described in a previous protocol (Ratnoff and Menzie, 1951), which after polymerization, fibrin was centrifuged at 500 xg for 5 min and the supernatant discarded. This step was repeated three times. Then, NaOH (Sigma-Aldrich, St Louis, USA) was added to the tubes containing fibrin and left in a water bath at 95 ºC for 10 min. After this time, the sample was treated with water, NA_2CO_3 and Folin-Ciocalteu's phenol reagent (Sigma-Aldrich, St Louis, USA) for 30 min, and absorbance measured at 650 nm. Results were expressed as fibrinogen concentration, calculated using a calibration curve previously prepared with commercial fibrinogen from human plasma (Sigma-Aldrich, St Louis, USA) ($R^2 = 0.993$). The experiment was performed in triplicate (n = 3) for each group.

3.3.2.6. Swelling behavior

In order to assess swelling behavior of hydrogels, dried fibrin and semi-IPNs were weighted (W_d) and dipped in phosphate buffer saline (PBS, pH 7.4, 37 ºC) until they reached the equilibrium. At predetermined times, hydrogels were weighted (W_s), and the swelling ratio calculated using Equation 3.3.3. The experiment was conducted in triplicate (n = 3) for each group.

$$Swelling\ ratio = \frac{W_s - W_d}{W_d} \qquad \textbf{Equation 3.3.3}$$

3.3.2.7. Hydrolytic degradation

The degradation profile of fibrin and semi-IPNs was determined by initially weighing the dried hydrogels (W_i) followed by immersion in PBS and incubation at 37 ºC. At predefined times, samples were dried and final weight (W_f) was measured. Mass loss was calculated according to Equation 3.3.4. The experiment was conducted in triplicate (n = 3) for each group.

$$Mass\ loss\ (\%) = \frac{W_f - W_i}{W_i} \text{ x } 100 \qquad \textbf{Equation 3.3.4}$$

3.3.2.8. FTIR analysis

After two weeks of incubation, the hydrogels were lyophilized in a lyophilizer L-101 (Liotop, São Carlos, Brazil) for two days. FTIR analyses of the dried samples were performed in a Thermo Scientific Nicolet 6700 spectrophotometer (Thermo Fisher Scientific, Madison, USA), using the single-reflection germanium attenuated total reflection (ATR) technique, in a Smart OMNI-Sampler (Thermo Fisher Scientific, Madison, USA). The wavelength range of the performance was 4000 - 750 cm^{-1} with a resolution of 4 cm^{-1}.

3.3.2.9. Rheological characterization

The rheology of L-PRP, L-PRP-HA mixtures, fibrin, and semi-IPNs was studied in an Anton Paar MCR-102 Modular Compact Rheometer (Anton Paar, Graz, Austria). The tests were conducted using a cone-plate geometry (CP50-1) of 50 mm in diameter, a cone angle of 0.9815° and a truncation of 0.97 μm. Steady-state shear tests were performed in the range of 0.01 to 1000 s^{-1} at 25 °C. The oscillatory measurements were conducted in the linear region with the amplitude gamma of 1% and in the angular frequency range of 0.1 to 100 rad/s. The experiment was performed in triplicate (n = 3) for each group. Experimental data were fitted using the power-law model, which is defined by Equation 3.3.5.

$$\tau = m\dot{\gamma}^n \qquad \textbf{Equation 3.3.5}$$

where τ is the shear stress, m the consistency index, $\dot{\gamma}$ is the shear rate and n is the power-law index.

3.3.2.10. h-AdMSCs culture in fibrin and semi-IPNs

h-AdMSCs from human subcutaneous adipose tissue were acquired from abdominal liposuction surgery of patients undergoing lipo-aspiration at the University Hospital. Then, cells were isolated and cultured as previously described (Manzini et al., 2015). The precultured cells were trypsinized and resuspended in L-PRP and L-PRP-HA mixtures to obtain 1 x 10^4 cells/ hydrogel. After homogenization, 160 µL of L-PRP and L-PRP-HA containing h-AdMSCs was added to a 48-well plate and activated with 40 µL of the serum-Ca^{2+}. Once the gels were formed, 750 µL low-glucose DMEM (Thermo Fisher Scientific, Waltham, MA, USA) was added to the wells, and cells were cultured for two weeks in a 37 ºC incubator with 5% CO_2 with the medium changes every three days. Culture medium was not supplemented with FBS due to the high capacity of L-PRP to provide nutrients for cell survival (Murphy et al., 2012). The experiment was performed in triplicate (n =3) for each group.

3.3.2.11. Assessment of h-AdMSCs viability

Cells viability was determined by a live/dead assay for two weeks using a Live/Dead Cell Imaging Kit (Thermo Fisher Scientific, Waltham, MA, USA). At predetermined days, the medium was removed from the wells, and IPNs were washed with PBS. Then, 200 µL of the live/dead reagent was added to the wells, and samples incubated for 30 min. After this period, samples were taken to a confocal microscope (Leica Microscope TCS SP5 II, Wetzlar, Germany) for imaging. The numbers of living and dead cells were calculated by counting cells from at least three different images using the ImageJ software.

3.3.2.12. h-AdMSCs proliferation rate

Cells growth was assessed by dimethyl-thia-zol-2-yl]-2,5-diphenyltetrazolium bromide (MTT) (Sigma-Aldrich, St Louis, USA) assay, which at predetermined days, samples were incubated with MTT for 4 hours at 37 ºC. Then, formazan formed by MTT reduction was dissolved in dimethyl sulfoxide (DMSO), and absorbance measured at 595 nm. Results were expressed as number of cells, estimated by a previously prepared calibration curve (R^2 = 0.9816). The experiment was conducted in triplicate (n = 3) for each group.

3.3.2.13. Statistical analysis

The results are presented as the mean ± standard deviation (SD). When relevant, one-way analysis of variance (ANOVA) with Tukey's test was used for statistical analysis. A 95% confidence level was considered significant ($p < 0.05$).

3.3.3. Results

3.3.3.1. Blood and L-PRP composition

Concentration of blood components in both whole blood and L-PRP is shown in Table 3.3.1. Platelet and leukocyte concentrations in L-PRP were 294 ± 1 x 10^3/mm^3 and 1.20 ± 0.00 x 10^3/mm^3, respectively, with a platelet/leukocyte ratio of 245 ± 0.8. The centrifugation conditions allowed the recovery of a higher concentration of lymphocytes compared to granulocytes, with a lymphocyte/granulocyte ratio of 2.60 ± 0.58. Monocytes corresponded to only 2.3% of total leukocytes present in the whole blood and were not identified in the prepared L-PRP.

Table 3.3.1. Concentrations of blood components in the whole blood and L-PRP.

	Whole blood	**L-PRP***
Platelets x 10^3/mm^3	181 ± 5	294 ± 1
Total leukocytes x 10^3/mm^3	4.30 ± 0.10	1.20 ± 0.00
Lymphocytes x 10^3/mm^3	1.47 ± 0.06	0.87 ± 0.06
Monocytes x 10^3/mm^3	0.10 ± 0.00	0.00 ± 0.00
Granulocytes x 10^3/mm^3	2.73 ± 0.06	0.33 ± 0.06
Erythrocytes x 10^6/mm^3	3.37 ± 0.04	0.20 ± 0.00
Platelets/leukocytes	42 ± 1.1	245 ± 0.8
Lymphocytes/granulocytes	0.54 ± 0.02	2.60 ± 0.58

* All concentrations in L-PRP were significantly higher in comparison to the whole blood ($p < 0.05$).

3.3.3.2. Effects of LMM and HMM HA on fibrin polymerization

Initially, the addition of the HAs to L-PRP resulted in phase separation, which was more pronounced for L-PRP-HMM HA (Figure S1). Therefore, preparation under controlled conditions (8 rpm, 30 min and 25 ºC) was crucial to assure homogeneous mixture and uniform formation of the hydrogel structures. After fibrin polymerization, highly hydrated hydrogels were obtained (Figure 3.3.1A), in which a reddish color was observed due to the presence of erythrocytes residues. Fibrin (Figure 3.3.1A (i)) and fibrin-LMM HA (Figure 3.3.1A (ii)) presented a similar aspect of size and shape, while the fibrin-HMM HA hydrogel was more viscous and elongated (Fig. 3.3.1A (iii)).

From the microstructural perspective, the effects of both HA were initially observed by the time-dependence of the polymerization reaction (Figure 3.3.1B). Polymerization of fibrin started very quickly, with the gel point at 3.7 ± 0.9 min. In the presence of both HAs, we observed a significant increase in optical density values, as well as an increase in the polymerization time, with values of 6.3 ± 0.8 min for fibrin-LMM HA and 10.5 ± 1.2 min for fibrin-HMM HA (Figure 3.3.1C).

The concentration of fibrinogen in L-PRP was determined as 4.7 ± 0.4 mg/mL. After hydrogels formation, fibrin was depolymerized with NaOH, and fibrinogen concentration was measured as 4.6 ± 0.5, 3.2 ± 0.1 and 3.5 ± 0.2 mg/mL for fibrin, fibrin-LMM HA and fibrin-HMM HA, respectively, indicating that presence of both HA prevented total fibrinogen from polymerizing (Figure 3.3.1D).

We also evaluated the capacity of fibrin networks to entrap platelets and leukocytes initially present in the L-PRP. Results showed that around 90% of the total platelets were entrapped within the three hydrogels. On the other hand, both fibrin-HA showed significantly higher capacity to entrap leukocytes (~94%) in comparison to fibrin (87.5 ± 0.5%) (Figure 3.3.1E).

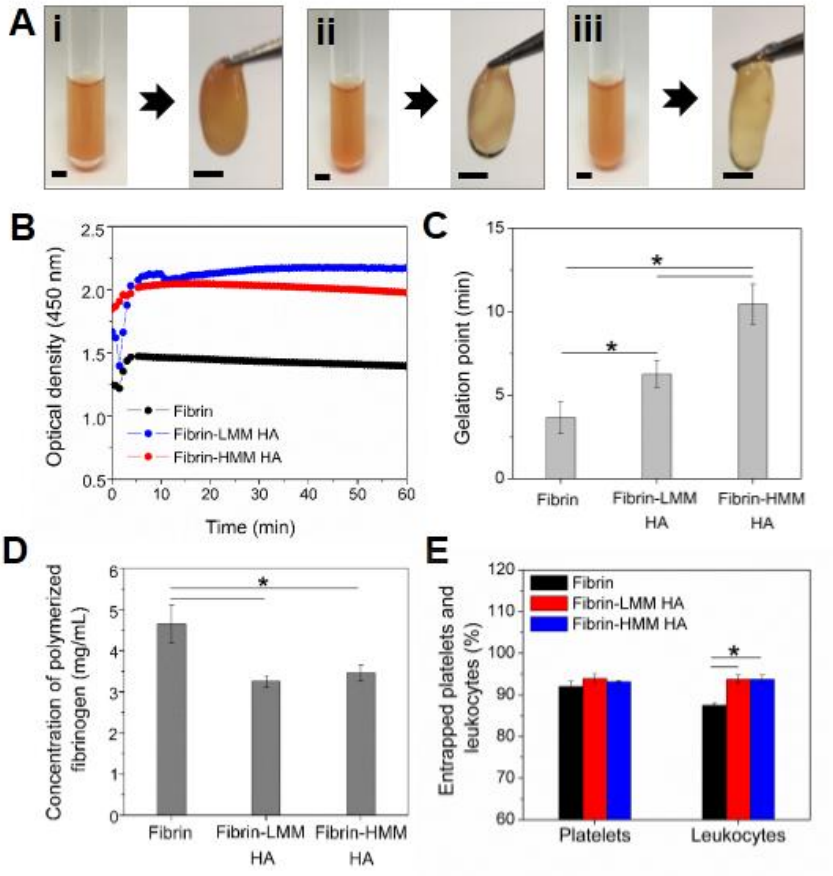

Figure 3.3.1. Fibrin and fibrin-HAs formation. (A) Images from before and after polymerization showing (i) L-PRP and fibrin, (ii) L-PRP-LMM HA and fibrin-LMM HA and (iii) L-PRP-HMM HA and fibrin-HMM HA. Scale bar = 0.5 cm (B) Polymerization kinetics monitored by optical density. (C) Gelation points obtained from the changes in the slope of kinetic curves. (D) The concentration of fibrinogen that polymerized forming fibrin fibers. (E) Percentage of total platelets and leukocytes entrapped within the networks. *$p < 0.05$.

3.3.3.3. Fibrin fibers characterization

SEM images show the fibrin networks structure and morphology, which presented an interconnected nanofibers organization, with density and porosity varying with the HA MM (Figure 3.3.2A). Fibers from fibrin hydrogel were thin and elongated, forming a more porous network (Figure 3.3.2A (i)), while fibrin-LMM HA fibers were thicker and arranged in peak and valley domains (Figure 3.3.2A (ii)). In both networks, it is possible to observe blood components adherent to the fibers. Greater structural changes were observed in fibrin-HMM HA fibers, in which thicker fibers formed a denser, more compact and less porous network with increased roughness (Figure 3.3.2A (iii)). Fibers diameter measured from the SEM images

showed mean values of 132 ± 35, 202 ± 40 and 205 ± 45 nm for fibrin, fibrin-LMM HA and fibrin-HMM HA, respectively (Figure 3.3.2B).

Turbidity is a useful parameter to calculate changes in fibrin fibers thickness (Carr et al., 1977). Here, we used the modified Carr's equation to estimate the diameter and mass/length ratio of the fibers from fibrin and fibrin-HAs (Yeromonahos et al., 2010). Results of diameter were consistent with those obtained from SEM images, being in the same order of magnitude, and presenting thicker fibers in fibrin-HA hydrogels than in fibrin. However, a smaller difference between the diameters of fibers from fibrin and fibrin-HAs was observed, as compared to those values obtained from SEM images (Figure 3.3.2C). Results from Carr's Equation also showed that fibers in fibrin-HAs were shorter, indicating that both HA prevented fiber elongation, thus favoring a lateral reaction (Figure 3.3.2D).

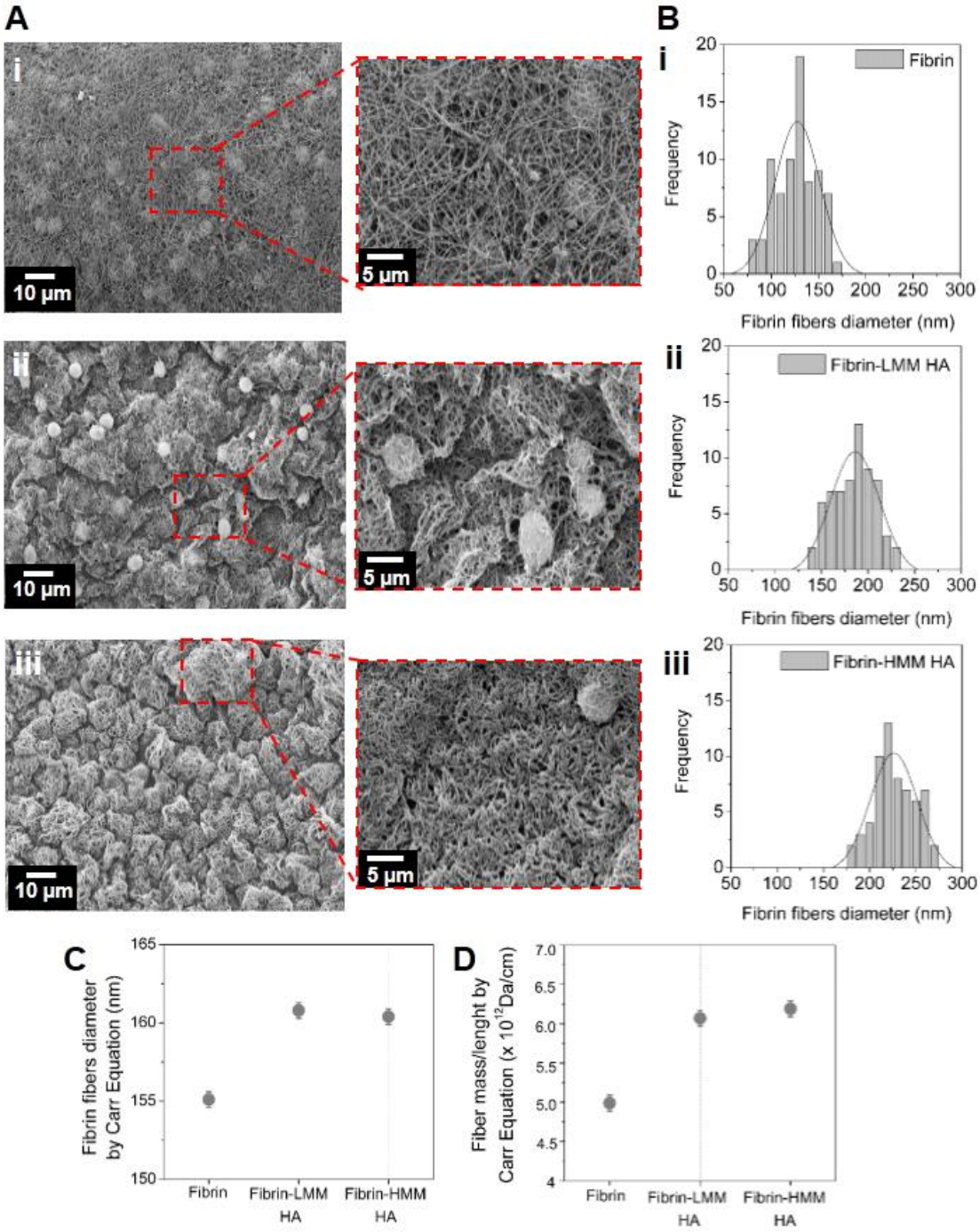

Figure 3.3.2. Fibrin fibers and networks morphology characterization. (A) SEM images of (i) fibrin, (ii) fibrin-LMM HA and (iii) fibrin-HMM HA, at 3 kX and 10 kX magnitude. (B) Fibers diameter distribution histograms of (i) fibrin, (ii) fibrin-LMM HA and (iii) fibrin-HMM HA. Characterization of fibers by Carr's Equation as (C) diameter and (D) mass/length ratio.

3.3.3.4. Physical and structural characterization of hydrogels

The swelling capacity and stability of fibrin and fibrin-HA hydrogels were assessed by studying their swelling ratio and hydrolytic degradation. A rapid swell was observed for the three hydrogels, which tended to stabilize in the second hour for fibrin, whereas both fibrin-HAs continued to swell up to 4 hours, reaching the equilibrium. Significantly higher swelling ratio was observed for the fibrin-HA hydrogels in comparison to fibrin, with HMM HA influencing to higher water uptake (Figure 3.3.3A).

Hydrolytic degradation showed a gradual mass loss with time, which tended to stabilize on day 10. No significant difference was observed between fibrin and fibrin-HAs, with the mass loss being less than 20% in 2 weeks, confirming the hydrogel's stability (Figure 3.3.3B).

The formation of semi-IPNs was investigated by performing FTIR analysis in dried hydrogels after 2 weeks of incubation (Figure 3.3.3C). The characteristic HA bands are highlighted in the spectra of LMM HA and HMM HA used as controls, and of both semi-IPNs (Gilli et al., 1994). The broad peak at 3300 cm^{-1} is characteristic of aqueous O-H stretching bands and is overlapped with the peak of N-H groups at 3100 cm^{-1}. The peaks with low intensity at 2900 cm^{-1} correspond to the C-H symmetrical and C-H_2 asymmetrical stretching. The C=O amide stretching band at 1650 cm^{-1} is overlapped with the carboxyl C-O asymmetrical stretching at 1615 cm^{-1}. The stretching band of symmetrical carboxyl C-O is shown at 1410 cm^{-1}, and the peak at 1045 cm^{-1} is attributed to the C-OH stretching. It is possible to observe a peak around 1550 cm^{-1} in the semi-IPNs spectra as well as one shoulder around 1270 cm^{-1}, more evidenced in fibrin-HMM HA, which are not present in the LMM HA and HMM HA controls, corresponding to the N-H stretching of amide II and III of fibrin, respectively. The N-H peak of amide I is overlapped with that of HA at 1650 cm^{-1} (Benedetti et al., 1998).

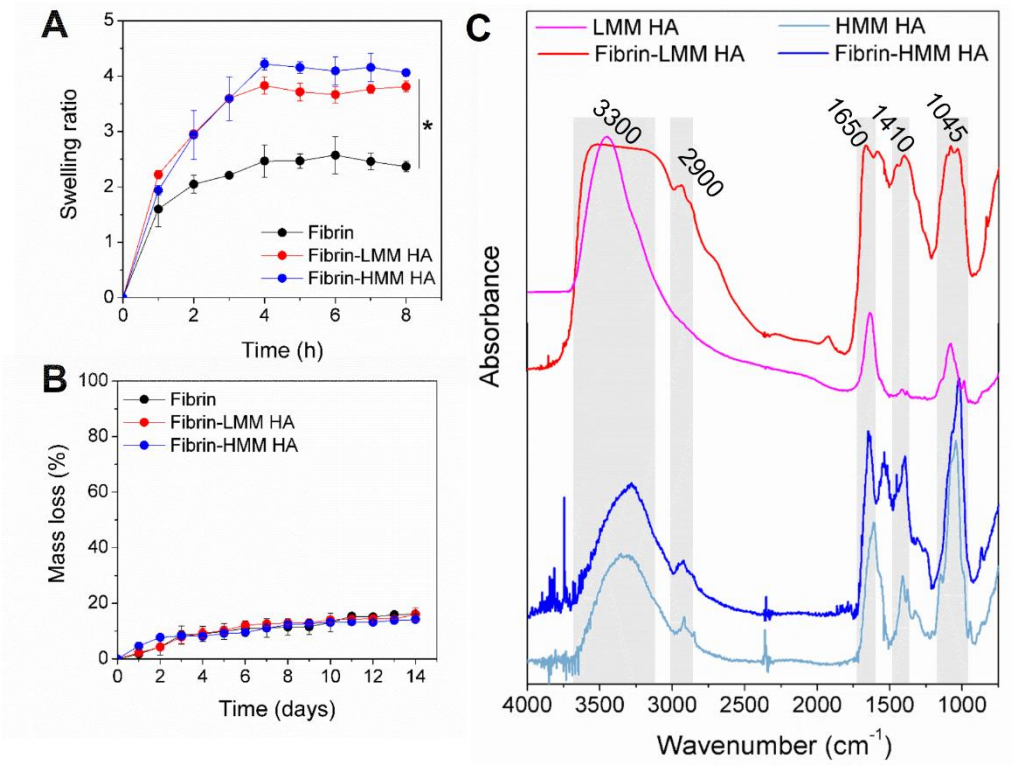

Figure 3.3.3. Physical characterization of fibrin and fibrin-HA hydrogels. (A) Swelling pattern and (B) hydrolytic degradation. (C) FTIR spectra of controls LMM HA, HMM HA, and semi-IPNs fibrin-LMM HA and fibrin-HMM HA dried after 2 weeks of incubation, showing the characteristic bands of HA (highlighted) and bands resulted from fibrin-HA interactions. The spectra were vertically shifted to avoid overlapping.

3.3.3.5. Rheological behavior of fibrin and semi-IPNs

We evaluated rheology of pre-hydrogels (initial mixing of L-PRP, L-PRP-LMM, and L-PRP-HMM HA) by a steady-state shear characterization. Curves of shear stress (Figure 3.3.4A) and viscosity (Figure 3.3.4B) in function of shear rate showed no changes between L-PRP-LMM HA and L-PRP, whereas L-PRP-HMM HA significantly increased shear stress and viscosity values, besides an increased shear-thinning behavior. Curves parameters were adjusted to the power law model and showed a significant increase in the consistency index (m) value for L-PRP-HMM HA compared to L-PRP-LMM HA and L-PRP. The power law index (n) values were < 1, characterizing the non-Newtonian behavior of the pre-hydrogels (Table 3.3.4).

The elastic behavior of samples before and after fibrin polymerization was characterized as the storage (G') and loss (G") moduli, determined as a function of angular frequency. For

the pre-hydrogels, a weak elastic behavior was observed, with L-PRP-HMM HA showing an increased fluid character (Figure 3.3.4C). After polymerization, curves confirm the elastic behavior of the hydrogels, with *G*' decreasing as MM HA increased, dropping from ~100 Pa for fibrin, to ~40 and ~10 Pa for fibrin-LMM HA and fibrin-HMM HA, respectively (Figure 3.3.4D).

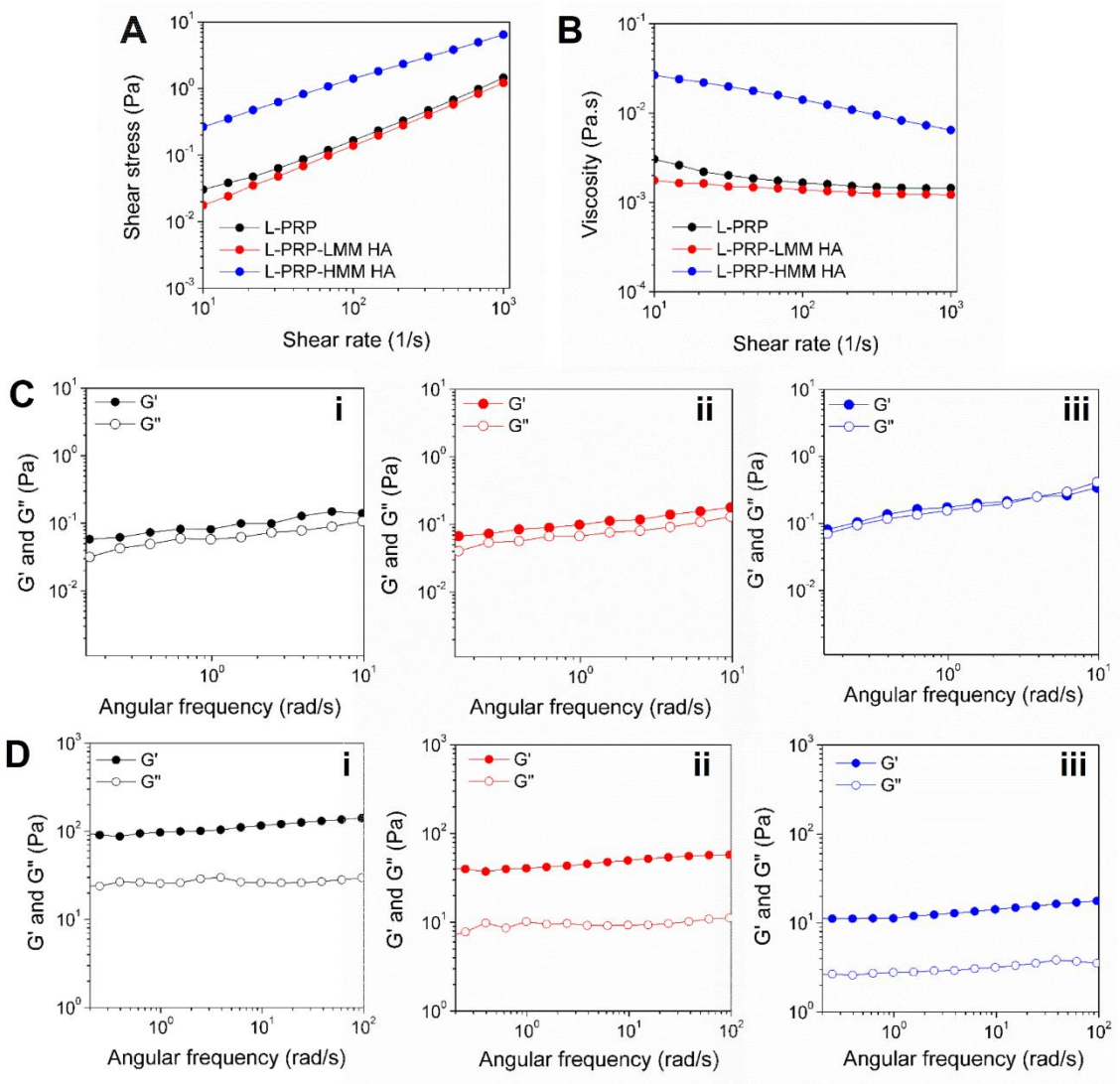

Figure 3.3.4. Steady-state shear characterization of L-PRP and L-PRP-HA pre-hydrogels as the (A) shear stress and (B) viscosity showing that HMM HA significantly affected rheological behavior of L-PRP. Variation of *G*' and *G*" with angular frequency of (C) pre-hydrogels (i) L-PRP, (ii) L-PRP-LMM HA and (iii) L-PRP-HMM HA and (D) hydrogels (i) fibrin, (ii) fibrin-LMM HA and (iii) fibrin-HMM HA.

Table 3.3.2. Parameters obtained from the power law model for L-PRP and L-PRP-HA mixtures.

	m (Pa.s^n)	n
L-PRP	0.003	0.897
L-PRP-LMM HA	0.002	0.892
L-PRP-HMM HA	0.050	0.698

From our results, we can assume that new structures were formed, possessing different viscoelasticity and network packing, due to interactions between crosslinked fibrin fibers and HA random coils, characterized as the semi-IPNs (Figure 3.3.5C).

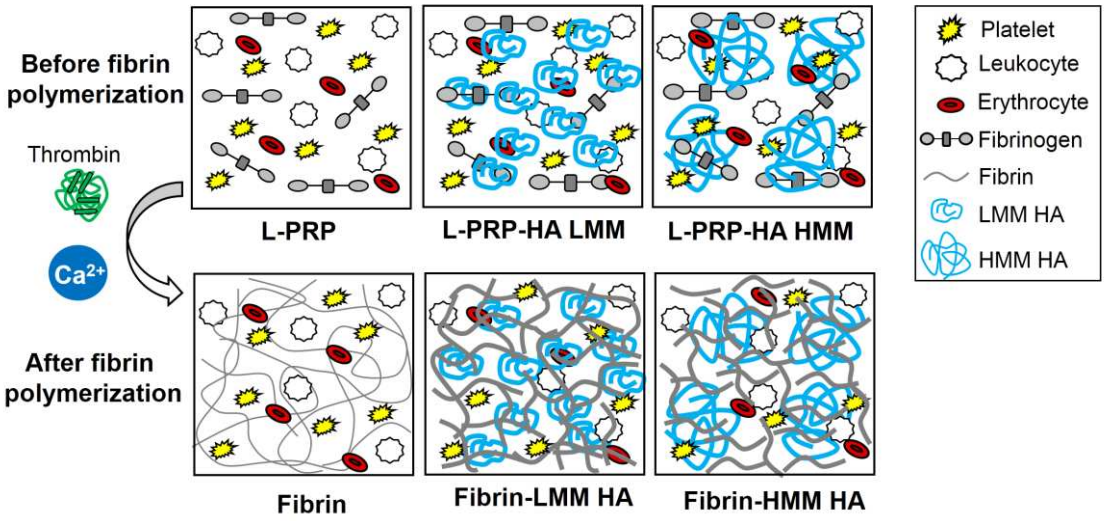

Fig. 3.3.5. Schematic representation of the pre-hydrogels and hydrogels microenvironment, showing the structural differences of fibrin and semi-IPNs networks.

3.3.3.6. h-AdMSCs viability in fibrin and semi-IPNs

As 3D cell culture and tissue formation are directly affected by a hydrogel structure and property (Drury and Mooney, 2003), we investigated the h-AdMSCs viability when seeded in fibrin and fibrin-HA semi-IPNs. Confocal microscopy images show cells on the 7th day of culture, which presented a more spread phenotype in the semi-IPNs compared to fibrin, where most cells had a round shape (Figure 3.3.6A). In addition, h-AdMSCs viability was significantly

higher in the semi-IPNs from day 7 and up to two weeks of culture (Figure 3.3.6B). Proliferation rate was higher for h-AdMSCs cultured in fibrin-HMM HA, as compared to cells in the other two hydrogels, with maximum proliferation being on day 10 (Figure 3.3.6C).

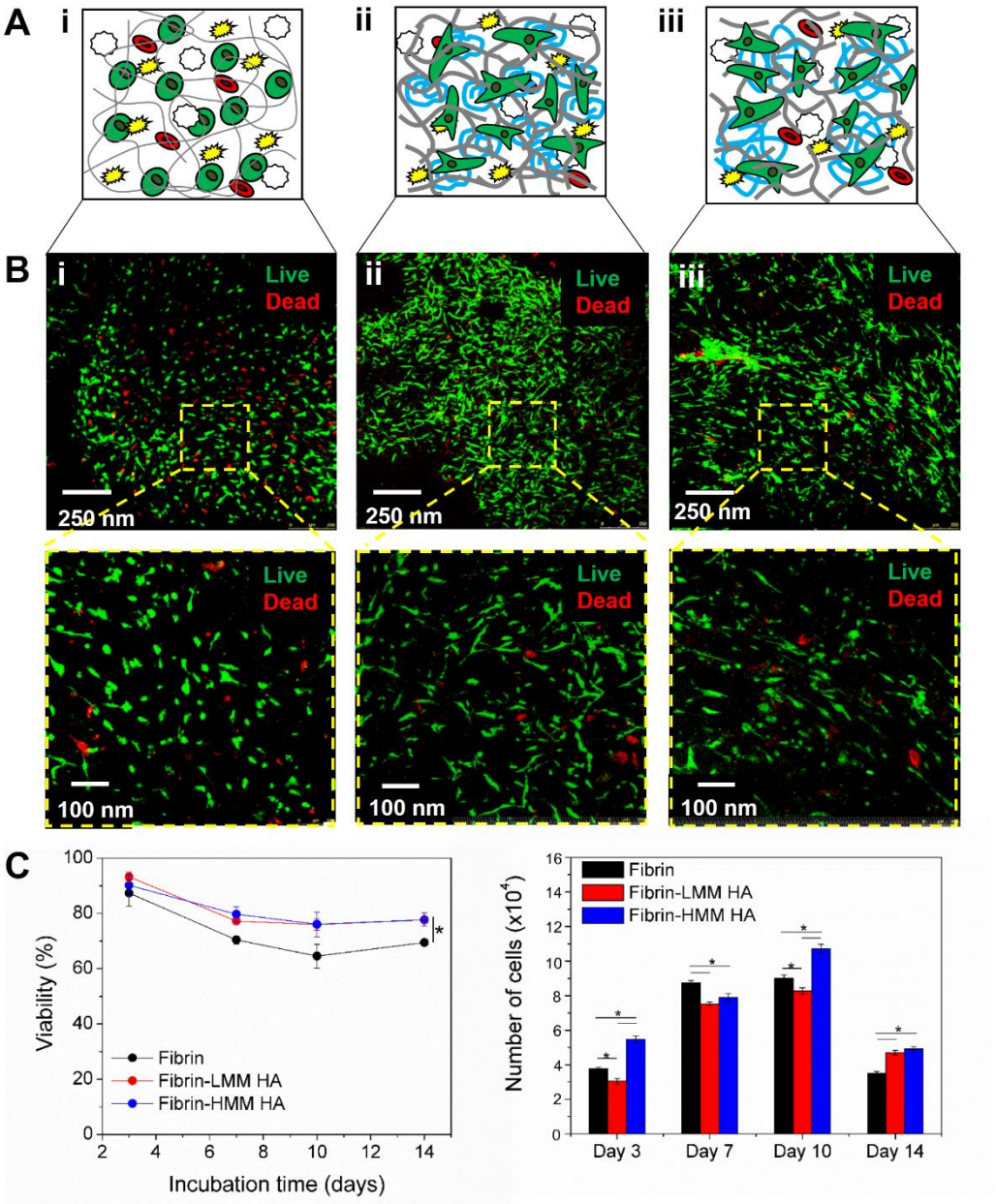

Figure 3.3.6. Assessment of h-AdMSCs behavior in fibrin and semi-IPNs. (A) Schematic illustration of h-AdMSCs in the three microenvironments. (B) Live/dead images taken on day 7 of cells in (i) fibrin, (ii) fibrin-LMM HA and (iii) fibrin-HMM HA. (B) Viability and (C) Proliferation rate of h-AdMSCs cultured in fibrin and semi-IPNs for 2 weeks.

3.3.4. Discussion

L-PRP is a concentrate of platelets and leukocytes that has been clinically applied in the treatment of injured bone and cartilage (Filardo et al. 2012; McCarrel et al. 2012; Riboh et al. 2015). The balance between anabolic and catabolic soluble factors provided by an optimal range of concentration of platelets and leukocytes was reported to be beneficial for the proper function of L-PRP and regeneration mechanisms (Parrish et al., 2016; Sundman et al., 2011). Thus, in a previous centrifugation study, we modulated the concentrations of blood components in L-PRP with the centrifugal acceleration, aiming to standardize the protocols.

Here, we used a mild centrifugation condition that allowed us to obtain the platelet/leukocyte and lymphocyte/granulocyte ratios within the first centrifugation range, as previously established (de Melo et al., 2018). Although granulocytic leukocytes have an essential role in the organism's defense, they also express many inflammatory cytokines and metalloproteins, in addition to producing reactive oxygen species, which in excess could be deleterious for h-AdMSC (Faurschou and Borregaard, 2003; Spooner and Yilmaz, 2011). As monocyte concentration in the whole blood corresponded to a minimum percentage of total leukocytes (2.3%), it was not possible to concentrate this component in our preparation. In further studies, we should focus on the strategies to increase monocyte concentration in L-PRP due to their importance in homeostasis, angiogenesis, and removal of necrotic cells, in addition to being macrophage precursors, that directly act in regeneration (Das et al., 2015).

By thrombin/calcium activation, L-PRP previously mixed to non-crosslinked HA formed semi-IPN hydrogel through physical crosslinking between fibrin and globular HA, with network architecture and properties that differed according to the HA MM. As known, HA alters the rate of fibrin formation due to the specific binding between HA and fibrinogen, which may affect the fibrinopeptide release and polymerization time (Leboeuf et al., 1987). We observed a significant delay in fibrin polymerization with the presence of both HA types, in addition to preventing some fibrinogen monomers from participating in the reaction. Due to the increased chain size of HMM HA, it forms larger coils that contributed to the slower protofibrillation process in comparison to LMM HA. The lower gelation point of fibrin-HA is interesting for clinical use, due to the longer time available for gel formation prior to application, which would avoid polymerization during the preparation. The presence of HA was also able to entrap more leukocytes within the fibrin-HA structures, which could affect biological responses (Sundman et al., 2011).

The variation of optical density with time was measured during fibrin-HA gelation, in which slight declines and curves oscillation were observed, indicating a possible reorganization of the fibers with HA diffusion through the network (Komorowicz et al., 2016). The increase in turbidity of semi-IPNs was directly associated with the increase in the fibrin fiber diameter and mass/length ratio (Carr and Hermans, 1978). In addition to steric exclusion, HA also stimulates lateral fibrillation due to specific binding between HA and fibrinogen, hindering vertical alignment and inhibiting fiber elongation (Komorowicz et al., 2016; Leboeuf et al., 1987). Carr & Gabriel (1980) have used the Carr's Equation to evaluate changes in fibrin fibers induced by dextran and observed that the polysaccharide led to side-to-side fibers aggregation, which similarly to our findings, resulted in thicker fibers. Although the difference between fibers thickness from fibrin and semi-IPNs was less sensitive by Carr's Equation than SEM images, the method showed to be suitable for estimating changes in fibers diameter and length.

The ability of hydrogels to swell under biological conditions makes then suitable for regenerative medicine applications, due to the facilitated diffusion of nutrients and soluble factors (Bajpai and Shrivastava, 2002). The greater swelling ability of HA could be attributed to the hydrophilic domains present in its structure, and to the acidic side groups positioned on both sides of chains that allow high access of water (Shah and Barnett, 1992). Thus, significantly higher swelling ratio was observed for fibrin-HAs in comparison to fibrin, with fibrin-HMM HA showing greater values due to the increased number of hydrophilic domains in the larger molecule.

We observed that hydrolytic degradation was less than 20% after two weeks of incubation, indicating moderate structural stability for supporting h-AdMSC for a long time. A previous study reported the fabrication of semi-IPN composed by crosslinked PEG and non-crosslinked HA, showing the high capacity of the HA to remain within the structure after a long time, with minimum diffusion to the supernatant. Authors also verified that HA loss increased by increasing its concentration (Dong et al., 2012). Here, FTIR analysis performed after two weeks of hydrogels incubation attested HA retention within the networks. In addition, it confirmed the formation of the semi-IPNs, with different structures formed by physical crosslinking between fibrin and HA coils. The increased intensity of fibrin-LMM HA peaks was probably due to the lower binding degree between fibrin-LMM HA and the smaller HA chains, which enables a faster changing in conformation and orientation of coils in comparison to the larger HA (Gilli et al., 1994).

The interactions between different polymer chains can affect rheological properties of the mixtures before and after semi-IPN formation, due to their sensitivity to changes in structure, molecular conformation, and viscosity (Rinaudo, 2008). The rheological results showed that L-PRP mixed with HMM HA presented an increased shear-thinning behavior. *G*' and *G*" of pre-hydrogels were only slightly dependent on angular frequency, and showed a weak elastic behavior, indicating structuration of the solid components such as platelets and leukocytes in L-PRP. Due to the increased viscosity of HMM HA, a more pronounced fluid-phase character was observed for L-PRP-HMM HA, with *G*" overlapping *G*'. These characteristics along with longer polymerization time make L-PRP-HMM HA a more suitable combination for clinical applications. Due to the greater shear-thinning behavior, in which it acts as a fluid under high shear stress and as a gel under low shear stress, its injection and polymerization in situ would be facilitated (Gaffey et al., 2015).

Hydrogels stiffening was affected by the presence of both HA, in which *G*' decreased about 0.5 order of magnitude as HA MM increased, indicating that semi-IPNs form less rigid hydrogels in comparison to fibrin. Similar behavior was observed previously, in which the *G*' of fibrin from PRP decreased from ~100 to 10 Pa in the presence of a HMM HA (Vadalá et al., 2017). Here, we obtained similar values for a much less concentrate HA of similar MM. As known, higher concentrations of HA contribute to the rigidity of semi-IPNs (Russo et al., 2016), therefore, the presence of platelets and leukocytes in the networks prepared here may have directly influenced the semi-IPNs reinforcement (Lam et al., 2011). Results obtained here showed the structural and rheological changes that different HA types provided to fibrin network packing, which could directly influence cell responses.

We assessed the viability of h-AdMSCs cultured in fibrin and semi-IPNs for 2 weeks. Live/dead images showed that h-AdMSCs cultured in the semi-IPNs had significantly higher viability compared to cells in fibrin, in addition to better cells attachment. The morphology of h-AdMSCs was elongated and seemed to spread out along the network, while in fibrin, round-shape cells were predominant. The same behavior was observed previously for MG63 cells, which showed a round morphology when cultured in commercial fibrin, and a more spread morphology when cultured in a full IPN composed of commercial fibrin-HA (Zhang et al., 2016). This was probably due to the formation of less porous networks in fibrin-HA, contributing to cells elongation. From ~1 kDa of MM, HA binds its specific cell membrane receptor CD44 (Cyphert et al., 2015). The binding capacity increase as HA MM increases, due to the larger chains and more sites available for binding, which contributes to a higher cell-cell

and cell-matrix interactions. Therefore, this may have favored the increased h-AdMSCs proliferation in fibrin-HMM HA in comparison to fibrin and fibrin-LMM HA.

Autologous and cell-friendly semi-IPNs were prepared here, showing that fibrin packing and hydrogel properties were tunable with HA MM. Further studies should focus on the chondrogenesis and osteogenesis capacity of h-AdMSCs in the fibrin-HA semi-IPNs.

3.3.5. Conclusions

In this work, we prepared fibrin-HA semi-IPN hydrogels by mixing L-PRP and non-crosslinked HA under controlled conditions, which showed to be a reproducible method to prepare standardized structures. Polymerization of fibrin in the presence of HA was slower, with time being adjusted by HA MM. In addition, rheological studies showed that L-PRP-HMM HA pre-hydrogel possessed increased shear-thinning behavior, being favorable for injectability. Fibers architecture and hydrogels properties were also affected by HA, and presented thicker and shorter fibers, in addition to increasing the network water uptake capacity by increasing HA MM. Semi-IPNs were stable with time, with HA coils remaining within the network through physical crosslinking after a long time of incubation. The lacking of covalent bonds contributed to the formation of less rigid and cell-friendly hydrogels, which were favorable for h-AdMSCs viability. This study presented the fabrication of reproducible fibrin-HA semi-IPNs, with tunable properties according to the HA MM, that represent a standardized preparation for clinical applications in regenerative medicine.

Statement

The authors declare no competing financial interest.

Acknowledgment

The authors gratefully acknowledge funding by The São Paulo Research Foundation (FAPESP) Grant numbers 2015/23134-8 and 2016/10132-0.

Supporting Information

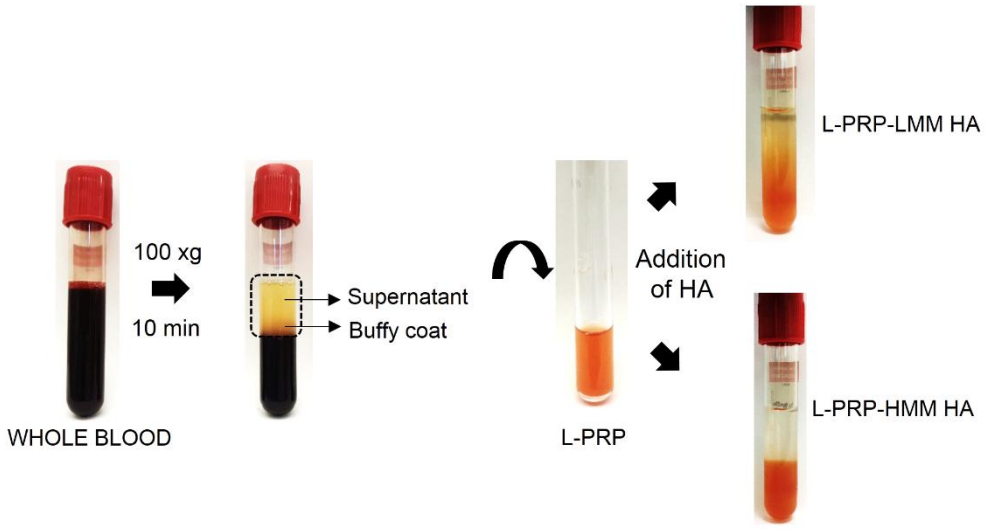

Figure S1. Schematic of L-PRP preparation by centrifuging the whole blood at 100 xg for 10 min, and collecting the supernatant and the buffy coat. The addition of LMM and HMM HA in L-PRP results in phase separation, which is more pronounced for L-PRP-HMM HA.

3.4. Investigating the role of fibrin from L-PRP-hyaluronic acid semi-IPNs in the release of soluble factors and in the chondrogenesis/osteogenesis of mesenchymal stem cells

Artigo a ser submetido à periódico internacional indexado.

Investigating the role of fibrin from L-PRP-hyaluronic acid semi-IPNs in the release of soluble factors and in the chondrogenesis/osteogenesis of mesenchymal stem cells

Bruna Alice Gomes de Melo[1], Carolina Caliari-Oliveira[2], Nilza Alzira Batista[3], Ângela Cristina Malheiros Luzo[4], José Fabio Santos Duarte Lana[5] & Maria Helena Andrade Santana[1*]

[1]Department of Engineering of Materials and Bioprocesses, School of Chemical Engineering, University of Campinas, 13083-852, Campinas, SP, Brazil.

[2]In Situ Cell Therapy, Supera Innovation and Technology Park, 14056-680 Ribeirão Preto, SP, Brasil.

[3]Orthopaedic Biomaterials Laboratory, Faculty of Medical Sciences, University of Campinas, 13083-887, Campinas, SP, Brazil.

[4]Haematology & Hemotherapy Center, Umbilical Cord Blood Bank, University of Campinas, 13083-878, Campinas, SP, Brazil

[5]Bone and Cartilage Institute, 13334-170, Indaiatuba, SP, Brazil

*Correspondence should be addressed to mariahelena.santana@gmail.com, +55 (19) 35213921

ABSTRACT

Leukocyte and platelet-rich plasma (L-PRP) associated with hyaluronic acid (HA) has been clinically used in the treatment of osteoarthritis, resulting in reduction of inflammation, pain relief, and tissue regeneration. From the L-PRP-HA mixture, a wide variety of structures can be formed, and their effects on the release of growth factors (GFs) and cytokines release, which directly affects cell behavior, have not been studied. In this work, we produced semi-interpenetrating polymer networks (semi-IPNs) composed by fibrin from L-PRP and HA of low (~15 kDa) and high (> 2000 kDa) molar mass (LMM and HMM, respectively) by used a standardized protocol. The influence of semi-IPNs on the release of soluble factors by platelets, leukocytes and h-AdMSCs was evaluated, as well as the chondrogenesis and osteogenesis of cells seeded in the hydrogels. We verified that the platelet/leukocyte ratio in L-PRP, and the presence of HA in semi-IPNs resulted in an anabolic/catabolic balance provided by released PDGF-BB and TNF-α, stimulating the secretion of TGF-β1, VEGF, IL-10, IL-1, IL-6 and IL-8, which drove cells behavior. Despite being an inflammatory microenvironment, fibrin-HMM HA was favorable for h-AdMSCs to grow and differentiate under stimulation. Collagen I, II and mineralized matrix deposition were observed after 4 weeks, indicating the chondrogenesis and osteogenesis capacity of h-AdMSCs. Gene expression analysis was performed after 3 weeks, and results showed the favorable effect of fibrin-HMM HA in earlier differentiation capacity, with higher expression of specific markers in comparison to fibrin and fibrin-LMM HA. This study reported unprecedent mechanisms insights on the role of fibrin-HA semi-IPNs

in the GFs and cytokines release from L-PRP and h-AdMSCs, as well as provided a standardized protocol for semi-IPNs preparation, being useful in clinical applications of L-PRP-HA.

Keywords: Leukocytes; platelets; fibrin; hyaluronic acid; growth factor; cytokine.

3.4.1. Introduction

Articular cartilage is a tissue with a limited capacity of self-repair, leading to joint diseases that affect millions of people around the world (Klein et al., 2009). Osteoarthritis is one of the most common cartilage diseases and contributes to the degeneration of hyaline cartilage and subchondral bone (Krishnan and Grodzinsky, 2018). The application of leukocyte and platelet-rich plasma (L-PRP) in patients with osteoarthritis has become a non-invasive alternative, as compared to surgery, to repair the damaged tissues, leading to the reduction of inflammation, pain, and cartilage and subchondral bone regeneration (Filardo et al. 2012; McCarrel et al. 2012; Riboh et al. 2015). Among the PRP formulations, L-PRP presents the most biologically rich composition, with a concentrate of platelets, leukocytes, proteins and other components that act as a reservoir of growth factors (GFs) and cytokines, each presenting different functions in the tissue regeneration process (Everts et al. 2006). These biomolecules are entrapped and gradually released from the fibrin fibers network formed after L-PRP activation by thrombin/calcium, which converts fibrinogen monomers into fibrin after a series of reactions (Scheraga, 2004).

PDGFs and TGF-β are the most produced factors by activated platelets, and their isoforms PDGF-BB and TGF-β1 are crucial molecules in the anabolic pathways of osteoarthritis, by stimulating cells proliferation, differentiation, and formation of cartilage and bone extracellular matrix (ECM) (Hutton et al., 2013; Roman-Blas et al., 2007). VEGF is less present in the platelets alpha granules and known for promoting angiogenesis of growing cartilage (Nagao et al., 2017). On the other hand, it is also related to inducing inflammatory changes that might be detrimental to the joints (Tanaka et al., 2005). Among the interleukins, IL-10 is an anti-inflammatory cytokine related to the immunoregulatory effects of MSCs (Putra et al., 2018). IL-6 and IL-8 are produced in osteoarthritic environments, and although known as a pro-inflammatory cytokine, IL-6 can act as an anabolic factor, being known to promote bone formation through different signaling pathways (Smith, 2018). In turn, IL-8 enhances the angiogenic potential of MSCs by increasing VEGF secretion. IL-1 and tumor necrosis factor (TNF-α) are also two inflammatory cytokines that stimulate secretion of many factors, such as IL-8 and VEGF by leukocytes, and in vivo, act independently or in synergy to induce articular cartilage degradation (Anitua et al., 2007; Zwerina et al., 2007).

These signaling molecules are responsible for the inductive capacity of L-PRP, which combined with hyaluronic acid (HA) in osteoarthritis treatments has shown synergist effects

that led to the reduction of inflammation, pain, and bone and cartilage regeneration (Lana et al., 2016; Marmotti et al., 2012). HA is a glycosaminoglycan (GAG) that exists in a wide range of molar mass (MM), from < 10 to > 1000 kDa, presenting different physical, mechanical and biological properties according to its MM (Gura et al., 1998; Wu et al., 2018). It is naturally present in the synovial fluid and extracellular matrix (ECM) of articular cartilage in the high MM (HMM) form, contributing to the viscoelasticity, lubrication of joints, and matrix organization (Balazs, 1968). Low MM (LMM) HA is formed from the degradation of the larger macromolecule and contributes to the stimulation of inflammation and the angiogenesis process (Noble 2002; West et al. 1985). Therefore, exogenous LMM and HMM HA have been used in different combinations with PRP in order to stimulate and improve the healing of damaged cartilage and bone (Kiliç & Güngörmüs 2016; Lana et al. 2016; Yu et al. 2018).

From this association, a 3D matrix composed of entangled HA coils and fibrin fibers network is formed, being characterized as a semi-interpenetrating polymer network (semi-IPN), due to the mixture of free (non-crosslinked) HA and the crosslinked fibrin (Dong et al., 2012; Vadalá et al., 2017). Their conductive capacity associated with the soluble factors induction, stimulates the genic capacity of autologous cells, completing the proliferation triangle (Barnett Jr and Pomeroy, 2007).

As a natural component of the ECM, HA can regulate the activity of soluble factors, by facilitating their immobilization and release, which modulates the responses of cells (Misra et al., 2015). In addition, the non-crosslinked form of HA avoids the introduction of chemical products into the organism. Previous works have shown the production of fibrin from PRP (poor leukocyte) and HA semi-IPNs, demonstrating their suitability to support cells proliferation and differentiation (Russo et al., 2016; Vadalá et al., 2017). However, a diversity of structures can be formed between fibrin and HA, which could make it difficult to compare results *in vitro* and *in vivo*. Furthermore, leukocytes are important players in the inflammatory phase of the regenerative process (Everts et al., 2007), and little is known about the effects of L-PRP-HA association and pathways that lead to their synergistic effects on chondrogenesis and osteogenesis.

In this work, we prepared fibrin-HA semi-IPNs by mixing L-PRP and HA (of LMM and HMM) under controlled conditions of homogenization before activation, aiming to evaluate the release kinetics of GFs (PDGF-BB, TGF-β1 and VEGF) and cytokines (IL-10, IL-1β, IL-6, IL-8 and TNF-α), in addition to evaluate the response of cell differentiation to the different fibrin-HA microenvironments. For this, human adipose-derived mesenchymal stem cells (h-AdMSCs)

was used, due to their high availability, easy isolation, and great chondrogenesis and osteogenesis ability (Araña et al., 2013).

Results obtained here showed that the semi-IPNs regulated chondrogenic and osteogenic differentiation of h-AdMSCs, being directly influenced by the anabolic/catabolic balance provided by the GFs and cytokines released from fibrin-HA. The superior performance of the fibrin-HA semi-IPNs compared to fibrin represents a promising alternative for the standardization of L-PRP-HA preparations for clinical uses. Furthermore, it elucidates the synergistic effects of the L-PRP-HA association that lead to cartilage and bone regeneration.

3.4.2. Material and Methods

3.4.2.1. Blood collection and L-PRP preparation

This study and the use of human blood was approved by the Ethics Committee of the School of Medical Sciences of Unicamp (Campinas; CAAE: 0972.0.146.000-11). L-PRP was prepared according to our previous protocol (de Melo et al., 2018), by collecting the whole blood from a healthy donor in a tube containing the anticoagulant acid citrate dextrose solution A (ACD-A) (BD Vacutainer®, USA). Then, 3.5 mL of the anticoagulated blood was centrifuged at 100 xg for 10 min at 25 ºC in a ROTINA 380R centrifuge (Hettich Zentrifugen, Tuttlingen, Germany). Tubes were positioned at 45° relative to the rotor. After centrifugation, the top and middle layers were collected and transferred to an empty tube homogenization and quantification of platelets and leukocytes using an ABX Micros ES 60 hematologic analyzer (Horiba ABX Diagnostics, Montpellier, France). Three measurements of each sample were made by the equipment.

3.4.2.2. Fibrin formation and semi-IPNs preparation

L-PRP was mixed to LMM HA (~15 kDa according to the fabricant, Lifecore Biomedical, Chaska, MN, USA) and HMM HA (> 2000 kDa according to the fabricant, Euflexxa® Ferring Pharmaceuticals, Saint-Prex, Switzerland) in a 1:1 ratio (v/v), obtaining a final concentration of 1 mg/mL HA. The mixtures L-PRP-LMM HA and L-PRP-HMM HA were left in a homogenizer AP22 (Phoenix Luferco, Araraquara, Brazil) for 30 min at 8 rpm and 25 ºC. Autologous serum containing thrombin was prepared by collecting the whole blood

in a Vacuette® tube with serum clot activator (Greiner Bio-One Kremsmünster, Austria), and centrifuging it for 15 min at 2,000 xg and 25 ºC. After centrifugation, serum was collected and mixed to 10% (w/v) calcium chloride (Sigma-Aldrich, St. Louis, MO, USA) in a volumetric ratio of 9:1 of serum to $CaCl_2$. Fibrin network and semi-IPNs were formed by adding the serum-Ca^{2+} mixture to the homogeneous L-PRP, L-PRP-LMM HA and L-PRP-HMM HA in a concentration of 20% (v/v).

3.4.2.3. h-AdMSCs isolation and culture

The h-AdMSCs were obtained from human subcutaneous adipose tissue, acquired from abdominal liposuction surgery. Adipose tissue was digested by collagenase A1 (Gibco Life Technologies, Carlsbad, USA), and cells isolated and cultured as previously reported.(Manzini et al., 2015) Briefly, cells were plated at a density of 1 x 10^6 per 25-cm^2 flask in Dulbecco's modified Eagle's medium (DMEM) low-glucose medium supplemented with fetal bovine serum (FBS) (Gibco Life Technologies, Carlsbad, USA), and incubated at 37 ºC in a humidified atmosphere containing 5% CO_2.

3.4.2.4. h-AdMSCs culture in fibrin and semi-IPNs

For proliferation assay, h-AdMSCs were trypsinized and resuspended in L-PRP and L-PRP-HA mixtures in order to obtain a final concentration of 1 x 10^4 cells per hydrogel. After homogenization, 160 µL of L-PRP and L-PRP-HA containing h-AdMSCs were added to a 48-well plate and activated with 40 µL of serum-Ca^{2+}. Once the gels were formed, 750 µL of DMEM was added to the wells, and samples were cultured for two weeks at 37 ºC in a humidified incubator with 5% CO_2, with the medium being changed every three days. Culture medium was not supplemented with FBS due to the high capacity of L-PRP to provide nutrients for cells survival and growth (Murphy et al., 2012). Induction to chondrogenesis and osteogenesis was made by culturing 3 x 10^5 cells per hydrogel for 3 or 4 weeks in 750 µL of StemPro™ osteogenesis and chondrogenesis differentiation kit (Thermo Fisher Scientific, Waltham, USA). Cells cultured in regular DMEM was used as the control for differentiation assay. Media were changed every three days. The experiment was performed in triplicate (n = 3) for each condition.

3.4.2.5. Quantification of GFs and cytokines kinetics release

Fibrin and semi-IPNs were incubated with and without 1 x 10^4 h-AdMSCs, and GFs and cytokines kinetics release was quantified by collecting all the medium (DMEM) at 3, 8, 24 and 72 hours, and storage at -80 ºC, with the new medium being added to the wells. The cumulative concentration of GFs (TGF-β1, PDGF-AB, and VEGF) and cytokines (IL-1β, IL-6, IL-8 and TNF-α,) was quantified using a Bio-plex Pro Kit in an equipment Bio-plex 200 (Bio-Rad, Hercules, USA). The experiment was performed in triplicate (n = 3) for each condition.

3.4.2.6. Assessment of h-AdMSCs proliferation in fibrin and semi-IPNs

The activity of h-AdMSCs was evaluated by quantifying the reduction of 3-[4,5-dimethyl-thia-zol-2-yl]-2,5-diphenyltetrazolium bromide (MTT) (Sigma-Aldrich, St Louis, USA). On days 3, 7, 10 and 14, the medium was aspirated, and 500 µL of 1 mg/mL MTT was added to the wells. Samples were incubated with MTT solution for 4 hours at 37 ºC, according to previous protocol (Mosmann, 1983). Then, MTT was replaced by 1 mL of dimethyl sulfoxide (DMSO) for dilution of formazan crystals. The microplate was incubated in a shaker for 30 minutes, and the absorbance of diluted formazan measured at 595 nm, in a FilterMax F5 Multi-Mode Microplate reader (Molecular Devices, Sunnyvale, USA). Analyses were performed in triplicate for each group, and results were expressed as the number of cells, estimated by a calibration curve previously prepared (R^2 = 0.9816). The experiment was performed in triplicate (n = 3) for each condition.

3.4.2.7. Scanning electron microscopy (SEM) analysis

Samples were fixed for 2 h in a 4% paraformaldehyde and 2.5 % glutaraldehyde solution, prepared in phosphate buffer (PBS), pH 7.4. Then, they were dehydrated in ethanol for 15 min intervals using different ethanol dilutions in deionized water (50, 70, 95 and 100%), and dried at the critical point. After gold coating in a Sputter Coater POLARON, SC7620 (VG Microtech, Uckfield, England), SEM images were taken using a LEO Electron Microscopy/Oxford (Cambridge, England). Elemental composition of the mineralized matrix formed in the hydrogels was characterized by mapping samples surface using a scanning

electron microscope-energy-dispersive X-ray spectrometry (SEM-EDS) (LEO Electron Microscopy/Oxford, Cambridge, England).

3.4.2.8. Immunocytochemistry (ICC)

The h-AdMSCs cultured for 4 weeks in fibrin and semi-IPNs were gently washed with PBS (pH 7.4) and fixed in a 4% paraformaldehyde solution for 2 hours at room temperature. h-AdMSCs were permeabilized with 0.2% Triton-100 (Sigma-Aldrich, St Louis, USA) for 30 min, and non-specific binding was inhibited using a blocking solution of 5% BSA (Sigma-Aldrich, St Louis, USA) for 1 hour at room temperature. Subsequently, samples were incubated at 4 ºC overnight with the primary polyclonal antibodies produced in mouse collagen I (1:2000) and collagen II (1:200) (Invitrogen, Carlsbad, USA), followed by 2 hours of incubation at room temperature with goat anti-mouse IgG secondary antibody (Alexa Fluor 488, 1:200) (Invitrogen, Carlsbad, USA). Nuclei were stained with DAPI (Sigma-Aldrich, St Louis, USA). Fluorescence images were taken in a confocal microscope by Z-stacking 10 to 15 images (Leica Microscope TCS SP5 II, Wetzlar, Germany). Total collagen area was calculated by measuring at least three different images for each condition using the ImageJ software.

3.4.2.9. Histological preparation

Fibrin and semi-IPNs containing the h-AdMSCs cultured for 4 weeks were gently washed with PBS (pH 7.4) and fixed in a 4% paraformaldehyde solution for 2 hours at 4 ºC. Afterward, the samples were rinsed twice with PBS, dehydrated 7 sequential times in ethanol 70% for 30 min each cycle, and diaphonized 3 times in xylol for 30 min each cycle. Hydrogels were sliced (sections of 5 µm) in paraffin blocks and kept in an oven at 60 ºC for 24 hours. The slices were deparaffinized in xylol and rehydrated in graded ethanol from 100 to 75% and water. Samples cultured under chondrogenic induction were stained with Picro-sirius red for collagen deposition, and samples cultured under osteogenic induction were stained with Alizarin red for calcium deposition.

3.4.2.10. Gene expression analysis

Quantitative real-time PCR (RT-PCR) was used to analyze gene expression profiles of h-AdMSCs cultured in fibrin and semi-IPNs for 3 weeks. Initially, RNA from each sample was extracted by using an RNAspin Mini Kit (GE Healthcare Life Sciences, Chicago, USA), and cDNA was formed using a High Capacity cDNA Reverse Transcription Kit (Applied Biosystems, Abingdon, RU) in a PCR thermocycler PTC-100 (MJ Research Inc, Waltham, MA). Subsequently, RT-PCR was performed in a 7500 real-time PCR system (Applied Biosystems, Foster City, USA) using the SYBR Green dye. The reaction volume comprising the SYBR Green, forward and reverse primer and cDNA template was set to 12 µL. Analysis condition was set as 55 ºC for 2 min followed by 95 ºC for 1 min, 45 cycles of 95 ºC for 15 s and 60 ºC for 1 min. Expression of the chondrogenic specific genes Sox 9, aggrecan, collagen I and collagen II, and the osteogenic specific genes, collagen I, collagen II and collagen X, osteocalcin and osteopontin were quantified. The obtained results were analyzed through a comparative $2^{-\Delta\Delta CT}$ method, with the expression of genes normalized to the housekeeping gene, Hypoxanthine-guanine phosphoribosyl transferase (HPRT) and the control (samples cultured in regular medium). Analyses were performed in triplicate (n = 3) for each group. The primers sequence is listed in Table S3.4.1.

3.4.2.11. Statistical analysis

Results are presented as the mean ± standard deviation (SD). One-way analysis of variance (ANOVA) with Tukey's test was used for statistical analysis, and a 95% confidence level was considered significant ($p < 0.05$).

3.4.3. Results

3.4.3.1. Concentration of blood components in the L-PRP

The concentration of platelets, leukocytes, and erythrocytes in the whole blood and L-PRP are presented in Table 3.4.1. Centrifugation of the whole blood at 100 xg for 10 min allowed to concentrate platelets ~1.6 times, and total leukocytes ~0.25 times in L-PRP. Lymphocytes were the leukocyte fraction with increased concentration in L-PRP, while

monocytes were not identified due to their low initial concentration. Platelet/leukocyte and lymphocyte/granulocyte ratios in L-PRP were 212 ± 4.4 and 6.7 ± 0.3, respectively.

Table 3.4.1. Concentration of blood components in the whole blood and L-PRP.

	Whole blood	**L-PRP***
Platelets x 10^3/mm^3	167 ± 11	325 ± 6
Total leukocytes x 10^3/mm^3	5.13 ± 0.15	1.53 ± 0.06
Lymphocytes x 10^3/mm^3	2.03 ± 0.06	1.33 ± 0.06
Monocytes x 10^3/mm^3	0.10 ± 0.00	0.00 ± 0.00
Granulocytes x 10^3/mm^3	2.00 ± 0.10	0.20 ± 0.00
Erythrocytes x 10^6/mm^3	3.27 ± 0.03	0.04 ± 0.01
Platelet/leukocyte	36.2 ± 5.4	189 ± 28
Lymphocyte/granulocyte	0.63 ± 0.07	4.7 ± 0.5

* All concentrations were significantly higher in comparison to the whole blood ($p < 0.05$).

3.4.3.2. Kinetics of GFs and cytokines release

We evaluated the gradual release of GFs (PDGF-BB, TGF-β1 and VEGF) and cytokines (IL-10, IL-1, IL-6, IL-8 and TNF-α) from fibrin and semi-IPNs in the presence and absence of h-AdMSCs. Results showed that semi-IPNs strongly influenced the secretion of soluble factors, especially inflammatory cytokines by leukocytes, due to the signaling capacity of HA. As LMM HA specifically binds to leukocytes TLR receptors, it triggered cytokines release, as well as HMM HA, which specifically binds to CD44 receptor. However, the CD44 clustering effect contributed to a lower secretion of cytokines (Figure 3.4.1).

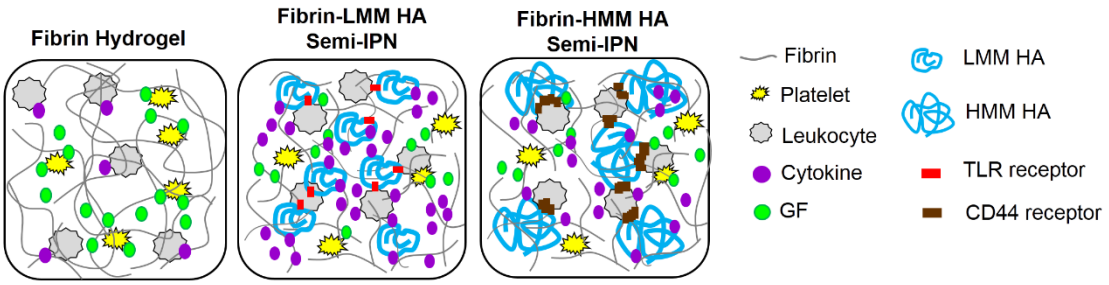

Figure 3.4.1. Schematic illustration of the fibrin and semi-IPNs microenvironments showing the increased cytokines secretion by leukocytes in semi-IPNs, stimulated by LMM HA-TLR binding, which contributed to an increased secretion of inflammatory cytokines by leukocytes, and by HMM HA-CD44 receptor, which has also contributed to these soluble factors release, but being less pronounced due to the CD44 clustering effect.

Concentration of PDGF-BB released in the presence of h-AdMSCs was lower than without cells, which stabilized in 24 hours. In both cases, with and without h-AdMSCs, the concentration of this GF released from fibrin was ~2-fold higher than that from semi-IPNs (Figure 3.4.2A). The inflammatory cytokine TNF-α was strongly released from semi-IPNs without cells, with values being 1550 ± 42 and 1240 ± 36 for fibrin-LMM HA and fibrin-HMM HA, respectively, at 72 hours. On the other hand, this cytokine was poorly released from fibrin, with concentration being < 50 pg/mL. In the presence of h-AdMSCs, the concentration of TNF-α released from fibrin increased, while decreased for semi-IPNs. (Figure 3.4.2B).

The concentration of TGF-β1 released from the three hydrogels without cells was higher in the first 8 hours of incubation. From this point, its concentration increased in the presence of h-AdMSCs, reaching values significantly higher at 72 hours, being 5420 ± 280, 3500 ± 83 and 3165 ± 80 pg/mL for fibrin, fibrin-LMM HA and fibrin-HMM HA, respectively (Figure 3.4.2C). VEGF concentration was less than 500 pg/mL for all conditions up to 24 hours of incubation. From this point, a sharp increase was observed in the presence of h-AdMSCs, with values reaching 3065 ± 490 pg/mL for fibrin, 2144 ± 240 pg/mL for fibrin-LMM HA and 1260 ± 363 pg/mL for fibrin-HMM HA (Figure 3.4.2D). Similar effects were observed for the anti-inflammatory cytokine IL-10, which kinetics release showed a higher concentration in the presence of h-AdMSCs from 24 hours. Overall, its final concentration was lower than 600 pg/mL (Figure 3.4.2E).

Differently from TNF-α, the release of the inflammatory cytokines IL-1β, IL-6 and IL-8 from hydrogels containing h-AdMSCs was significantly higher than from samples without cells. IL-1β released from fibrin-LMM HA at 72 hours was ~2- and ~4.5-fold higher than from

fibrin and fibrin-HMM HA, respectively (Figure 3.4.2F). The concentration of IL-6 in the presence of h-AdMSCs was about ten times greater than in hydrogels without cells, being around 20,000 pg/mL for all three conditions at 72 hours (Figure 3.4.2G). IL-8 also showed high released concentrations for the three hydrogels containing h-AdMSCs, reaching approximately 40,000 pg/mL at 72 hours (Figure 3.4.2H).

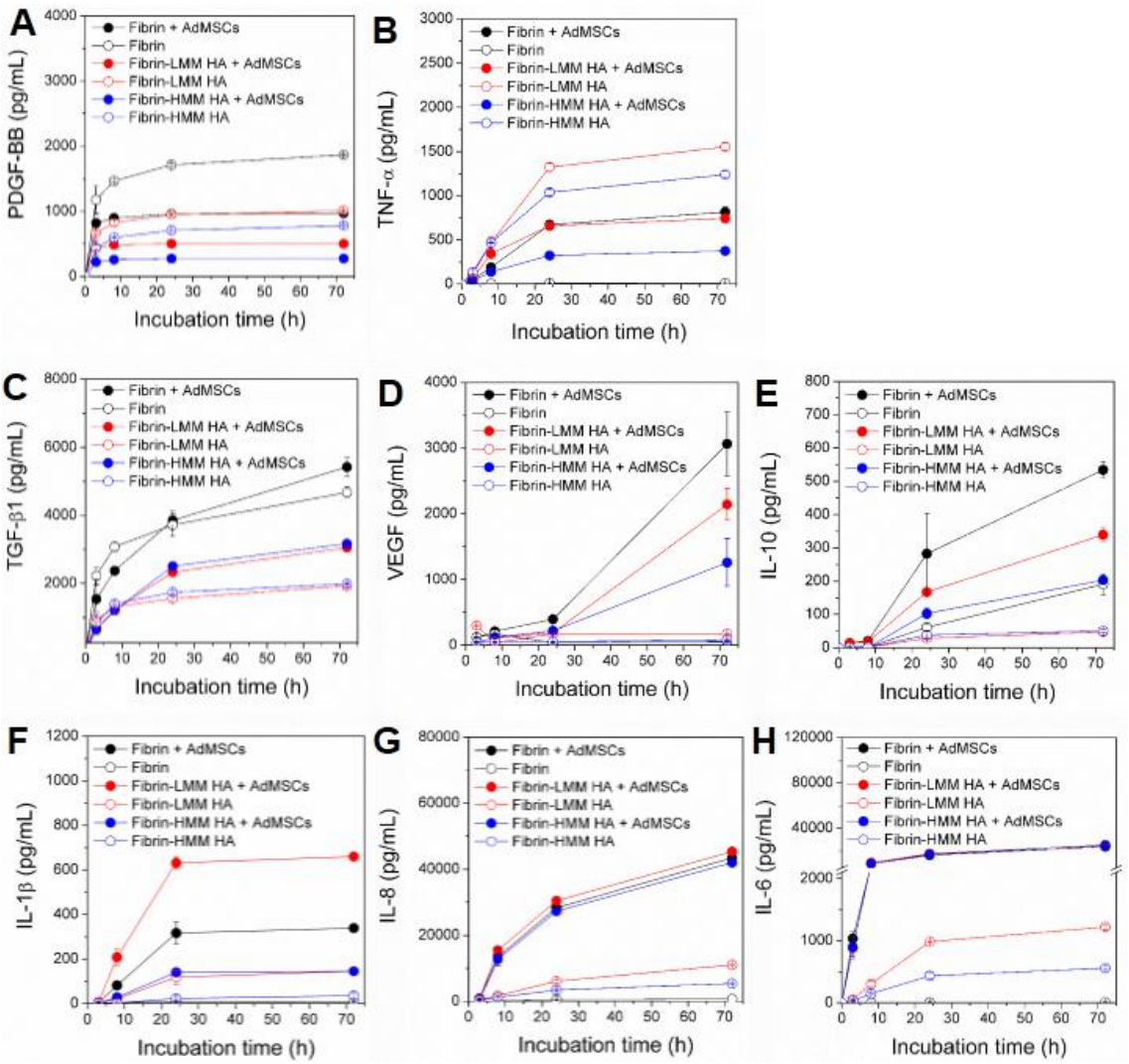

Figure 3.4.2. Kinetics of GFs and cytokines released from fibrin and semi-IPNs with and without the presence of h-AdMSCs. (A) PDGF-BB, (B) TNF-α, (C) TGF-β1, (D) VEGF, (E) IL-10, (F) IL-1β, (G) IL-6 and (H) IL-8.

3.4.3.3. h-AdMSCs proliferation rate

The proliferation rate of h-AdMSCs seeded in fibrin and semi-IPNs was assessed during two weeks by MTT reduction. Maximum proliferation was observed on days 7 and 10, with the number of cells in fibrin-HMM HA being significantly higher than in the other two hydrogels on the 10th day. The proliferation rate of h-AdMSCs in fibrin-LMM HA was similar to that in fibrin (Figure 3.4.3A). After 7 days of culture, samples were fixed, and images of fibers and cells were obtained using SEM. It is possible to observe a denser and less porous network for semi-IPNs. Images highlight the h-AdMSCs cells and other L-PRP components within the networks (Figure 3.4.3B).

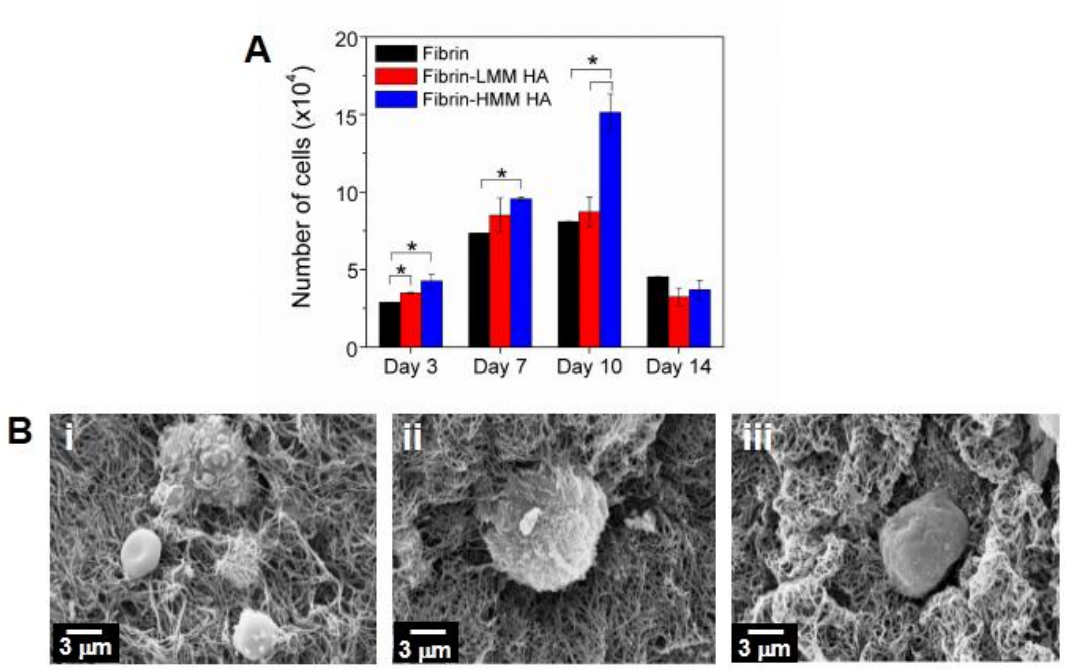

Figure 3.4.3. Cells behavior in fibrin and semi-IPNs. (A) Number of cells during 2 weeks of culture. *$p < 0.05$. (B) SEM images showing the morphology of fibers, highlighting the h-AdMSCs in (i) fibrin, (ii) fibrin-LMM HA and (iii) fibrin-HMM HA.

3.4.3.4. ECM deposition

Deposition of ECM by h-AdMSCs in fibrin and semi-IPNs was evaluated after 4 weeks of culture. Hydrogels incubated in chondrogenic medium were analyzed as collagen II deposition by ICC, and as collagen deposition by histological analysis using Picro-sirius red

staining. Hydrogels incubated in osteogenic medium were analyzed as collagen I deposition by ICC, and mineralized matrix deposition was evaluated by histological analysis using Alizarin red staining, and by SEM-EDS.

Results of chondrogenesis showed a most abundant and homogeneous distribution of collagen II in fibrin-HMM HA (Figure 3.4.4A). Semi-quantitative results showed a significantly higher collagen II area in fibrin-HMM HA (2.0 ± 0.4 mm^2) in comparison to fibrin-LMM HA (0.9 ± 0.3 mm^2) and fibrin (1.0 ± 0.3 mm^2), while samples incubated in regular medium showed low covered area (< 0.5 mm^2) (Figure 3.4.4B and S3.4.1A). Similarly, histological images showed an intense red staining in fibrin-HMM HA, indicating higher collagen deposition by h-AdMSCs (Figure 3.4.4C). The mean pixel intensity of Picro-sirius red was analyzed using the ImageJ software, and showed a significantly higher intensity in fibrin-HMM HA (Figure 3.4.4D). The semi-IPNs showed to be favorable to stimulate collagen deposition compared to fibrin when cultured without stimulus, i.e., in regular medium (Figure 3.4.4D and S3.4.1B).

Fibrin-HMM HA seemed to favor the deposition of collagen I, with a strong presence of the protein in the pericellular matrix region of cells (Figure 3.4.4E). Measured area showed no significant difference of collagen I distribution between the three samples, with values varying from 1 to 2 mm^2 (Fig. 3.4.4F). Low deposition of the protein was observed in all samples cultured in regular medium (Figures 3.4.4F and S3.4.1C). Alizarin red staining showed the presence of calcified material in the three hydrogels (Figure 3.4.4G), and measured area indicated significantly higher deposition in semi-IPNs than in fibrin (Figure 3.4.4H). Fibrin-HMM HA showed to favor the calcification under no stimulus (Figure 3.4.4H and S3.4.1D).

SEM images showed high deposition of mineralized matrix in the hydrogels cultured with osteogenic stimulus, covering a large area of the fibrin and semi-IPNs surface. Elemental analysis and EDS spectrograms confirmed the presence of calcium and phosphorous, the main components of hydroxyapatite, in the produced matrix (Figure 3.4.4I). We have also observed the deposition of a few matrix vesicles in the surface of samples induced to chondrogenesis (Figure S3.4.2). Control samples showed low matrix deposition (Fig. S3.4.3A), with elemental analysis and Ca/P mapping indicanting a small presence of calcium and no phosphorous in the materials surface (Fig. S3.4.3B). As shown in Table S3.4.2, concentration of calcium was around 13 to 15%, while phosphorous was around 7 to 8% of total elemental concentration.

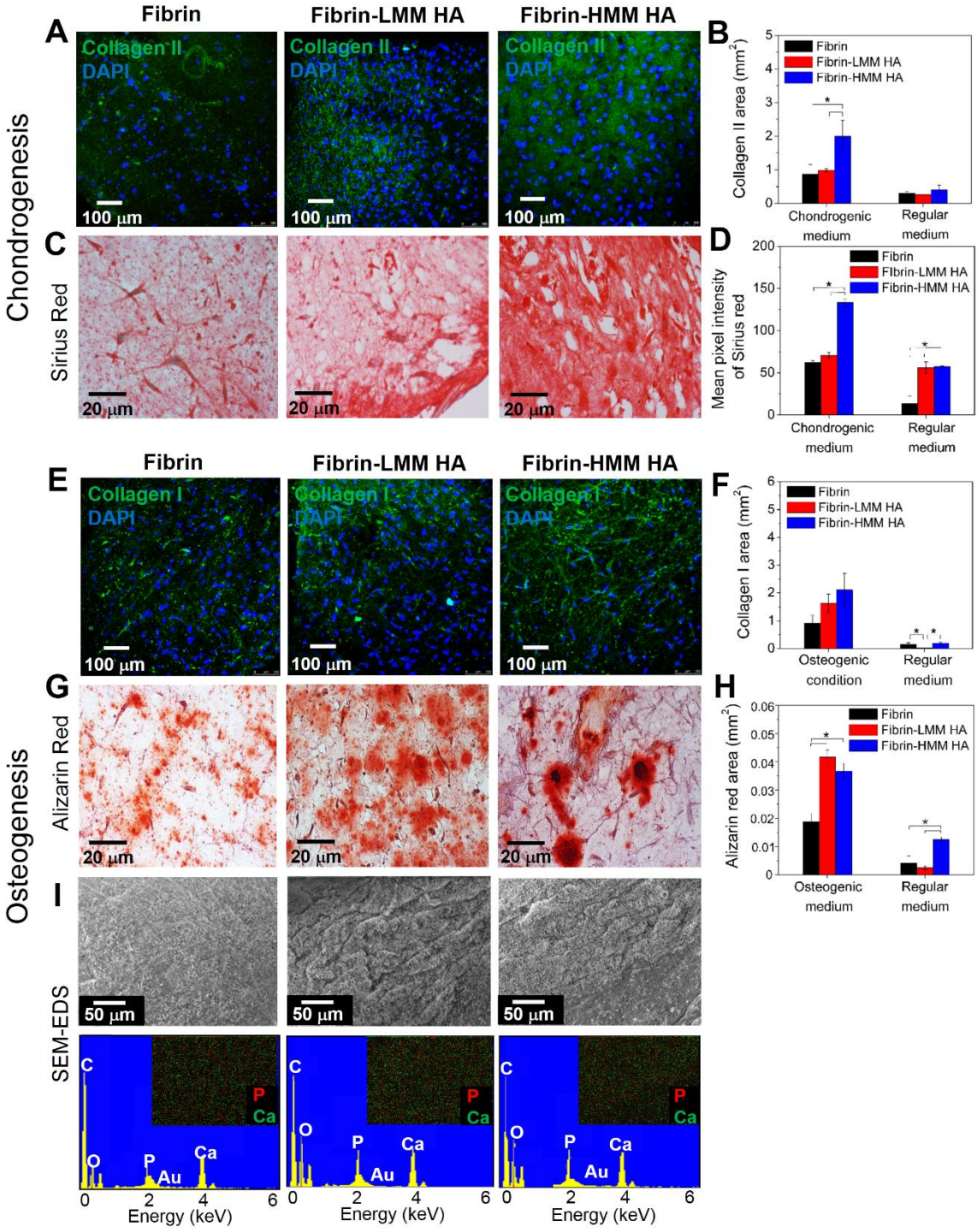

Figure 3.4.4. ECM matrix deposition in fibrin and semi-IPNs after 4 weeks of h-AdMSCs culture with chondrogenic and osteogenic stimulus. (A) ICC Images of collagen II deposition in samples induced to chondrogenesis. (B) Total area of collagen II calculated using the ImageJ software. (C) Histological images of Picro-sirius red staining for collagen deposition of samples induced to chondrogenesis. (D) Mean pixel intensity of Picro-sirius red calculated using the ImageJ software. (E) ICC Images of collagen I deposition in samples induced to osteogenesis.

(F) Total area of collagen I calculated using the ImageJ software. (G) Histological images of Alizarin red staining for calcium deposition of samples induced to chondrogenesis. (H) Total area of Alizarin red calculated using the ImageJ software. (I) SEM images of samples cultured with osteogenic medium and EDS spectra for calcium and potassium mapping. $*p < 0.05$.

3.4.3.5.Gene expression analysis

Expression levels of chondrogenic and osteogenic specific genes were analyzed using RT-PCR, in order to evaluate the h-AdMSCs response to fibrin and fibrin-HA semi-IPNs after 3 weeks of culture. Results were expressed relative to the reference gene HPRT and to the levels expressed by each control. Cells induced to chondrogenesis showed that Sox 9 was highly expressed by cells in fibrin-HMM HA, being 2.5 and 4 times higher than in fibrin and fibrin-LMM HA, respectively (Figure 3.4.5A). The chondrocyte-specific gene aggrecan was upregulated by cells in both semi-IPNs, presenting pronounced levels and showing no significant difference between them. On the other hand, aggrecan expression by cells in fibrin was 5-fold lower than in the semi-IPNs (Figure 3.4.5B). Differentiating cells decrease their collagen I expression, while increase collagen II. Results showed no significant difference for collagen I expression between fibrin and semi-IPNs (Figure 3.4.5C), whereas pronounced expression of collagen II by h-AdMSCs in fibrin-HMM HA was observed. The level of collagen II in fibrin-LMM HA was too low to be quantified by PCR (Figure 3.4.5D). Collagen II/collagen I ratio was calculated and showed higher value for fibrin-HMM HA (0.78 ± 0.07) as compared to fibrin (0.34 ± 0.04) (Figure 3.4.5E).

Osteocyte-like phenotype was analyzed by detecting expression levels of collagen types I, II and X, osteocalcin and osteopontin. Semi-IPNs greatly stimulated collagen I expression, as compared to fibrin, with fibrin-HMM HA showing significantly higher value than fibrin-LMM HA (Figure 3.4.5F). Similarly to the chondrogenesis induction, upregulated level of collagen II was observed for cells in fibrin-HMM HA, whereas levels in fibrin-LMM HA was too low to be quantified by PCR (Figure 3.4.5G). Collagen type X expression showed the same trend as collagen I, with significant higher values for cells cultured in semi-IPNs compared to only in fibrin (Figure 3.4.5H). Mineralization-related genes osteocalcin and osteopontin were quantified and showed different trends. No significant difference in osteocalcin expression was observed between the three conditions (Figure 3.4.5I), while a pronounced expression of osteopontin was observed for h-AdMSCs in both fibrin and fibrin-HMM HA, being

approximately 4 times higher than the level expressed by cells in the fibrin-LMM HA semi-IPN (Figure 3.4.5J).

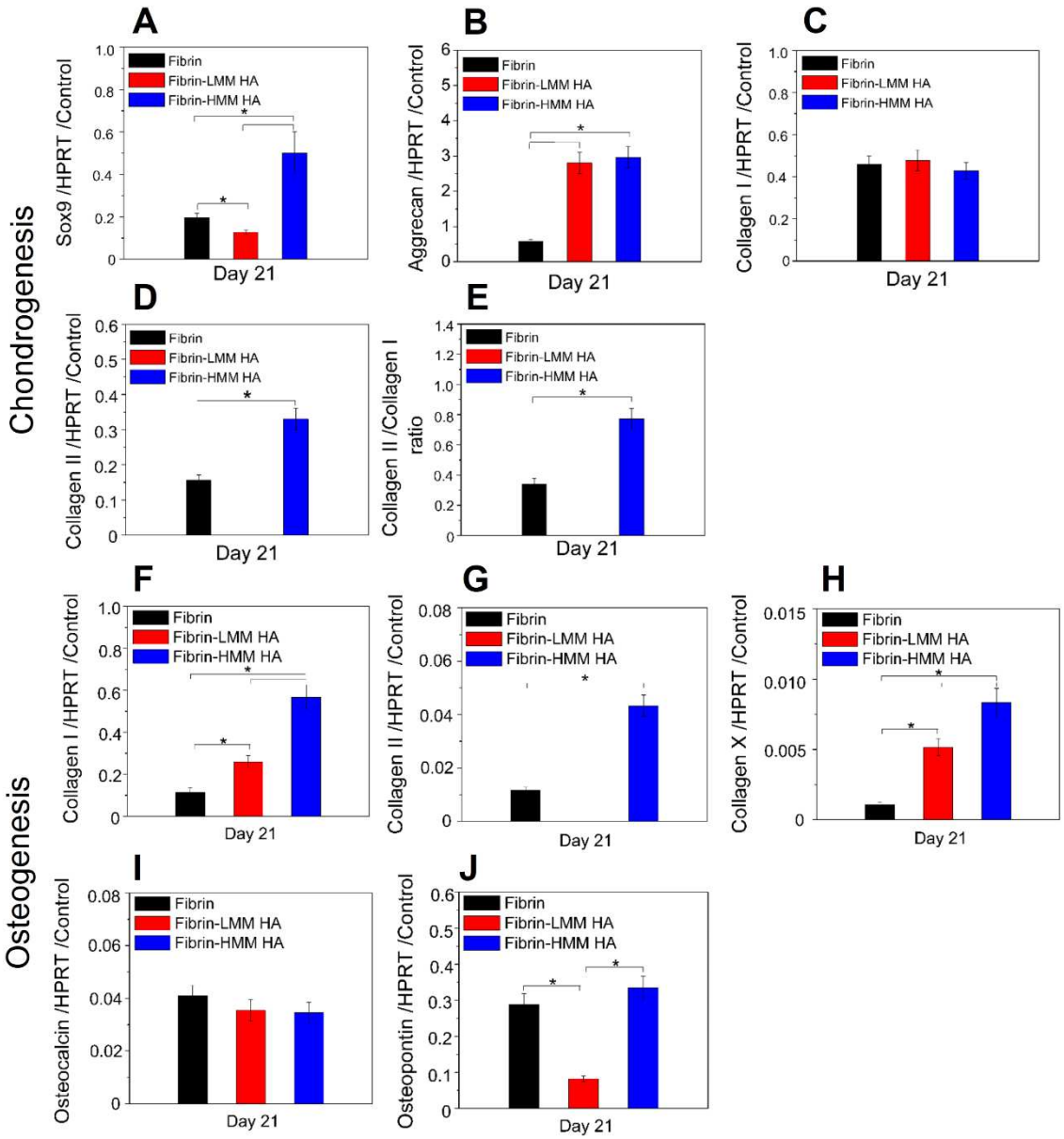

Figure 3.4.5. (A-E) Cartilage specific genes expression in fibrin and semi-IPNs on day 21, relative to the HPRT gene and control. (A) Sox 9, (B) aggrecan, (C) collagen I (D) collagen II and (E) collagen II/collagen I ratio. (F-J) Bone specific genes expression in fibrin and semi-IPNs on day 21 relative to the HPRT gene and control. (F) Collagen I, (G) collagen II, (H) collagen X (I) osteocalcin and (J) osteopontin.

3.4.4. Discussion

Chondrogenesis and osteogenesis of MSCs are driven by many soluble and physical factors that lead to differentiation (Yaylaci et al., 2016). Fibrin from activated L-PRP provides a 3D microenvironment for cells to attach, proliferate and differentiate, and the semi-IPNs formed from fibrin-HA possess properties that are tunable by the HA MM, which implicate in different cell response. The semi-IPNs prepared under controlled conditions represent a more reproducible and biologically richer structure, compared to its components (fibrin or free HA). Therefore, as a hydrogel, the semi-IPNs are capable of supporting the proliferation and differentiation cycle of the cells. Furthermore, their standardized preparation reduces variability and could allow the comparison of results when applied in osteoarthritis treatments.

In this study, the prepared L-PRP showed a moderate concentration factor of platelets (~1.6-fold) and low concentration of leukocytes (~0.25-fold), with platelet/leukocyte and lymphocyte/granulocyte ratios presenting a predominance of platelets and lymphocytes, respectively. This microenvironment rich in anabolic and catabolic factors regulate the proliferation and differentiation of MSCs, so determining its effectiveness. The anabolic effects of L-PRP are ensured by the presence of platelets that release GFs upon activation, while the catabolic effects are due to inflammatory cytokines secreted by leucocytes. In synergy, a balanced platelet/leukocyte ratio modulates the regeneration of cartilage and bone tissues (Parrish and Roides, 2017; Parrish et al., 2016; Sundman et al., 2011). As many of these soluble factors are secreted by MSCs (Ortiz et al., 2007), we evaluated the release kinetics of GFs and cytokines from fibrin and semi-IPNs incubated with and without h-AdMSCs.

The kinetics profile showed similar trends for the released PDGF-BB and TNF-α. Concentration was higher in the absence of h-AdMSCs, indicating they were secreted by activated platelets and leukocytes. Previous works reported the low capacity of MSCs to secrete PDGF-BB and TNF-α, even under a stimulus (Berk et al., 2010; Salazar et al., 2009). As shown here, the cells did not produce but responded to the presence of these soluble factors, with concentrations of PDGF-BB and TNF-α being lower in the presence of h-AdMSCs. These results suggest that they are key factors in the anabolic/catabolic balance provided by the fibrin-HA semi-IPNs. It was corroborated by the high levels of TGF-β1, VEGF and the anti-inflammatory cytokine IL-10 secreted by h-AdMSCs after 24 hours of incubation. TNF-α is a potent inflammatory factor, but also activates MSCs through different signaling pathways, stimulating them to secrete TGF-β1, VEGF and IL-10, and therefore, playing an essential role

in modulating different cell functions (Jiang et al., 2011; Nakajima et al., 2017; Yan et al., 2018). It was interesting to note that the concentration of these biomolecules released from semi-IPNs was significantly lower than from fibrin. Due to their denser and less porous networks, semi-IPNs acted as a diffusive barrier, especially fibrin-HMM HA, which contributed to a higher entrapment of VEGF and IL-10. As having the smallest size, the release of TGF-β1 from fibrin-HMM HA was facilitated, reaching similar levels to those released from fibrin-LMM HA.

Activated leukocytes secrete inflammatory cytokines, and our results indicated that HA, as part of semi-IPN structures, had a crucial role in leukocytes activation. Without h-AdMSCs, a low concentration of all cytokines was collected from fibrin supernatant, while higher concentrations were observed for semi-IPNs, especially fibrin-LMM HA. LMM HA is known for having an inflammatory character, which through activation of leukocytes TLR4 and TLR2 receptors, triggers the secretion of cytokines such as TNF-α, IL-1, IL-6 and IL-8 that modulate inflammatory responses (de la Motte, 2011; Rayahin et al., 2015). On the other hand, HMM HA is known by its anti-inflammatory capacity, due to its specific affinity with the CD44 receptor present in cells and leukocytes membrane. As HMM HA has many sites available for binding, its large chains contribute to CD44 clustering, which protects cells against inflammatory mediators binding (Day and De La Motte, 2005; Isa et al., 2015). However, it was previously reported that the HMM HA-CD44 binding could also activate leukocytes and stimulate cytokines release (Majors et al., 2003). Results obtained here showed that inflammatory cytokines were released from fibrin-HMM HA, but at lower concentrations than from fibrin-LMM HA, indicating that fibrin-HMM HA stimulated cytokines release, while controlled leukocytes activation.

In the presence of h-AdMSCs, we observed a higher concentration of IL-1β, IL-6, and IL-8, as compared to fibrin and semi-IPNs without cells. These results indicate that not only leukocytes but also h-AdMSCs were stimulated to secrete cytokines, suggesting that an inflammatory phenotype was acquired by the cells. A previous report proposed an MSCs paradigm, in which they polarize into two distinct phenotypes, the inflammatory MSC1 and the anti-inflammatory MSC2, activated by TLR-4 and TLR-3 receptors, respectively (Waterman et al., 2010). Here, the inflammatory phenotype of h-AdMSCs was activated in the three hydrogels, secreting expressive and similar amounts of IL-6 and IL-8. In turn, IL-1β release was around 10 to 100 times less than IL-6 and IL-8, with the concentration being more expressive for h-AdMSCs in fibrin-LMM HA. This evidence indicated that different pathways

might have activated and stimulated h-AdMSCs to secrete different inflammatory mediators in the fibrin-HA semi-IPNs.

Despite being an inflammatory microenvironment, semi-IPNs was favorable for h-AdMSCs growth, indicating that there was an essential anabolic/catabolic balance provided by PDGF-BB and TNF-α released from platelets and leukocytes, which modulated cells response. It was corroborated by attesting the proliferative capacity of h-AdMSCs in semi-IPNs. Proliferation rate was similar for all conditions up to day 7, and then a sharp increase was observed for cells in fibrin-HMM HA on the 10th day of culture. The increased concentration of GFs entrapped within this structure, and the cell-cell and cell-matrix communication through HMM HA-CD44 binding could have contributed to the increased proliferation of h-AdMSCs in fibrin-HMM HA.

The chondrogenic and osteogenic differentiation capacity of h-AdMSCs also showed to be greater in fibrin-HMM HA in comparison to fibrin and fibrin-LMM HA, as verified by ICC and histological images. In chondrogenesis, collagen deposition is regulated by Sox 9, which plays an essential role in the early stages of differentiation (Hardingham et al., 2006). The level of this marker was significantly higher in fibrin-HMM HA and may have contributed to a higher stimulus of collagen deposition. Undifferentiated MSCs phenotype is marked by the synthesis of collagen I, whose expression decreases during differentiation, while collagen II increases, marking the chondrocyte phenotype (Yaylaci et al., 2016). Therefore, to commit to the chondrogenic lineage, the collagen II/collagen I ratio is expected to be higher than 1 (Lee et al., 2004). Here, we observed that fibrin-HMM HA presented the highest ratio, close to 1 and more than 2-fold than that of fibrin. Fibrin-LMM HA downregulated collagen II expression, with values being too low to be quantified by RT-PCR, indicating its reduced capacity to stimulate chondrogenesis in 3 weeks. These results suggest that fibrin-LMM HA probably delayed the chondrogenic differentiation of h-AdMSCs, once collagen II deposition was observed after 4 weeks by ICC fluorescence images. Previous work reported that different MM HA affected the chondrogenic response of h-AdMSCs, with HMM HA (2,000 kDa) highly stimulated chondrogenesis as compared to LMM HA (80 kDa), via CD44 clustering and Sox 9 signaling pathway, which is in agreement with our results (Wu et al., 2018).

Similar effects were observed for osteogenesis, with collagen I and mineralized-matrix, the two main components of bone, being observed in fibrin and semi-IPNs after 4 weeks of culture, indicating the successful osteogenic differentiation of h-AdMSCs. However, the gene expression analysis performed after 3 weeks showed higher levels of specific bone markers in

fibrin-HMM HA as compared to fibrin and fibrin-LMM HA. Collagen II and X are secreted before calcification (Chiu et al., 2014; Mwale et al., 2011), followed by osteocalcin and osteopontin, two mineralization-related genes expressed in the late stages of the osteogenesis (Choi et al., 2011). We verified that collagen II was upregulated by fibrin-HMM HA, while it was not able to be quantified in fibrin-LMM HA. No significant difference was observed for osteocalcin level between all three conditions. On the other hand, fibrin-LMM HA showed to downregulate expression of osteopontin, while a pronounced expression was observed for fibrin and fibrin-HMM HA. These results suggest that fibrin-LMM HA could have delayed osteogenesis of h-AdMSCs, while fibrin-HMM HA presented favorable microenvironment for cells to differentiate and secrete ECM. Similarly to our findings, previous work has reported the increased effect of HMM HA on early osteogenic markers expression by MSCs, in comparison to LMM HA after 14 days of culture. Then, after 28 days, a mineralized matrix was observed in the presence of both HA (Zhao et al., 2015).

Although being an inflammatory microenvironment, fibrin-HMM HA highly stimulated h-AdMSCs response to proliferation, chondrogenic and osteogenic differentiation, through a favorable anabolic/catabolic balance. Therefore, it represents a standardized structure that is promising to modulate cartilage and bone regeneration in the treatment of osteoarthritis.

3.4.5. Conclusion

In this work, we prepared fibrin-HA semi-IPNs by controlled mixing L-PRP with non-crosslinked LMM HA and HMM HA and evaluated the effects of the different microenvironments on h-AdMSCs responses. Results showed that the anabolic/catabolic balance was regulated by PDGF-BB and TNF-α released from platelets and leukocytes, which modulated the secretion of TGF- β1, VEGF, IL-1β, IL-6, and IL-8 by h-AdMSCs. Despite being the fibrin-HMM HA an inflammatory microenvironment, it was highly favorable to stimulating h-AdMSCs proliferation, chondrogenesis and osteogenesis, in which a higher deposition of ECM and expression of specific markers were observed. This evidence might shed light on the results obtained clinically from the applications of L-PRP-HA in osteoarthritic patients. In addition, our standardized structure could represent a promising biomaterial to stimulate cartilage and bone regeneration.

Statement

The authors declare no competing financial interest.

Acknowledgment

The authors gratefully acknowledge Prof. Dr. Willian Dias Belangero and Dr. Adriana da Silva Santos Duarte for the helpful assistance. This work was supported by The São Paulo Research Foundation (FAPESP) Grant numbers 2015/23134-8 and 2016/10132-0.

Supporting Information

Table S3.4.1. RT-PCR primer sequences used in this study.

Gene	Primer sequence (5'→ 3')
Sox 9	F: AGCGAACGCACATCAAGAC R: GCTGTAGTGTGGGAGGTTGAA
Aggrecan	F: TGCATTCCACGAAGCTAACCTT R: GACGCCTCGCCTTCTTGAA
Collagen I	F: CAGCCGCTTCACCTACAGC R: TTTTGTATTCAATCACTGTCTTGCC
Collagen II	F: GGCAATAGCAGGTTCACGTACA R: CGATAACAGTCTTGCCCCACTT
Collagen X	F: CAAGGCACCATCTCCAGGAA R: AAAGGGTATTTGTGGCAGCATATT
Osteocalcin	F: GAAGCCCAGCGGTGCA R: CACTACCTCGCTGCCCTCC
Osteopontin	F: TCGCAGACCTGACATCCAGTACCC R: CGCGTTCAGGTCCTGGGCAA

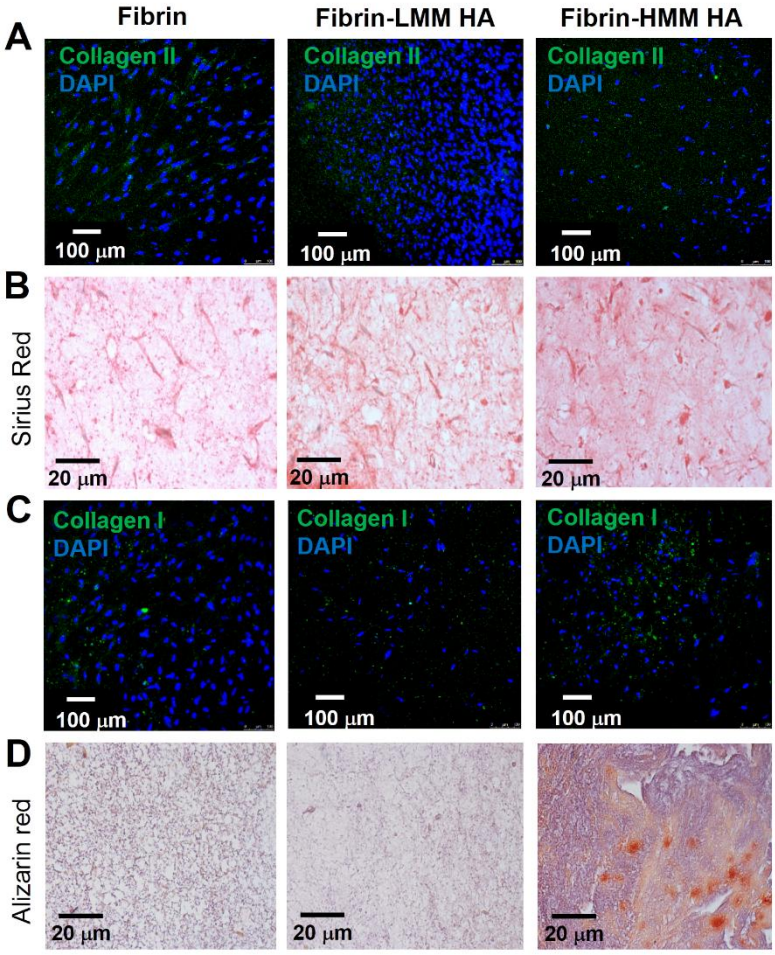

Figure S3.4.1. ECM deposition in fibrin and semi-IPNs cultured in regular medium for 4 weeks (A) ICC images for collagen II deposition. (B) Histological images with Picro-sirius red staining for collagen deposition. (C) ICC images for collagen I deposition. (D) Histological images with Alizarin red staining for calcium deposition.

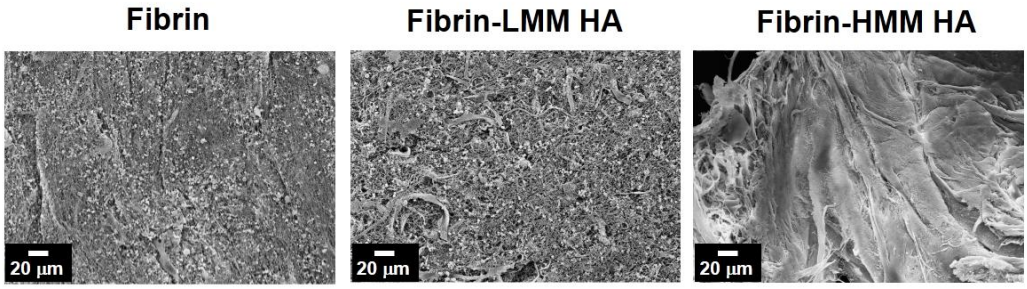

Figure S3.4.2. SEM images of h-AdMSCs in fibrin and semi-IPNs cultured for 4 weeks under chondrogenic induction.

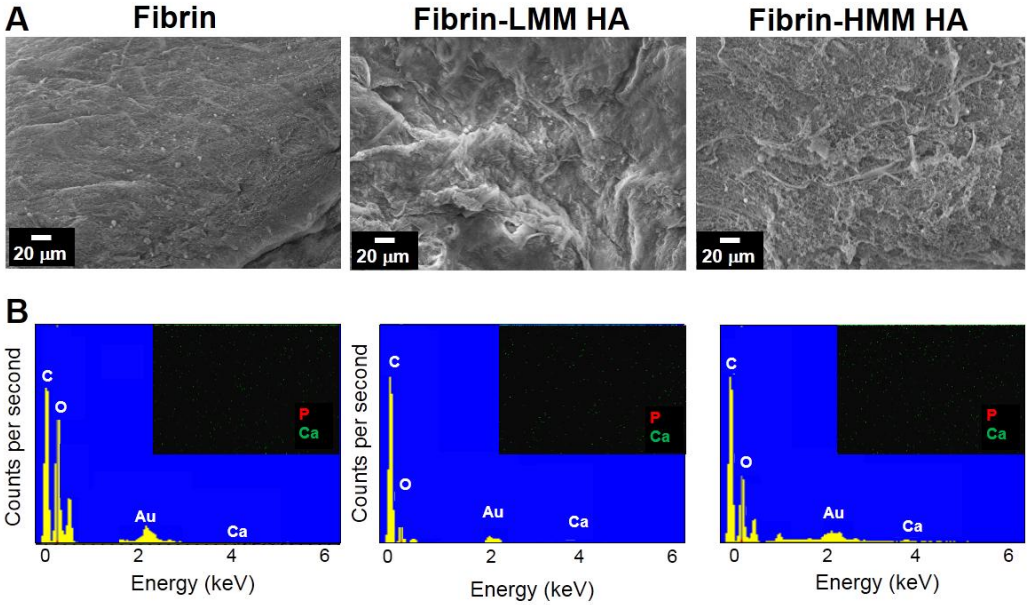

Figure S3.4.3. Evaluation of mineralized matrix deposition in control samples. (A) SEM images of fibrin and semi-IPNs after 4 weeks of culture under regular condition, showing no matrix on samples surface. (B) EDS spectrograms for the different samples, highlighting the calcium and phosphorous mapping.

Table S3.4.2. Elemental composition of the mineralized matrix deposited on the surface of fibrin and semi-IPNs, after h-AdMSCs culture for 4 weeks under osteogenic and regular conditions.

	Elemental concentration (%)			
Osteogenic condition	**C**	**O**	**P**	**Ca**
Fibrin	39.0	37.9	7.2	13.9
Fibrin-LMM HA	37.1	38.0	7.3	15.1
Fibrin-HMM HA	31.6	43.9	7.9	14.8
Control				
Fibrin	56.4	42.1	-	0.3
Fibrin-LMM HA	58.1	39.4	-	0.7
Fibrin-HMM HA	55.5	39.9	-	0.7

CAPÍTULO 4:
CONCLUSÕES

4. CONCLUSÃO GERAL

Os resultados obtidos nesse trabalho mostraram que a razões plaquetas/leucócitos e linfócitos/granulócitos no L-PRP afetaram o balanço anabólico/catabólico do microambiente celular, modulando o comportamento das h-AdMSCs. A associação de L-PRP-AH em semi-RPIs (fibrina-AH) mostrou resultados mais favoráveis à proliferação e diferenciação condrogênica e osteogênica das h-AdMSCs em fibrina-AH de alta MM, em relação à fibrina e fibrina-AH de baixa MM. Esse estudo apresentou a padronização tanto do preparo de L-PRP quanto da mistura L-PRP-AH e semi-RPIs.

As conclusões específicas desse trabalho foram:

- A centrifugação do sangue total entre 50 e 800 xg, 10 min, mostraram os efeitos da aceleração na recuperação dos componentes do sangue no L-PRP, onde plaquetas foram mais concentradas sob acelerações mais baixas (50 – 120 xg) e granulócitos foram mais concentrados sob acelerações mais altas (300 – 800 xg), resultando em diferentes faixas de razões plaquetas/leucócitos e linfócitos/granulócitos;

- As diferentes razões em L-PRPs resultaram em perfis de liberação de FCs e citocinas distintos, levando à uma variação no balanço anabólico/catabólico no microambiente celular, modulando a resposta das h-AdMSCs. Esses resultados mostraram que as razões plaquetas/leucócitos e linfócitos/granulócitos conferem maior eficiência do L-PRP em relação à concentração dos componentes de forma individual;

- A associação entre o L-PRP e AH não reticulado sob condições controladas de mistura resultou na formação de semi-RPIs de fibrina-AH com propriedades estruturais e reológicas variáveis com a MM do AH;

- As semi-RPIs também apresentaram respostas distintas quanto ao comportamento biológico do L-PRP e das h-AdMSCs, em relação à liberação de FCs e citocinas, que variaram de acordo com a presença das células e MM do AH. Mesmo as semi-RPIs apresentando um microambiente inflamatório, a proliferação e diferenciação condrogênica e osteogênica das h-AdMSCs, sendo significativamente maior em fibrina-AH de alta MM.

CAPÍTULO 5:
SUGESTÕES PARA TRABALHOS FUTUROS

5. SUGESTÕES PARA TRABALHOS FUTUROS

Os resultados obtidos nessa tese de doutorado abrem espaço para uma série de trabalhos futuros envolvendo o L-PRP e L-PRP-AH. Dentre eles, algumas sugestões são citadas abaixo:

- Estudo das variações das razões plaquetas/leucócitos e linfócitos granulócitos no L-PRP, preparado utilizando o sangue total de um número maior de doadores, a fim de se obter um melhor delineamento das respostas biológicas, como liberação de fatores de crescimento e citocinas.

- Como mencionado no trabalho, as condições controladas de mistura L-PRP-AH permitiram obter estruturas padronizadas e com resultados reprodutíveis. Sendo assim, existe a possibilidade de se estudar a formação de novas estruturas variando-se a velocidade e tempo de preparo, concentração de AH, razão L-PRP/AH e proporção L-PRP-AH/trombina-cálcio.

- O trabalho também abre espaço para a caracterização da liberação de um grande leque de outros fatores solúveis e proteínas secretados não somente pelas plaquetas e leucócitos, mas também pelas células mesenquimais, tais como metaloproteinases, Wnt signaling, proteínas morfogenéticas ósseas, dentre outras. Além disso, um estudo mais aprofundado de diferentes vias de sinalização que promovem a proliferação e diferenciação celular nas semi-RPIs será de grande valia para entender melhor os mecanismos de ação do L-PRP-AH na regeneração da cartilagem e osso.

- Estudos pré-clínicos e clínicos das semi-RPIs padronizadas nesse trabalho, para validação *in vivo* dos resultados obtidos *in vitro*.

CAPÍTULO 6:
REFERÊNCIAS

6. REFERÊNCIAS

Anitua, E., Sánchez, M., Zalduendo, M. M., De La Fuente, M., Prado, R., Orive, G. and 56, I. (2009). Fibroblastic response to treatment with different preparations rich in growth factors. *Cell Prolif.* 42, 162–170.

Abbadessa, A., Landín, M., Oude Blenke, E., Hennink, W. E. and Vermonden, T. (2017). Two-component thermosensitive hydrogels: Phase separation affecting rheological behavior. *Eur. Polym. J.* 92, 13–26.

Altman, R. (2000). Intra-articular Sodium Hyaluronate in Osteoarthritis of the Knee. *Semin. Arthritis Rheum.* 30, 11–18.

Amable, P. R., Carias, R. B. V., Teixeira, M. V. T., da Cruz Pacheco, I., Corrêa do Amaral, R. J. F., Granjeiro, J. M. and Borojevic, R. (2013). Platelet-rich plasma preparation for regenerative medicine: optimization and quantification of cytokines and growth factors. *Stem Cell Res. Ther.* 4, 67.

Andia, I. and Abate, M. (2014). Therapy Knee osteoarthritis: hyaluronic acid , platelet-rich plasma or both in association ? *Expert Opin. Biol. Ther.* 2598,.

Andia, I. and Maffulli, N. (2013). Platelet-rich plasma for managing pain and. *Nat. Rev. Rheumatol.* 9, 721–730.

Anitua, E., Andia, I., Sanchez, M., Azofra, J., Zalduendo, M. del M., Nurden, P. and Nurden, A. T. (2005). Autologous preparations rich in growth factors promote proliferation and induce VEGF and HGF production by human tendon cells in culture. *J. Orthop. Res.* 23, 281–286.

Anitua, E., Sánchez, M., Nurden, A. T., Zalduendo, M. M., De la Fuente, M., Azofra, J. and Andía, I. (2007). Platelet-released growth factors enhance the secretion of hyaluronic acid and induce hepatocyte growth factor production by synovial fibroblasts from arthritic patients. *Rheumatology* 46, 1769–1772.

Anitua, E., Aguirre, J. J., Algorta, J., Ayerdi, E., Cabezas, A. I., Orive, G. and Andia, I. (2008). Effectiveness of autologous preparation rich in growth factors for the treatment of chronic cutaneous ulcers. *J. Biomed. Mater. Res. B. Appl. Biomater.* 84, 415–421.

Anitua, E., Alkhraisat, M. H. and Orive, G. (2012). Perspectives and challenges in regenerative medicine using plasma rich in growth factors. *J. Control. Release* 157, 29–38.

Anitua, E., Zalduendo, M., Troya, M., Padilla, S. and Orive, G. (2015). Leukocyte inclusion within a platelet rich plasma-derived fibrin scaffold stimulates a more pro-inflammatory

environment and alters fibrin properties. *PLoS One* 10, 1–19.

Apte, R. N. (1995). Mechanisms of Cytokine Production by Fibroblasts-Implications for Normal Connective Tissue Homeostasis and Pathological Conditions. *Folia Microbiol.* 40, 392–404.

Araña, M., Mazo, M., Aranda, P., Pelacho, B. and Prosper, F. (2013). Adipose Tissue-Derived Mesenchymal Stem Cells: Isolation, Expansion, and Characterization. In *Cellular Cardiomyoplasty. Methods in Molecular Biology (Methods and Protocols)* (ed. Kao R.), p. Humana Press, Totowa, NJ.

Arulmoli, J., Wright, H. J., Phan, D. T. T., Sheth, U., Que, R. A., Botten, G. A., Keating, M., Botvinick, E. L., Pathak, M. M., Zarembinski, T. I., et al. (2016). Combination scaffolds of salmon fibrin, hyaluronic acid, and laminin for human neural stem cell and vascular tissue engineering. *Acta Biomater.* 43, 122–138.

Aya, K. L. and Stern, R. (2014). Hyaluronan in wound healing: Rediscovering a major player. *Wound Repair Regen.* 22, 579–593.

Bajpai, A. K. and Shrivastava, M. (2002). Swelling kinetics of a hydrogel of poly(ethylene glycol) and poly(acrylamide-co-styrene). *J. Appl. Polym. Sci.* 85, 1419–1428.

Balazs, E. A. (1968). Viscoelastic properties of hyaluronic acid and biological lubrication. *Univ. Mich. Med. Cent. J.* 255–9.

Balazs, E. A. and Denlinger, J. L. (1993). Viscosupplementation: A new concept in the treatment of osteoarthritis. *J. Rheumatol.* 3, 20.

Balazs, E. a, Watson, D., Duff, I. F. and Roseman, S. (1967). Hyaluronic acid in synovial fluid. I. Molecular parameters of hyaluronic acid in normal and arthritis human fluids. *Arthritis Rheum.* 10, 357–376.

Barba-Recreo, P., Del Castillo Pardo De Vera, J. L., Georgiev-Hristov, T., Ruiz Bravo-Burguillos, E., Abarrategi, A., Burgueño, M. and García-Arranz, M. (2015). Adipose-derived stem cells and platelet-rich plasma for preventive treatment of bisphosphonate-related osteonecrosis of the jaw in a murine model. *J. Cranio-Maxillofacial Surg.* 43, 1161–1168.

Barnett Jr, M. D. and Pomeroy, G. C. (2007). Use of Platelet-Rich Plasma and Bone Marrow-Derived Mesenchymal Stem Cells in Foot and Ankle Surgery. *Tech. Foot Ankle Surg.* 6, 89–94.

Benedetti, E., Sagripanti, A., Papineschi, F. and Benedetti, E. (1998). Determination of Secondary Structure of Normal Fibrin from Human Peripheral Blood. *Biopolymers*.

Bensaïd, W., Triffitt, J. T., Blanchat, C., Oudina, K., Sedel, L. and Petite, H. (2003). A biodegradable fibrin scaffold for mesenchymal stem cell transplantation. *Biomaterials* 24, 2497–2502.

Berk, L. C. J. Van Den, Jansen, B. J. H., Siebers-vermeulen, K. G. C., Roelofs, H., Figdor, C. G., Adema, G. J. and Torensma, R. (2010). Mesenchymal stem cells respond to TNF but do not produce TNF. *J. Leukoc. Biol. 283* 87, 283–289.

Bhandari, M., Bannuru, R. R., Babins, E. M., Martel-Pelletier, J., Khan, M., Raynauld, J.-P., Frankovich, R., Deanna Mcleod, Devji, T., Phillips, M., et al. (2017). Intra-articular hyaluronic acid in the treatment of knee osteoarthritis: a Canadian evidence-based perspective Mohit. *Ther. Adv. Musculoskelet. Dis. Rev.* 9, 231–246.

Bielecki, T., Gazdzik, T. S. and Szczepanski, T. (2008). Benefit of percutaneous injection of autologous platelet-leukocyte-rich gel in patients with delayed union and nonunion. *Eur. Surg. Res.* 40, 289–296.

Bielecki, T., Wójcik, K., Bold, T., Osadnik, B. and Szczepański, T. (2015). The Influence of Leukocyte and Platelet Concentrate Enrich in Stem Cells on Bone Regeneration Processes: A Clinical and Flow Cytometry Study. *J. Biomed. Sci. Eng.* 08, 659–664.

Blundell, C. D., Deangelis, P. L. and Almond, A. (2006). Hyaluronan: the absence of amide-carboxylate hydrogen bonds and the chain conformation in aqueous solution are incompatible with stable secondary and tertiary structure models. *Biochem. J.* 396, 487–98.

Boswell, S. G., Schnabel, L. V, Mohammed, H. O., Sundman, E. A., Minas, T. and Fortier, L. A. (2013). Increasing Platelet Concentrations in Leukocyte-Reduced Platelet-Rich Plasma Decrease Collagen Gene Synthesis in Tendons. *Am. J. Sports Med.* 42, 42–49.

Brat, D. J., Bellail, A. C. and Van Meir, E. G. (2005). The role of interleukin-8 and its receptors in gliomagenesis and tumoral angiogenesis. *Neuro. Oncol.* 7, 122–33.

Brown, R. I. (1989). The physics of continuous flow centrifugal cell separation. *Artif. Organs* 13, 4–20.

Buckwalter, J. A., Einhorn, T. A. and Simon, S. R. (2001). *Orthopaedic basic science: biology and biomechanics of the musculoskeletal system*. 2nd ed. American Academy of Orthopaedic Surgeons.

Burdick, J. A., Chung, C., Jia, X., Randolph, M. A. and Langer, R. (2005). Controlled Degradation and Mechanical Behavior of Photopolymerized Hyaluronic Acid Networks. *Biomacromolecules* 6, 386–391.

Caplan, A. I. (1991). Mesenchymal stem cells. *J. Orthop. Res.* 9, 641–650.

Caplan, A. I. (2007). Adult Mesenchymal Stem Cells for Tissue Engineering Versus Regenerative Medicine. *J. Cell Physiol.* 47, 341–347.

Caplan, A. I. and Correa, D. (2011). PDGF in Bone Formation and Regeneration: New Insights into a Novel Mechanism Involving MSCs. *J. Orthop. Res.* 1795–1803.

Carlyon, J. A., Latif, D. A., Pypaert, M., Lacy, P. and Fikrig, E. (2004). Anaplasma phagocytophilum utilizes multiple host evasion mechanisms to thwart NADPH oxidase-mediated killing during neutrophil infection. *Infect. Immun.* 72, 4772–4783.

Carr, M. E. and Gabriel, D. A. (1980). Dextran-induced Changes in Fibrin Fiber Size and Density Based on Wavelength Dependence of Gel Turbidity. *Macromolecules* 13, 1473–1477.

Carr, M. E. and Hermans, J. (1978). Size and Density of Fibrin Fibers from Turbidity1 Size and Density of Fibrin Fibers from Turbidity. *Macromolecules* 575, 46–50.

Carr, M. E., Shen, L. L., Hermans, J. A. N. and Chapel, H. (1977). Mass-Length Ratio of Fibrin Fibers from Gel Permeation and Light Scattering. *Biopolymers* 16, 1–15.

Chaly, Y. V, Selvan, R. S., Fegeding, K. V, Kolesnikova, T. S. and Voitenok, N. N. (2000). Expression of IL-8 Gene in Human Monocytes and Lymphocytes: Differential Regulation By TNF and IL-1. *Cytokine* 12, 636–643.

Chen, J., Li, Y., Wang, B., Yang, J., Heng, B. C., Yang, Z., Ge, Z. and Lin, J. (2018). TGF-β1 affinity peptides incorporated within a chitosan sponge scaffold can significantly enhance cartilage regeneration. *J. Mater. Chem. B* 6, 675–687.

Chiu, L., Lai, W. T., Chang, S., Wong, C., Fan, C., Fang, C. and Tsai, Y. (2014). The effect of type II collagen on MSC osteogenic differentiation and bone defect repair. *Biomaterials* 35, 2680–2691.

Choi, M., Noh, W., Park, J., Lee, J. and Suh, J. (2011). Gene expression pattern during osteogenic differentiation of human periodontal ligament cells in vitro. *J Periodontal Implant Sci* 41, 167–175.

Choukroun, J. and Ghanaati, S. (2017). Reduction of relative centrifugation force within injectable platelet-rich-fibrin (PRF) concentrates advances patients ' own inflammatory cells , platelets and growth factors: the first introduction to the low speed centrifugation concept. *Eur. J. Trauma Emerg. Surg.* Maech,.

Choukroun, J. and Ghanaati, S. (2018). Reduction of relative centrifugation force within injectable platelet-rich-fibrin (PRF) concentrates advances patients' own inflammatory

cells, platelets and growth factors: the first introduction to the low speed centrifugation concept. *Eur. J. Trauma Emerg. Surg.* 44, 87–95.

Cieslik-Bielecka, A., Bielecki, T., Gazdzik, T. S., Arendt, J., Król, W. and Szczepanski, T. (2009). Autologous platelets and leukocytes can improve healing of infected high-energy soft tissue injury. *Transfus. Apher. Sci.* 41, 9–12.

Cieslik-Bielecki, A., Dohan Ehrenfest, D. M., Lubkowska, A. and Bielecki, T. (2012). Microbicidal Properties of Leukocyte- and Platelet-Rich Plasma/Fibrin (L-PRP/L-PRF): New Perspectives. *J. Biol. Regul. Homeost. Agents* 26.

Collins, M. N. and Birkinshaw, C. (2013). Hyaluronic acid based scaffolds for tissue engineering - A review. *Carbohydr. Polym.* 92, 1262–1279.

Couper, K. N., Blount, D. G. and Riley, E. M. (2008). IL-10: The Master Regulator of Immunity to Infection. *J. Immunol.* 180, 5771–5777.

Crane, D. and Everts, P. A. M. (2008). Platelet Rich Plasma (PRP) Matrix Grafts. *Pract. PAIN Manag.* 1–10.

Cui, N., Qian, J., Liu, T., Zhao, N. and Wang, H. (2015). Hyaluronic acid hydrogel scaffolds with a triple degradation behavior for bone tissue engineering. *Carbohydr. Polym.* 126, 192–198.

Cyphert, J. M., Trempus, C. S. and Garantziotis, S. (2015). Size Matters: Molecular Weight Specificity of Hyaluronan Effects in Cell Biology. *Int. J. Cell Biol.* 2015,.

Dallari, D., Stagni, C., Rani, N., Sabbioni, G., Pelotti, P., Torricelli, P., Tschon, M. and Giavaresi, G. (2016). Ultrasound-Guided Injection of Platelet-Rich Plasma and Hyaluronic Acid, Separately and in Combination, for Hip Osteoarthritis: A Randomized Controlled Study. *Am. J. Sports Med.* 44, 664–71.

Das, A., Sinha, M., Datta, S., Abas, M., Chaffee, S., Sen, C. K. and Roy, S. (2015). Monocyte and Macrophage Plasticity in Tissue Repair and Regeneration. *Am. J. Pathol.* 185, 2596–2606.

Day, A. J. and De La Motte, C. A. (2005). Hyaluronan cross-linking: A protective mechanism in inflammation? *Trends Immunol.* 26, 637–643.

de la Motte, C. A. (2011). Hyaluronan in intestinal homeostasis and inflammation: implications for fibrosis. *AJP Gastrointest. Liver Physiol.* 301, G945–G949.

de Melo, B. A. G., Shimojo, A. A. M., Perez, A. G. M., Lana, J. F. S. D. and Santana, M. H. A. (2018). Distribution, recovery and concentration of platelets and leukocytes in L-PRP prepared by centrifugation. *Colloids Surfaces B Biointerfaces* 161, 288–295.

Delong, J. M., Russell, R. P. and Mazzocca, A. D. (2012). Platelet-rich plasma: The PAW classification system. *Arthrosc. - J. Arthrosc. Relat. Surg.* 28, 998–1009.

Di Bella, C., Fosang, A., Donati, D. M., Wallace, G. G. and Choong, P. F. M. (2015). 3D Bioprinting of Cartilage for Orthopedic Surgeons: Reading between the Lines. *Front. Surg.* 2, 1–7.

Dohan, D. M., Choukroun, J., Diss, A., Dohan, S. L., Dohan, A. J. J., Mouhyi, J. and Gogly, B. (2006). Platelet-rich fibrin (PRF): A second-generation platelet concentrate. Part I: Technological concepts and evolution. *Oral Surgery, Oral Med. Oral Pathol. Oral Radiol. Endodontology* 101.

Dohan Ehrenfest, D. M., Rasmusson, L. and Albrektsson, T. (2009). Classification of platelet concentrates: from pure platelet-rich plasma (P-PRP) to leucocyte- and platelet-rich fibrin (L-PRF). *Trends Biotechnol.* 27, 158–167.

Dohle, E., Bagdadi, K. El, Sader, R., Choukroun, J., Kirkpatrick, C. J. and Ghanaati, S. (2017). Platelet- rich fibrin- based matrices to improve angiogenesis in an in vitro co-culture model for bone tissue engineering. *J. Tissue Eng. Regen. Med.* 1–13.

Dong, Y., Hassan, W. and Zheng, Y. (2012). Thermoresponsive hyperbranched copolymer with multi acrylate functionality for in situ cross-linkable hyaluronic acid composite semi-IPN hydrogel. *J Mater Sci Mater Med* 23, 25–35.

Doran, P. M. (2015). *Cartilage Tissue Engineering*. (ed. Doran, P. M.) Human Press.

Drury, J. L. and Mooney, D. J. (2003). Hydrogels for tissue engineering: Scaffold design variables and applications. *Biomaterials* 24, 4337–4351.

Dubravec, D. B., Spriggst, D. R., Mannick, J. A. and Rodrick, M. L. (1990). Circulating human peripheral blood granulocytes synthesize and secrete tumor necrosis factor a. *Proc Natl Acad Sci USA* 87, 6758–6761.

Ehrenfest, D. M. D., Bielecki, T., Jimbo, R., Barbe, G., Corso, M. Del, Inchingolo, F. and Sammartino, G. (2012). Do the Fibrin Architecture and Leukocyte Content Influence the Growth Factor Release of Platelet Concentrates? An Evidence-based Answer Comparing a Pure Platelet-Rich Plasma (P-PRP) Gel and a Leukocyte- and Platelet-Rich Fibrin (L-PRF). *Curr. Pharm. Biotechnol.* 13, 1145–1152.

Ehrenfest, D. M. D., Andia, I., Zumstein, M. A., Zhang, C.-Q., Pinto, N. R. and Bielecki, T. (2014). Classification of platelet concentrates (Platelet-Rich Plasma-PRP, Platelet-Rich Fibrin-PRF) for topical and infiltrative use in orthopedic and sports medicine: current consensus, clinical implications and perspectives. *Muscles. Ligaments Tendons J.* 4, 3–9.

Ehrenfest, D. M. D., Pinto, N. R., Pereda, A., Jiménez, P., Corso, M. Del, Kang, B., Nally, M., Lanata, N., Quirynen, M., Dohan, D. M., et al. (2018). The impact of the centrifuge characteristics and centrifugation protocols on the cells , growth factors , and fibrin architecture of a leukocyte- and platelet-rich fibrin (L-PRF) clot and membrane. *Platelets* 29, 171–184.

Espinosa, S. C. and Foster, E. J. (2016). Articular cartilage: from formation to tissue engineering. *Biomater. Sci.*

Everts, P. A. M., Knape, J. T. A., Weibrich, G., Schönberger, J. P. A. M., Hoffmann, J., Overdevest, E. P., Box, H. A. M. and van Zundert, A. (2006a). Platelet-rich plasma and platelet gel: a review. *J. Extra. Corpor. Technol.* 38, 174–187.

Everts, P. A. M., Devilee, R. J. J., Brown Mahoney, C., Eeftinck-Schattenkerk, M., Box, H. A. M., Knape, J. T. A. and Van Zundert, A. (2006b). Platelet gel and fibrin sealant reduce allogeneic blood transfusions in total knee arthroplasty. *Acta Anaesthesiol. Scand.* 50, 593–599.

Everts, P. A., Overdevest, E. P., Jakimowicz, J. J., Oosterbos, C. J., Schönberger, J. P., Knape, J. T. and van Zundert, A. (2007). The use of autologous platelet-leukocyte gels to enhance the healing process in surgery, a review. *Surg. Endosc.* 21, 2063–8.

Faurschou, M. and Borregaard, N. (2003). Neutrophil granules and secretory vesicles in inflammation. *Microbes Infect.* 5, 1317–1327.

Filardo, G., Kon, E., Buda, R., Timoncini, A., Di, A., Annarita, M., Pier, C., Fornasari, M., Giannini, S. and Marcacci, M. (2011). Platelet-rich plasma intra-articular knee injections for the treatment of degenerative cartilage lesions and osteoarthritis. *Knee* 528–535.

Filardo, G., Kon, E., Teresa, M., Ruiz, P., Cenacchi, A., Maria, P. and Maurilio, F. (2012a). Platelet-rich plasma intra-articular injections for cartilage degeneration and osteoarthritis: single- versus double-spinning approach. *Knee Surg Sport. Traumatol Arthrosc* 20, 2082–2091.

Filardo, G., Kon, E., Di Martino, A., Di Matteo, B., Merli, M. L., Cenacchi, A., Fornasari, P. M. and Marcacci, M. (2012b). Platelet-rich plasma vs hyaluronic acid to treat knee degenerative pathology: study design and preliminary results of a randomized controlled trial. *BMC Musculoskelet. Disord.* 13, 229.

Freeman, M. R., Schneck, F. X., Gagnon, M. L., Corless, C., Soker, S., Niknejad, K., Peoples, G. E. and Klagsbrun, M. (1995). Peripheral blood T lymphocyte sand lymphocytes infilitrating human cancers express vascular endothelial growth factor: a potential role for

T cells in angiogenesis. *Cancer Res* 55, 4140–4145.

Gaffey, A. C., Chen, M. H., Venkataraman, C. M., Trubelja, A., Rodell, C. B., Dinh, P. V., Hung, G., Macarthur, J. W., Soopan, R. V., Burdick, J. A., et al. (2015). Injectable shear-thinning hydrogels used to deliver endothelial progenitor cells, enhance cell engraftment, and improve ischemic myocardium. *J. Thorac. Cardiovasc. Surg.* 150, 1268–1276.

Gao, C., Peng, S., Feng, P. and Shuai, C. (2017). Bone biomaterials and interactions with stem cells. *Bone Res.* 5,.

Garg, H. G. and Hales, C. A. (2004). *Chemistry and Biology of Hyaluronan*. Elsevier.

Gawai, K. T. and Sobhana, C. R. (2015). Clinical evaluation of use of platelet rich plasma in bone healing. *J. Maxillofac. Oral Surg.* 14, 67–80.

Ghanaati, S., Booms, P., Orlowska, A., Kubesch, A., Lorenz, J., Rutkowski, J., Landes, C., Sader, R., Kirkpatrick, C. and Choukroun, J. (2014). Advanced Platelet-Rich Fibrin: A New Concept for Cell- Based Tissue Engineering by Means of Inflammatory Cells. *Clinical* XL, 679–689.

Ghosh, P. and Guidolin, D. (2002). Potential Mechanism of Action of Intra-articular Hyaluronan Therapy in Osteoarthritis : Are the Effects Molecular Weight Dependent ? *Semin. Arthritis Rheum.* 32, 10–37.

Gibbs, D. A., Merrill, E. W., Smith, K. A. and Balazs, E. A. (1968). Rheology of hyaluronic acid. *Biopolymers* 6, 777–791.

Gilli, R., Kacuráková, M., Mathlouthi, M., Navarini, L. and Paoletti, S. (1994). FTIR studies of sodium hyaluronate and its oligomers in the amorphous solid phase and in aqueous solution. *Carbohydr. Res.* 263, 315–326.

Goodison, S., Urquidi, V. and Tarin, D. (1999). CD44 cell adhesion molecules. *Mol. Pathol.* 52, 189–196.

Graham, J. (2001). *Biological Centrifugation*. BIOS Scientific Publishers.

Guadilla, J., Andia, I. and Sa, M. (2012). Original article Ultrasound-guided platelet-rich plasma injections for the treatment of osteoarthritis of the hip. *Rheumatology* 51, 144–150.

Gura, E., Hückel, M. and Müller, P.-J. (1998). Specific degradation of hyaluronic acid and its rheological properties. *Polym. Degrad. Stab.* 59, 297–302.

Hardingham, T. E., Oldershaw, R. A. and Tew, S. R. (2006). Cartilage, SOX9 and Notch signals in chondrogenesis. *J. Anat.* 209, 469–480.

Hass, R., Kasper, C., Böhm, S. and Jacobs, R. (2011). Different populations and sources of human mesenchymal stem cells (MSC): A comparison of adult and neonatal tissue-derived

MSC. *Cell Commun. Signal.* 9, 12.

Holmes, H. L., Wilson, B., Goerger, J. P., Silverberg, J. L., Cohen, I., Zipfel, W. R. and Fortier, L. A. (2018). Facilitated recruitment of mesenchymal stromal cells by bone marrow concentrate and platelet rich plasma. *PLoS One* 13, 1–12.

Huang, Y., Liu, X., Xu, X. and Liu, J. (2019). Intra-articular injections of platelet-rich plasma , hyaluronic acid or corticosteroids for knee osteoarthritis A prospective randomized controlled study. *Orthopäde*.

Huber, M., Trattnig, S. and Lintner, F. (2000). Anatomy, Biochemistry, and Physiology of Articular Cartilage : Investigative Radiology. *Invest. Radiol.* 35, 573–580.

Hung, B. P., Hutton, D. L., Kozielski, K. L., Bishop, C. J., Naved, B., Green, J. J., Caplan, A. I., Gimble, J. M., Dorafshar, A. H. and Grayson, W. L. (2015). Platelet-Derived Growth Factor BB Enhances Osteogenesis of Adipose-Derived But Not Bone Marrow-Derived Mesenchymal Stromal/Stem Cells. *Stem* 33,.

Hunter, R. J. (2009). *Foundations of Colloid Science: Volume I*. 2nd ed. Oxford Science Publications.

Hunziker, E. B. (2001). Articular cartilage repair: basic science and clinical progress. A review of the current status and prospects. *Osteoarthr. Cartil.* 10, 432–463.

Hutton, D. L., Moore, E. M., Gimble, J. M. and Grayson, W. L. (2013). Platelet-Derived Growth Factor and Spatiotemporal Cues Induce Development of Vascularized Bone Tissue by Adipose-Derived Stem Cells. *TISSUE Eng. Part A* 19, 2076–2086.

Iijima, H., Isho, T., Kuroki, H., Takahashi, M. and Aoyama, T. (2018). Effectiveness of mesenchymal stem cells for treating patients with knee osteoarthritis : a meta-analysis toward the establishment of effective regenerative rehabilitation. *Nat. Partners Journals*.

Isa, I. L. M., Srivastava, A., Tiernan, D., Owens, P., Rooney, P., Dockery, P. and Pandit, A. (2015). Hyaluronic acid based hydrogels attenuate inflammatory receptors and neurotrophins in interleukin-1β induced inflammation model of nucleus pulposus cells. *Biomacromolecules* 16, 1714–1725.

Janssens, K., Ten Dijke, P., Janssens, S. and Van Hul, W. (2005). Transforming growth factor-β1 to the bone. *Endocr. Rev.* 26, 743–774.

Jia, J., Wang, S., Ma, L., Yu, J., Guo, Y. and Wang, C. (2018). The Differential Effects of Leukocyte-Containing and Pure Platelet-Rich Plasma on Nucleus Pulposus-Derived Mesenchymal Stem Cells : Implications for the Clinical Treatment of Intervertebral Disc Degeneration. *Stem Cells Int.* 2018,.

Jiang, G., Zhao, X., Li, R., Gao, L., Zhao, Q., Wu, M. and Wei, L. (2011). Effects of Inflammatory Factors on Mesenchymal Stem Cells and Their Role in the Promotion of Tumor Angiogenesis in Colon Cancer. *J. Biol. Chem.* 286, 25007–25015.

Jubert, N. J., Rodríguez, L., Reverté-Vinaixa, M. M. and Navarro, A. (2017). Platelet-Rich Plasma Injections for Advanced Knee Osteoarthritis. A Prospective, Randomized, Double-Blinded Clinical Trial. *Orthop. J. Sport. Med.* 5, 1–11.

Karin, M. and Clevers, H. (2016). Reparative inflammation takes charge of tissue regeneration. *Nature* 529, 307–315.

Kazemi, D. and Fakhrjou, A. (2015). Leukocyte and Platelet Rich Plasma (L-PRP) Versus Leukocyte and Platelet Rich Fibrin (L-PRF) For Articular Cartilage Repair of the Knee: A Comparative Evaluation in an Animal Model. *Iran. Red Crescent Med. J.* 17, e19594.

Kiliç, C. S. and Güngörmüs, M. (2016). Is arthrocentesis plus platelet- rich plasma superior to arthrocentesis plus hyaluronic acid for the treatment of temporomandibular joint osteoarthritis: a randomized clinical. *J Oral Maxillofac Surg* 12, 1538–1544.

Klein, T. J., Rizzi, S. C., Reichert, J. C., Georgi, N., Malda, J., Schuurman, W., Crawford, R. W. and Hutmacher, D. W. (2009). Strategies for zonal cartilage repair using hydrogels. *Macromol. Biosci.* 9, 1049–1058.

Koh, Y.-G., Jo, S.-B., Kwon, O.-R., Suh, D.-S., Lee, S.-W., Park, S.-H. and Choi, Y.-J. (2013). Mesenchymal Stem Cell Injections Improve Symptoms of Knee Osteoarthritis. *Arthrosc. J. Arthrosc. Relat. Surg.* 29, 748–755.

Kolesky, D. B., Homan, K. A., Skylar-Scott, M. A. and Lewis, J. A. (2016). Three-dimensional bioprinting of thick vascularized tissues. *Proc. Natl. Acad. Sci.* 113, 3179–3184.

Komorowicz, E., Balázs, N., Varga, Z., Szabó, L., Bóta, A. and Kolev, K. (2016). Hyaluronic acid decreases the mechanical stability, but increases the lytic resistance of fibrin matrices. *Matrix Biol.*

Kon, E., Buda, R., Filardo, G., Di, A., Timoncini, A., Cenacchi, A. and Maria, P. (2009). Platelet-rich plasma : intra-articular knee injections produced favorable results on degenerative cartilage lesions. *Knee Surg Sport. Traumatol Arthrosc*.

Kon, E., Mandelbaum, B., Buda, R., Filardo, G., Delcogliano, M., Timoncini, A., Fornasari, P. M., Giannini, S. and Marcacci, M. (2011). Platelet-rich plasma intra-articular injection versus hyaluronic acid viscosupplementation as treatments for cartilage pathology: From early degeneration to osteoarthritis. *Arthrosc. - J. Arthrosc. Relat. Surg.* 27, 1490–1501.

Krishnan, Y. and Grodzinsky, A. J. (2018). Cartilage diseases. *Matrix Biol.* 51–69.

Kurapati, K., Tapadia, S., Rao, M. and Anbarasu, K. (2018). Efficacy of Intra-Articular Injection of Platelet Rich Plasma and Hyaluronic Acid in Early Knee Osteoarthritis – Case Series. *Eur. J. Mol. Clin. Med.* 5, 30–36.

Lai, F., Kakudo, N., Morimoto, N., Taketani, S., Hara, T. and Ogawa, T. (2018). Platelet-rich plasma enhances the proliferation of human adipose stem cells through multiple signaling pathways. *Stem Cell Res. Ther.* 9, 1–10.

Lam, W. A., Chaudhuri, O., Crow, A., Webster, K. D., Li, T. De, Kita, A., Huang, J. and Fletcher, D. A. (2011). Mechanics and contraction dynamics of single platelets and implications for clot stiffening. *Nat. Mater.* 10, 61–66.

Lam, J., Truong, N. F. and Segura, T. (2014). Design of cell – matrix interactions in hyaluronic acid hydrogel scaffolds. *Acta Biomater.* 10, 1571–1580.

Lana, J. F. S. D., Santana, M. H. A., Belangero, W. D. and Luzo, A. C. M. (2014). *Platelet-Rich Plasma. Regenerative Medicine: Sports Medicine, Orthopedic, and Recovery of Musculoskeletal Injuries*. I. Springer.

Lana, J. F. S. D., Weglein, A., Sampson, S., Vicente, E. F., Huber, S. C., Souza, C. V., Ambach, M. A., Vincent, H., Urban-Paffaro, A., Onodera, C. M. K., et al. (2016). Randomized controlled trial comparing hyaluronic acid, platelet-rich plasma and the combination of both in the treatment of mild and moderate osteoarthritis of the knee. *J. Stem Cells Regen. Med.* 12, 1–10.

Lana, J. F. S. D., Purita, J., Paulus, C., Huber, S. C., Rodrigues, B. L., Rodrigues, A. A., Santana, M. H., Madureira, J. L., Malheiros Luzo, Â. C., Belangero, W. D., et al. (2017). Contributions for classification of platelet rich plasma - Proposal of a new classification: MARSPILL. *Regen. Med.* 12, 565–574.

Lapčík, L., Lapčík, L., De Smedt, S., Demeester, J. and Chabreček, P. (1998). Hyaluronan: Preparation, Structure, Properties, and Applications †. *Chem. Rev.* 98, 2663–2684.

Leboeuf, R. D., Gregg, R. R., Weigel, P. H. and Fuller, G. M. (1987). Effects of Hyaluronic Acid and Other Glycosaminoglycans on Fibrin Polymer Formation. *Biochemistry* 26, 6052–6057.

LeBoeuf, R. D., Raja, R. H., Fuller, G. M. and Weigel, P. H. (1986). Human fibrinogen specifically binds hyaluronic acid. *J. Biol. Chem.* 261, 12586–12592.

Lee, K. S. (2013). The Effects of the Shear-thinning Property of Injection Fluid on the Performance of Polymer Flood. *Energy Sources* 35, 1550–1559.

Lee, F. and Kurisawa, M. (2013). Formation and stability of interpenetrating polymer network hydrogels consisting of fibrin and hyaluronic acid for tissue engineering. *Acta Biomater.* 9, 5143–5152.

Lee, J. W., Kim, Y. H., Han, S. H. and Hahn, S. B. (2004). Chondrogenic Differentiation of Mesenchymal Stem Cells and Its Clinical Applications. *Yonsei Med. J.* 45, 41–47.

Leijten, J., Moreira Teixeira, L. S., Bolander, J., Ji, W., Vanspauwen, B., Lammertyn, J., Schrooten, J. and Luyten, F. P. (2016). Bioinspired seeding of biomaterials using three dimensional microtissues induces chondrogenic stem cell differentiation and cartilage formation under growth factor free conditions. *Sci. Rep.* 6, 1–12.

Li, L., Yu, F., Shi, J., Shen, S., Teng, H., Yang, J., Wang, X. and Jiang, Q. (2017). In situ repair of bone and cartilage defects using 3D scanning and 3D printing. *Sci. Rep.* 7, 1–12.

Li, L., Duan, X., Fan, Z., Chen, L., Xing, F., Xu, Z. and Chen, Q. (2018). Mesenchymal Stem Cells in Combination with Hyaluronic Acid for Articular Cartilage Defects. *Sci. Rep.* 8, 1–11.

Liou, J.-J., Rothrauff, B. B., Alexander, P. G. and Tuan, R. S. (2018). Effect of Platelet-Rich Plasma on Chondrogenic Differentiation of Adipose- and Bone Marrow-Derived Mesenchymal Stem Cells. *Tissue Eng. Part A* 24, 1432–1443.

Liu, M., Zeng, X., Ma, C., Yi, H., Ali, Z., Mou, X., Li, S., Deng, Y. and He, N. (2017). Injectable hydrogels for cartilage and bone tissue engineering. *Bone Res.* 5,.

Liu, J., Qu, W., Li, R., Zheng, C. and Zhang, L. (2018). Efficacy of autologous platelet-rich gel in the treatment of deep grade II burn wounds. *Int J Clin Exp Med* 11, 2654–2659.

Lyublinskaya, O. G., Borisov, Y., Pugovkina, N. A., Smirnova, I. S., Obidina, J. V., Ivanova, J. S., Zenin, V. V., Shatrova, A. N., Borodkina, A. V., Aksenov, N. D., et al. (2015). Reactive oxygen species are required for human mesenchymal stem cells to initiate proliferation after the quiescence exit. *Oxid. Med. Cell. Longev.* 2015,.

Magalon, J., Chateau, A. L., Bertrand, B., Louis, M. L., Silvestre, A., Giraudo, L., Veran, J. and Sabatier, F. (2016). DEPA classification: a proposal for standardising PRP use and a retrospective application of available devices. *BMJ Open Sport Exerc. Med.* 2, e000060.

Majors, A. K., Austin, R. C., De, C. A., Pyeritz, R. E., Hascall, V. C., Kessler, S. P., Sen, G. and Strong, S. A. (2003). Endoplasmic Reticulum Stress Induces Hyaluronan Deposition and Leukocyte Adhesion. *J. Biol. Chem.* 278, 47223–47231.

Manzini, B. M., da Silva Santos Duarte, A., Sankaramanivel, S., Ramos, A. L., Latuf-Filho, P., Escanhoela, C., Kharmandayan, P., Olalla Saad, S. T., Boin, I. and Malheiros Luzo, Â. C.

(2015). Useful properties of undifferentiated mesenchymal stromal cells and adipose tissue as the source in liver-regenerative therapy studied in an animal model of severe acute fulminant hepatitis. *Cytotherapy* 17, 1052–1065.

Marenzi, G., Riccitiello, F., Tia, M., di Lauro, A. and Sammartino, G. (2015). Influence of Leukocyte- and Platelet-Rich Fibrin (L-PRF) in the Healing of Simple Postextraction Sockets: A Split-Mouth Study. *Biomed Res. Int.* 2015, 369273.

Marmotti, A., Bruzzone, M., Bonasia, D. E., Castoldi, F., Rossi, R., Piras, L., Maiello, A., Realmuto, C. and Peretti, G. M. (2012). One-step osteochondral repair with cartilage fragments in a composite scaffold. *Knee Surg Sport. Traumatol Arthrosc* 20, 2590–2601.

Marx, R. E. (2004). Platelet-rich plasma: evidence to support its use. *J. Oral Maxillofac. Surg.* 62, 489–496.

Marx, R. E., Carlson, E. R., Eichstaedt, R. M., Schimmele, S. R., Strauss, J. E. and Georgeff, K. R. (1998). Platelet-rich plasma: Growth factor enhancement for bone grafts. *Oral Surg. Oral Med. Oral Pathol. Oral Radiol. Endod.* 85, 638–646.

McCarrel, T. M., Minas, T. and Fortier, L. a (2012). Optimization of leukocyte concentration in platelet-rich plasma for the treatment of tendinopathy. *J. Bone Joint Surg. Am.* 94, e143(1-8).

Middleton, K. K., Barro, V., Muller, B., Terada, S. and Fu, F. H. (2012). Evaluation of the Effects of Platelet-Rich Plasma (PRP) Therapy Involved in the Healing of Sports-Related Soft Tissue Injuries. *Iowa Orthop. J.* 32, 150–163.

Miron, R. J., Fujioka-Kobayashi, M., Bishara, M., Zhang, Y., Hernandez, M. and Choukroun, J. (2016). Platelet-Rich Fibrin and Soft Tissue Wound Healing: A Systematic Review. *Tissue Eng. Part B* 23,.

Misra, S., Hascall, V. C., Markwald, R. R. and Ghatak, S. (2015). Interactions between Hyaluronan and Its Receptors (CD44, RHAMM) Regulate the Activities of Inflammation and Cancer. *Front. Immunol.* 6, 201.

Mosmann, T. (1983). Rapid colorimetric assay for cellular growth and survival: Application to proliferation and cytotoxicity assays. *J. Immunol. Methods* 65, 55–63.

Murphy, M. B., Blashki, D., Buchanan, R. M., Yazdi, I. K., Ferrari, M., Simmons, P. J. and Tasciotti, E. (2012). Adult and umbilical cord blood-derived platelet-rich plasma for mesenchymal stem cell proliferation, chemotaxis, and cryo-preservation. *Biomaterials* 33, 5308–5316.

Mwale, F., Rampersad, S., Guoying, Y., Rowas, S. Al, Madiraju, P., Antoniou, J. and Laverty,

S. (2011). The Constitutive Expression of Type X Collagen in Mesenchymal Stem Cells from Osteoarthritis Patients Is Reproduced in a Rabbit Model of Osteoarthritis. *J. Tissue Eng.* 2011,.

Nagao, M., Hamilton, J. L., Kc, R., Berendsen, A. D., Duan, X., Cheong, C. W., Li, X., Im, H. J. and Olsen, B. R. (2017). Vascular Endothelial Growth Factor in Cartilage Development and Osteoarthritis. *Sci. Rep.* 7, 1–16.

Nakajima, M., Nito, C., Sowa, K., Suda, S., Nishiyama, Y., Nakamura-takahashi, A., Nitahara-kasahara, Y., Imagawa, K., Hirato, T., Ueda, M., et al. (2017). Mesenchymal Stem Cells Overexpressing Interleukin-10 Promote Neuroprotection in Experimental Acute Ischemic Stroke. *Am. Soc. Gene Cell Ther.* 6, 102–111.

Noble, P. W. (2002a). Hyaluronan in tissue injury and repair. *Matrix Biol.* 21, 25–29.

Noble, P. W. (2002b). Hyaluronan and its catabolic products in tissue injury and repair. *Matrix Biol.* 21, 25–29.

O'Connell, G., Garcia, J. and Amir, J. (2017). 3D Bioprinting: New Directions in Articular Cartilage Tissue Engineering. *ACS Biomater. Sci. Eng.* 3, 2657–2668.

Ortiz, L. A., Dutreil, M., Fattman, C., Pandey, A. C., Torres, G., Go, K. and Phinney, D. G. (2007). Interleukin 1 receptor antagonist mediates the antiinflammatory and antifibrotic effect of mesenchymal stem cells during lung injury. *Proc. Natl. Acad. Sci. U. S. A.* 104, 11002–11007.

Pak, J., Chang, J. J., Lee, J. H. and Lee, S. H. (2013). Safety reporting on implantation of autologous adipose tissue-derived stem cells with platelet-rich plasma into human articular joints. *BMC Musculoskelet. Disord.* 14,.

Papakonstantinou, E., Roth, M. and Karakiulakis, G. (2012). Hyaluronic acid: A key molecule in skin aging. *Dermatoendocrinol.* 4, 253–258.

Parrish, W. R. and Roides, B. (2017). Platelet rich plasma in osteoarthritis: more than a growth factor therapy. *Musculoskelet. Regen.* 3, 1–9.

Parrish, W. R., Roides, B., Hwang, J., Mafilios, M., Story, B. and Bhattacharyya, S. (2016). Normal platelet function in platelet concentrates requires non-platelet cells: a comparative in vitro evaluation of leucocyte-rich (type 1a) and leucocyte-poor (type 3b) platelet concentrates. *BMJ Open Sport Exerc. Med.* 2, e000071.

Perez, A. G. M., Lichy, R., Lana, J. F. S. D., Rodrigues, A. A., Luzo, A. C. M., Belangero, W. D. and Santana, M. H. a (2013). Prediction and modulation of platelet recovery by discontinuous centrifugation of whole blood for the preparation of pure platelet-rich

plasma. *Biores. Open Access* 2, 307–14.

Perez, A. G. M., Lana, J. F. S. D., Rodrigues, A. A., Luzo, A. C. M., Belangero, W. D. and Santana, M. H. A. (2014a). Relevant aspects of centrifugation step in the preparation of platelet-rich plasma. *ISRN Hematol.* 2014, 176060.

Perez, A. G. M., Rodrigues, A. a., Luzo, A. C. M., Lana, J. F. S. D., Belangero, W. D. and Santana, M. H. a. (2014b). Fibrin network architectures in pure platelet-rich plasma as characterized by fiber radius and correlated with clotting time. *J. Mater. Sci. Mater. Med.* 25, 1967–1977.

Perez, A. G. M., Lana, J. F. S. D., Rodrigues, A. A., Luzo, A. C. M., Belangero, W. D. and Santana, M. H. A. (2014c). Relevant aspects of centrifugation step in the preparation of platelet-rich plasma. *ISRN Hematol.* 2014, 176060.

Peterson, J. M., Barbul, A., Breslin, R. J., Wasserkrug, H. L. and Efron, G. (1987). Significance of T-lymphocytes in wound healing. *Surgery* 102, 300–5.

Petrella, R. J., Decaria, J. and Petrella, M. J. (2011). Long term efficacy and safety of a combined low and high of osteoarthritis of the knee. *Rheumatol. Reports* 3,.

Pribush, A., Meyerstein, D. and Meyerstein, N. (2010a). The mechanism of erythrocyte sedimentation. Part 1: Channeling in sedimenting blood. *Colloids Surfaces B Biointerfaces* 75, 214–223.

Pribush, A., Meyerstein, D. and Meyerstein, N. (2010b). The mechanism of erythrocyte sedimentation. Part 2: The global collapse of settling erythrocyte network. *Colloids Surfaces B Biointerfaces* 75, 224–229.

Putra, A., Ridwan, F. B., Putridewi, A. I., Kustiyah, A. R., Wirastuti, K., Sadyah, N. A. C., Rosdiana, I. and Munir, D. (2018). The Role of TNF-α induced MSCs on Suppressive Inflammation by Increasing TGF-β and IL-10. *ID Des. Press* 6, 1779–1783.

Qian, Y., Han, Q., Chen, W., Song, J. and Zhao, X. (2017). Platelet-Rich Plasma Derived Growth Factors Contribute to Stem Cell Differentiation in Musculoskeletal Regeneration. *Front. Chem.* 5, 1–8.

Ratnoff, O. D. and Menzie, C. (1951). A new method for the determination of fibrinogen in small samples of plasma. *J. Lab. Clin. Med.* 37, 516–520.

Rayahin, J. E., Buhrman, J. S., Zhang, Y., Koh, T. J. and Gemeinhart, R. A. (2015). High and low molecular weight hyaluronic acid differentially influence macrophage activation. *ACS Biomater. Sci. Eng.* 1, 481–493.

Renevier, J.-L., Marc, J.-F., Adam, P., Sans, N., Coz, J. Le and Prothoy, I. (2018). “Cellular

matrix™ PRP-HA": A new treatment option with platelet-rich plasma and hyaluronic acid for patients with osteoarthritis having had an unsatisfactory clinical response to hyaluronic acid alone : Results of a pilot , multicenter French study with l. *Int. J. Clin. Rheumtol.* 13, 230–238.

Riboh, J. C., Saltzman, B. M., Yanke, A. B., Fortier, L. and Cole, B. J. (2015). Effect of Leukocyte Concentration on the Efficacy of Platelet-Rich Plasma in the Treatment of Knee Osteoarthritis. *Am. J. Sports Med.* 44, 792–800.

Rinaudo, M. (2008). Rheological investigation on hyaluronan-fibrinogen interaction. *Int. J. Biol. Macromol.* 43, 444–450.

Roman-Blas, J. A., Stokes, D. G. and Jimenez, S. A. (2007). Modulation of TGF-β signaling by proinflammatory cytokines in articular chondrocytes. *Osteoarthr. Cartil.* 15, 1367–1377.

Rooney, P., Wang, M., Kumar, P. and Kumar, S. (1993). Angiogenic oligosaccharides of hyaluronan enhance the production of collagens by endothelial cells. *J. Cell Sci.* 105 (Pt 1, 213–8.

Rosenbaum, A. J., Grande, D. a and Dines, J. S. (2008). The use of mesenchymal stem cells in tissue engineering: A global assessment. *Organogenesis* 4, 23–27.

Russo, F., Este, M. D., Vadal, G., Cattani, C. and Papalia, R. (2016). Platelet Rich Plasma and Hyaluronic Acid Blend for the Treatment of Osteoarthritis : Rheological and Biological Evaluation. *PLoS One* 1–12.

Salazar, K. D., Lankford, S. M. and Brody, A. R. (2009). Mesenchymal stem cells produce Wnt isoforms and TGF-β1 that mediate proliferation and procollagen expression by lung fibroblasts. *Am J Physiol Lung Cell Mol Physiol* 297, 1002–1011.

Sampson, S., Reed, M., Silvers, H., Meng, M. and Mandelbaum, B. (2010). Injection of Platelet-Rich Plasma in Patients with Primary and Secondary Knee Osteoarthritis. *Am. J. Phys. Med. Rehabil.* 89, 961–969.

Sánchez, M., Azofra, J., Anitua, E., Andi, I., Padilla, S., Santisteban, J. and Mujika, I. (2003). Plasma Rich in Growth Factors to Treat an Articular Cartilage Avulsion : A Case Report. *Med. Sci. Sport. Exerc.* 1648–1652.

Schäffer, M. and Barbul, A. (1998). Lymphocyte function in wound healing and following injury. *Br. J. Surg.* 85, 444–460.

Scheller, J., Chalaris, A., Schmidt-Arras, D. and Rose-John, S. (2011). The pro- and anti-inflammatory properties of the cytokine interleukin-6. *Biochim. Biophys. Acta - Mol. Cell*

Res. 1813, 878–888.

Scheraga, H. A. (2004). The thrombin-fibrinogen interaction. *Biophys. Chem.* 112, 117–130.

Schinagl, R. M., Gurskis, D., Chen, A. C. and Sah, R. L. (1997). Depth-Dependent Confined Compression Modulus of Full-Thickness Bovine Articular Cartilage. *J. Orthop. Res.* 15, 499–506.

Schmidt, M. B., Chen, E. H. and Lynch, S. E. (2006). A review of the effects of insulin-like growth factor and platelet derived growth factor on in vivo cartilage healing and repair. *Osteoarthr. Cartil.* 14, 403–412.

Shah, C. B. and Barnett, S. M. (1992). Swelling Behavior of Hyaluronic Acid Gels. *J. Appl. Polym. Sci.* 45, 293–298.

Shewale, A. R., Barnes, C. L., Fischbach, L. A., Ounpraseuth, S., Painter, J. T. and Martin, B. C. (2017). Comparative effectiveness of low, moderate and high molecular weight hyaluronic acid injections in delaying time to knee surgery. *J. Arthroplasty* 32, 2952–2957.

Shimojo, A. A. M., Galdames, S. E. M., Perez, A. G. M., Ito, T. H., Luzo, Â. C. M. and Santana, M. H. A. (2016). In vitro performance of injectable chitosan-tripolyphosphate scaffolds combined with platelet-rich plasma. *Tissue Eng. Regen. Med.* 13, 21–30.

Shiojima, I. and Walsh, K. (2004). The Role of Vascular Endothelial Growth Factor in Restenosis. *Circulation* 110, 2283–2286.

Slevin, M., Kumar, S. and Gaffney, J. (2002). Angiogenic Oligosaccharides of Hyaluronan Induce Multiple Signaling Pathways Affecting Vascular Endothelial Cell Mitogenic and Wound Healing Responses. *J. Biol. Chem.* 277, 41046–41059.

Smith, J. K. (2018). IL-6 and the dysregulation of immune , bone , muscle , and metabolic homeostasis during space fl ight. *Nat. Partners Journals Microgravity* 1–8.

Smyth, M. J., Zachariae, C. C., Norihisa, Y., Ortaldo, J. R., Hishinuma, A. and Matsushimat, A. N. D. K. (1991). IL-8 gene expression and production in human peripheral blood lymphocyte subsets. *J. Immunol.* 146, 3815–3823.

Söderström, A. C., Nybo, M., Nielsen, C. and Vinholt, P. J. (2016). The effect of centrifugation speed and time on pre-analytical platelet activation. *Clin Chem Lab Med* 54, 1913–1920.

Spakova, T., Rosocha, J., Lacko, M., Harvanova, D. and Gharaibeh, A. (2012). Treatment of knee joint osteoarthritis with autologous platelet-rich plasma in comparison with hyaluronic acid. *Am. J. Phys. Med. Rehabil.* 91, 411–417.

Spooner, R. and Yilmaz, Ö. (2011). The role of reactive-oxygen-species in microbial persistence and inflammation. *Int. J. Mol. Sci.* 12, 334–352.

Sundman, E. A., Cole, B. J. and Fortier, L. A. (2011). Growth Factor and Catabolic Cytokine Concentrations Are Influenced by the Cellular Composition of Platelet-Rich Plasma. *Am. J. Sports Med.* 39, 2135–2140.

Tajima, S., Tobita, M., Orbay, H., Hyakusoku, H. and Mizuno, H. (2015). Direct and Indirect Effects of a Combination of Adipose-Derived Stem Cells and Platelet-Rich Plasma. *Tissue Eng. Part A* 21, 895–905.

Tamama, K. and Kerpedjieva, S. S. (2012). Acceleration of Wound Healing by Multiple Growth Factors and Cytokines Secreted from Multipotential Stromal Cells/Mesenchymal Stem Cells. *Adv. Wound Care* 1, 177–182.

Tanaka, E., Aoyama, Æ. J. and Miyauchi, Æ. M. (2005). Vascular endothelial growth factor plays an important autocrine/paracrine role in the progression of osteoarthritis. *Histochem. Cell Biol.* 123, 275–281.

Taub, D. D., Anver, M., Oppenheim, J. J., Longo, D. L. and Murphy, W. J. (1996). T lymphocyte recruitment by interleukin-8 (IL-8). IL-8-induced degranulation of neutrophils releases potent chemoattractants for human T lymphocytes both in vitro and in vivo. *J. Clin. Invest.* 97, 1931–1941.

Tayapongsak, P., Brien, D. A. O., Monteiro, B. and Arceo-diaz, L. Y. N. Y. (1994). Autologous Fibrin Adhesive in Mandibular Reconstruction With Particulate Cancellous Bone and Marrow. *J Oral Maxillofac Surg* 52, 161–165.

Tobita, M., Tajima, S. and Mizuno, H. (2015). Adipose tissue-derived mesenchymal stem cells and platelet-rich plasma: stem cell transplantation methods that enhance stemness. *Stem Cell Res. Ther.* 6, 1–7.

Vadalá, G., Russo, F., Musumeci, M., Este, M. D., Cattani, C., Catanzaro, G., Tirindelli, M. C., Lazzari, L., Alini, M., Giordano, R., et al. (2017). Clinically Relevant Hydrogel-Based on Hyaluronic Acid and Platelet Rich Plasma as a Carrier for Mesenchymal Stem Cells : Rheological and Biological Characterization. *J. Orthop. Res.* 1–8.

Van Pham, P., Bui, K. H.-T., Ngo, D. Q., Vu, N. B., Truong, N. H., Phan, N. L.-C., Le, D. M., Duong, T. D., Nguyen, T. D., Le, V. T., et al. (2013). Activated platelet-rich plasma improves adipose-derived stem cell transplantation efficiency in injured articular cartilage. *Stem Cell Res. Ther.* 4, 91.

Vischer, S., Fourmestraux, V. de and Turz, A. (2018). Technology rationale for the development of CellularMatrix ® A-CP-HA Kit, certified medical device allowing the combination of platelet rich plasma and hyaluronic acid for the treatment of osteoarthritis.

Int. J. Clin. Rheumtol. 13, 319–327.

Wang, L., Zhao, Y. and Shi, S. (2012). Interplay between mesenchymal stem cells and lymphocytes: implications for immunotherapy and tissue regeneration. *J. Dent. Res.* 91, 1003–10.

Wang, W., Rigueur, D. and Lyons, K. M. (2014). TGFβ signaling in cartilage development and maintenance. *Birth Defects Res. Part C - Embryo Today Rev.* 102, 37–51.

Wasterlain, A. S., Braun, H. J. and Dragoo, J. L. (2012). Contents and Formulations of Platelet-Rich Plasma. *Oper. Tech. Orthop.* 22, 33–42.

Waterman, R. S., Tomchuck, S. L., Henkle, S. L. and Betancourt, A. M. (2010). A New Mesenchymal Stem Cell (MSC) Paradigm : Polarization into a Pro-Inflammatory MSC1 or an Immunosuppressive MSC2 Phenotype. *PLoS One* 5,.

Weibrich, G., Kleis, D. D. S. W. K. G., Kunz-kostomanolakis, M., Loos, A. H. and Wagner, W. (2001). Correlation of Platelet Concentration in Platelet-rich Plasma to the Extraction Method , Age , Sex , and Platelet Count of the Donor. *Int. J. Oral Maxillofac. Implants* 693–699.

Weigelt, P. H., Fuller, G. M. and Leboeuf, R. D. (1986). A Model for the Role of Hyaluronic Acid and Fibrin in the Early Events during the Inflammatory Response and Wound Healing Department of Human Biological Chemistry and Genetics , University of Texas. *J. Theor. Biol.* 119, 219–234.

West, D. C., Hampson, I. N., Arnold, F. and Kumar, S. (1985). Angiogenesis Induced by Degradation Products of Hyaluronic Acid. *Science* 228, 1324–1326.

Wilgus, T. A., Roy, S. and McDaniel, J. C. (2013). Neutrophils and Wound Repair: Positive Actions and Negative Reactions. *Adv. Wound Care* 2, 379–388.

Wolberg, A. S. (2007). Thrombin generation and fibrin clot structure. *Blood Rev.* 21, 131–142.

Wu, S., Chen, C., Wang, J., Lin, Y., Chang, J. and Ho, M. (2018). Hyaluronan size alters chondrogenesis of adipose-derived stem cells via the CD44/ERK/SOX-9 pathway. *Acta Biomater.* 66, 224–237.

Xie, X., Wang, Y., Zhao, C., Guo, S., Liu, S., Jia, W., Tuan, R. S. and Zhang, C. (2012). Comparative evaluation of MSCs from bone marrow and adipose tissue seeded in PRP-derived scaffold for cartilage regeneration. *Biomaterials* 33, 7008–7018.

Xu, Z., Yin, W., Zhang, Y., Qi, X., Chen, Y., Xie, X. and Zhang, C. (2017). Comparative evaluation of leukocyte- and platelet-rich plasma and pure platelet-rich plasma for cartilage regeneration. *Sci. Rep.* 7, 43301.

Xu, X., Zheng, L., Yuan, Q., Zhen, G., Crane, J. L., Zhou, X. and Cao, X. (2018). Transforming growth factor-β in stem cells and tissue homeostasis. *Bone Res.* 6,.

Yan, L., Zheng, D. and Xu, R. (2018). Critical Role of Tumor Necrosis Factor Signaling in Mesenchymal Stem Cell-Based Therapy for Autoimmune and inflammatory Diseases. *Front. Immunol.* 9, 1–13.

Yaylaci, S. U., Sen, M., Bulut, O., Arslan, E., Guler, M. O. and Tekinay, A. B. (2016). Chondrogenic Differentiation of Mesenchymal Stem Cells on Glycosaminoglycan-Mimetic Peptide Nanofibers. *ACS Biomater. Sci. Eng.* 2,.

Yerlikaya, M., Çaliş, H. T., Sütbeyaz, S. T., Sayan, H., Ibiş, N., Koç, A. And karakükçü, Ç. (2018). Comparison of Effects of Leukocyte-Rich and Leukocyte-Poor Platelet-Rich Plasma on Pain and Functionality in Patients With Lateral Epicondylitis. *Arch. Rheumatol.* 33, 73–79.

Yeromonahos, C., Polack, B. and Caton, F. (2010). Nanostructure of the Fibrin Clot. *Biophys. J.* 99, 2018–2027.

Yin, W., Qi, X., Zhang, Y., Sheng, J., Xu, Z., Tao, S., Xie, X., Li, X. and Zhang, C. (2016). Advantages of pure platelet-rich plasma compared with leukocyte- and platelet-rich plasma in promoting repair of bone defects. *J. Transl. Med.* 14, 73.

Yu, W., Xu, P., Huang, G. and Liu, L. (2018). Clinical therapy of hyaluronic acid combined with platelet-rich plasma for the treatment of knee osteoarthritis. *Exp. Ther. Med.* 16,.

Zhang, Y., Heher, P., Hilborn, J., Redl, H. and Ossipov, D. A. (2016). Hyaluronic acid-fibrin interpenetrating double network hydrogel prepared in situ by orthogonal disulfide cross-linking reaction for biomedical applications. *Acta Biomater.* 38, 23–32.

Zhao, N., Wang, X., Qin, L., Guo, Z. and Li, D. (2015). Effect of molecular weight and concentration of hyaluronan on cell proliferation and osteogenic differentiation in vitro. *Biochem. Biophys. Res. Commun.* 465, 569–574.

Zhao, Q., Ren, H. and Han, Z. (2016). Mesenchymal stem cells: Immunomodulatory capability and clinical potential in immune diseases. *J. Cell. Immunother.* 2, 3–20.

Zhou, Y., Zhang, J., Wu, H., Hogan, M. V and Wang, J. H.-C. (2015). The differential effects of leukocyte-containing and pure platelet-rich plasma (PRP) on tendon stem/progenitor cells - implications of PRP application for the clinical treatment of tendon injuries. *Stem Cell Res. Ther.* 6, 173.

Zhu, Y., Yuan, M., Meng, H. Y., Wang, a Y., Guo, Q. Y., Wang, Y. and Peng, J. (2013). Basic science and clinical application of platelet-rich plasma for cartilage defects and

osteoarthritis : a review. *Osteoarthr. Cartil.* 21, 1627–1637.

Zhu, W., Cui, H., Boualam, B., Masood, F., Flynn, E., Rao, R. D., Zhang, Z. Y. and Zhang, L. G. (2018). 3D bioprinting mesenchymal stem cell-laden construct with core-shell nanospheres for cartilage tissue engineering. *Nanotechnology* 29, 2017–2019.

Zwerina, J., Redlich, K., Polzer, K., Joosten, L., Kro, G., Distler, J., Hess, A., Pundt, N., Pap, T., Hoffmann, O., et al. (2007). TNF-induced structural joint damage is mediated by IL-1. *Proc Natl Acad Sci USA* 104, 1–6.

APÊNDICE I

Artigo publicado no periódico *Applied Biochemistry and Biotechnology* (doi.org/10.1007/s12010-018-02935-6), referente ao trabalho preliminar realizado no início das atividades do doutorado.

Structural Modifications and Solution Behavior of Hyaluronic Acid Degraded with High pH and Temperature

Bruna Alice Gomes de Melo[1] & Maria Helena Andrade Santana[1]*

[1]Department of Engineering of Materials and Bioprocesses, School of Chemical Engineering, University of Campinas, P.O. Box 6066, 13083-852, Campinas, SP, Brazil.
*Correspondence should be addressed to mariahelena.santana@gmail.com

ABSTRACT

Hyaluronic acid (HA) is a macromolecule with valuable benefits over its range of molar masses (MM). Degradation studies are relevant to maintain the purity level of the original source, when HA of different MM are intended to be used in biomedical studies. We degraded HA via high pH and temperature and evaluated its MM, solution behavior and structure over time. After 24 hours, low MM HA was predominant, and the MM decreased from 753 to 36.2 kDa. Dynamic light scattering (DLS) showed a decrease in the number of HA populations, and solution tended to be less polydispersed. The zeta potential varied from -10 to -30 mV, close to the stable range. FTIR showed that the primary structure of HA was affected after only 48 hours of reaction. These results are relevant for the production of low MM HA to be used or mixed with high MM HA, generating structured biomaterials for biomedical applications.

Keywords: Hyaluronic acid; depolymerization; low molar mass; alkaline hydrolysis; thermal degradation.

1. Introduction

Hyaluronic acid (HA) is a glycosaminoglycan (GAG) that exists in a wide range of molar masses (MM) from < 10 to > 1000 kDa. It is a natural polysaccharide with repeated disaccharides containing one D-glucuronic acid and one n-acetyl-D-glucosamine, linked by β(1-3') and β(1'-4) binding. In nature, HA is found in mammalian skin, eye vitreous humor and the synovial fluid surrounding joints, promoting elasticity and lubrication (Garg and Hales, 2004). This property is due to the high MM (> 1000 kDa) of this HA (Lee and Cowman, 1994), which gives it a high viscoelasticity.

Low MM HA (< 100 kDa) is found *in vivo* as a product of polysaccharide degradation, mediated by the endoglycosidase hyaluronidase enzyme (Slevin et al., 2002). The result of this degradation, as observed by West et al. (West et al., 1985) is a series of mechanisms that lead to angiogenic activities. This evidence has raised many questions about the importance of low MM HA and oligo-HA in the healing process, increasing the number of works concerning the potential applications and use of LMM HA (Stern et al., 2006). However, this number is still not as expressive as that of studies involving high MM HA.

The stimulation of endothelial cell proliferation and migration (Sattar et al., 1992), the expression of inflammatory cytokines (Noble, 2002), and the production of different types of collagen (Rooney et al., 1993) gives low MM HA the ability to stimulate wound healing and tissue repair (Gao et al., 2010; Schlesinger and Powell, 2012; Shewale et al., 2017). In addition, it assumes a chondroprotective role by forming a layer around chondrocytes, preventing them from interacting with free radicals and metalloproteinases degradation (Ghosh and Guidolin, 2002). Their smaller molecules penetrate cartilage cavities that high MM HA are unable to, preserving chondrocyte integrity (Euppayo et al., 2015). Therefore, the use of mixed HA could be advantageous, as observed by Petrella et al. (Petrella et al., 2011), in which patients treated with a combination of high and low MM HA showed improvements in an osteoarthritis treatment.

Currently, commercial HA is available in different MM, with their production deriving from different sources such as microorganism fermentation and animal extraction. However, to obtain HA with a wide range of MM maintaining the same purity level, studies involving HA cleavage are becoming important.

Polysaccharide can be cleaved by different mechanisms using biological, chemical and physical agents (Stern et al., 2007). Biologically, HA is degraded by hyaluronidases enzymes,

as mentioned above, and provide fragments and products that occurs physiologically (Cardoso et al., 2016). The options for chemical and physical degradation are numerous and are the most used methods in the literature. HA can be cleaved hydrolytically, as shown by Tokita & Okamoto (Tokita and Okamoto, 1995) in pioneering work that elucidated the mechanisms for the acidic and alkaline hydrolysis of HA. Since then, other works have studied the effects of pH on HA degradation and rheological properties (Gatej et al., 2004; Maleki et al., 2008; Tømmeraas and Melander, 2008). HA can be degraded through exposition to reactive oxygen species, which are also responsible for its physiological depolymerization and occur from various pathways and sources, including exposition to ultraviolet (UV) light irradiation (Šoltés et al., 2006). In addition to these methods, the decrease of HA MM was observed after high temperature treatments (Caspersen et al., 2014; Mondek et al., 2015), ultrasonication (Dřímalová et al., 2005; Gura et al., 1998), ozone (Wu, 2012), electron bean (Choi et al., 2010), gamma ray and microwave irradiation (Chen et al., 2015). Simulescu et al. (Simulescu et al., 2016) reported that HA degraded only after being stored at room temperature for two months and observed that the lower the initial MM, the greater the degradation.

Concerning the quantification of HA MM, a very common and simple method is measuring the intrinsic viscosity ([η]) (Laurent et al., 1960; Sun et al., 2012), which assumed that HA has a coil configuration according to the Mark–Houwink–Kuhn–Sakurada equation. Currently, size exclusion chromatography, in tandem with multi-angle laser light scattering (SEC-MALLS), has been the most commonly used method to determine HA MM and its polymolecularity or polydispersity (Schiraldi et al., 2010).

In this work, we aimed to produce low MM HA from the larger polysaccharide in order to obtain HA of different MM useful for biomedical studies and HA formulations. In addition to the controlled degradation, the control of purity degree in high and low MM is extremely important for the mentioned applications. Here, we combined high temperature and high pH to cleave HA, two known methods for controlled degradation. As previously reported, at 60 ºC the chains scission can be assured, but only even higher temperatures provide faster degradation (Mondek et al., 2015). Similarly, HA degradation under alkaline condition is significant only at extreme pH (13) and long times, as verified by Maleki et al. (Maleki et al., 2008). Therefore, we intended to combine both methods, high temperature (60 ºC) and pH (12), to study HA degradation kinetics, aiming to optimize the time of low MM HA production. As mentioned above, Tokita & Okamoto (Tokita and Okamoto, 1995) first described the mechanisms for

hydrolytic cleavage of HA at 40 and 60 ºC, showing that the rate of degradation increased at the higher temperature.

The originally of this study consists in investigating the degradation of HA with high pH and temperature from the point of view of the decrease in its MM with time and of its colloidal behavior during the degradation process. Thus, we intended to present to the readers an in-depth view of the phenomena that occur in the system during degradation. For this, we used size exclusion chromatography (SEC) to obtain the MM distribution, and dynamic light scattering (DLS) techniques to evaluate the hydrodynamic diameter distribution, polydispersity index (PdI) and zeta potential of the entangled HA coils. Fourier transformed infrared (FTIR) spectroscopy was used to analyze the structure of the degraded HA over time.

2. Materials and Methods

2.1. Materials

HA (MM > 100 kDa) was purchased from Spec-Chem Ind. (Nanjing, China). All other reagents were purchased from Merck unless otherwise specified. Ultrapure water was used throughout all the experimental studies.

2.2. Determination of HA purity relative to the protein concentration

The purity of HA was calculated relative to the concentration of protein, as we previously reported (Cavalcanti et al., 2018). HA concentration was determined by the cetyltrimethylammonium bromide turbidimetric method (CTAB), as described by Chen & Wang (Chen and Wang, 2009). For protein quantification, it was used the Bicinchoninic acid (BCA) Protein Assay Kit, based on the method proposed by Smith et al. (Smith et al., 1985). Experiments were performed at 25 ºC. Percentage of purity was calculated according to the Equation 1. The experiment was performed in triplicate.

$$Purity\ (\%) = \frac{C_{HA}}{(C_{HA} + C_P)}.100 \qquad \textbf{Equation 1}$$

Where C_{HA} and C_P are the concentrations of the HA and soluble proteins, respectively.

2.3. HA cleavage by alkaline hydrolysis and temperature

To evaluate the effects of alkaline pH on HA cleavage, HA was dissolved in a pH 12 p*otassium chloride*/s*odium hydroxide* buffer to obtain a 2 mg/mL solution. The buffer was prepared by mixing the appropriated portions of 0.2 mol/L KCl and 0.2 mol/L NaOH. The solution was placed in mechanical agitation (500 rpm) in a water bath at 60 ºC, and aliquots were collected at different times: 0 (immediately after preparation) (HA-0), 1 (HA-1), 5 (HA-5), 8 (HA-8), 24 (HA-24), 48 (HA-48) and 72 hours (HA-72). HA prepared in phosphate-buffered saline (PBS), pH 7.4 was used as a control (HAc). Similar ionic strength was assured in all HA solutions.

2.4. Determination of HA MM

MM of the HAc and the degraded HA was determined by SEC in a Shimadzu chromatography system (Shimadzu Corporation, Kyoto, Japan), using a Polysep-GFC-P column guard (35 × 7.8 mm) (Phenomenex, Torrance, CA, USA) connected to a Poly-sep-GFC-P6000 gel filtration column (300 × 7.8 mm) (Phenomenex, Torrance, CA, USA). HA detection was performed by a Shimadzu RID-6A refractive index detector (Shimadzu Corporation, Kyoto, Japan). Samples were injected (20 µL) using 0.1 mol/L $NaNO_3$ as the mobile phase at a flow rate of 1 mL/min at 25 ºC. Dextran (American Polymer Standards corporation, Mentor, USA was used as an indirect standard to estimate HA MM, as previously reported (Balke et al., 1969; Pan et al., 2017; Pires and Eguchi, 2010). The experiment was performed in triplicate. Retention time of protein was previously determined by injecting soy protein in the equipment in order to exclude its interference in the chromatogram (Cavalcanti et al., 2018).

2.5. Viscosity measurements

The viscosities of the control and degraded samples were measured at 25 ºC using a A&D Vibro Viscometer SV-10 (A&D Company, Tokyo, Japan), by detecting the driving electric current of the solutions at constant frequency of 30 Hz and amplitude < 1 mm.

2.6. Hydrodynamic diameter, polydispersity (PdI) and zeta potential measurements

The DLS technique was used to measure the hydrodynamic diameter, PdI and zeta potential of the HAc and the degraded HA, in an Autosizer 4700, Zetasizer Nano (Malvern Instruments, Malvern, UK) at 25 ºC.The equipment measured each sample ten times.

2.7. FTIR analysis

Samples were lyophilized in a lyophilizer L-101 (Liotop, São Carlos, Brazil) for three days. FTIR analyses of the solid HA were performed in a Thermo Scientific Nicolet 6700 spectrophotometer (Thermo Fisher Scientific, Madison, USA), using the single-reflection germanium attenuated total reflection (*ATR*) technique, in a *Smart OMNI-Sampler* (Thermo Fisher Scientific, Madison, USA). The wavelength range of the performance was 4000 - 750 cm^{-1} with a resolution of 4 cm^{-1}.

2.8. Statistical Analysis

Data were expressed as the mean ± SD obtained from three independent experiments. When relevant, one-way analysis of variance (ANOVA) with Tukey's Test was used for statistical analysis. A 95% confidence level was considered significant ($p \leq 0.05$).

3. Results and Discussion

3.1. Distribution of HA MM with time reaction

Purity of HA was calculated relative to the concentration of protein (0.154 ± 0.03 mg/mL), being 92.5 ± 1.2%. The chromatograms of the control and aliquots from different reaction times are presented in Fig. 1 and exhibit an elongated HA peak, between 7 and 10 minutes for HAc. This peak comprises the presence of three ranges of MM, as determined using dextran standards (Pires and Santana, 2011) corresponding to 34.8 ± 1.4% of HA 1000 kDa, 61.2 ± 1.5% of HA 100 kDa and 4.0 ± 0.1% of HA 10 kDa. After approximately 11 minutes, we observed a weak peak related to the presence of small amounts of protein.

By dissolving HA in the pH 12 buffer, we observed a progressive degradation over time. For sample HA-0, there was a slight displacement of the HA peak to the right, indicating a decrease in the HA with a higher MM. Under high temperature and after 1 hour of reaction (HA-1), the displacement of the HA peak became more pronounced, whereas the protein peak increased in intensity. This was likely due to the formation of low MM HA and other fragments whose retention time is located in the same region as the proteins, causing an overlapping of the peaks. This overlapping became more intense after 24 hours of reaction (HA-24 to HA-72), where the presence of the HA of 1000 and 100 kDa was practically nonexistent, allowing low MM HA to dominate.

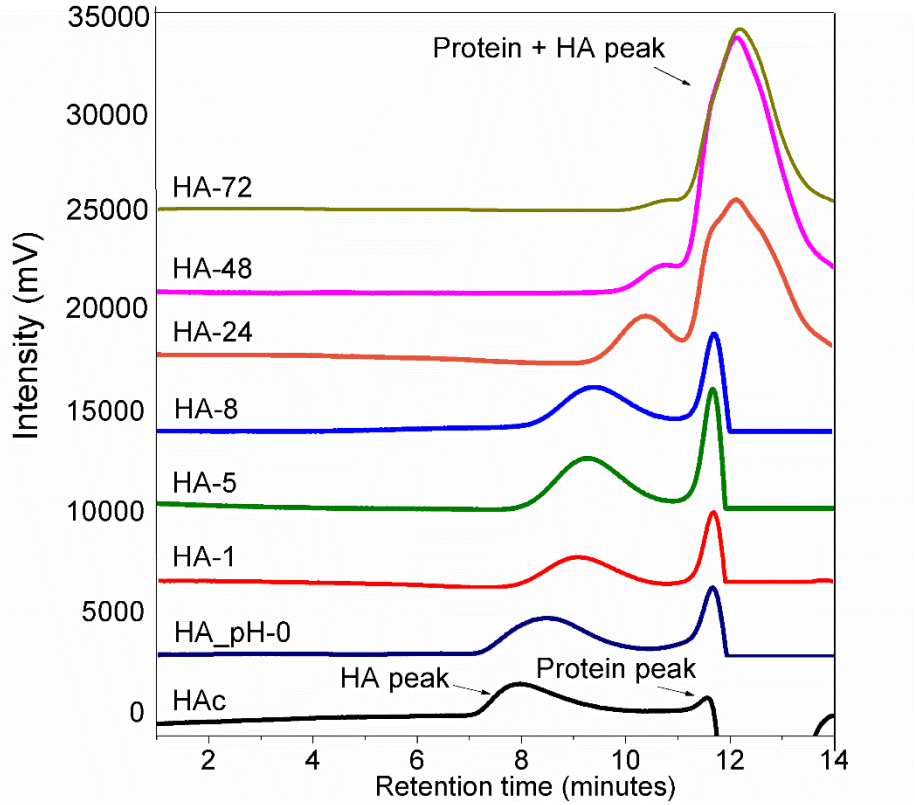

Fig. 1. Chromatograms of the HAc (pH 7.4, 25 ºC), HA degraded at pH 12 and 25 ºC (HA-0), and HA degraded at pH 12 and 60 ºC under mechanical agitation for 1 (HA-1), 5 (HA-5), 8 (HA-8), 24 (HA-24), 48 (HA-48) and 72 hours (HA-72) were obtained from the SEC analysis, showing the displacement of HA peaks with reaction time, which indicates the decrease of its MM.

The quantitative data of the HA MM distribution is shown in Fig. 2. Significant changes were observed in the first hour of reaction, with high MM HA showing a fast degradation, and decreasing its content from 19.6 ± 1.9% to 3.1 ± 2.3%, while intermediate MM HA decreased

from 74.3 ± 0.1% to 63.3 ± 6.5%, and low MM HA increased from 6.1 ± 1.8 to 16.9 ± 4.1%. After 8 hours, the amount of 100 kDa HA decreased to 43.9 ± 7.7% at the same time that the low MM HA percentage increased to 54.4 ± 11.2%. Therefore, 8 hours was the reaction time where we obtained a sample with almost equal portions of HA with the two different MM types. After 24 hours, no significant changes in the high, intermediate and high MM HA were observed.

It was observed that MM decreased when HA was in alkaline pH, from 753.2 ± 132.3 kDa (HAc) to 597.7 ± 60.0 (HA-0), however a more significant change was obtained after 1 hour of reaction at 60 ºC, with MM decreasing to 43.1 ± 1.1 kDa (HA-1) and reaching 25.4 ± 2.6 kDa after 72 hours (HA-72), as shown in Table 1. These results evidenced the positive effect of high temperature on a faster alkaline degradation of HA molecules. Therefore, combination of pH 12 and 60 ºC provided a synergistic effect of hydrolytic and thermal degradation, resulting in an irreversible change in the HA MM fractions, which was more expressive than the isolated effects of pH or temperature as usually reported in the literature (Reháková et al., 1994).

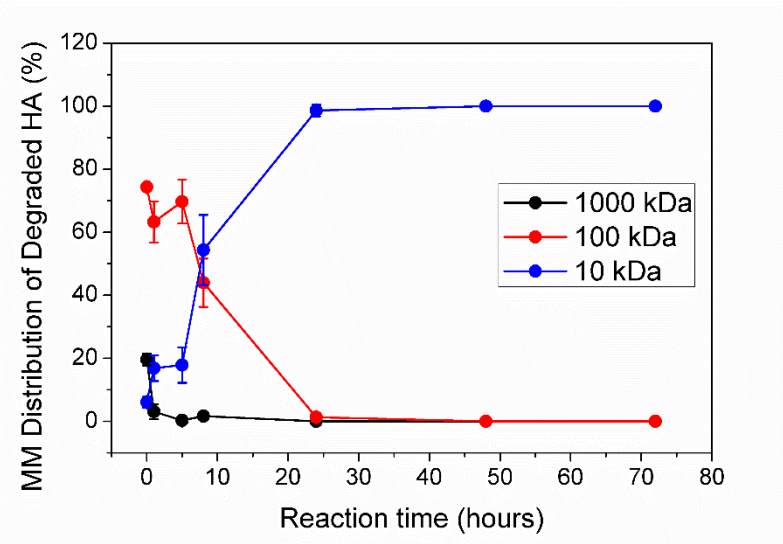

Fig. 2. Degradation kinetics of HA and its MM distribution, calculated from the SEC analysis. High and intermediate MM HA percentage decreased with time, whereas low MM HA increased, reaching the equilibrium in 24 hours of reaction.

Table 1. Average MM of HAc (pH 7.4, 25ºC), HA degraded at pH 12 and 25 ºC (HA-0), and HA degraded at pH 12 and 60 ºC under mechanical agitation for 1 (HA-1), 5 (HA-5), 8 (HA-

8), 24 (HA-24), 48 (HA-48) and 72 hours (HA-72). Values were calculated from the SEC analysis.

Condition	MM (kDa)
HAc	753.2 ± 132.3
HA-0	597.7 ± 60.0
HA-1	43.1 ± 1.1
HA-5	41.5 ± 18.4
HA-8	36.2 ± 5.6
HA-24	36.2 ± 2.7
HA-48	36.3 ± 14.6
HA-72	25.4 ± 2.6

According to Morris et al. (Morris et al., 1980), an alkaline condition results in reversible decrease in viscosity, suggesting a non-covalent breakage of chains due to the reduction of intramolecular H-bonds. This was observed by Maleki et al. (Maleki et al., 2008), which studied the effects of a wide range of pH values on HA structure, varying from 1 to 13, and observed that after 24 hours of reaction, only at the extreme pH values (1 and 13) an irreversible degradation occurred, especially at pH 13. Here, results strongly suggest the irreversible cleavage of HA chains, due to the synergistic effect of pH 12 and 60 ºC, once both viscosity and MM significantly decreased after 1 hour of reaction.

3.2. Effects of time reaction on HA viscosity

Viscosity is proportional to polymer's MM due to the physical crosslinking from the entanglement of their chains (Gura et al., 1998). However, degradation is a kinetic process with initial and intermediate steps that do not affects MM immediately. As observed by Gatej et al. (Gatej et al., 2004), even for a large decrease in the viscosity of the HA solution at pH to 12.6, the MM was only slightly changed. From these results, the authors concluded that a reversible decrease in HA stiffness occurred, due to intra and intermolecular cleavage of the hydrogen bonds (Ghosh et al., 1993; Morris et al., 1980). Here, results showed the reversible behavior of HA-0, followed by an irreversible chains cleavage from 1 hour of reaction at pH 12 and 60 ºC,

with viscosity dropping to to 1.15 ± 0.01 mPa.s, and stabilizing in 24 hours around 1 mPa.s (Fig. 3), presenting viscosity values similar to that of water (Bothner and Waaler, 1988).

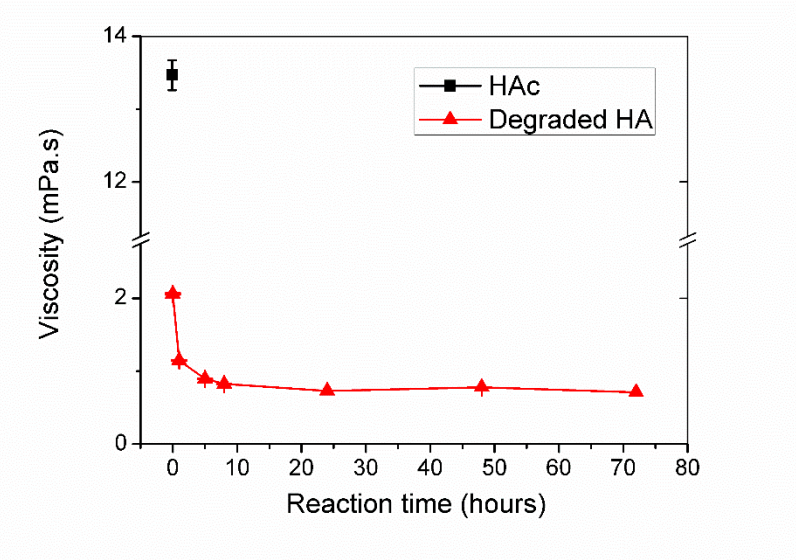

Fig. 3. Viscosity of the of HAc (pH 7.4, 25ºC), HA degraded at pH 12 and 25 ºC (HA-0), and HA degraded at pH 12 and 60 ºC under mechanical agitation for 1 (HA-1), 5 (HA-5), 8 (HA-8), 24 (HA-24), 48 (HA-48) and 72 hours (HA-72), measured at 25 ºC.

3.3. Hydrodynamic diameter distribution, polydispersity and zeta potential of the HA

In solutions with concentration above 1 mg/mL, HA randomly entangles forming elongated coil structures (Laurent et al., 1996). By DLS technique, we verified the hydrodynamic diameter of these entanglements using the intensity distribution (Fig. 4), which is proportional to the diameter to the sixth power ($I \alpha d^6$).

Figure 4A (i) shows the diameter distribution of the control (HAc), where we observed a large variety of populations, from 1 to 5,000 nm, which is likely due to the presence of HA with different MM, as shown in Section 3.1, and added to the random aggregation of the coils. The PdI value corroborates this result, which is close to 1 (0.88 ± 0.04), indicating the sample was highly polydispersed (Fig. 4C).

HA in the alkaline medium is shown in Figs. 4A (ii) and (iii). From time zero, we observed a restructuration of the coil entanglements, probably due to the effects of the hydrogen bond cleavage. According to Ghosh et al. (Ghosh et al., 1993), this cleavage leads to a contraction of the coils, which would result in a size decrease. Here, we observed that the 5,000 nm population in HAc is not present, indicating that they may have contracted and formed

smaller structures. At the same time, the 1 and 5 nm populations were also not observed, likely due to aggregation. Figure 4A (ii) shows a more organized environment, with the presence of only two populations of 10-50 nm and 100-400 nm, resulting in a decrease of PdI of almost 2-fold, corresponding to 0.48 ± 0.05 for HA-0, 0.38 ± 0.05 for HA-1, 0.42 ± 0.02 for HA-5, 0.51 ± 0.05 for HA-8, 0.48 ± 0.04 for HA-24, and 0.52 ± 0.01 for HA-48 (Fig. 4C).

The hydrodynamic diameter distribution of HA-72 is shown in Fig. 4A (iii). Different from the lower reaction times, we observed only one large peak for the population with a 100 nm mean diameter. Similar to the sample HA-48, there was a complete degradation of the high and intermediate MM HA, forming HA of 10 kDa. However, after only 72 hours, the coils seem to have self-organized into one entanglement, which decreased the PdI to 0.29 ± 0.02 (Fig. 4C).

When in a neutral solution, the carboxyl groups of the HA are deprotonated, which leads to electrostatic repulsion, favoring the formation of structures with coils that are distant from each other and have a high level of hydration (Lapčík et al., 1998; Scott and Heatley, 1999). With the increase of pH, the net HA charge increases, which contributes to the destabilization of the hydrogen bond network and causes aggregation (Gatej et al., 2004), as observed in Section 3.3.

To evaluate variations in the HA net charge, we analyzed the zeta potential of the samples. Zeta potential is commonly used to evaluate ionic charge exposition and to estimate colloidal stability by electrostatic repulsion, preventing aggregation. Therefore, recommended levels of zeta potential for long-term stability are higher than 30 mV or lower than -30 mV (Hunter et al., 1981). Zeta potential is a valuable parameter for understanding HA behavior in solution and determining stability after degradation. However, few works in the literature describe results from this analysis. Mondek et al. (Mondek et al., 2015) observed that after 12 hours at 60 ºC, the zeta potential of HA changed only slightly and remained below -30 mV, which is stable and resistant to aggregation.

For our control, i.e., pH 7.4, the zeta potential was -31.4 ± 5.0 mV, within the stable range, due to the polyanionic character of HA in neutral medium. The results for the diameter distribution exhibited an aggregation of entanglements in the alkaline medium, which was likely due to the structural changes during the degradation process. This is corroborated by our zeta potential values, which tended to increase from 0 (-18.3 ± 3.1 mV) to 48 hours (-14.3 ± 5.8 mV) during the initial and intermediate steps of degradation, resulting in changes of conformation and less exposition of the COO^- groups. After 48 hours of reaction, the intermediate structures were modified due to the completely chains scission and more

exposition of COO^- groups, resulting in a decrease in the zeta potential to -27.2 ± 1.7 mV for HA-72 (Fig. 4B) (Mondek et al., 2015). These structures were electrostatically stable coils of 100 to 1000 nm with low PdI (Fig. 4C).

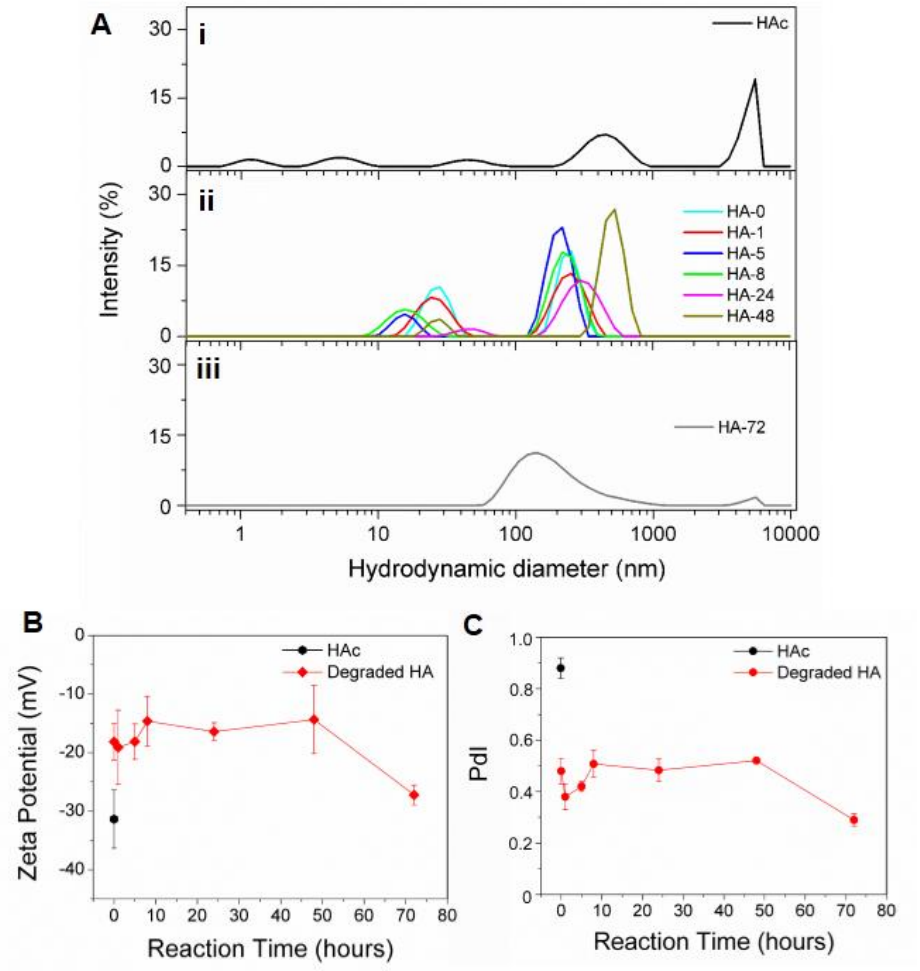

Fig. 4. (A) Intensity distribution of the hydrodynamic diameter of (i) HAc (pH 7.4, 25 ºC), (ii) HA degraded at pH 12 and 25 ºC (HA-0), and HA degraded at pH 12 and 60 ºC for 1 (HA-1), 5 (HA-5), 8 (HA-8), 24 (HA-24) and 48 hours (HA-48) and (iii) HA degraded at 72 hours (HA-72). (B) zeta potential and (C) PdI of HAc and degraded HAs. Results were obtained from DLS analysis at 25 ºC for 0 to 48 hours, (C) HA-72, (D) PdI and (E) zeta potential values of all the samples.

3.4. FTIR analysis

After investigating the effects of pH, temperature and reaction time on the MM distribution and HA entanglement behavior in solution, we performed an FTIR analysis to more

accurately investigate the changes in the HA structure. Figure 5 shows the spectra of HAc and the degraded samples. The transmission bands were interpreted according to Günzler & Gremlich (Günzler and Gremlich, 2002).

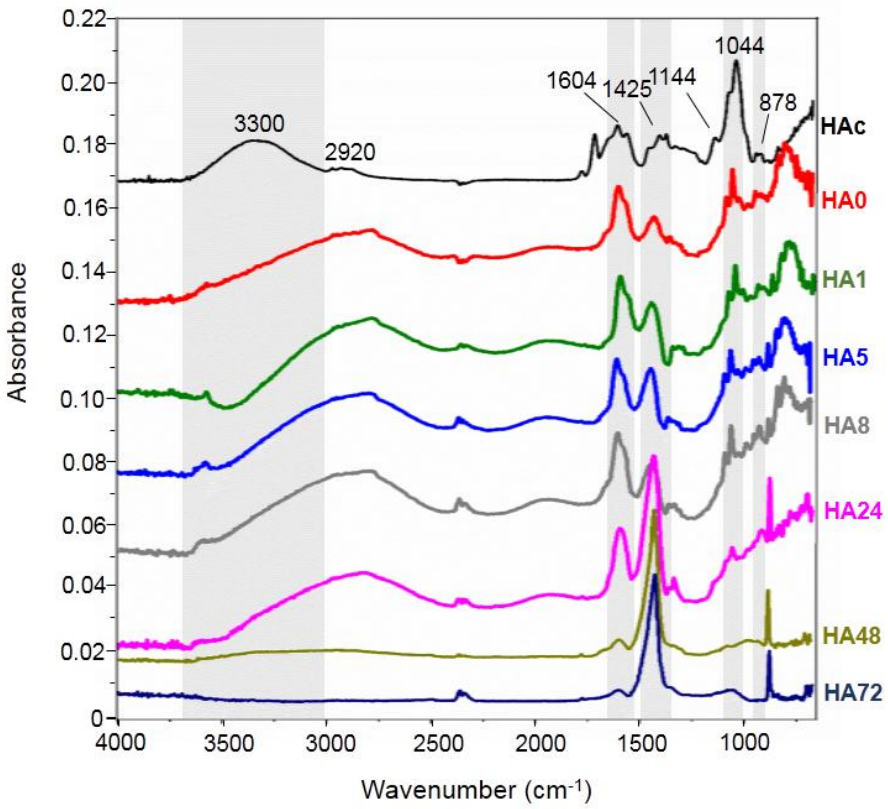

Fig. 5. FTIR spectra of the of HAc (pH 7.4, 25ºC), HA degraded at pH 12 and 25 ºC (HA-0) and HA degraded at pH 12 and 60 ºC for 1 (HA-1), 5 (HA-5), 8 (HA-8), 24 (HA-24), 48 (HA-48) and 72 hours (HA-72). The main peaks are highlighted to a better visualization of the displacements and intensities changes caused by degradation. Data were vertically shifted to avoid overlapping.

For the control, it was observed characteristic bands of HA (Gilli et al., 1994), as also observed by Choi et al. (Choi et al., 2010), in which HA purity was around 95%, a similar level to that used in this work. Here, we observed a large peak from 3600 to 3000 cm^{-1}, which is characteristic of the O-H stretching band of aqueous solutions, and of C-O and N-H HA stretching bands. A less intense peak was observed at 2904 cm^{-1}, corresponding to the C-H vibration. At a high pH for samples HA-0 to HA-24, there was a displacement of the hydroxyl peak to a lower wavenumber, overlapping the alkane band. This displacement suggests the

formation of strong O-H bonds between the water molecules and Na^+ cations (Madejová, 2003). For sample HA-48, the intensity of this large peak significantly decreased, and for HA-72, it was nonexistent, showing that long periods in high pH conditions may have caused modifications to the primary structure of the HA molecules.

At 1604 cm^{-1}, we observed the peak corresponding to the C=O stretching band of the amide, which decreased in intensity after 48 hours of reaction. At 1425 cm^{-1}, the peak of the carboxyl C-O streching band significantly increased with time, indicating the formation of carboxylic acid groups during degradation. The shoulder at 1144 cm^{-1} in the control is attributted to the C-O-C stretching band, and the peak at 1042.49 cm^{-1} was assigned to C-C-O stretching, which significantly decreased in the HA at an alkaline pH. Finally, at 878 cm^{-1}, we observed a peak in the degraded samples that became more intense after 24 hours, corresponding to out-of-ring deformations (C-O-H, C-C-H and O-C-H). The results obtained from the FTIR analysis showed that time strongly affected the HA primary structure, indicating that to obtain low MM HA under the conditions used in this work without compromising the molecule, the reaction time should be no longer than 24 hours.

4. Conclusions

HA progressively degraded with time when dissolved in an alkaline buffer at high temperature. The results showed that after 8 hours of reaction, low MM HA dominated, being the only HA present in solution after 2 days. We observed that the viscosity sharply decreased initially. From the MM distribution, we concluded that this rheological parameter did not vary only with the decrease of MM but also due to the intra and intermolecular cleavage of the hydrogen bonds. This cleavage resulted in structural changes and a reorganization of coils entanglements, as observed in the hydrodynamic diameter distribution, which contributed to a less polydispersed solution. The zeta potential indicated that the lower the polydispersity, the more stable the HA entanglements tended to be. Finally, from FTIR analyses, we verified that the primary structures of the HA may have been compromised by the degradation processes after only 48 hours. In this work, we showed the synergistic effect of high temperature and pH on a fast degradation of HA, producing low MM HA with low polydispersity that was stable with respect to aggregation. This method could be used for the fabrication of HA of different MM that would maintain the same level of purity and could be applied on medical,

pharmaceutical and cosmetic studies. Further studies should focus on the degradation kinetics of HA using different pH and temperatures.

Acknowledgements

The authors acknowledge the financial support of Fapesp (São Paulo Research Foundation), grant # 2015/23134-8 and 2016/10132-0.

Compliance with Ethical Standards

Conflicts of Interest

The authors declare no conflicts of interest.

References

Balke, S. T., Hamielec, A. E., Leclair, B. P. and Pearce, S. L. (1969). GEL PERMEATION CHROMATOGRAPHY: Calibration Curve from Polydisperse Standards. *I EC Prod. Res. Dev.* 8, 54–57.

Bothner, H. and Waaler, T. (1988). Limiting viscosity number and weight average molecular weight of hyaluronate samples produced by heat degradation. *Int. J. Biol. Macromol.* 10, 287–291.

Cardoso, M. J., Caridade, S. G., Costa, R. R. and Mano, J. F. (2016). Enzymatic Degradation of Polysaccharide-Based Layer-by-Layer Structures. *Biomacromolecules* 17, 1347–1357.

Caspersen, M. B., Roubroeks, J. P., Liu, Q., Huang, S., Fogh, J., Zhao, R. and Tømmeraas, K. (2014). Thermal degradation and stability of sodium hyaluronate in solid state. *Carbohydr. Polym.* 107, 25–30.

Cavalcanti, A. D. D., Melo, B. A. G. and Oliveira, R. C. (2018). Recovery and Purity of High Molar Mass Bio-hyaluronic Acid Via Precipitation Strategies Modulated by pH and Sodium Chloride. *Appl. Biochem. Biotechnol.*

Chen, Y. H. and Wang, Q. (2009). Establishment of CTAB Turbidimetric method to determine hyaluronic acid content in fermentation broth. *Carbohydr. Polym.* 78, 178–181.

Chen, S., Chen, H., Gao, R., Li, L., Yang, X., Wu, Y. and Hu, X. (2015). Degradation of

hyaluronic acid derived from tilapia eyeballs by a combinatorial method of microwave, hydrogen peroxide, and ascorbic acid. *Polym. Degrad. Stab.* 112, 117–121.

Choi, J. il, Kim, J. K., Kim, J. H., Kweon, D. K. and Lee, J. W. (2010). Degradation of hyaluronic acid powder by electron beam irradiation, gamma ray irradiation, microwave irradiation and thermal treatment: A comparative study. *Carbohydr. Polym.* 79, 1080–1085.

Dřímalová, E., Velebný, V., Sasinková, V., Hromádková, Z. and Ebringerová, A. (2005). Degradation of hyaluronan by ultrasonication in comparison to microwave and conventional heating. *Carbohydr. Polym.* 61, 420–426.

Euppayo, T., Siengdee, P., Buddhachat, K., Pradit, W., Viriyakhasem, N., Chomdej, S., Ongchai, S., Harada, Y. and Nganvogpanit, K. (2015). Effects of low molecular weight hyaluronan combined with carprofen on canine osteoarthritis articular chondrocytes and cartilage explants in vitro. *In Vitro Cell. Dev. Biol. Anim.* 51, 857–865.

Gao, F., Liu, Y., He, Y., Yang, C., Wang, Y., Shi, X. and Wei, G. (2010). Hyaluronan oligosaccharides promote excisional wound healing through enhanced angiogenesis. *Matrix Biol.* 29, 107–116.

Garg, H. G. and Hales, C. A. (2004). *Chemistry and Biology of Hyaluronan*. Elsevier.

Gatej, I., Popa, M. and Rinaudo, M. (2004). Role of the pH on hyaluronan behavior in aqueous solution. *Biomacromolecules* 6, 61–7.

Ghosh, P. and Guidolin, D. (2002). Potential Mechanism of Action of Intra-articular Hyaluronan Therapy in Osteoarthritis : Are the Effects Molecular Weight Dependent ? *Semin. Arthritis Rheum.* 32, 10–37.

Ghosh, S., Kobal, I., Zanette, D. and Reed, W. F. (1993). Conformational Contraction and Hydrolysis of Hyaluronate in Sodium Hydroxide Solutions. *Macromolecules* 26, 4685–4693.

Gilli, R., Kacuráková, M., Mathlouthi, M., Navarini, L. and Paoletti, S. (1994). FTIR studies of sodium hyaluronate and its oligomers in the amorphous solid phase and in aqueous solution. *Carbohydr. Res.* 263, 315–326.

Günzler, H. and Gremlich, H.-U. (2002). *IR Spectroscopy: An Introduction*. Wiley-VCH.

Gura, E., Hückel, M. and Müller, P.-J. (1998). Specific degradation of hyaluronic acid and its rheological properties. *Polym. Degrad. Stab.* 59, 297–302.

Hunter, R. J., Ottewill, R. H. and Rowell, R. L. (1981). *Zeta Potential in Colloid Science*. 3rd ed. Academic Press.

Lapčík, L., Lapčík, L., De Smedt, S., Demeester, J. and Chabreček, P. (1998). Hyaluronan: Preparation, Structure, Properties, and Applications †. *Chem. Rev.* 98, 2663–2684.

Laurent, T. C., Ryan, M. and Pietruszkiewicz, A. (1960). Fractionation of Hyaluronic Acid. The Polydispersity of Hyaluronic Acid from the Bovine Vitreous Body. *Biochim. Biophys. Acta - Mol. Cell Res.* 42, 476–485.

Laurent, T. C., Laurent, U. B. and Fraser, J. R. E. (1996). The structure and function of hyaluronan: An overview. *Immunol. Cell Biol.* 74, A1–A7.

Lee, H. G. and Cowman, M. K. (1994). An agarose gel electrophoretic method for analysis of hyaluronan molecular weight distribution. *Anal.Biochem.* 219, 278–287.

Madejová, J. (2003). FTIR Technique in clay mineral studies. *Vib. Spectrosc.* 31, 1–10.

Maleki, A., Kjøniksen, A. L. and Nyström, B. (2008). Effect of pH on the behavior of hyaluronic acid in dilute and semidilute aqueous solutions. *Macromol. Symp.* 274, 131–140.

Mondek, J., Kalina, M., Simulescu, V. and Pekař, M. (2015). Thermal degradation of high molar mass hyaluronan in solution and in powder; comparison with BSA. *Polym. Degrad. Stab.* 120, 107–113.

Morris, E. R., Rees, D. A. and Welsh, E. J. (1980). Conformation and Dynamic Interactions in Hyaluronate Solutions. *J. Mol. Biol.* 138, 383–400.

Noble, P. W. (2002). Hyaluronan and its catabolic products in tissue injury and repair. *Matrix Biol.* 21, 25–29.

Pan, N. C., Cristina, H., Pereira, B., Lourdes, M. De, Flora, A., Vasconcelos, D., Antonia, M. and Colabone, P. (2017). Improvement Production of Hyaluronic Acid by Streptococcus zooepidemicus in Sugarcane Molasses. *Appl. Biochem. Biotechnol.* 182, 276–293.

Petrella, R. J., Decaria, J. and Petrella, M. J. (2011). Long term efficacy and safety of a combined low and high of osteoarthritis of the knee. *Rheumatol. Reports* 3,.

Pires, A. M. B. and Eguchi, S. Y. (2010). The Influence of Mineral Ions on the Microbial Production and Molecular Weight of Hyaluronic Acid. *Appl. Biochem. Biotechnol.* 162,

2125–2135.

Pires, A. M. B. and Santana, M. H. A. (2011). Rheological aspects of microbial hyaluronic acid. *J. Appl. Polym. Sci.* 122, 126–133.

Reháková, M., Bakoš, D., Soldán, M. and Vizárová, K. (1994). Depolymerization reactions of hyaluronic acid in solution. *Int. J. Biol. Macromol.* 16, 121–124.

Rooney, P., Wang, M., Kumar, P. and Kumar, S. (1993). Angiogenic oligosaccharides of hyaluronan enhance the production of collagens by endothelial cells. *J. Cell Sci.* 105 (Pt 1, 213–8.

Sattar, A., Kumar, S. and West, D. C. (1992). Does Hyaluronan have a role in endothelial cell proliferation of the synovium? *Semin. Arthritis Rheum.* 22, 37–43.

Schiraldi, C., Andreozzi, L., Marzaioli, I., Vinciguerra, S., D'Avino, A., Volpe, F., Panariello, A. and De Rosa, M. (2010). Hyaluronic acid degradation during initial steps of downstream processing. *Biocatal. Biotransformation* 28, 83–89.

Schlesinger, T. and Powell, C. R. (2012). Efficacy and Safety of a Low-Molecular Weight Hyaluronic Acid Topical Gel in the Treatment of Facial Seborrheic Dermatitis Final Report. *J. Clin. Aesthetic Dermatology* 7, 15–18.

Scott, J. E. and Heatley, F. (1999). Hyaluronan forms specific stable tertiary structures in aqueous solution: A 13 C NMR study. *Biochemistry* 96, 4850–4855.

Shewale, A. R., Barnes, C. L., Fischbach, L. A., Ounpraseuth, S., Painter, J. T. and Martin, B. C. (2017). Comparative effectiveness of low, moderate and high molecular weight hyaluronic acid injections in delaying time to knee surgery. *J. Arthroplasty* 32, 2952–2957.

Simulescu, V., Kalina, M., Mondek, J. and Pekař, M. (2016). Long-term degradation study of hyaluronic acid in aqueous solutions without protection against microorganisms. *Carbohydr. Polym.* 137, 664–668.

Slevin, M., Kumar, S. and Gaffney, J. (2002). Angiogenic Oligosaccharides of Hyaluronan Induce Multiple Signaling Pathways Affecting Vascular Endothelial Cell Mitogenic and Wound Healing Responses. *J. Biol. Chem.* 277, 41046–41059.

Smith, P. K., Krohn, R. I., Hermanson, G. T., Mallia, A. K., Gartner, F. H., Provenzano, M. D., Fujimoto, E. K., Goeke, N. M., Olson, B. J. and Klenk, D. . (1985). Measurement of protein using bicinchoninic acid.pdf. *Anal. Chem.* 150, 76–85.

Šoltés, L., Mendichi, R., Kogan, G., Schiller, J., Stankovská, M. and Arnhold, J. (2006). Degradative action of reactive oxygen species on hyaluronan. *Biomacromolecules* 7, 659–668.

Stern, R., Asari, A. a. and Sugahara, K. N. (2006). Hyaluronan fragments: An information-rich system. *Eur. J. Cell Biol.* 85, 699–715.

Stern, R., Kogan, G., Jedrzejas, M. J. and Šoltés, L. (2007). The many ways to cleave hyaluronan. *Biotechnol. Adv.* 25, 537–557.

Sun, J., Wang, M., Chen, Y., Shang, F., Ye, H. and Tan, T. (2012). Understanding the Influence of Phosphatidylcholine on the Molecular Weight of Hyaluronic Acid Synthesized by Streptococcus zooepidemicus. *Appl. Biochem. Biotechnol.* 168, 47–57.

Tokita, Y. and Okamoto, A. (1995). Hydrolytic degradation of hyaluronic. *Polym. Degrad. Stab.* 48, 269–273.

Tømmeraas, K. and Melander, C. (2008). Kinetics of hyaluronan hydrolysis in acidic solution at various pH values. *Biomacromolecules* 9, 1535–1540.

West, D. C., Hampson, I. N., Arnold, F. and Kumar, S. (1985). Angiogenesis Induced by Degradation Products of Hyaluronic Acid. *Science* 228, 1324–1326.

Wu, Y. (2012). Preparation of low-molecular-weight hyaluronic acid by ozone treatment. *Carbohydr. Polym.* 89, 709–712.

APÊNDICE II

Artigo submetido para publicação no periódico *Advanced Functional Materials* (Manuscript number adfm.201901892), referente ao trabalho realizado durante o doutorado sanduíche na Harvard Medical School/Brigham and Women's Hospital, sob supervisão da Dra. Su Ryon Shin.

3D Printed Cartilage with Spatially Controlled Mechanical Properties to Mimic Native Cartilage Matrix Organization

Bruna A. G. de Melo[1,2], Shreya Mehrotra[1,3], Michelle A. Calabrese[4], Yasamin A. Jodat[1,5], Biman B. Mandal[3], Maria H. A. Santana[2], Eben Alsberg[6], Jeroen Leijten[7*], Su Ryon Shin[1*]

[1]Division of Engineering in Medicine, Department of Medicine, Harvard Medical School, Brigham and Women's Hospital, Cambridge, MA 02139, USA.
[2]Department of Engineering of Materials and Bioprocesses, School of Chemical Engineering, University of Campinas, Campinas, SP 13083-852, Brazil.
[3]Department of Biosciences and Bioengineering, Indian Institute of Technology Guwahati, Guwahati, 781039, India.
[4]Department of Chemical Engineering, Massachusetts Institute of Technology, Cambridge, MA 02139, USA.
[5]Department of Mechanical Engineering, Stevens Institute of Technology, Hoboken, NJ, 07030, USA.
[6]Departments of Bioengineering and Orthopaedics, University of Illinois, Chicago, IL 60607, USA.
[7]Department of Developmental BioEngineering, University of Twente, Enschede, Overijssel, 7522 NB, The Netherlands

[*] S.R. Shin and J. Leijten contributed equally as corresponding authors.
[*]E-mail: sshin4@bwh.harvard.edu
[*]E-mail: jeroen.leijten@utwente.nl

ABSTRACT

Developing biomimetic cartilaginous tissues that support locomotion while maintaining chondrogenic behavior is a major challenge in the tissue engineering field. Specifically, while locomotive forces demand tissues with strong mechanical properties, chondrogenesis of encapsulated cells requires a soft microenvironment. To address this challenge, three-dimensional (3D) cartilage-like tissue was bioprinted using two biomaterials with different mechanical properties: a hard biomaterial to reflect the macro-mechanical properties of native cartilage, and a soft biomaterial to create a chondrogenic microenvironment. To this end, a hard biomaterial (MPa order compressive modulus) composed of an interpenetrating polymer network (IPN) of polyethylene glycol (PEG) and alginate hydrogel was developed as an extracellular matrix (ECM) mimicking support bath with self-healing properties. Within this bath supplemented with thrombin, fibrinogen containing human mesenchymal stem cell (hMSCs) spheroids was bioprinted forming fibrin, as the soft biomaterial (kPa order compressive modulus) to mimic cartilage's pericellular matrix. The hMSC spheroids printed within the hard hydrogel showed improved viability and chondrogenic behavior without adversely affecting the macromechanical properties of the tissue. Therefore, the ability to print locally soft and cell stimulating microenvironments inside of a mechanically robust hydrogel was demonstrated, thereby uncoupling the micro and macro-mechanical properties of the 3D printed tissues such as cartilage.

Keywords: Cartilage; bioprinting; spheroids; fibrin; IPN.

1. Introduction

Articular cartilage has a limited capacity of self-repair, resulting in currently incurable degenerative joint diseases that affect millions of people around the world (Klein et al., 2009). Consequently, the engineering of cartilage-like tissue constructs that possess chondrogenic and mechanical properties similar to those of native tissue represents a promising tool for effective cartilage repair. Native articular cartilage has evolved to possess a spatially organized mechanical heterogeneity within its architecture. Specifically, chondrocytes are localized within a soft pericellular matrix (2 to 25 kPa) maintaining their round phenotype, being in turn localized in a hard extracellular matrix (ECM) (0.5 to 4 MPa) (Bas et al., 2017; Buxboim et al., 2010; Schinagl et al., 1997; Zhang et al., 2016). Therefore, biomimicry of cartilage in engineered equivalents is challenging, as the biomaterial must be simultaneously both stiff and soft to bear high cyclical loads and support the cell's chondrogenic functions, respectively.

To overcome this challenge and abstractly emulate native cartilage organization, here we have developed two different biomaterials, which mimic the mechanical properties along with viscoelastic behavior of either the hard extracellular matrix or soft pericellular matrix. To locally integrate soft and cell stimulating biomaterials inside of mechanically robust three-dimensional (3D) constructs, bioprinting technology is a good candidate to create spatially organized and functional 3D cartilage-like tissues. Prior studies have explored the bioprinting of cartilage, which have advanced our capability to mimic anatomical shapes, cells densities, and zonal organizations (Constantini et al., 2016; Daly et al., 2016; Klein et al., 2009). However, a key limitation of current bioprinting technologies is the difficulty in precisely controlling the position of biomaterials in the Z direction to create freestanding biological architectures and multi-component structures (Highley et al., 2015). Among various bioprinting technologies, an embedded 3D bioprinting technology using a self-healing and supporting hydrogel was used to achieve shape-stable deposition of the desired biomaterials in the X-Y-Z directions (Highley et al., 2015; Hinton et al., 2015; Jeon et al., 2019; Loebel et al., 2017; Song et al., 2018).

For developing 3D bioprinted cartilage-like tissue constructs, we designed a strategy to print a chondrogenic cells-laden soft biomaterial within a supporting bath of a stiff biomaterial in a spatially controlled manner using the embedded bioprinting technique. For the mechanically robust biomaterial, we used an interpenetrating polymer network (IPN) hydrogel composed of a light-induced covalently crosslinked poly (ethylene glycol) (PEG) network and

a cation-induced physically crosslinked alginate network. These biocompatible polymer networks can possess high mechanical properties up to the MPa range, which mimic the native extracellular cartilage matrix, showing great potential for applications in cartilage repair (Guo et al., 2017; O'Connell et al., 2017). Furthermore, these IPN hydrogels take up a large amount of water while maintaining stiff, tough and viscoelastic mechanical properties (Bootsma et al., 2017). In contrast, fibrin gel has lower mechanical properties that are comparable to cartilage's pericellular matrix, and pre-gel fibrinogen was used as the soft bioink with which the printed cells would interface. In previous studies, fibrin-based composite hydrogels showed strong capacity to maintain the phenotype of chondrocytes and promote synthesis of cartilage ECM (Little et al., 2014; Perka et al., 2000). By printing the fibrinogen in the PEG-alginate supporting bath, a living construct with hierarchical mechanical properties was engineered, stiff and tough on the tissue level yet soft and degradable at the cellular level (Janmey et al., 2009).

Mesenchymal stem cells (MSCs) were selected as the chondrogenic cell source as they can be easily obtained from various different types of human tissues and allow for expansive and efficient cartilage matrix production (Fu et al., 2017). Furthermore, chondrogenesis of MSCs can be substantially boosted via cellular micro-aggregation (Kosher et al., 1986; Leijten et al., 2016). Accordingly, we used human bone marrow-derived MSC (hMSC) spheroids laden within a soft fibrin gel as the chondrogenic bioink, which was printed into a mechanically robust supporting bath using embedded bioprinting. We then demonstrated the capacity to spatially control the mechanical properties of 3D bioprinted cartilaginous tissue, which enabled the construct to exhibit stiffness on the tissue level, and softness around the cells to allow their chondrogenic function.

5. Material and Methods

2.1. Material

Fibrinogen from bovine plasma, thrombin from bovine plasma, alginic acid sodium salt from brown algae (low viscosity, 100-300 cP), calcium chloride ($CaCl_2$), photoinitiator (2-Hydroxy-4′-(2-hydroxyethoxy)-2-methylpropiophenone), proline, ascorbic acid, sodium pyruvate and dexamethasone were purchased from Sigma-Aldrich (St. Louis, MO, USA). Polyethylene glycol (PEG) dimethacrylate (M_w = 1000 Da) was purchased from Polysciences, Inc. (Warrington, PA, USA). Polydimethylsiloxane (PDMS) (Sylgard 184 Silicone Elastomer

Kit) was purchased by Dow Corning (Midland, MI, EUA). Phosphate-Buffered Saline (PBS), Fetal Bovine Serum (FBS), Insulin-Transferrin-Selenium (ITS-Premix), Penicillin-Streptomycin (P/S), Dulbecco's Modified Eagle Medium (DMEM), Minimum Essential Media α (α-MEM), Live/dead® Viability/Cytotoxicity Kit, PrestoBlue™ Kit and paraformaldehyde ampules were purchased from Thermo Fisher Scientific (Waltham, MA, USA). Basic fibroblast growth factor (FGF-b) and transforming growth factor β1 (TGF-β1) were purchased from R&D Systems (Minneapolis, MN, EUA).

2.2. Fabrication of PDMS molds

The negative for bioprinting the bath mold was fabricated by cutting (6 x 6 mm) a 6 mm thickness PMMA sheet using a laser cutting machine (VLS 2.30 Desktop Laser, Universal Laser Systems Inc, Richmond, VA), and the negative for the spheroids' mold consisted of 576 wells of 200 μm of height and diameter each, fabricated using standard soft photolithography technique. PDMS was prepared at a ratio of 10:1 of base to curing agent and poured into the negatives. After degassing in a vacuum chamber, the PDMS molds were cured at 80 ºC for 1 hour, cooled to room temperature, and demolded from their negative replicate.

2.3. Microscope imaging

All bright field and fluorescent images were taken in a Nikon Eclipse Ti-S Microscope (Nikon, Tokyo, Japan) and all confocal images were taken in a ZEISS LSM 880 with Airyscan Microscope (Carl Zeiss, Jena, Germany). Scanning electron microscopy (SEM) images were taken on a LEO Electron Microscopy/Oxford (Cambridge, England).

2.4. PEG-alginate hydrogels fabrication

Dimethylacrylate PEG was dissolved in deionized (DI) water at concentrations of 30, 40, and 50%. Alginate solution in DI water (5%) was mixed with each PEG solution at a 1:1 ratio in order to prepare solutions with final concentrations of PEG 15, 20, and 25% with alginate 2.5%. After adding photoinitiator 0.25% and degassing, the mixture was carefully poured into the cubic PDMS mold, and placed in a UV chamber under UV light (365 nm wavelength) with a source of 200 mW cm^{-2} (Omnicure S2000, Excelitas Technologies, Salem,

MA, USA) for 80 s. After the covalent PEG crosslinking, the hydrogel was removed from the mold and soaked in a 0.1 mol L^{-1} $CaCl_2$ solution for 1 hour to ionically crosslink the alginate. After both PEG and alginate crosslinking, the hydrogels were taken to rheological and mechanical tests.

2.5. Rheological and mechanical characterization

Rheological properties of pre-polymers and hydrogels were analyzed using an Anton Paar MCR 702 TwinDrive rheometer (Anton Paar, Graz, Austria), operating with the top drive only. A ten millimeter diameter parallel plate geometry was used for all measurements. For fibrinogen and PEG-alginate pre-polymer solution, approximately 1 mL of samples was used, and for crosslinked fibrin and PEG-alginate hydrogels, samples had approximately 1 mm thickness; accordingly, the gap size was 1 mm in all cases. Temperature control was maintained using the P-PTD200 (bottom plate) and H-PTD200 (hood enclosure) attachments from Anton Paar, with cooling supplied by a Julabo circulating chiller. Results were recorded and analyzed using Anton Paar RheoCompass software. All measurements were performed at 25 ºC. Prior to the measurement of each sample, the measuring system inertia (of the upper geometry) was calibrated to compensate for acceleration torque, and the motor was calibrated to compensate for residual friction. After these adjustments, the gap was recalibrated after which the samples were loaded and allowed to equilibrate for thirty minutes or until normal force had decayed. Mineral oil was added to the perimeter of the sample to prevent the sample from drying; frequency sweeps performed at the start and end of the measurements suggest that sample drying was not a significant issue. Mechanical tests were performed using a Zwick mechanical tester (Zwick/Roell, Ulm, Germany) with custom parallel plates. Compression measurements were recorded in the Test Xpert software by Zwick. All measurements were performed at room temperature. Samples were cut to have a circular cross section of 10.5 mm in diameter (L_0) and approximately 1 mm in thickness. Prior to measurement, the zero gap was determined using the "approach" feature in the Test Xpert software. All measurements were performed at 1% L_0 s^{-1} (0.105 mm s^{-1}). For cyclic tests, after loading each sample, five cycles from 0% to 10% were performed sequentially; after the end of this test, the process was repeated to ensure that the results were reproducible up until 10% strain. Next, five cycles were performed from 0% to 20% strain. The final cycles were performed with increasing strain, starting at 0% strain and returning to 0% strain after each strain threshold: 10%, 20%, 30%, and 40%. Results from the

final cycles, increasing strain cyclic tests at 10% and 20% were consistent with the individual trials at these strains. Compressive modulus was calculated as the slope of the stress-strain curve between 10 and 20% loading.

2.6. Swelling degree of IPN hydrogels

PEG-alginate IPN hydrogels were dried under vacuum, and the dry weights (W_d) were measured. Afterward, samples were immersed in PBS for 72 h, and at predetermined time points, swollen hydrogels were weighed (W_s), and swelling degrees calculated by (%) = (W_s - W_d) / W_d x 100.

2.7. Bioprinting fibrin in PEG-alginate bath

In order to obtain fibrin as bioink, fibrinogen was dissolved in saline solution (10 mg mL^{-1}) by gently mixing in a 37 ºC water bath. PEG 20%-alginate 2.5% solution was used as the bath containing 0.25% photoinitiator and supplemented with 1 U per mL^{-1} thrombin to allow fibrin crosslinking during bioprinting. The bath was poured into the PDMS mold and left at 4 ºC for at least 2 hours. The bioprinting system consisted of two needles (diameter = 500 μm) glued to each other, with one needle connected to a 1 mm Teflon tube that in turn was connected to a 1 mL syringe containing the fibrinogen solution. The needle was placed in a syringe pump (New Era Pump Systems Inc., Suffolk County, NY) for bioink extrusion, with a controlled flow rate ranging from 5 to 10 μL min^{-1}. The bioprinting was performed using an INKREDIBLE 3D Bioprinter (Cellink, Gothenburg, Sweden) with the double needle connected to the print head, and the deposition was automatically controlled by a G-code. The nozzle speed ranged from 50 to 600 mm min^{-1}. Fibrin fibers were printed in at 5 different densities, 36, 60, 84, 108 and 132 lines cm^{-2}. At the end of the deposition step, the constructs were exposed to UV light (200 mW cm^{-2}) for 80 seconds and soaked in a 0.1 mol L^{-1} $CaCl_2$ solution for 1 hour. To analyze the printed constructs, the fibrinogen was stained with pink dye during printing preparation, and images were taken using an optical microscope.

2.8. Cell culture

Whole bone marrow was obtained by harvesting the iliac crest of healthy patients at the Case Comprehensive Cancer Center Hematopoietic Biorepository and Cellular Therapy Core, previously approved by the University Hospitals of Cleveland Institutional Review Board. Isolation of hMSCs from the marrow was via a Percoll (Sigma) gradient and the differential cell adhesion method (Jeon et al., 2013). hMSCs were cultured in α-MEM, supplemented with 10% of FBS, 1% of P/S and 10 ng mL^{-1} of FGF-b. Culture media was refreshed every two days.

2.9. Spheroids fabrication

The spheroids' PDMS mold was sterilized with ethanol 70%, changed at least four times every 30 min, and washed three times with PBS and two times with media. After trypsinization, hMSCs from passage 3 or 5 were seeded at a concentration of 1 x 10^6 cells in 200 μL media per mold, and allowed to settle in the wells for 1 h at 37 ºC in a 5% CO_2 humidified incubator. Media was added to 1 mL and cells were kept in incubation until spheroids had formed. After 1 day, spheroids were carefully harvested via flow agitation and collected for culture and bioprinting. Spheroids were quantified in size distribution using the ImageJ software.

2.10. Spheroids culture in fibrin hydrogel

In order to evaluate their viability in fibrin, harvested spheroids fabricated with hMSCs from passage 5 were mixed in 160 μL of 10 mg mL^{-1} fibrinogen solution and added to a 48 well plate, followed by 36 μL of 0.1 U mL^{-1} thrombin and 4 μL of 0.1 mol L^{-1} $CaCl_2$ to allow for crosslinking. After gel formation, 700 μL of supplemented α-MEM was added to the wells and the plate was kept in incubation for 7 days, with 50% of the media changed every two days. To evaluate the spheroids' viability in a fibrin-hydrogel, spheroids were mixed in 50 μL of the fibrinogen solution, and added using a micropipette to the PDMS mold filled with PEG 20%-alginate 2.5% hydrogel containing 0.25% photoinitiator and supplemented with 1 U mL^{-1} thrombin to allow for fast fibrin crosslinking. PEG was crosslinked by UV light exposition (200 mW cm^{-2}) for 80 s, and alginate was crosslinked by soaking the hydrogel in a 0.1 mol L^{-1} $CaCl_2$ solution for 30 minutes. Hydrogels were placed in a 48 well plate containing 700 μL of supplemented α-MEM, and kept in incubation for 7 days, with 50% of the media changed every

two days. Viability and metabolic activity of the spheroids were evaluated by using PrestoBlue reagent and live/dead kits.

2.11. Bioprinting spheroids

Spheroids fabricated from hMSCs passage 5 were mixed to the 10 mg mL^{-1} fibrinogen solution and added to a 1 mL syringe to be used as the bioink. Vertical constructs were bioprinted in a PEG 20%-alginate 2.5% hydrogel containing 0.25% photoinitiator and supplemented with 1 U mL^{-1} thrombin, using 200 mm min^{-1} as the flow rate and 6 μL min^{-1} as the extrusion speed. After bioprinting, the hydrogels were exposed to UV light (200 mW cm^{-2}) for 2 x 40 s, followed by soaking in 0.1 mol L^{-1} $CaCl_2$ for 30 minutes. The bioprinted constructs were placed in a 48 well plate filled with 700 μL of supplemented α-MEM, and kept in incubation for 7 days, with 50% of the media changed every two days until an assessment of viability.

2.12. Assessment of spheroids viability

PrestoBlue reagent was used to assess metabolic activity at days 3, 5, and 7. During each day, media was replaced by 10% of PrestoBlue reagent in α-MEM and spheroids were incubated for 3 h at 37 ºC. An aliquot of 200 μL of the incubated reagent was transferred to a 96 well plate and absorbance read at 570 and 600 nm. The percentage of PrestoBlue reduction was calculated and results expressed as normalized absorbance (to the first day of culture and number of spheroids). Live/dead assay was carried out at days 3, 5, and 7 using Live/dead kits. After washing the samples with PBS, samples were incubated for 30 min with an ethidium homodimer-1 and calcein mixture, previously prepared in a ratio of 3:1 in PBS. Then, samples were carefully washed with PBS and taken to a confocal microscope for imaging. Spheroids were visualized by Z-stacking 10 to 15 images, and the number of live and dead cells was calculated using the ImageJ software. For each condition, 3 spheroids containing approximately 1,700 cells were counted.

2.12. Chondrogenic differentiation

Bioprinted spheroids fabricated using hMSCs from passage 3 were cultured in chondrogenic medium DMEM, supplemented with 10% FBS, 1% P/S, 40 µg mL^{-1} proline, 50 µg mL^{-1} ITS-premix, 50 µg mL^{-1} ascorbic acid, 100 µg mL^{-1} sodium pyruvate, 10 mol L^{-1} dexamethasone and 10 ng mL^{-1} TGF-beta for 21 days. Chondrogenic media was changed every third day.

2.13. Histological preparations

Bioprinted constructs cultured in chondrogenic and control media were washed with PBS and fixed with 4% paraformaldehyde for 2 h. Afterward, the samples were rinsed twice with PBS, sliced (50 µm section) in paraffin blocks and kept in an oven at 65 ºC for 2 hours. The slices were deparaffinized in xylene and rehydrated in graded ethanol from 100 to 75%. Samples were stained with Alcian blue for GAG's, and Masson's trichrome and Picro-sirius red for collagen deposition. Samples were scanned by digital slides scanner (3D Histech, MIDI).

2.14. Statistical Analysis

All data are expressed as mean ± standard deviation. One-way ANOVA with Tukey tests were performed when appropriate with $p < 0.05$ being viewed as significant.

6. Results and Discussion

3.1. Design of bioinks and embedded bioprinting system

To develop mechanically robust 3D cartilage-like tissue constructs, the crosslinked supporting bath should possess stiff and tough mechanical properties that are able to withstand high mechanical stresses and cyclic loads, while fibrin provides a soft and stimulating environment to cells. To this end, we first designed a hydrogel-based supporting bath possessing self-healing properties. This bath allowed successful printing of hMSC spheroid-laden bioink, without causing any permanent cracks, via an embedded bioprinting system

(Figure 1). Cracks lead to the weakening of the supporting hydrogel as a whole *via* crack propagation under high mechanical cyclic loads; therefore, the self-healing process should occur rapidly (within a few seconds) around the printed bioink, ideally without using any added cytotoxic compounds or external stimuli to maintain high cell viability. To achieve these requirements, a combination of dimethyl acrylate PEG and alginate pre-polymer mixture was used as the self-healing supporting bath. These materials have the capability of mechanically interlocking based on non-covalent (physical) supramolecular interactions between the two polymers, which is generally reversible (Hong et al., 2015). In addition, the shear thinning behavior of the non-crosslinked alginate makes it a suitable candidate for one of the supporting bath materials (Li et al., 2016). In a previous study, the PEG-alginate mixture was used as a bioink by Hong et al. to obtain a 3D cartilage tissue *via* extrusion-based bioprinting, and was shown to be a cytocompatible material, maintaining high cell viability for several days after printing (Hinton et al., 2015). Although the use of hard biomaterials as bioinks has proven to be suitable for cell growth, these materials may cause cellular stress associated with the hard mechanical microenvironments post-gelation (Hendriks et al., 2015). In addition, a direct interface with a stiff biomaterial is known to adversely affect cell survival and chondrogenic behavior after a few weeks of culture (Park et al., 2011a). Therefore, to maintain chondrogenic function, a fibrin hydrogel was used as an appropriately soft biomaterial that is formed following enzymatic polymerization of fibrinogen by thrombin (Park et al., 2011b; Sheykhhasan et al., 2015). However, as fibrin is a relatively viscous material, it will associate with poor cell viabilities when printing at high resolutions using small nozzles or high feeding speeds due to resulting high shear and extensional forces (Colosi et al., 2016; Zhu et al., 2017). To solve this challenge, the hMSC spheroid-laden bioink utilized was fibrinogen. The mixture was printed in a PEG-alginate self-healing supporting bath containing thrombin, which diffused into printed fibrinogen to form a stable fibrin hydrogel. The diffusion based crosslinking process for the fibrin gel is ideal for locally depositing hMSC spheroid-laden soft matrices with high cell viability and high printing resolution due to fibrinogen's low viscoelastic properties and fast gelation (Cui and Boland, 2009). After bioprinting and polymerization of the hMSC spheroid-laden fibrinogen bioink, the PEG-alginate pre-polymer was dual-crosslinked to form an IPN hydrogel that possessed macro-mechanical properties similar to that of native cartilage, presenting high stiffness and toughness, which was assured by reversible physical crosslinks that allows for energy dissipation, and covalent crosslinks that maintain hydrogel elasticity under deformation (Hong et al., 2015; Jeon et al., 2017; Sun et al., 2012).

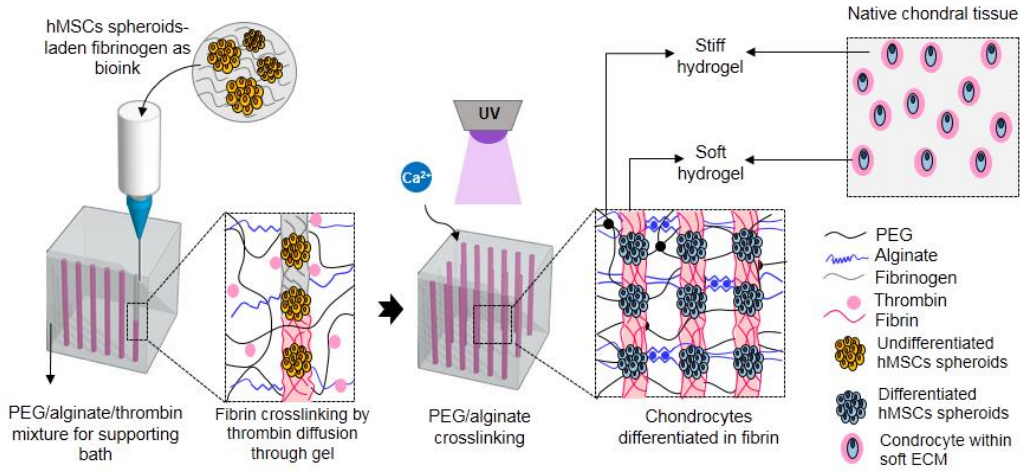

Figure 1. Schematic of the 3D bioprinting approach for the engineering of articular cartilage. hMSCs-laden fibrinogen was used as a bioink for printing in a self-healing supporting bath of PEG-alginate pre-polymer mixture, supplemented with thrombin. Thrombin interacts with fibrinogen and polymerizes during bioprinting, forming soft fibrin fibers inside the hard PEG-alginate hydrogel, creating a suitable environment for chondrocyte differentiation within a mechanically robust construct. This system allows for the bioengineering of 3D native-like cartilage tissue.

3.2. Stiff and viscoelastic PEG-alginate IPN hydrogel

Using a PEG and alginate pre-polymer mixture, a multi-material IPN hydrogel was fabricated through UV light and Ca^{2+} mediated dual-crosslinking (Figure 2A). To optimize the polymer blend for use as a mechanically robust supporting hydrogel, PEG concentrations of 15, 20 and 25% were investigated, while the alginate concentration was fixed at 2.5%. Storage (*G'*) and loss (*G"*) moduli analysis of the three hydrogel compositions demonstrated that the IPNs were predominatly elastic in nature as no *G'* variation was observed when varying the angular frequency from 1 rad s^{-1} to 100 rad s^{-1} (Figure 2B). PEG concentration directly influenced the hydrogel mechanical properties, with *G'* values around 0.15, 0.5, and 1 MPa for PEG 15, 20, and 25%, respectively. Additionally, the phase angle was close to zero for all PEG concentrations, indicating a high stiffness (Grillet et al., 2012). The maximum loss modulus was on the order of 10 kPa, indicating that more energy is stored in the hydrogels than is dissipated, which could cause cracks during compression to release energy (Fulcher et al., 2009). However, no cracks were observed in the hydrogels, indicating that PEG chains were

able to stabilize the deformation (Hong et al., 2015; Sun et al., 2012). The compressive moduli were calculated from stress-strain curves, which showed a positive correlation with PEG concentration with values of 2.57 ± 0.04 MPa, 3.08 ± 0.09 MPa, and 4.43 ± 0.21 MPa for 15, 20, and 25% PEG-2.5% alginate, respectively (Figure 2C). These moduli demonstrate that PEG concentration positively correlates with material stiffness, in line with the existing literature (Bas et al., 2017; Li et al., 2014). As articular cartilage has a compressive modulus ranging from 0.08 to 2.5 MPa, the 15% PEG-2.5% alginate hydrogel possessed mechanical properties similar to native cartilage tissue (Bartnikowski et al., 2015; Schinagl et al., 1997).

We also demonstrated the capacity of the PEG-alginate hydrogel to withstand mechanical loading by applying a cyclical strain of up to 40% compression. Hydrogels could return to their original shape without cracking at 30% compressive strain (Figure 2D; Video S1, Supplementary information). The resilience capacity of the hydrogel was confirmed by their ability to recover their original shape after being loaded 4 times, and each time reaching larger values, with a maximum of 1.2, 1.7, and 2.4 MPa in the last cycle for PEG 15%, 20%, and 25%, respectively, indicating a PEG-concentration dependent effect on the materials' mechanical properties (Figures 2E-G). Moreover, the pronounced and stable hysteresis after 5 cycles confirmed the hydrogels' ability to dissipate energy when compressed, which is assured by the reversible alginate-Ca^{2+} crosslinking (Figure 2H).

To assess the PEG-alginate IPN hydrogel's fluid phase, the swelling behavior of the PEG-alginate IPN hydrogel within phosphate buffered saline (PBS) was evaluated. PBS was used here in order to simulate the fluid phase present in the native articular cartilage tissue. After 8 hours, the degree of swelling reached equilibrium and no significant changes in time were observed, with a maximum swelling degree of 89.1 ± 12.6%, 135.5 ± 3.1%, and 130.3 ± 1.7% for PEG 15%, 20%, and 25%, respectively (Figure 2I). Consequently, the degree of swelling significantly increased by increasing PEG concentration from 15% to 20%. This was likely due to the increase of the hydrophilic contents such as PEG in the IPN, resulting in a greater degree of binding of water molecules and a larger amount of water being contained in the networks. However, at 25% PEG, the degree of swelling plateaued, likely due to the IPN's crosslinking density countering the osmotic pressure of additional water molecules above 20% PEG (Bajpai and Shrivastava, 2002). As a result, the 15% PEG-alginate IPN hydrogels contain similar amounts of water as native cartilage tissue, which is ~80% of the wet weight of the tissue. Scanning electron microscopy (SEM) images of the freeze-dried PEG-alginate hydrogels showed a highly dense morphology that was observed for all three compositions (Figure 2J).

Interestingly, micro-cracks were observed with increasing PEG concentration, and cavity size positively correlated with PEG concentration. As aforementioned, these micro-cracks may self-heal through the reversible alginate-Ca^{2+} ionic crosslinking networks. These results corroborate the formation of IPNs from the intra/intermolecular interactions, resulting in stiff hydrogels (Hild, 1997). The high stiffness and capacity to withstand mechanical loading from cyclic strain suggested that our IPN hydrogels could have great potential for cartilage engineering and regeneration strategies.

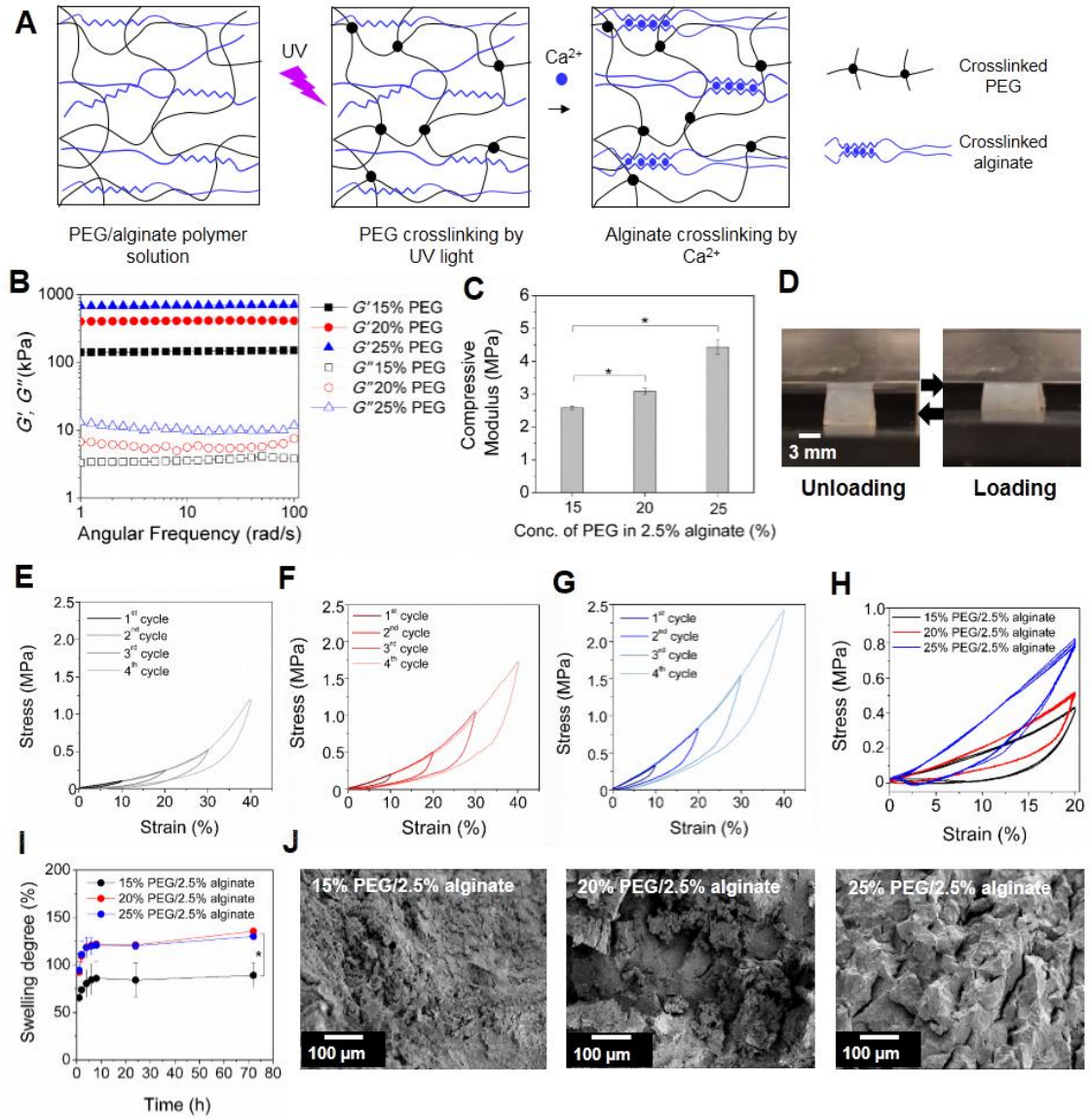

Figure 2. Characterization of PEG-alginate hydrogels with different PEG concentrations. A) Schematic illustration of the dual-crosslinking process to create the PEG-alginate IPN hydrogel. B) Linear rheological properties and C) compressive modulus of the PEG-alginate IPN hydrogels with various concentrations of PEG. *$p < 0.05$. D) Photographs of the 20% PEG-

2.5% alginate IPN hydrogel under compressive strain at 30%. E-G) Cyclic compression test of the PEG-alginate IPN hydrogels with increased strain by a 10% increment with each compressive cycle from 10 to 40% for E) PEG 15%, F) PEG 20% and G) PEG 25%. H) Cyclic compression test of the PEG-alginate IPN hydrogels with various concentrations of PEG under five repeated cycles up to 20% strain. I) Swelling behavior of the PEG-alginate IPN hydrogels with various concentrations of PEG within PBS. J) SEM images of the PEG-alginate hydrogels with various concentrations of PEG within PBS.

3.3. Assessment of bioprinting conditions

In terms of compressive modulus, 15% PEG-2.5% alginate hydrogels performed similarly to native cartilage. However, we postulated that incorporation of the soft fibrin hydrogel within a bulk of stiff PEG-alginate hydrogels would result in a decrease in the overall mechanical properties of the hydrogel. Here, the 20% PEG-2.5% alginate composition was chosen for the supporting bath due to its stronger mechanical properties that might offset the expected reduced mechanical performance of the PEG-alginate hydrogel. Fibrinogen is a bioink with low viscosity and Newtonian behavior (Figure 3A and S1A, Supporting information) that is difficult to bioprint *via* conventional extrusion-based bioprinting techniques without using thrombin to create stable microprinted lines (Grillet et al., 2012). This limitation was overcome by using the embedded bioprinting technique with the PEG-alginate supporting bath, which displays a non-Newtonian, shear thinning (pseudoplastic) behavior (Figure S1B-C, Supporting information). Pre-polymers with increased concentrations of PEG (20 and 25%) presented an increased flow consistency index (K) and a decreased power law index (n) compared to that with 15% of PEG, showing that higher concentrations of PEG led to increased shear thinning (Table S1, Supporting information). Shear thinning is an ideal flow characteristic for support baths to provide low mechanical resistance to the nozzle when bioprinting in an otherwise viscous bath. Moreover, pseudoplastic fluids behave as a rigid body at low shear stresses, making it possible to sustain the shape and location of the printed microstructure (Figure 3A) (Zhu et al., 2017). The presence of thrombin increased the zero-shear viscosity of PEG-alginate pre-polymer solution, which was 20.5 ± 6.4 Pa·s as compared to the bath without the enzyme (11.7 ± 1.9 Pa·s). This viscosity increase is likely due to the thrombin induced non-covalent supramolecular interactions, such as the ionic interaction between negatively charged carboxylate groups of sodium alginate and positively charged thrombin (Akkaya, 2017). As

expected, the fibrin zero-shear viscosity was substantially higher than that of fibrinogen, 16.9 ± 3.3 Pa·s vs. 3.9 ± 0.8 Pa·s, respectively (Figure 3B).

The polymerization of fibrin gel is associated with increased turbidity (Figure 3C). The storage modulus of fibrin was significantly lower than that of the PEG-alginate hydrogels at equivalent frequencies, as was expected, reaching a maximum of 10 Pa (Figure 3D). The fibrin gel behaved distinctly from the tough hydrogels, showing a more prominent viscous behavior with increasing frequency, indicating its low capacity to store energy at higher frequencies. Mechanical analysis of fibrin showed low fracture stress (6.4 kPa) (Figure 3E), resulting in a much lower compressive modulus than the PEG-alginate hydrogels (2.4 ± 0.8 kPa) at the same strain rate (10 to 20%), and confirmed the material's softness. It is anticipated that a fibrin hydrogel could therefore provide a softer microenvironment to encapsulated cells, which is expected to reduce the physical constraints compared to the dense and hard PEG-alginate IPN hydrogel for the hMSC spheroids. Moreover, fibrin hydrogels possessed a high permeability (Moreno-Arotzena et al., 2015), which could also further improve hMSC spheroids viability within the PEG-alginate IPN hydrogel.

To locally combine the fibrin micro hydrogel within a bulk of hard PEG-alginate IPN hydrogel, vertically oriented fibers were printed to control the arranged direction of chondrocytes, partially mimicking the overall native cartilage organization (Huber et al., 2000). Bioprinting was characterized by testing the influence of the nozzle speed and bioink flow rate on the diameter of printed fibers. A needle with a 500 µm inner diameter was used for extrusion, and bioprinting was performed by varying bioink flow rates from 5 to 10 µL min^{-1} and nozzle speed from 50 to 600 mm min^{-1}. After printing, the PEG-alginate supporting bath was subsequently dual-crosslinked using UV light and 0.1 mol L^{-1} $CaCl_2$. By printing a fibrinogen bioink containing pink stain, it was optically verified that the printed lines possessed diameters between approximately 50 to 250 µm, which was tightly controlled by the printing parameters bioink flow rate and nozzle speed (Figures 3F-G, S2 and video S2, Supporting information). The minimum diameter of the printed lines was ~50 µm, which is difficult to achieve via conventional extrusion-based printing. The bioprinted constructs presented a very precise alignment and high resolution deposition of fibrin, with width consistency along the construct length (Figure 3H, i, ii, and iii). Furthermore, the printing nozzle could continuously move up and down in the supporting bath without crack formation. Finally, the 3D printing created a complex-structured, multi-material composite composed of a high resolution array of parallel lines within a distinct material bulk (Figure 3H, iv and v).

To evaluate the effects of the internal soft fibrin hydrogel patterns on the overall mechanical properties of the PEG-alginate IPN hydrogel, the fibrinogen bioink was printed with various densities (36, 60, 84, 108 and 132 lines cm^{-2}), as well as different orientations (Figure 3 I-K, Figure S3, Supporting information). Results were expressed as the loss percentage of the compressive modulus, relative to the lowest concentration of printed lines (36 lines cm^{-2}). Up to 80 lines cm^{-2}, compressive modulus loss was below 10%, while a significant increase was observed for 108 lines cm^{-2} and 132 lines cm^{-2}, with the loss being higher than 50%, demonstrating that printing density adversely affected the macro-mechanical properties of the IPN hydrogel when exceeding a threshold value (Figure 3I). It was also demonstrated that the printed line orientation could endow the engineered constructs with an anisotropic mechanical behavior (Figure 3J). It is of note that, especially for low density printed constructs, a strain-stiffening behavior was observed, which may be interesting for the engineering of cartilage tissues that self-protect against trauma or rapid-loading induced rupture (Figure 3K) (Chen et al., 2012).

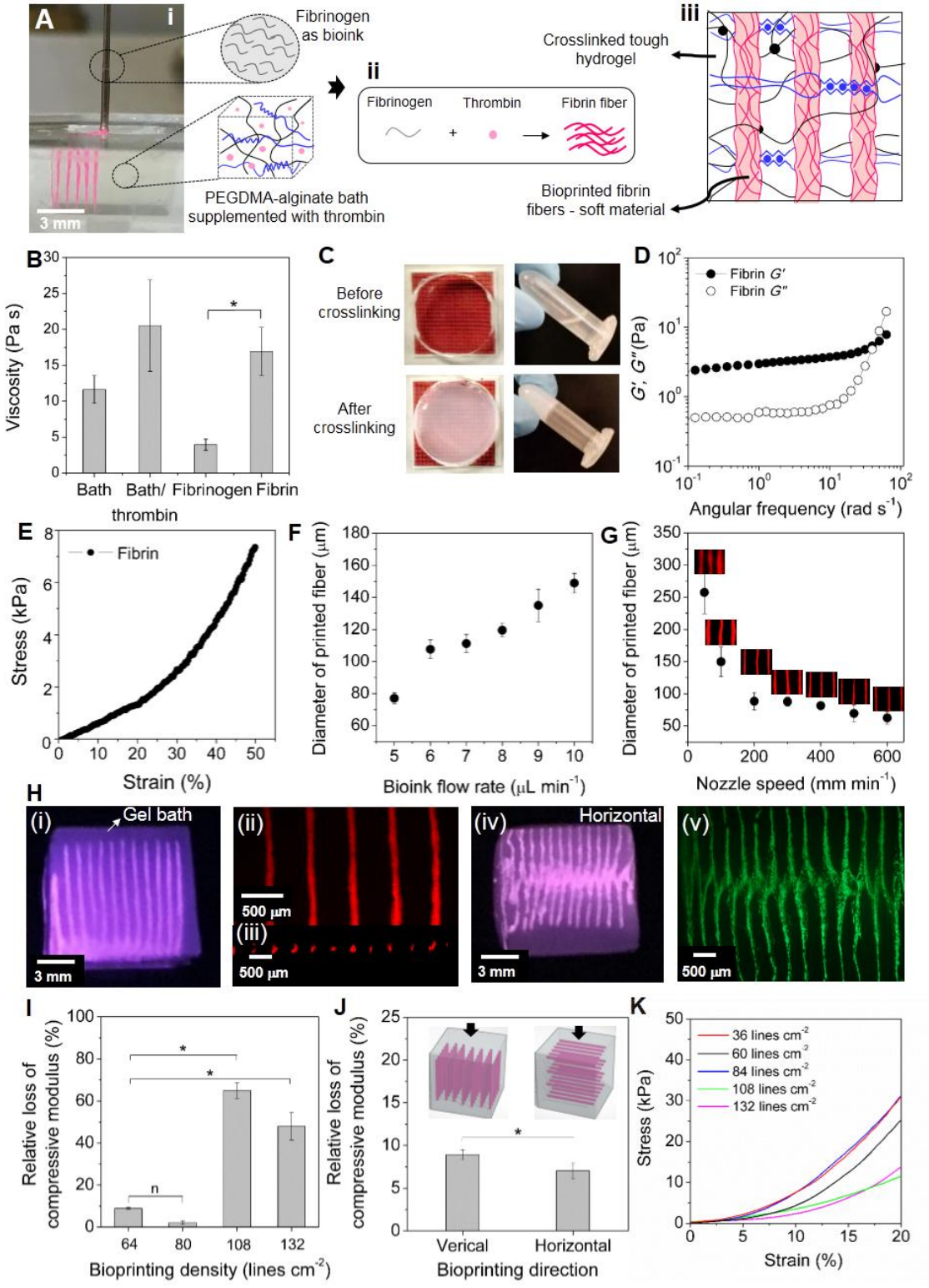

Figure 3. Characterization of the bioink and bioprinting conditions. A) Schematic of the 3D printing approach. i) Printing using fibrinogen solution as bioink stained pink, and PEG-alginate supplemented with thrombin as bath. ii) Schematic of the polymerization reaction between fibrinogen and thrombin forming fibrin. iii) Schematic of the fibrin printed lines in PEG-alginate bath, after crosslinking. B) Viscosity of the supporting bath (20% PEG-2.5%

alginate) in the presence and absence of thrombin, and of the bioink before (fibrinogen) and after (fibrin) crosslinking. $^{*}p < 0.05$. C) Images of bioink taken before and after crosslinking. D) Rheological properties and E) stress-strain curve of fibrin gel. F) Diameter of printed fibrin fibers as a function of bioink flow rate. G) Diameter of printed fibrin fibers with respect to nozzle speed. H) Images of bioprinted fibrin in 20% PEG-2.5% alginate. (i) Photograph of vertically printed fibrin. Optical images of vertically printed fibrin from ii) side and iii) top views. (iv) Photomicrograph of horizontally printed fibrin and (v) optical image of horizontally printed fibrin from top view. I) Relative loss of compressive modulus of hydrogels containing different densities of printed lines. J) Relative loss of compressive modulus of IPN hydrogels in vertical and horizontal orientation. ^{n}non-significant and *significant at $p < 0.05$. K) Stress-strain curves of PEG-alginate hydrogels without printing and with printed fibers at different densities.

2.4. hMSCs spheroids fabrication and survival in soft and stiff hydrogels

A polydimethylsiloxane (PDMS) microwell technique was used to form hMSCs spheroids in high throughput (Figure 4A) (Bhise et al., 2016). The PDMS mold was composed of 576 microwells with 200 µm height × 200 µm diameter (Figures 4B and C). Micrometer sized hMSCs spheroids self-assembled over the course of 24 hours when seeded in the microwells due to the significantly higher cell-cell interactions as compared to cell-substrate interactions (Smeets et al., 2016). In addition, the poor cell-substrate interaction properties of the PDMS microwell allowed for facile harvesting of the intact spheroids after one day of culture (Figure 4D and E). The harvested hMSC spheroids were characterized as having a narrow size distribution with diameters of 110 ± 22 µm (Figure 4F). This equated to approximately 1,700 cells per spheroid, which correlated with the expected number of cells based on seeding density. Live/dead analysis confirmed that hMSC spheroids remained viable and did not form a necrotic core (Figure 4G).

To evaluate cell viability in the soft and hard hydrogels, hMSC spheroids were encapsulated and cultured for seven days in bulk fibrin, bulk PEG-alginate, and fibrin that was homogeneously mixed into PEG-alginate (fibrin/PEG-alginate) (Figure 4H-K). Live/dead results revealed that there was a higher viability of hMSC spheroids in the soft fibrin (94.3 ± 0.4%) hydrogel as compared to the hard PEG-alginate IPN (77.6 ± 3.1%), and mixed fibrin/PEG-alginate (77.7 ± 0.4%) hydrogels, proven that fibrin gel is an excellent matrix to

promote cell viability and growth (Figure 4H and S4, Supporting information) (Guo et al., 2010; Murphy et al., 2014; Sakai and Nakazawa, 2007). In contrast, hMSCs spheroids within the PEG-alginate hydrogel had become smaller than hMSC spheroids embedded in fibrin, demonstrating lower cellular viability, and showing a less rounded shape due to the physical constraints generated by the dense and high mechanical properties of the PEG-alginate hydrogel (Figure 4I). Importantly, endowing hard PEG-alginate hydrogels homogeneously with fibrin did not improve spheroid viability and growth, indicating the essential nature of spatial separation between the soft fibrin and the hard PEG-alginate hydrogel to allow for improved construct performance.

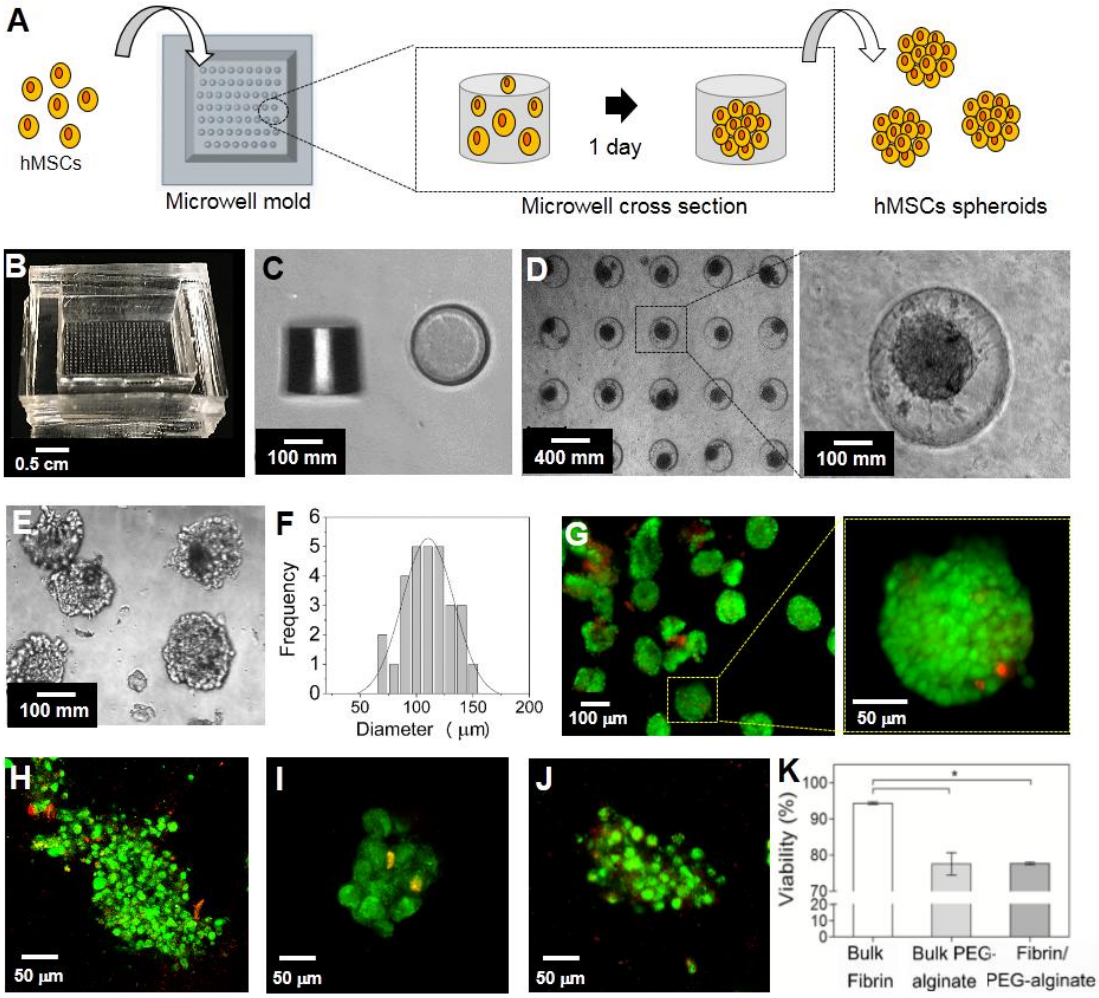

Figure 4. hMSC spheroid fabrication and characterization. A) Schematic of hMSC spheroid fabrication showing single cells being added to the microwell mold and forming spheroids after 1 day of culture. B) Picture of the PDMS mold. C) Optical image of a microwell mold. D) Optical image of hMSC spheroids in the PDMS mold after 1 day. E) Optical image of harvested spheroids after 1 day. F) Size distribution histogram of harvested spheroids. G) Confocal

live/dead images of harvested spheroids, and spheroids cultured in H) fibrin, I) PEG-alginate and J) fibrin-laden in PEG-alginate after 7 days. K) Viability of spheroids cultured for 7 days in fibrin, bulk gel (PEG-alginate hydrogel) and fibrin/bulk gel (PEG-alginate hydrogel homogeneously mixed with fibrin). *$p < 0.05$.

2.5. Mechanically robust 3D printed hMSC spheroid-laden cartilage-like tissue constructs

Vertically aligned fibrin lines were bioprinted, allowing for an organized deposition of spheroids inside the PEG-alginate IPN hydrogel (Figure 5A). SEM analysis confirmed the incorporation of hMSC spheroids within the fiber networks of the printed fibrin hydrogel (Figures 5B). The bioprinted hMSC spheroid-laden fibrin in the PEG-alginate IPN hydrogel showed good viability in both the core and the shell after 3, 5, and 7 days (Figure 5C). In addition, the hMSC spheroid-laden fibrin showed higher viability (91.2 ± 1.0%) on day 5 compared to hMSC spheroids that were directly encapsulated in PEG-alginate IPN hydrogel without printed fibrin gel (79.3 ± 1.8%) (Figure 5D). Furthermore, bioprinted hMSC spheroids that had their own soft pericellular matrix with the fibrin gel showed high viability compared with that of the simply mixed fibrin/PEG-alginate hydrogels (Figure 4K). The metabolic activity of hMSC spheroids within fibrin fibers that were printed in the PEG-alginate IPN hydrogel was significantly greater than that of spheroids cultured directly in the PEG-alginate hydrogel by day 3 and this increase was maintained over 7 days (Figure 5E). We assumed the soft fibrin gel could facilitate enhanced nutrient and oxygen diffusion compared to the PEG-alginate IPN hydrogel, resulting in higher viability and growth of spheroids and even induced cell spreading into the soft matrix (Lee et al., 2015). Therefore, these findings show the positive effects of a locally bioprinted soft pericellular matrix (kPa) on cell survival and metabolic activity within the stiff PEG-alginate hydrogel (MPa), indicating a potential for enhanced performance of hMSC spheroids.

We also assessed the chondrogenic activity of hMSC spheroids that were co-printed with fibrin gel in the PEG-alginate IPN hydrogel, and cultured in chondrogenic and regular media for 21 days. Chondrogenic differentiation was histologically visualized using Alcian blue for sulfated GAG's (Adolphe et al., 1996), and Picro-sirius red and Masson's trichrome for collagen (Junqueira et al., 1979). Mean pixel intensity of ECM deposition was determined using ImageJ software. Chondrogenic behavior and round morphology were observed in the hMSC spheroid-laden fibrin gel printed within the PEG-alginate IPN hydrogel under the chondrogenic

culture medium (Figure 5F (ii)). In addition, the formation of α-smooth muscle actin was observed in bioprinted spheroids stained with Picro-sirius red and Masson's trichrome (Figure S5, Supporting information). Actin is expressed by hMSCs during cell contraction, a cell-cell mechanism that drives chondrogenesis (Shu et al., 2009). Indeed, microaggregating cells in micrometer sized spheroids is known to favor chondrogenic differentiation (Leijten et al., 2016; Moreira Teixeira et al., 2012).

Differently, cells present in spheroids cultured in regular medium (control) showed greater eccentricity, or lengthening, which is characteristic of non-differentiated hMSCs (Haasters et al., 2009). Low deposition of GAG's and collagen were observed for bioprinted single cells-laden fibrin gel in the PEG-alginate IPN hydrogel, cultured in a chondrogenic medium (Figure 5F (iii)). These observations were in line with those reported in previous studies, reporting a higher capacity of hMSCs in spheroids to differentiate into chondrocytes in both *in vitro* and *in vivo* conditions, compared to single cells (Johnstone et al., 1998; Suzuki et al., 2012). Measurements of mean pixel intensity showed that an ECM deposited by bioprinted spheroids cultured in a chondrogenic medium had a significantly high color intensity compared to the two control samples (Figure 5G).

This work showed that hMSCs spheroids were successfully co-bioprinted with fibrin in a stiff and tough hydrogel, presenting high cell viability and a high capacity to differentiate into chondrocytes. Results indicated that the cartilage-like tissue engineering approach used here presents a great potential for further applications in cartilage regeneration studies.

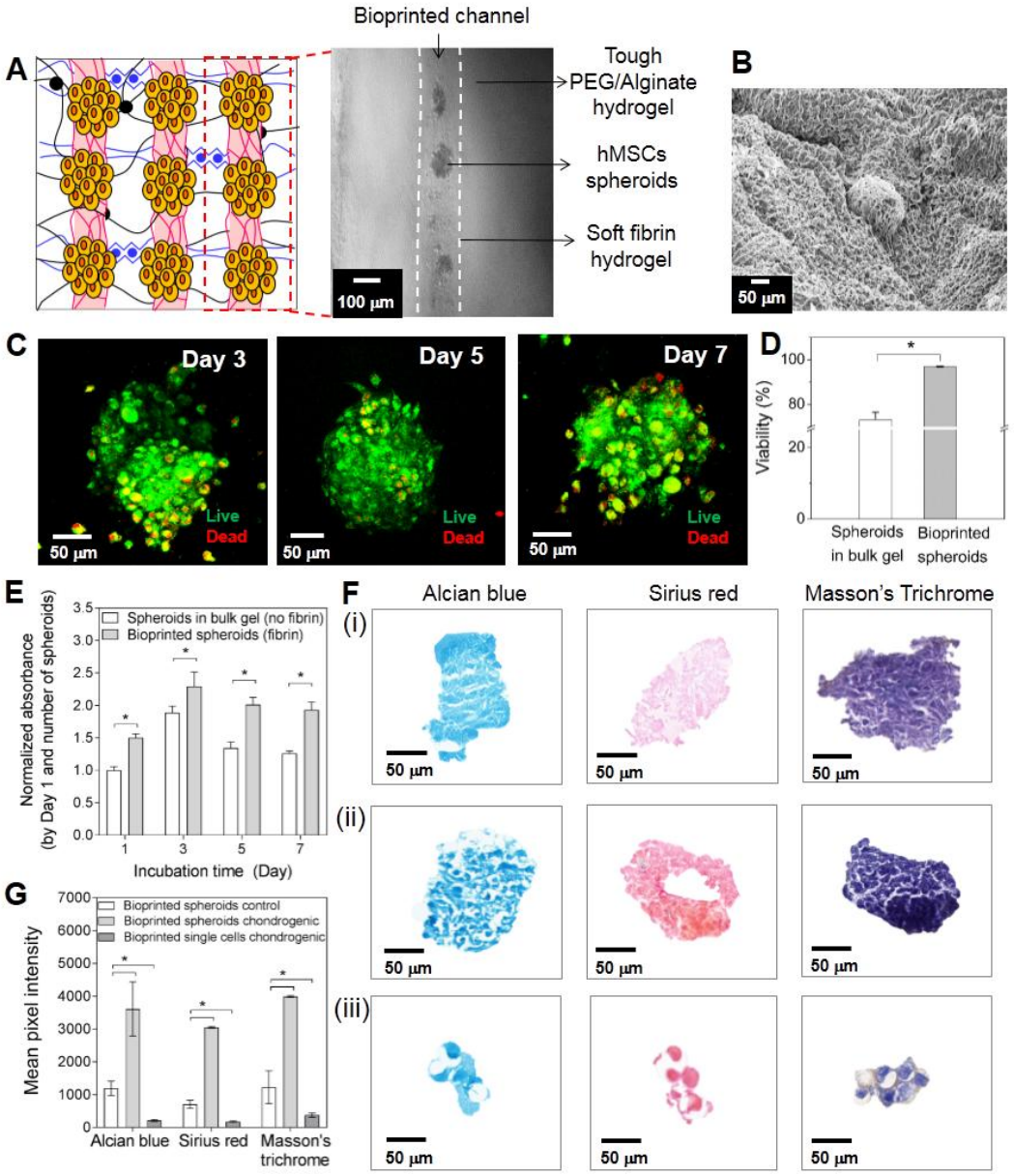

Figure 5. Characterization of bioprinted hMSCs spheroids in PEG-alginate hydrogel as a bioengineered cartilage construct. A) Bioprinted line showing a schematic illustration of the bioprinted spheroids in a tough hydrogel and a bright field image of the bioprinted line. B) Images captured by SEM of bioprinted spheroid-laden fibrin in a PEG-alginate hydrogel after 7 days. C) Live/dead images obtained by confocal of bioprinted spheroids on days 3, 5 and 7. D) Viability and E) Metabolic activity of spheroids in PEG-alginate and bioprinted spheroid-laden fibrin in PEG-alginate. F) Histological images of i) bioprinted spheroids cultured in regular medium (control), ii) chondrogenic medium and iii) single cells cultured in chondrogenic medium for 21 days and stained with Alcian blue for GAG's deposition, and Picro-sirius red and Masson's trichrome for collagen deposition. G) Mean pixel intensity of

stained bioprinted spheroids (in regular and chondrogenic medium) and bioprinted single cells (in chondrogenic medium) measured using the ImageJ software. *$p < 0.05$.

4. Conclusion

We have developed a cartilage-like tissue by 3D bioprinting hMSC spheroid-laden fibrin in a stiff and tough biomaterial. It was demonstrated that dual crosslinking of PEG-alginate resulted in IPN hydrogels with mechanical properties in the MPa range, which is comparable to that of the native tissue, indicating the ability to withstand the mechanical loads that articular cartilage is typically exposed to. In addition, IPN hydrogels showed a great capacity for resilience and elasticity, recovering their original shape after up to 40% compressive cyclic loadings. A low viscosity bioink composed of fibrin was successfully printed in vertically oriented arrays within the PEG-alginate supporting bath in a macroscale crack-free manner, due to the shear-thinning behavior of the mixture. The colloidal bioink composed of hMSCs spheroids embedded in fibrin was readily extruded through the nozzle without damaging the cells, allowing the material to mimic the overall articular cartilage organization abstractly. Bioprinted hMSCs spheroids showed significantly higher viability and metabolic activity after 7 days of culture as compared to spheroids in bulk PEG-alginate IPNs, demonstrating that the soft environment provided by fibrin and organized deposition contributed to cell survival. This environment favored chondrogenic differentiation, in which spheroids showed substantial GAG and collagen deposition after 3 weeks of culture. This innovative approach for cartilage-like tissue fabrication may be promising for further preclinical investigations of its utility for cartilage replacement and regeneration.

Acknowledgment

The authors declare no conflict of interests in this work. The authors acknowledge funding from the National Institutes of Health (R01AR074234 and R21EB026824) and the Qatar national Research Fund (a part of Qatar Foundation, NPRP9-144-3-021). S.R.S. would like to recognize and thank Brigham and Women's Hospital President Betsy Nabel, MD, and the Reny family, for the Stepping Strong Innovator Award through their generous funding. B.A.G.M. gratefully acknowledges funding by The São Paulo Research Foundation (FAPESP), (Process # 2017/02913-4). J.L. acknowledges financial support from an Innovative Research Incentives

Scheme Veni award (#14328) from the Netherlands Organization for Scientific Research (NWO), the European Research Council (ERC, Starting Grant, #759425), and the Dutch Arthritis Society (#17-1-405).

Supporting Information

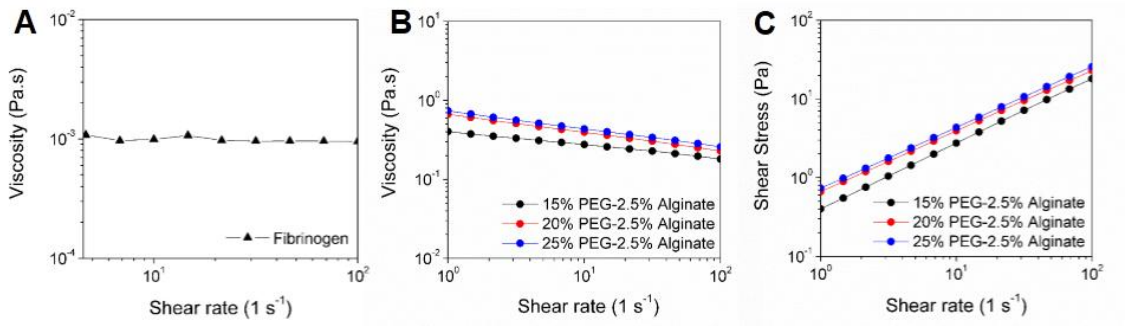

Figure S1. A) Shear rheology of the fibrinogen bioink, exhibiting a constant viscosity with shear that indicates Newtonian behavior. Shear rheology of pre-polymers 15, 20 and 15% PEG-2.5% alginate. B) Viscosity and C) shear stress as a function shear rate, showing the higher viscosity and pseudoplastic behavior for increased concentrations of PEG.

Table S1. Rheological characterization of the pre-polymers PEG-alginate by the power law model, showing their flow consistency index (*K*), and power law index (*n*).

	***K* (Pa.s^n)**	***n***
15% PEG-2.5% alginate	0.409	0.828
20% PEG-2.5% alginate	0.668	0.771
25% PEG-2.5% alginate	0.730	0.776

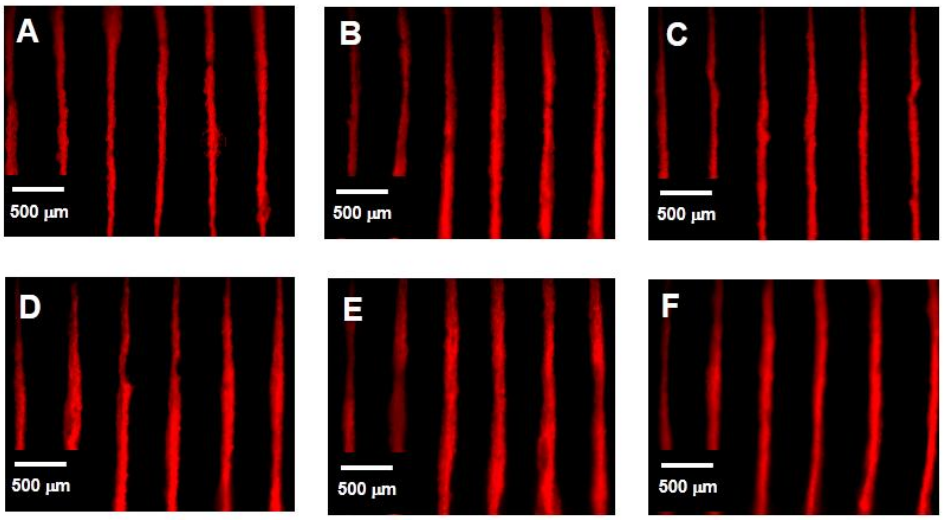

Figure S2. Optical images of bioprinted fibrin at different flow rates. A) 5, B) 6, C) 7, D) 8, E) 9 and F) 10 mL min^{-1} at a constant extrusion speed of 200 mm min^{-1}.

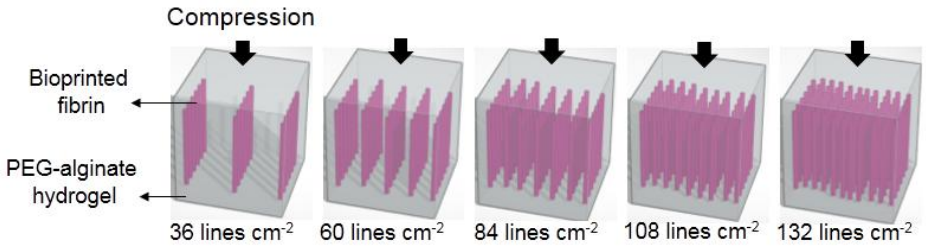

Figure S3. Schematic illustration showing the 5 different densities of vertical fibrin lines (compression perpendicular to the structure) printed in 20% PEG-2.5% alginate.

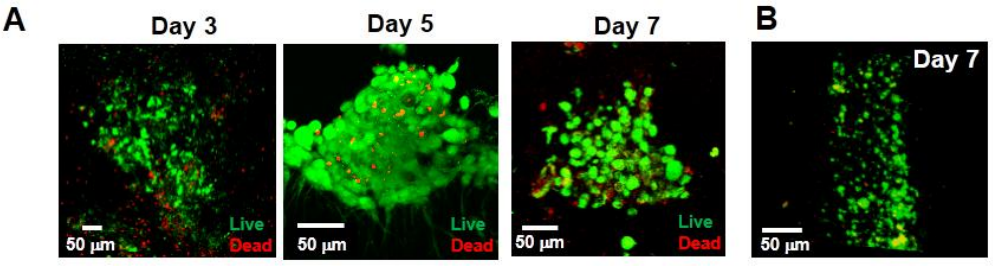

Figure S4. Live/dead images of A) hMSC spheroids-laden fibrin on days 3, 5, and 7 and B) bioprinted single cells-fibrin laden in PEG-alginate hydrogel on day 7.

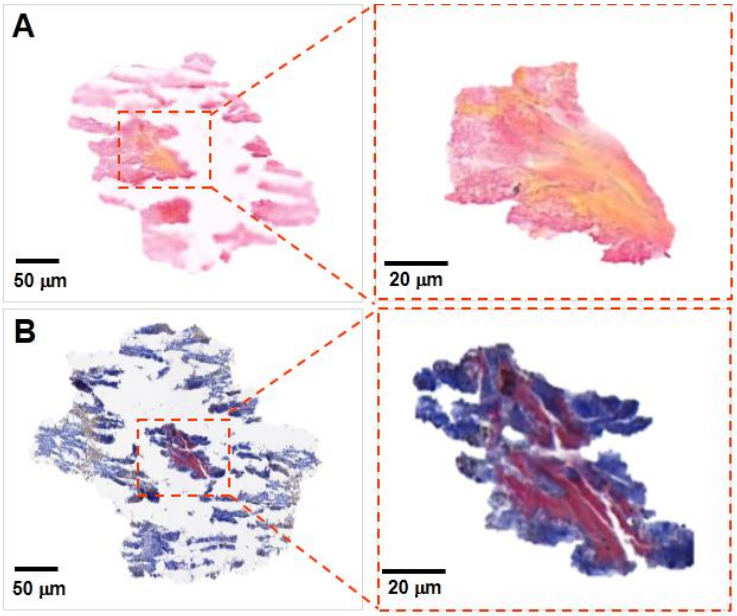

Figure S5. Histological images bioprinted spheroids cultured in chondrogenic medium for 21 days. A) Picro-sirius red and B) Masson's trichrome stain, highlighting the formation of α-smooth muscle actin.

Video S1. Crosslinked 20% PEG-2.5% alginate hydrogel under a compressive strain of 30% and returning to its original shape.

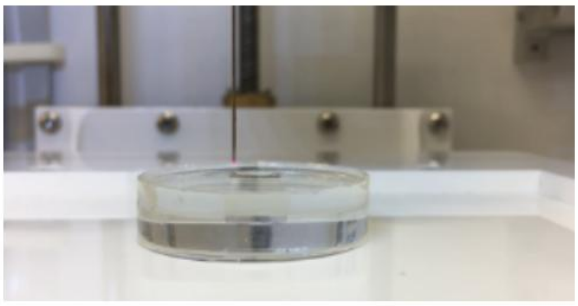

Video S2. Printing of fibrinogen stained pink in a 20% PEG-2.5% alginate bath supplemented with thrombin, allowing for fibrin crosslinking during printing.

References

Adolphe, M., Thenet-Gauci, S. and Demignot, S. (1996). Chondrocyte Culture: A Target System to Evaluate Pharmacotoxicological Effects of Drugs. In *In Vitro Methods in Pharmaceutical Research*, pp. 181–207.

Akkaya, A. (2017). Immobilization of Thrombin to Alginate Gel and. *J. Biol. Chem.* 45, 287–294.

Bajpai, A. K. and Shrivastava, M. (2002). Swelling kinetics of a hydrogel of poly(ethylene glycol) and poly(acrylamide-co-styrene). *J. Appl. Polym. Sci.* 85, 1419–1428.

Bartnikowski, M., Wellard, R. M., Woodruff, M. and Klein, T. (2015). Tailoring hydrogel viscoelasticity with physical and chemical crosslinking. *Polymers (Basel).* 7, 2650–2669.

Bas, O., De-Juan-Pardo, E. M., Meinert, C., D'Angella, D., Baldwin, J. G., Bray, L. J., Wellard, R. M., Kollmannsberger, S., Rank, E., Werner, C., et al. (2017). Biofabricated soft network composites for cartilage tissue engineering. *Biofabrication* 9,.

Bhise, N. S., Manoharan, V., Massa, S., Tamayol, A., Ghaderi, M., Miscuglio, M., Lang, Q., Zhang, Y. S., Shin, S. R., Calzone, G., et al. (2016). A liver-on-a-chip platform with bioprinted hepatic spheroids. *Biofabrication* 8,.

Bootsma, K., Fitzgerald, M. M., Free, B., Dimbath, E., Conjerti, J., Reese, G., Konkolewicz, D., Berberich, J. A. and Sparks, J. L. (2017). 3D printing of an interpenetrating network hydrogel material with tunable viscoelastic properties. *J. Mech. Behav. Biomed. Mater.* 70, 84–94.

Buxboim, A., Ivanovska, I. L. and Discher, D. E. (2010). Matrix elasticity, cytoskeletal forces and physics of the nucleus: how deeply do cells "feel" outside and in? *J. Cell Sci.* 123, 297–308.

Chen, P., Mckittrick, J. and Meyers, M. A. (2012). Biological materials: Functional adaptations and bioinspired designs. *Prog. Mater. Sci.* 57, 1492–1704.

Colosi, C., Shin, S. R., Manoharan, V., Massa, S., Costantini, M., Barbetta, A., Dokmeci, M. R., Dentini, M. and Khademhosseini, A. (2016). Microfluidic Bioprinting of Heterogeneous 3D Tissue Constructs Using Low-Viscosity Bioink. *Adv. Mater.* 28, 677–684a.

Constantini, M., Idaszek, J., Szöke, K., Jaroszewicz, J., Dentini, M., Barbetta, A., Brinchmann,

J. E. and Święszkowski, W. (2016). 3D bioprinting of BM--MSCs--loaded ECM biomimetic hydrogels for in vitro neocartilage formation. *Biofabrication* 8, 1–27.

Cui, X. and Boland, T. (2009). Human microvasculature fabrication using thermal inkjet printing technology. *Biomaterials* 30, 6221–6227.

Daly, A. C., Cunniffe, G. M., Sathy, B. N., Jeon, O., Alsberg, E. and Kelly, D. J. (2016). 3D Bioprinting of Developmentally Inspired Templates for Whole Bone Organ Engineering. *Adv. Healthc. Mater.* 5, 2353–2362.

Fu, Y., Karbaat, L., Wu, L., Leijten, J. C. H., Both, S. and Karperien, M. (2017). Trophic effects of mesenchymal stem cells in tissue regeneration. *Tissue Eng. Part B Rev.* 23, ten.TEB.2016.0365.

Fulcher, G. R., Hukins, D. W. L. and Shepherd, D. E. T. (2009). Viscoelastic properties of bovine articular cartilage attached to subchondral bone at high frequencies. *BMC Musculoskelet. Disord.* 10, 1–7.

Grillet, A. M., Wyatt, N. B. and Gloe, L. M. (2012). Polymer Gel Rheology and Adhesion. In *Rheology* (ed. Vicente, J. De), p. IntechOpen.

Guo, H. D., Cui, G. H., Wang, H. J. and Tan, Y. Z. (2010). Transplantation of marrow-derived cardiac stem cells carried in designer self-assembling peptide nanofibers improves cardiac function after myocardial infarction. *Biochem. Biophys. Res. Commun.* 399, 42–48.

Guo, T., Lembong, J., Zhang, L. G. and Fisher, J. P. (2017). Three-Dimensional Printing Articular Cartilage: Recapitulating the Complexity of Native Tissue. *Tissue Eng. Part B Rev.* 23, 225–236.

Haasters, F., Prall, W. C., Anz, D., Bourquin, C., Pautke, C., Endres, S., Mutschler, W., Docheva, D. and Schieker, M. (2009). Morphological and immunocytochemical characteristics indicate the yield of early progenitors and represent a quality control for human mesenchymal stem cell culturing. *J. Anat.* 214, 759–767.

Hendriks, J., Willem Visser, C., Henke, S., Leijten, J., Saris, D. B. F., Sun, C., Lohse, D. and Karperien, M. (2015). Optimizing cell viability in droplet-based cell deposition. *Sci. Rep.* 5, 1–10.

Highley, C. B., Rodell, C. B. and Burdick, J. A. (2015). Direct 3D Printing of Shear-Thinning Hydrogels into Self-Healing Hydrogels. *Adv. Mater.* 27, 5075–5079.

Hild, G. (1997). Interpretation of equilibrium swelling data on model networks using affine and ‘ phantom’ network models. *Polymer (Guildf).* 38, 3279–3293.

Hinton, T. J., Jallerat, Q., Palchesko, R. N., Park, J. H., Grodzicki, M. S., Shue, H.-J., Ramadan,

M. H., Hudson, A. R. and Feinberg, A. W. (2015). Three-dimensional printing of complex biological structures by freeform reversible embedding of suspended hydrogels. *Sci. Adv.* 1, e1500758–e1500758.

Hong, S., Sycks, D., Chan, H. F. a., Lin, S., Lopez, G. P., Guilak, F., Leong, K. W. and Zhao, X. (2015). 3D Printing of Highly Stretchable and Tough Hydrogels into Complex, Cellularized Structures. *Adv. Mater.* 27, 4034.

Huber, M., Trattnig, S. and Lintner, F. (2000). Anatomy, Biochemistry, and Physiology of Articular Cartilage : Investigative Radiology. *Invest. Radiol.* 35, 573–580.

Janmey, P. A., Winer, J. P., Murray, M. E. and Wen, Q. (2009). The Hard Life of Soft Cells. *Cell Motil Cytoskelet.* 66, 597–605.

Jeon, O., Alt, D. S., Linderman, S. W. and Alsberg, E. (2013). Biochemical and physical signal gradients in hydrogels to control stem cell behavior. *Adv. Mater.* 25, 6366–6372.

Jeon, O., Shin, J. Y., Marks, R., Hopkins, M., Kim, T. H., Park, H. H. and Alsberg, E. (2017). Highly elastic and tough interpenetrating polymer network-structured hybrid hydrogels for cyclic mechanical loading-enhanced tissue engineering. *Chem. Mater.* 29, 8425–8432.

Jeon, O., Lee, Y. B., Hinton, T. J., Feinberg, A. W. and Alsberg, E. (2019). Cryopreserved cell-laden alginate microgel bioink for 3D bioprinting of living tissues. *Mater. Today Chem.* 12, 61–70.

Johnstone, B., Hering, T. M., Caplan, A. I., Goldberg, V. M. and Yoo, J. U. (1998). In vitro chondrogenesis of bone marrow-derived mesenchymal progenitor cells. *Exp. Cell Res.* 272, 265–272.

Junqueira, L. C. U., Bignolas, G. and Brentani, R. R. (1979). Picrosirius staining plus polarization microscopy, a specific method for collagen detection in tissue sections. *Histochem. J.* 11, 447–455.

Klein, T. J., Rizzi, S. C., Reichert, J. C., Georgi, N., Malda, J., Schuurman, W., Crawford, R. W. and Hutmacher, D. W. (2009). Strategies for zonal cartilage repair using hydrogels. *Macromol. Biosci.* 9, 1049–1058.

Kosher, R. A., Kulyk, W. M. and Gay, S. W. (1986). Collagen gene expression during limb cartilage differentiation. *J. Cell Biol.* 102, 1151–1156.

Lee, B. H., Kim, M. H., Lee, J. H., Seliktar, D., Lay, N. J. C. and Tan, P. (2015). Modulation of Huh7.5 spheroid formation and functionality using modified peg-based hydrogels of different stiffness. *PLoS One* 10, 1–20.

Leijten, J., Moreira Teixeira, L. S., Bolander, J., Ji, W., Vanspauwen, B., Lammertyn, J.,

Schrooten, J. and Luyten, F. P. (2016). Bioinspired seeding of biomaterials using three dimensional microtissues induces chondrogenic stem cell differentiation and cartilage formation under growth factor free conditions. *Sci. Rep.* 6, 1–12.

Li, J., Suo, Z. and Vlassak, J. J. (2014). Stiff, strong, and tough hydrogels with good chemical stability. *J. Mater. Chem. B* 2, 6708–6713.

Li, H., Liu, S. and Lin, L. (2016). Rheological study on 3D printability of alginate hydrogel and effect of graphene oxide. *Int. J. Bioprinting* 2, 10–12.

Little, C., Kulyk, W. and Chen, X. (2014). The Effect of Chondroitin Sulphate and Hyaluronic Acid on Chondrocytes Cultured within a Fibrin-Alginate Hydrogel. *J. Funct. Biomater.* 5, 197–210.

Loebel, C., Rodell, C. B., Chen, M. H. and Burdick, J. A. (2017). Shear-thinning and self-healing hydrogels as injectable therapeutics and for 3D-printing. *Nat. Protoc.* 12, 1521–1541.

Moreira Teixeira, L. S., Leijten, J. C. H., Sobral, J., Jin, R., van Apeldoorn, A. A., Feijen, J., van Blitterswijk, C., Dijkstra, P. J. and Karperien, M. (2012). High throughput generated micro-aggregates of chondrocytes stimulate cartilage formation in vitro and in vivo. *Eur. Cells Mater.* 23, 387–399.

Moreno-Arotzena, O., Meier, J. G., Amo, C. Del and García-Aznar, J. M. (2015). Characterization of fibrin and collagen gels for engineering wound healing models. *Materials (Basel).* 8, 1636–1651.

Murphy, K. C., Fang, S. Y. and Leach, J. K. (2014). Human mesenchymal stem cell spheroids in fibrin hydrogels exhibit improved cell survival and potential for bone healing. *Cell Tissue Res.* 357, 91–99.

O'Connell, G., Garcia, J. and Amir, J. (2017). 3D Bioprinting: New Directions in Articular Cartilage Tissue Engineering. *ACS Biomater. Sci. Eng.* 3, 2657–2668.

Park, J. S., Chu, J. S., Tsou, A. D., Diop, R., Tang, Z., Wang, A. and Li, S. (2011a). The Effect of Matrix Stiffness on the Differentiation of Mesenchymal Stem Cells in Response to TGF-β. *Biomaterials* 32, 3921–3930.

Park, J. S., Yang, H. N., Woo, D. G., Jeon, S. Y. and Park, K. (2011b). Chondrogenesis of human mesenchymal stem cells in fibrin constructs evaluated in vitro and in nude mouse and rabbit defects models. *Biomaterials* 32, 1495–1507.

Perka, C., Spitzer, R. S., Lindenhayn, K., Sittinger, M. and Schultz, O. (2000). Matrix-mixed culture: New methodology for chondrocyte culture and preparation of cartilage

transplants. *J. Biomed. Mater. Res.* 49, 305–311.

Sakai, Y. and Nakazawa, K. (2007). Technique for the control of spheroid diameter using microfabricated chips. *Acta Biomater.* 3, 1033–1040.

Schinagl, R. M., Gurskis, D., Chen, A. C. and Sah, R. L. (1997). Depth-Dependent Confined Compression Modulus of Full-Thickness Bovine Articular Cartilage. *J. Orthop. Res.* 15, 499–506.

Sheykhhasan, M., Qomi, R. T. and Ghiasi, M. (2015). Fibrin Scaffolds Designing in order to Human Adipose-derived Mesenchymal Stem Cells Differentiation to Chondrocytes in the Presence of TGF- β 3. *Int. J. Stem Cells* 8, 219–227.

Shu, K., Thatte, H. and Spector, M. (2009). Chondrogenic differentiation of adult mesenchymal stem cells and embryonic stem cells. *2009 IEEE 35th Annu. Northeast Bioeng. Conf.*

Smeets, B., Alert, R., Pešek, J., Pagonabarraga, I., Ramon, H. and Vincent, R. (2016). Emergent structures and dynamics of cell colonies by contact inhibition of locomotion. *Proc. Natl. Acad. Sci.* 113, 14621–14626.

Song, K. H., Highley, C. B., Rouff, A. and Burdick, J. A. (2018). Complex 3D-Printed Microchannels within Cell-Degradable Hydrogels. *Adv. Funct. Mater.* 28, 1–10.

Sun, J. Y., Zhao, X., Illeperuma, W. R. K., Chaudhuri, O., Oh, K. H., Mooney, D. J., Vlassak, J. J. and Suo, Z. (2012). Highly stretchable and tough hydrogels. *Nature* 489, 133–136.

Suzuki, S., Muneta, T., Tsuji, K., Ichinose, S., Makino, H., Umezawa, A. and Sekiya, I. (2012). Properties and usefulness of aggregates of synovial mesenchymal stem cells as a source for cartilage regeneration. *Arthritis Res. Ther.* 14,.

Zhang, Q., Yu, Y. and Zhao, H. (2016). The effect of matrix stiffness on biomechanical properties of chondrocytes. *Acta Biochim. Biophys. Sin. (Shanghai).* 48, 958–965.

Zhu, K., Shin, S. R., van Kempen, T., Li, Y. C., Ponraj, V., Nasajpour, A., Mandla, S., Hu, N., Liu, X., Leijten, J., et al. (2017). Gold Nanocomposite Bioink for Printing 3D Cardiac Constructs. *Adv. Funct. Mater.* 27,.